

**Tunable photoluminescence from rare
earth and transition metal ions activated silicate
glasses and glass ceramics**

Dissertation

zur Erlangung des akademischen Grades Doktor-Ingenieur
(Dr. -Ing.)

vorgelegt dem Rat der Chemisch-Geowissenschaftlichen Fakultät der
Friedrich-Schiller-Universität Jena

von M.Sc. Guojun Gao

geboren am 14.01.1983 in Shanxi, China

Gutachter:

1. Prof. Dr. Lothar Wondraczek, Otto-Schott Institut für Materialforschung
2. HDoz. Dr. Doris Ehrt, Otto-Schott Institut für Materialforschung

Tag der öffentlichen Verteidigung: 06.11.2013

The experimental work for this thesis was carried out primarily at the Chair of Glass and Ceramics (WW3), Department of Materials Science, University of Erlangen-Nuremberg from October 1st 2009 to January 31th 2013, and partly at the Otto-Schott-Institut, University of Jena from February 1st 2013 to August 1st 2013, all the time under the supervision of Prof. Dr. Lothar Wondraczek.

Die experimentelle Arbeit für diese Promotion wurde vornehmlich am Lehrstuhl für Glas und Keramik (WW3), Abteilung Werkstoffwissenschaften der Friedrich-Alexander-Universität Erlangen-Nürnberg vom 1. Oktober 2009 bis 31. Januar 2013 und vom 1. Februar 2013 bis 1. August 2013 am Otto-Schott-Institut, Friedrich-Schiller-Universität Jena, jeweils unter der Betreuung von Prof. Dr. Lothar Wondraczek durchgeführt.

Contents

List of symbols and abbreviations	I
Hypothesis	III
Abstract.....	VI
1. Introduction	1
1.1. Motivation	1
1.2. Photoluminescence	4
1.3. Rare earth ions	8
1.3.1. Energy transfer	12
1.3.2. Line-type $4f^n \rightarrow 4f^n$ PL.....	13
1.3.3. Band-type $4f^{n-1}5d \rightarrow 4f^n$ PL.....	19
1.4. Transition metal ions	23
1.4.1. Octahedrally coordinated TM ions	24
1.4.2. Tetrahedrally coordinated TM ions	27
1.4.3. Other TM ion: $V^{5+}(3d^0)$	29
1.5. White light-emitting diodes	30
1.6. Solar cells	32
1.6.1. Down-shifting.....	33
1.6.2. Up-conversion	34
1.6.3. Down-conversion	35
1.7. Glasses and glass ceramics	36
1.7.1. Glasses.....	36
1.7.2. Glass ceramics	37
2. Cumulative summary.....	40
2.1. Enhanced photoluminescence from mixed-valence Eu-doped nanocrystalline silicate glass ceramics	40
2.2. Tunable dual-mode photoluminescence from nanocrystalline Eu-doped Li_2ZnSiO_4 glass ceramic phosphors	50
2.3. Enhanced broadband green and red photoluminescence from transparent Mn^{2+} -doped nanocrystallized silicate glass ceramics.....	57
2.4. Broadband UV-to-green photoconversion in V-doped lithium zinc silicate glasses and glass ceramics.....	63

2.5. Broadband NIR photoluminescence from Ni ²⁺ -doped nanocrystalline Ba–Al titanate glass ceramics	71
2.6. Temperature dependence and quantum efficiency of ultrabroad NIR photoluminescence from Ni ²⁺ centers in nanocrystalline Ba–Al titanate glass ceramics	79
2.7. Near-infrared downconversion in Pr ³⁺ /Yb ³⁺ co-doped boro-aluminosilicate glasses and LaBO ₃ glass ceramics	83
2.8. Near-Infrared down-conversion in Mn ²⁺ –Yb ³⁺ co-doped Zn ₂ GeO ₄	96
2.9. Thermal collapse of SAPO-34 molecular sieve towards a perfect glass.....	104
3. Summary.....	110
4. Zusammenfassung	113
5. References	117
Acknowledgements	123
List of publications	126
Oral presentations	127
Posters.....	128
Lebenslauf	129
Declaration of authorship/Selbständigkeitserklärung.....	130

List of symbols and abbreviations

CIE	Commission International d'Eclairage
CN	coordination number
CRI	color rendering index
CT	charge transfer
CW	continuous-wave
DSC	differential scanning calorimetry
DTA	differential thermal analysis
EDFAs	erbium doped fiber amplifiers
ESA	excited state absorption
ESR	electron spin resonance
ETE	energy transfer efficiency
ETU	energy transfer up-conversion
FEDs	field emission displays
FTIR	Fourier transform infrared spectroscopy
FWHM	full width at half maximum
GSA	ground state absorption
JCPDS	joint committee on powder diffraction standards
J-O	Judd-Ofelt
LCDs	liquid crystal displays
LDs	laser diodes
Ln^{2+}	divalent lanthanide ion
Ln^{3+}	trivalent lanthanide ion
MIR	middle infrared
NIR	near infrared
NUV	near-ultraviolet
PA	photon avalanche
pc-WLEDs	phosphor-converted W-LEDs
PDPs	plasma display panels
PL	photoluminescence
PLE	photoluminescence excitation
PMT	photomultiplier tube
RE	rare earth
SABBL	$\text{SiO}_2\text{-Al}_2\text{O}_3\text{-B}_2\text{O}_3\text{-BaO-L}_2\text{O}_3$

SEM	scanning electron microscope
SLABS	SrO–La ₂ O ₃ –Al ₂ O ₃ –B ₂ O ₃ –SiO ₂
SLZAKP	SiO ₂ –Li ₂ O–ZnO–Al ₂ O ₃ –K ₂ O–P ₂ O ₅
TBSA	TiO ₂ –BaO–SiO ₂ –Al ₂ O ₃
TCSPC	time correlated single photon counting
TEM	transmission electron microscopy
T _g	glass transition temperature
TM	transition metal
T _p	glass crystallization peak temperature
UV	ultraviolet
Vis	visible
WDM	wavelength division multi-plexing
W-LEDs	white light-emitting diodes
XPS	X-ray photoelectron spectroscopy
XRD	X-ray diffractometry
η _{EQE}	external quantum efficiency
η _{IQE}	internal quantum efficiency
λ	wavelength, lambda
τ	lifetime

Hypothesis

Glass phosphors activated by rare earth (RE) and transition metal (TM) ions have been well accepted and they have broad applications in many areas, due to their unique properties, e.g., easy mass production and easy fabrication into various shapes such as fibers and large size plates.¹⁻¹⁰ Firstly, they have been widely used as laser materials.⁴⁻⁶ One good example is erbium doped fiber amplifiers (EDFAs), which have been commonly used for telecommunication. Another example is Nd³⁺ doped phosphate glasses which are used as laser medium in extremely high power (terawatt scale) lasers. Secondly, they have been widely reported in literature as red, green and blue emitting phosphors in combination with near-ultraviolet- (NUV) and blue-light-emitting diodes (LEDs) to create white light emission for solid state lighting.^{7,8} Thirdly, they also have great potential to be used as spectral converters to improve the solar energy harvesting by up-, down-conversion, and down shifting processes.^{9,10}

However, due to inhomogeneous broadening, the absorption and emission cross section of the dopant ions in a glass are normally much smaller than in a crystal host.^{11,12} This intrinsic disadvantage of glasses results in low external quantum efficiency (η_{EQE}) of dopant ions and thus greatly limits their large scale applications in aforementioned areas. Glass ceramics which combine the advantages of amorphous and crystalline phosphors are attractive candidates to break this limit. As a prerequisite to get a practically usable glass ceramic phosphor, the crystal phases must be deposited homogeneously in the glass body (bulk crystallization), the crystal size must be controlled normally in nm scale, and dopant ions must actually enter the crystal phases rather than remaining in the residual glass phase. But glass ceramics which meet these conditions are rather limited. Fundamental for this thesis is the anticipation, that the precipitated crystalline phases will be specifically selected in order to stabilize RE or TM ions, provide a specific coordination environment for Tm ions, and offer the possibility of intrinsic reduction of RE ions.¹³⁻¹⁶ Consequently, different types of silicate glass ceramics are developed to realize improved photoluminescence (PL) properties of RE and TM ions activated glass ceramic phosphors. In this thesis, the advantages and disadvantages of glass and glass ceramic phosphors in their practical applications will be discussed in detail.

Glass ceramics containing Eu³⁺ and Eu²⁺ are especially interesting as control of the relative Eu²⁺ and Eu³⁺ PL intensity may lead to glass ceramics with tunable dual-mode PL of from blue (Eu²⁺) to red (Eu³⁺). In order to incorporate and stabilize the relatively large Eu²⁺ and Eu³⁺ ions (i.e., ionic radii of 117.0 and 94.7 pm, respectively, in octahedral

sites¹⁷⁾ in the crystalline phases, glass ceramics with relatively large lattice sites are selected, e.g., BaAl₂Si₂O₈/LaBO₃¹⁸ and Li₂ZnSiO₄¹⁹. For BaAl₂Si₂O₈/LaBO₃ glass ceramics, Eu³⁺ species may be incorporated on La³⁺ sites in LaBO₃ crystallites, which may lead to enhanced PL intensity of Eu³⁺. More interestingly, Eu³⁺ species may also be incorporated on Ba²⁺ sites in BaAl₂Si₂O₈ crystallites. Like in crystalline phosphors, such incorporation may reduce Eu³⁺ to Eu²⁺, which could be applied in tuning the dual-mode PL.¹⁶ Correspondingly, for Li₂ZnSiO₄ glass ceramics, Eu³⁺ species may be partially incorporated on Zn²⁺ sites in Li₂ZnSiO₄ crystallites and reduced to Eu²⁺. Both glass ceramic systems may thus offer routes to obtain tunable dual-mode PL.

Li₂ZnSiO₄ glass ceramic systems may also be used for the stabilization of TM ions, (e.g., Mn²⁺ and V⁵⁺), whose PL properties are sensitive to their local environment.^{20–24} Normally, in a glass host, Mn²⁺ ions are octahedrally coordinated (^{IV}Mn²⁺) and show a broad PL from orange to red.²² During crystallization, Mn²⁺ ions may be incorporated into the tetrahedral Zn²⁺ sites of the Li₂ZnSiO₄ crystalline phase, enabling the relatively sharp green emission of ^{IV}Mn²⁺. Consequently, the ratio of [^{IV}Mn²⁺]/[^{VI}Mn²⁺] and the emission color may be tailored by the degree of crystallization in this glass ceramic system.

The broad green PL (~400–700 nm) as well as broad excitation band (~200–400 nm) of V⁵⁺ allows its applications in many areas.^{23,24} Nevertheless, the knowledge on the PL properties of V⁵⁺ doped glasses and in particular glass ceramics is limited, and the luminescence is rarely observed. V⁵⁺ may exhibit broad green PL band in glass host at room temperature. It is expected, that the incorporation of V⁵⁺ in the Li₂ZnSiO₄ crystalline phase may result in an enhanced PL intensity from V⁵⁺.

The PL properties of Ni²⁺ are strongly dependent on the coordination number (CN) of Ni²⁺.^{25–27} In general, there are three possible CN for Ni²⁺ in solid matrices, but only octahedrally coordinated ^{VI}Ni²⁺ gives rise to broadband NIR PL, which permits its applications in tunable lasers and optical amplifiers.²⁷ Perovskite-type BaTiO₃ based glass ceramics, which offers one potential octahedral ^{VI}Ti⁴⁺ (60.5 pm) site for ^{VI}Ni²⁺ (69.0 pm) ions, are chosen for the present study.¹⁷ Glass ceramic systems of this type may thus offer a good way of controlling the CN of Ni²⁺, which may lead to efficient NIR PL of ^{VI}Ni²⁺.

In down-conversion processes, Pr³⁺ ions are known as good sensitizers for Yb³⁺ by absorbing photons in the range of 415–505 nm and transferring the absorbed energy to Yb³⁺ ions, resulting in an emission at ~1000 nm.²⁸ A borosilicate glass matrix is excellent host material for Yb³⁺ and Pr³⁺ due to well controlled and homogeneous doping of Yb³⁺ and Pr³⁺ ions.⁶ It is expected, that precipitation of a crystalline phase (e.g., LaBO₃²⁹) incorporating both Yb³⁺ and Pr³⁺ species will improve PL properties.

Another potential sensitizer for the Yb^{3+} ion is Mn^{2+} due to its broad absorption band in the range of 320–550 nm.²⁰⁻²² Crystalline Zn_2GeO_4 is chosen as host materials for Mn^{2+} , due to its broad absorption band in the range of ~280–400 nm, which can efficiently transfer the corresponding energy to Mn^{2+} .³⁰ The absorbed energy of $\text{Zn}_2\text{GeO}_4:\text{Mn}^{2+}$ in the UV-Vis region (280–550 nm) arising from Zn_2GeO_4 host lattice and Mn^{2+} ions is expected to be transferred to Yb^{3+} ions.

Abstract

Inorganic materials doped with RE and TM ions have attracted extensive attention over recent decades owing to their wide applicability in phosphors, imaging, lasers and displays.¹⁻³ In this thesis, silicate glasses and especially the corresponding glass ceramics are used as host materials for RE and TM ions due to their easy fabrication, broad compositional flexibility, high homogeneity, well-controlled dopant concentration, and good optical activity for dopants.¹³⁻¹⁵

The motivation of this thesis is given in the introduction, followed by the corresponding background. The key conception of PL is then explained. Following this, the origin and properties of PL induced by RE and TM ions are summarized. Thereafter, the background of white light-emitting diodes (W-LEDs) and solar cells is presented. Finally, the history and properties of the glasses and glass ceramics are reviewed.

The second chapter gives the results and discussions in the form of a list of publications in peer reviewed journals. Firstly, tunable dual-mode and enhanced PL of mixed valence $\text{Eu}^{3+}/\text{Eu}^{2+}$ doped silicate glasses and glass ceramics are investigated. A glass ceramic route of reducing Eu^{3+} to Eu^{2+} is demonstrated. During the controlled nucleation and crystallization processes in a normal atmosphere, Eu^{3+} ions are partially incorporated into the newly deposited crystalline phases, (i.e., $\text{BaAl}_2\text{Si}_2\text{O}_8/\text{LaBO}_3$ and $\text{Li}_2\text{ZnSiO}_4$), and gradually reduced to Eu^{2+} due to the charge compensation effect. Furthermore, it is investigated how to obtain and control the band-type blue PL of Eu^{2+} and the line-type red PL of Eu^{3+} in these glass ceramics by tunable ratio of $\text{Eu}^{2+}/\text{Eu}^{3+}$. A mechanism for the internal reduction of Eu^{3+} to Eu^{2+} is proposed. For $\text{SiO}_2\text{-Al}_2\text{O}_3\text{-B}_2\text{O}_3\text{-BaO-L}_2\text{O}_3$ (SABBL) glass and corresponding $\text{BaAl}_2\text{Si}_2\text{O}_8/\text{LaBO}_3$ glass ceramics, crystallization at elevated temperatures also results in the enhancement of PL intensity and PL lifetime of $\text{Eu}^{3+}:^5\text{D}_0$ state. Eu^{3+} species are mostly incorporated on La^{3+} sites in LaBO_3 crystallites, whereas the Eu^{2+} ions are located on Ba^{2+} sites in the hexacelsian phase. For $\text{SiO}_2\text{-Li}_2\text{O-ZnO-Al}_2\text{O}_3\text{-K}_2\text{O-P}_2\text{O}_5$ (SLZAKP) $\text{Li}_2\text{ZnSiO}_4$ glass ceramic, tunable dual-mode PL can be generated. The resulting PL color, ranging from orange/red to blue, can be tuned by adjusting the annealing temperature and the degree of crystallization.

Secondly, tunable $[\text{IVMn}^{2+}]/[\text{VMn}^{2+}]$ PL properties of $\text{Li}_{4-2(x+y)}\text{Zn}_x\text{Mn}_y\text{SiO}_4$ glass ceramics are displayed. The PL color of Mn^{2+} is sensitive to the local environment. The Mn^{2+} ions are octahedrally coordinated in the SLZAKP precursor glass and show broad orange to red emission. During the controlled crystallization process, Mn^{2+} can be partially incorporated into the crystalline phase, which offers tetrahedral sites for Mn^{2+} species,

giving rise to the green emission of ${}^{\text{IV}}\text{Mn}^{2+}$. Consequently, the ratio of $[\text{IVMn}^{2+}]/[\text{VMn}^{2+}]$ and the emission color can be tailored by the degree of crystallization in the glass ceramic. It is demonstrated how such tuned dual-mode luminescence can be obtained in Mn^{2+} doped $\text{Li}_2\text{ZnSiO}_4$ glass ceramics.

Thirdly, the investigations on broadband green PL of V^{5+} doped lithium zinc silicate glasses and corresponding nanocrystalline $\text{Li}_2\text{ZnSiO}_4$ glass ceramics with possible use as broadband UV-to-Vis photoconverters are presented. The V^{5+} ion shows a broad PL band from 400 to 700 nm and is a potential green emitting activator center. In the investigated glass system, visible PL from $[\text{VO}_4]^{3-}$ is centered at 550–590 nm and occurs over a full width at half maximum (FWHM) of ~ 250 nm with a lifetime of ~ 34 μs , depending on dopant concentration and synthesis conditions. The corresponding excitation band covers the complete UV-B to UV-A spectral region. After crystallization, a tenfold increase in the emission intensity is observed.

Fourthly, broadband NIR PL of ${}^{\text{VI}}\text{Ni}^{2+}$ doped nanocrystalline Ba-Al titanate glass ceramics from $\text{TiO}_2\text{-BaO-SiO}_2\text{-Al}_2\text{O}_3$ (TBSA) glass is investigated. The CN of Ni^{2+} is well controlled by the crystallization process. Ni^{2+} ions are tetrahedrally coordinated in precursor glasses, whereas Ni^{2+} -species are incorporated into the crystalline environment in octahedral sites. The broadband NIR PL of ${}^{\text{VI}}\text{Ni}^{2+}$ spans the spectral range of 1.0–1.6 μm with a FWHM greater than 300 nm and a lifetime of ~ 60 μs . For UV-LED excitation at 352 nm, an internal quantum efficiency (η_{IQE}) of 65% is obtained. Decay kinetics as well as position and shape of the emission band can be adjusted by dopant concentration and synthesis conditions.

Lastly in this chapter, down-conversion based on $\text{Pr}^{3+}/\text{Yb}^{3+}$ and $\text{Mn}^{2+}/\text{Yb}^{3+}$ pairs is presented in two different systems. In the first system, down-conversion of one blue photon to two NIR photons ($\sim 10,000$ cm^{-1}) is obtained from the $\text{Pr}^{3+}/\text{Yb}^{3+}$ co-doped $\text{SrO-La}_2\text{O}_3\text{-Al}_2\text{O}_3\text{-B}_2\text{O}_3\text{-SiO}_2$ (SLABS) glasses and the corresponding LaBO_3 glass ceramics. Pr^{3+} ions act as sensitizers by absorbing 415–505 nm photons and transferring the absorbed energy to Yb^{3+} ions in a cooperative down-conversion process resulting in NIR emission at ~ 1000 nm. The energy transfer from Pr^{3+} to Yb^{3+} is indicated by decreased intensity of all Pr^{3+} PL lines and lifetimes of both $\text{Pr}^{3+}:{}^3\text{P}_0$ and $\text{Pr}^{3+}:{}^1\text{D}_2$ levels with increasing Yb^{3+} doping concentration. The optimal doping concentration of Yb_2O_3 for down-conversion is ~ 0.5 mol% and the highest total theoretical quantum efficiency is as high as 183% for 5 mol% Yb^{3+} doped glass. After crystallization, both Pr^{3+} and Yb^{3+} ions occupy the La^{3+} ion sites in the LaBO_3 crystal structure, resulting in improved PL properties. For the second system, NIR down-conversion by $\text{Mn}^{2+}/\text{Yb}^{3+}$ pair in crystalline $\text{Zn}_{1.96-}$

$x\text{GeO}_{4+1/2x}:\text{Mn}_{0.04}\text{Yb}_x$ is presented. In the Zn_2GeO_4 lattice, intrinsic defect transitions and Mn^{2+} ions act as broadband spectral sensitizers by absorbing UV-Vis (280–500 nm) photons. The absorbed energy is transferred to Yb^{3+} ions in a cooperative down-conversion process, resulting in NIR emission at ~ 1000 nm. The sharp decrease in the excited state lifetime and the green PL from tetrahedrally coordinated ${}^{\text{IV}}\text{Mn}^{2+}$ with increasing Yb^{3+} concentration reflects the efficient energy transfer from Mn^{2+} to Yb^{3+} . Maximal energy transfer efficiency (ETE) from Mn^{2+} to Yb^{3+} and total theoretical quantum efficiency of 63.8% and 163.8% are estimated, respectively.

The third chapter summarizes the thesis

1. Introduction

1.1. Motivation

Oxide glasses and glass ceramics are well known host materials for RE and TM ions.¹⁻³ In 1961, one of the first solid state lasers operating at 1.06 μm utilized Nd^{3+} doped glass.³¹ Glass ceramics permit the use of all the advantages of glass processing, such as broad compositional flexibility, high homogeneity, well-controlled dopant concentration and easy fabrication.¹³⁻¹⁵ During controlled heat treatment, one or more crystalline phases are precipitated in the base glass matrix, preferably by internal nucleation without affecting macroscopic geometry of the as-processed body. The properties of glass ceramic are mainly determined by the precipitated crystallite species, which can be adjusted by the glass composition and the applied annealing procedure. RE and TM ions can be incorporated into these crystal phases because of the correlation of their ionic radii and valence states to those of the atoms in the lattice sites. Consequently, PL properties can be improved by multiple scattering at the glass-crystal interface, the changing of ligand field around the dopants, the absorption cross-section of the dopants, and the phonon energy (which, if decreased, may reduce the probability of non-radiative processes). These changes may lead to increased PL intensity, enhanced η_{IQE} and longer PL lifetime of dopants. As a prerequisite to get a practically usable glass ceramic phosphor, the crystal phases must be deposited homogeneously in the glass body (bulk crystallization), and RE and TM ions must actually enter the crystal phases rather than remaining in the residual glass phase. However, glass ceramics suitable for hosting TM and RE ions can only be obtained from a limited number of glass compositions. While some glasses are too stable to crystallize; other glasses crystallize uncontrollable, resulting in undesirable microstructures. In this thesis, several RE and TM ions activated glasses and glass ceramics with controllable crystallization are studied systematically for improved PL properties. More specifically, the controlled formation of glass ceramics from specific systems with specific dopants will be applied in answers to a row of significant challenges for glass ceramic phosphors.

Zukauskas *et al.*³² reported that the optimal red light-emitting phosphors for a warm white light-emitting diode (W-LED) with a high lumen output and color rendering should have a narrow band emission with a FWHM < 30 nm in the spectral region of 615–655 nm. The background of W-LEDs is shown in detail in Chapter 1.5. As efficient red light-

emitting phosphors, Eu^{3+} doped inorganic materials meet these conditions.³³ The PL spectrum of Eu^{3+} is composed of various sharp PL lines in the orange to red spectral region arising from the intra-configurational parity-forbidden $4f \rightarrow 4f$ electronic transitions.^{34–39} Due to this shielding effect by the outer $5s^2$ and $5p^6$ shells, the $4f \rightarrow 4f$ transitions of Eu^{3+} ions are independent on the host materials. Because a glass lacks a center of symmetry, the $4f$ orbitals of Eu^{3+} can mix with opposite parity orbitals.⁴⁰ As a result, the red emission line at ~ 610 nm due to the electric-dipole allowed transition of $\text{Eu}^{3+}: ^5\text{D}_0 \rightarrow ^7\text{F}_2$ dominate the PL spectra in glass phosphors, therefore, the PL of Eu^{3+} doped glasses shows excellent red CRI.⁴⁰

As an efficient light-emitting activator center, Eu^{2+} shows a broad band-type PL due to the spin-allowed inter-configurational transition of $5d \rightarrow 4f$.^{41–44} The outer $5d$ electron of Eu^{2+} is not completely shielded by the surrounding ligands, and the position and width of the PL excitation (PLE) and PL band is strongly dependent on its local environment. Eu^{2+} and Eu^{3+} activated oxide glasses and glass ceramics possessing all the advantages of glass processing could have potential advantageous application in phosphor-converted W-LEDs (pc-WLEDs).^{45–47} However, europium exists mainly as their most stable trivalent oxidation state in nature. Stabilization of Eu^{2+} in host materials has been a research topic in last decade. Four reducing strategies of Eu^{3+} to Eu^{2+} have been developed, and they will be reviewed in chapter 1.3.3. A glass ceramic route to stabilize Eu^{2+} is by intrinsic reduction investigated in this thesis. The method may greatly improve the PL properties of Eu^{3+} and stabilize Eu^{2+} in crystalline phases, resulting in tunable PL properties of $\text{Eu}^{2+}/\text{Eu}^{3+}$.

Mn^{2+} activated inorganic materials show a broad PL band varying from deep green to far red due to the parity-forbidden transition of $3d \rightarrow 3d$. The emission color of Mn^{2+} is sensitive to its local environment.^{20–22} In an octahedral environment, Mn^{2+} presents a broad orange to red PL, whereas Mn^{2+} shows a relatively narrow green PL in a tetrahedral environment. Tunable dual-mode PL of Mn^{2+} from green to red is expected, when the CN of Mn^{2+} can be controlled in a host material. The Mn^{2+} ions are octahedrally coordinated in the precursor glass, while during the controlled crystallization process, Mn^{2+} can be partially incorporated into the crystalline phase, which may offer tetrahedral sites for Mn^{2+} . In this thesis, it is demonstrated how the CN of Mn^{2+} and tuned dual-mode PL can be obtained and controlled in Mn^{2+} doped $\text{Li}_2\text{ZnSiO}_4$ glass ceramics.

V^{5+} ions show a broad green PL band from 400 to 700 nm due to the relaxation of $\equiv\text{V}-\text{O}^-$ to $\equiv\text{V}=\text{O}$.^{23,24} The corresponding PLE band from ~ 200 to 400 nm covers the complete UV-B (280–315 nm) to UV-A (315–380 nm) spectral region. The broad green PL band as well as broad PLE band of V^{5+} from UV-A to UV-B allow its applications in many areas,

including solar energy harvesting, luminescent lighting, UV-detection and imaging. However, the PL properties of V^{5+} doped glasses and in particular glass ceramics are seldom reported. In this thesis, it is demonstrated how dopant concentration and synthesis conditions influence on the broad green PL band of V^{5+} in a V^{5+} doped zinc silicate model glass. Crystallization of the precursor glass is performed to further optimize the optical properties of V^{5+} .

The spectroscopic properties of $VI Ni^{2+}$ doped glasses, glass ceramics and single crystals have attracted great attention over the last decade due to the broad band-type NIR PL of $VI Ni^{2+}$.²⁵⁻²⁷ Efficient NIR PL has been reported on $VI Ni^{2+}$ activated single crystals, (e.g., $LiGa_5O_8$ and MgF_2).²⁶ However, the complex fabrication processes and poor machinability into special shapes severely limit their applications. Interestingly, these drawbacks can be overcome by the glass ceramic route if the Ni^{2+} species could precipitate into the crystalline phase on octahedral sites rather than remaining in the residual glass phase, in which they are fivefold coordinated. In order to ensure optical transparency and a high crystallite volume fraction, the crystalline phase must be homogeneously distributed, with crystal sizes of not larger than several tens of nanometers. With these objectives, nanocrystallized $MgGa_2O_4:VI Ni^{2+}$ and $\beta-Ga_2O_3:VI Ni^{2+}$ glass ceramics featuring the efficient NIR PL have been reported by Suzuki²⁷ and Zhou⁴⁸ respectively. However, for these phosphors high cost of the raw materials (i.e., Ga_2O_3) limits their practical applicability. In this thesis, a nanocrystalline Ba-Al hollandite ($Ba_{1.24}(Al_{2.48}Ti_{5.52})O_{16}$) glass ceramic based on TBSA glasses for $VI Ni^{2+}$ species has been studied.

Down-conversion of one UV-Vis photon of high energy to two or more NIR photons of high energy is one of the potential routes to overcome the Shockley-Queisser limit of solar cells by the modification of the solar spectrum to better match the solar cells.⁴⁹⁻⁵⁴ Considering the energy level of all Ln^{3+} , Yb^{3+} has been recognized as the most suitable candidate for down-conversion. Yb^{3+} has only a single excited state $^2F_{5/2}$, which allows Yb^{3+} to pick up energy packages of $\sim 10,000\text{ cm}^{-1}$, which falls in the range of the highest spectral response of the solar cells. However, the Yb^{3+} ion itself cannot absorb the high energy light in the UV-Vis region. As a consequence, a sensitizer with an energy level $\sim 20,000\text{ cm}^{-1}$ and capacity to absorb high energy photons in the spectral region at 280–550 nm is required to obtain an efficient down-conversion PL of Yb^{3+} . The background of the solar cells and down-conversion is presented in detail in chapter 1.6. Various Ln^{3+} ions have been considered as sensitizers for Yb^{3+} , e.g., Pr^{3+} , Er^{3+} , Nd^{3+} , Ho^{3+} , Tm^{3+} and Tb^{3+} .⁴⁹⁻⁵⁴ Pr^{3+} is chosen as a donor ion to sensitize Yb^{3+} for the following reasons. The absorption bands of Pr^{3+} ions cover a broad spectral window from 415 to 505 nm in the blue region

due to the successive energy levels of $\text{Pr}^{3+}:^3\text{P}_{\text{J}(\text{J}=0, 1 \text{ and } 2)}$. More importantly, these absorption bands are close to the maximum radiation of the solar spectrum and located at approximately twice the absorption energy of $\text{Yb}^{3+}:^2\text{F}_{2/7} \rightarrow ^2\text{F}_{2/5}$ ($\sim 10,000 \text{ cm}^{-1}$). The precursor SLABS glass is selected in view of its high compositional flexibility for well-controlled and homogeneous doping. Interestingly, LaBO_3 crystallites could precipitate by controlled nucleation and crystallization.²⁹ Due to the equivalent charge and similar ionic radii of La^{3+} (1.16 Å, CN = 9), Pr^{3+} (1.13 Å, CN = 9) and Yb^{3+} (0.99 Å, CN = 9), it is expected that the dopant species could readily be incorporated into the lattice of crystalline LaBO_3 , which might result in improved PL properties.¹⁷

The Ln^{3+} ions show a narrow PL and low absorption efficiency due to their characteristic parity forbidden $4f \rightarrow 4f$ transitions with an oscillator strength of $\sim 10^{-6}$. As a result, only a small fraction of the sunlight in the UV-Vis region can be absorbed. Therefore, it is important to explore new kinds of donors, which show high absorption efficiency in the spectral range of 280–550 nm, and then efficiently transfer the absorbed energy to Yb^{3+} ions through down-conversion processes. In this thesis, the 3d TM ion $^{\text{IV}}\text{Mn}^{2+}$ is explored as sensitizer for Yb^{3+} . Its excitation bands cover a broad spectral window from 350 to 500 nm.^{20–22} The position of the first excited state of $\text{Mn}^{2+}:^4\text{T}_2(^4\text{G})$ ($\sim 21,000 \text{ cm}^{-1}$) is approximately twice the absorption energy of $\text{Yb}^{3+}:^2\text{F}_{2/7} \rightarrow ^2\text{F}_{2/5}$ ($\sim 10,200 \text{ cm}^{-1}$). Willemite-type zinc orthogermanate (Zn_2GeO_4) is chosen as a host material for $^{\text{IV}}\text{Mn}^{2+}$ to enhance the absorption efficient of Mn^{2+} in the spectral region of 300–400 nm.²² In this thesis, energy transfer from Mn^{2+} to Yb^{3+} and from Zn_2GeO_4 to Yb^{3+} via Mn^{2+} , are investigated.

The background of this thesis is structured as follows. Firstly, the key conception of PL is explained. Afterwards, the origin and properties of PL induced by RE and TM ions are summarized, followed by an overview of the background of W-LEDs and solar cells. Finally, the history and properties of the glasses and glass ceramics are reviewed.

1.2. Photoluminescence

The term of “luminescence” was first introduced by a German scientist Wiedemann in 1888.⁵³ Luminescence means the emission of light by a material with energy beyond equilibrium after absorbing excitation energy.^{1,2,55,56} The role of the luminescent materials is absorbing the energy from the excitation sources and then transferring the absorbed energy into light emission in the UV-NIR region. Luminescent inorganic solid state

materials are also termed as phosphors. Many kinds of luminescence can be classified according to the nature of the excitation sources, such as:

- photoluminescence (induced by photons),
- electroluminescence (induced by electrochemical reactions),
- chemoluminescence (induced by chemical reactions),
- bioluminescence (induced by biochemical reactions in a living organism),
- piezoluminescence (induced by pressure)⁵⁷, and
- triboluminescence (induced by mechanical stresses).⁵⁸

The photon-induced luminescence, i.e., photo-luminescence (PL) will be discussed in detail in this chapter. Normally, X-ray, cathode ray, UV-Vis light and NIR light are used as the excitation sources to excite the phosphors.

According to the luminescence mechanisms, the luminescent materials can be subdivided into two groups: metal ion activator based and non-activator based luminescent materials.² Metal ion activator based luminescent materials are host materials doped with relatively small amount of impurity centers, typically a few mol% or less. TM (e.g., Mn²⁺ and Ni²⁺) and RE (e.g., Ce³⁺, Eu³⁺ and Yb³⁺) ions with rich energy levels normally serve as activator centers. Most luminescent materials are based on this type. In the second group of materials, luminescence is caused by semiconductors or defects. The luminescence of semiconductors derives from the band-to-band excitation between defect states within the bandgap.^{1,2,59} The metal ion activator based luminescent materials will be discussed in detail in the following.

In general, the process of PL involves three main steps: energy absorption, energy transfer, and emission.^{1,2} The excitation energy can be absorbed both extrinsically by the host materials and intrinsically by the activators. Subsequently, the absorbed energy is transferred to the individual excited state of the activators. The relaxation from the excited energy level to the lower lying energy level of the activators results in the final emission. The energy levels and possible transitions of RE and TM ions will be explained thoroughly in chapter 1.3 and 1.4.

The PL properties of a phosphor are mainly characterized by the absorption spectrum, PLE spectrum, PL spectrum, PL decay curve, and quantum efficiency.¹⁻³ A PLE spectrum is obtained by monitoring the PL at a constant wavelength and scanning a range of excitation wavelengths. Normally, the PLE spectrum of a luminescent material is almost identical to its absorption spectrum. The maximum PLE wavelength is used to excite the

phosphor to get the corresponding PL spectrum. Thus, a PL spectrum is obtained at a fixed excitation wavelength, and recording the PL intensity as a function of wavelength.^{60,61}

Under the excitation of an UV or a visible photon, the valence electron is excited from the ground state to an excited state. The excited electron will stay at the metastable excited state for a short time before decaying to a lower lying excited state or returning back to the ground state by emission of energy in the form of a photon or by heat. The average time an electron stays in its excited state before relaxing back to the ground state is the decay lifetime of the excited state.¹⁻³ Lifetime is normally determined by the decay curve, which is measured after excitation with a short pulse of the excitation sources and recorded as time dependent PL intensity. It typically follows a first exponential function,

$$I = I_0 \exp(-t/\tau) \quad (1)$$

where $I(t)$ is the PL intensity at a given time, I_0 is the initial intensity, and τ is the lifetime of the active centers.^{60,61}

According to the duration of the decay lifetime, PL can be divided into two types: phosphorescence and fluorescence.^{55,62} In most PL processes, luminescent materials emit a photon immediately after absorbing a photon. Such PL process is fluorescence, a short-lived luminescence with decay times of lower than 10 ms. Unlike fluorescence, phosphorescence stores up the absorbed light and emits it gradually. Thus it results in a long-lived luminescence with decay times of more than 100 ms.^{55,62}

For a normal luminescence process, the emitted photon has a lower energy than the absorbed photon, and the energy difference is described as Stokes shift.⁶³ It is mainly caused by the vibrational relaxation (non-radiative decay to the lowest vibrational energy level of the excited state) and the tendency of the electron to relax from the excited state to the highest vibrational level of the ground state. If the emitting photon has a higher energy than the absorbed photon, such process is called anti-Stokes shift.⁶³ Up-conversion which will be discussed in 1.6.2 is an anti-Stokes shift process.

The conversion efficiency of phosphors is an important parameter for luminescent materials. External quantum efficiency (η_{EQE} , also known as quantum yield) is defined as the ratio of the number of emitted photons to the number of input photons, while internal quantum efficiency (η_{IQE}) is defined as the ratio of the number of emitted photons to the number of absorbed photons.⁶⁴ A good phosphor should absorb the excitation light efficiently and transfer the absorbed energy to light-emission as efficiently as possible, i.e., the η_{EQE} should be as large as possible.

When electrons are excited, they decay from the excited state to the lower lying excited state or ground state through competitive radiative and non-radiative decay processes

(including vibrational relaxation and collisional quenching). The decay rate of k (units s^{-1}) can be written as:²

$$k = k_r + k_{nr} \quad (2)$$

Where, k_r and k_{nr} are the radiative and non-radiative decay rate, respectively. If N is the population density of the luminescence activator center in the excited state, the temporal evolution of the excited state can be expressed as:

$$dN/dt = -(k_r + k_{nr})N \quad (3)$$

The PL lifetime can be evaluated by:

$$\tau = 1/(k_r + k_{nr}) \quad (4)$$

It is worth to note that the measured lifetime τ which combines radiative and non-radiative processes can be evaluated by the intensity decay curves. The fraction of radiative transition that contributes to the total transitions is $k_r/(k_r + k_{nr})$, thus the η_{IQE} can be calculated by:

$$\eta_{IQE} = k_r/(k_r + k_{nr}) = \tau/\tau_R \quad (5)$$

Where, $\tau_R = 1/k_r$ is the radiative lifetime in the absence of the non-radiative processes. However, the radiative lifetime cannot be experimentally determined. It can be evaluated either by the Judd–Ofelt (J–O) theory or by low temperature measurements.²

By the energy gap law proposed by van Dijk and Schuurmans,⁶⁵ the non-radiative relaxation rate can be estimated from the following equation:

$$k_{nr} = \beta_{el}(-\alpha(\Delta E - \hbar\omega_{max})) \quad (6)$$

Where, β_{el} and α are constants for a given host lattice, ΔE is the energy gap between the considered energy levels, and $\hbar\omega_{max}$ is the maximum phonon energy of the host material. For two given energy levels of a luminescent center, non-radiative relaxation will dominate the relaxation process when the energy gap ΔE is lower than five times that of the $\hbar\omega_{max}$ of the given host. Whereas, if the energy gap ΔE is more than five times that of the $\hbar\omega_{max}$ of the given host, the relaxation process will be dominated by radiative relaxation.

The maximum phonon energy of several inorganic host materials is summarized as follows: iodides ($\sim 160 \text{ cm}^{-1}$) < bromides ($\sim 175\text{--}190 \text{ cm}^{-1}$) < chalcogenides ($\sim 200\text{--}300 \text{ cm}^{-1}$) < fluorides ($\sim 500\text{--}600 \text{ cm}^{-1}$) < tellurites ($\sim 600\text{--}850 \text{ cm}^{-1}$) < germanates ($\sim 800\text{--}975 \text{ cm}^{-1}$) < silicates ($\sim 1000\text{--}1100 \text{ cm}^{-1}$) < phosphates ($\sim 1100 \text{ cm}^{-1}$) < borates ($\sim 1400 \text{ cm}^{-1}$).⁶⁶ In general, the host materials with low maximum phonon energy prefer doping with TM and RE ions due to the low probability of the non-radiative multi-phonon relaxation between

two closely spaced energy levels, leading to high PL efficiency. For instance, fluorides such as $\text{LiGdF}_4:\text{Eu}^{3+}$ and $\text{SrF}_2:\text{Pr}^{3+}/\text{Yb}^{3+}$ with a maximum phonon energy of $\sim 500\text{ cm}^{-1}$ and 400 cm^{-1} show a high theoretical quantum cutting efficiency of $\sim 190\%$ and $\sim 200\%$, respectively.^{67,68} However, inorganic materials with low phonon energy, such as iodides, bromides, chalcogenides and fluorides, exhibit poor chemical and thermal stability which greatly limit their applications.⁶⁹ The high price of tellurites and germanates also impedes their applications to a large scale. For other oxide phosphors with low price and excellent chemical stability such as silicates, phosphates and borates, normally at least 8 phonons are needed to bridge the energy gap for normal visible and NIR PL. Consequently, oxide phosphors are the most promising hosts for RE and TM ions for visible and NIR PL applications.

Besides the phonon energy of the host material, water content can significantly increase the non-radiative relaxation rate and thus greatly weaken radiative transitions of RE and TM ions.⁷⁰ For example, only one or two incorporated hydroxyl group (OH^-) ions are enough to bridge the gap between $^4\text{I}_{11/2}$ and $^4\text{I}_{13/2}$ of Er^{3+} , which is the typical transition for $\sim 2.7\text{ }\mu\text{m}$ PL of Er^{3+} .⁷¹ Thus, residual OH^- concentration should be kept to a minimum, especially for the NIR and MIR PL.

Due to the abundant energy levels and thus plentiful possible electronic transitions in a broad energetic range, RE and TM ions activated inorganic luminescent materials (such as poly-crystals and glasses) to date have drawn more and more attention. They have found extraordinary wide applicability in lighting, batteries, magnets, phosphors, catalysts, lasers, superconductors, pigments, displays, optical communications, data storages, biological imaging and various other fields.^{1,72} In the following part, the origins and properties of the abundant PL colors for RE and TM ions will be reviewed.

1.3. Rare earth ions

RE ions, also known as lanthanides (Ln), are a group of 15 geochemically similar elements from lanthanum (La, atomic number 57) to lutetium (Lu, atomic number 71) with an electronic configuration of $4f^n 5s^2 5p^6$ ($n = 0$ La to 14 Lu), only differing in the number of $4f(n)$ electrons.^{9,49-52}

RE ions are valuable, but not really rare in the earth's crust despite their name. For instance, the most abundant RE, cerium is the 25th most abundant element in the earth's crust (60 ppm) as common as copper.⁷³ The least abundant RE Tm (0.53 ppm) is ~ 170 times more abundant than gold. Unfortunately, RE ions tend to disperse and are not found

concentrated in exploitable ores. As a result, they are only available from very limited sources and produced in a few countries (over 90% of world's RE ions production is supplied by China at the moment).⁷³ Besides, complex production procedures of milling, refining and recycling of RE ions also contribute to their high price.

The diverse electron arrangements of the partially filled 4f shell result in abundant energy levels in the UV to MIR spectral range, and thus unique optical and magnetic properties of RE ions.⁵¹ There are $14!/n!(14-n)!$ possible configurations (e.g., up to 3432 for Gd^{3+}) for the gradual filled inner shell of 4f in 14 possible orbitals and all configurations have different energies.⁷⁴

In general, there are three types of electronic transitions for RE ions: (I) $4f^n \leftrightarrow 4f^n$, (II) $4f^n \leftrightarrow 5d4f^{n-1}$, and (III) charge transfer (CT) transitions.⁷⁵

I. $4f^n \leftrightarrow 4f^n$ transitions

The faint intra-configurational $4f^n \leftrightarrow 4f^n$ electronic transitions are parity forbidden by the Laporte selection rule, because there are no changes in the dipole moment inside the $4f^n$ configurations. However, $4f^n \leftrightarrow 4f^n$ transitions of Ln^{3+} can be observed due to the fact that the interaction of the Ln^{3+} ions with the crystal field or with the lattice vibrations could admix different parity states into the $4f^n$ states.⁷⁶ Consequently, Ln^{3+} ions show relatively weak absorption coefficients by direct excitation within the $4f^n$ levels, in the order of 10^{-21} cm^2 , and slow emission rates leading to their characteristic long lived and sharp line-type emission with high purity emission color.^{1,3} Generally the use of sensitizers is required to overcome the problem of weak absorption efficiency of the $4f^n \leftrightarrow 4f^n$ transitions of Ln^{3+} ions. The sensitizers absorb the excitation light, transfer the absorbed energy to the surrounding Ln^{3+} , and then the activated Ln^{3+} emits light. The energy transfer process from sensitizers to Ln^{3+} is very complex, involving several mechanisms and energy levels, and will be discussed in 1.3.1.

II. $4f^n \leftrightarrow 5d4f^{n-1}$ transitions

Contrary to the $4f^n \leftrightarrow 4f^n$ transitions, the $4f^n \leftrightarrow 5d4f^{n-1}$ transitions are allowed by the parity rule and are characterized by broadband excitation/emission with relatively high absorption efficiency. However, the $4f^{n-1}5d$ configurations of Ln^{3+} ions (with energies $> 50,000 \text{ cm}^{-1}$, $\lambda < 200 \text{ nm}$) are isolated and located at higher energy than the $4f^n$ configurations of Ln^{3+} ions, except for Ce^{3+} ($> 32,000 \text{ cm}^{-1}$, $\lambda < 310 \text{ nm}$), Pr^{3+} and Tb^{3+} ($> 40,000 \text{ cm}^{-1}$, $\lambda < 250 \text{ nm}$).⁷⁷ Whereas, for divalent lanthanide (Ln^{2+}) ions, the $4f^{n-1}5d$ configurations are located at a lower position than that of the corresponding Ln^{3+} ($4f^n$) with the same electronic configurations. Thus, the $4f^n \leftrightarrow 5d4f^{n-1}$ transitions are easily observed for Ln^{2+} ions.

III). CT transitions

Both transfers from ligand to metal and from metal to ligand belong to this type. Like $4f^n \leftrightarrow 5d4f^{n-1}$ transitions, they are allowed by Laporte selection rule and characterized by broadband excitation/emission. They present relatively high absorption efficiency comparable to the $4f^n \leftrightarrow 5d4f^{n-1}$ transitions. For Ln^{3+} ions, the transition energy of CT transitions is usually higher than $40,000 \text{ cm}^{-1}$ ($\lambda < 250 \text{ nm}$) and only CT bands of Eu^{3+} and Yb^{3+} are commonly observed. While, for the Ln^{2+} ions (e.g., Sm^{2+} , Eu^{2+} , Tm^{2+} and Yb^{2+}), it occurs as low as $30,000 \text{ cm}^{-1}$ ($\lambda \approx 330 \text{ nm}$).

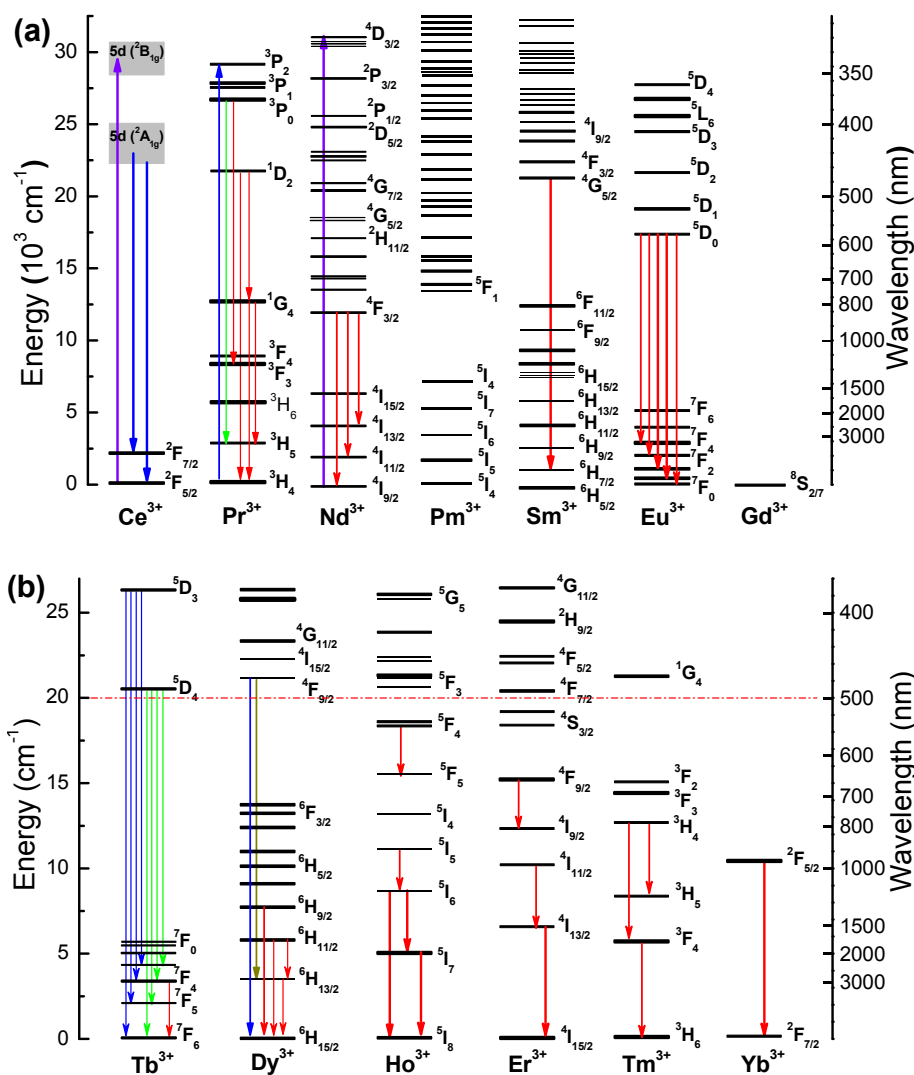


Fig. 1. Energy levels diagram for light (a) and heavy (b) RE ions from Ce^{3+} to Gd^{3+} , and from Tb^{3+} to Yb^{3+} , respectively.

In nature, RE ions exist mainly as their most stable trivalent oxidation state with a $4f^n$ configuration, in minor cases divalent (e.g., Eu^{2+} , Sm^{2+} , Tm^{2+} and Yb^{2+}) and tetravalent (e.g., Ce^{4+}) species can be found. Accordingly, there are two distinct types of PL

depending on their electronic structure and valence state: (I) line-type PL from the intra-configurational $4f^n \rightarrow 4f^n$ transitions, and (II) the band-type PL from the inter-configurational $4f^{n-1}5d \rightarrow 4f^n$ transitions.⁵¹ Generally, all Ln^{3+} ions except Ce^{3+} belong to type I, while Ln^{2+} ions (e.g., Sm^{2+} , Eu^{2+} , Tm^{2+} and Yb^{2+}) along with trivalent Ce^{3+} are attributed to type II.

The partial filled 4f orbitals of Ln^{3+} are well shielded by the outer filled octet of electrons in the $5s^2$ and $5p^6$ shells. Due to this shielding effect, the $4f^n \rightarrow 4f^n$ transitions of Ln^{3+} ions are normally independent on the host materials, whereas only the intensities and fine structure of these transitions vary for different host materials.^{49,51} Additionally, there is a very small Stoke's shift for the $4f^n \rightarrow 4f^n$ transitions. The electronic states are denoted as the Stark levels of $^{2S+1}L_J$ for $4f^n$ configuration electrons of Ln^{3+} , where, S, 2S+1, L and J are the spin angular momentum, the maximum number of different possible states of J for a given (L,S) combination, the orbital angular momentum and total angular momentum, respectively. S and J represents 0, 1/2, 1, 3/2, etc., while L is equal to 0, 1, 2, 3, 4, 5, 6, etc., nominated by S, P, D, F, G, H, etc., respectively.⁵⁰ Additionally, the energy levels of Ln^{3+} can be split by ligand-field effects into several Stark sub-levels, which can be determined by the site symmetry of Ln^{3+} . The energy level diagrams of the Ln^{3+} ions from Ce^{3+} ($4f^1$) to Yb^{3+} ($4f^{13}$), i.e., so-called Dieke diagram, is shown in Fig. 1a and 1b.⁷⁸ Due to the aforementioned shielding effect from the outer $5d^26s^6$ shells, the energy scheme of the Ln^{3+} ions is almost independent on the host crystal. Thus, by applying the Dieke diagram, we can predict the PLE and PL spectra of Ln^{3+} ions. The emitting color of the Ln^{3+} ions occurs over a wide spectral region from UV via visible to NIR, even up to MIR, upon UV to NIR light excitation. For instance, Gd^{3+} shows NUV emission, Tm^{3+} shows blue emission, Tb^{3+} and Dy^{3+} show green emission, Sm^{3+} shows orange emission, Eu^{3+} and Pr^{3+} show red emission, Yb^{3+} , Er^{3+} , Nd^{3+} , Sm^{3+} , Pr^{3+} , Ho^{3+} and Tm^{3+} exhibit emission in the IR region from 0.8 to 5 μm (Fig. 1a and 1b).^{1,2}

The energy separation between $4f^{n-1}5d$ and $4f^n$ configurations of Ln^{2+} ions is smaller than that of Ln^{3+} ions with the same electronic configurations. Thus, Ln^{2+} ions containing one more f electron (e.g., the Sm^{2+} ion has identical electronic configuration as the Eu^{3+} ion, the next element in the periodic table) show dipole allowed inter-configurational transitions of $4f^{n-1}5d \rightarrow 4f^n$.⁷¹ Differently from the $4f^n \rightarrow 4f^n$ transitions, $4f^{n-1}5d \rightarrow 4f^n$ transitions obey the parity selection rules of $\Delta l = 1$. Therefore, they are electric-dipole allowed and consequently very fast. The PL properties of Ln^{2+} ions are characterized by large absorption and emission cross-sections with short lifetime. Additionally, unlike the shielding effect for the $4f^n \rightarrow 4f^n$ transitions of Ln^{3+} ions, 5d electrons are unshielded by

the outer orbitals, and the strong electron-phonon coupling results in broad absorption and emission bands, which are sensitive to local environment.⁵¹ In addition, band-type PL of $4f^{n-1}5d \rightarrow 4f^n$ transitions show a large Stoke's shift, differing from the line-type PL of $4f^n \rightarrow 4f^n$ transitions. Therefore, Ln^{3+} and Ln^{2+} ions show different PL properties, which will be discussed separately in 1.3.2 and 1.3.3, respectively.

So far, RE ions are used as dopants in different inorganic materials, such as crystals, glasses, ceramics and glass ceramics. They play very important roles in modern lighting and displays, finding usage in tube lighting, W-LEDs, plasma display panels (PDPs), cathode ray tubes (CRTs), field emission displays (FEDs) and liquid crystal displays (LCDs).^{6,52,56,79}

1.3.1. Energy transfer

Absorption can be sub-divided into two types: ground state absorption (GSA) and excited state absorption (ESA).^{60,61} GSA is defined as the process by which an electron jumps from the ground state to an excited state after absorbing energy. It is characterized by the absorption coefficient α and the GSA cross-section σ_{GSA} , which indicates the ability of an active ion to absorb a photon in a fixed wavelength. These values can be calculated from the absorption spectrum using the Lambert-Beer law.

$$I(\lambda) = I_0(\lambda)e^{-\alpha(\lambda)d} = I_0(\lambda)e^{-n\sigma_{\text{GSA}}(\lambda)d} \quad (7)$$

Where, $I(\lambda)$ is the intensity transmitted through the samples, $I_0(\lambda)$ is the intensity in front of the samples, n is the ion concentration, $\alpha(\lambda)$ is the absorption coefficient, σ_{GSA} is the absorption cross-section, and d is the thickness of the samples. The GSA offers information about the energy level structure of the active ions and the oscillator strengths (defined as the strength of a fixed transition between levels) of the observed transitions.⁸⁰ Whereas the ESA occurs when the absorption of excitation energy from an excited state to a higher excited state.

The absorbed energy of an activator ion can migrate between identical ions or transfer from one ion species to another, i.e., by energy transfer, which occurs between a sensitizer and an activator. For an energy transfer process, a sensitizer absorbs excitation light, and then transfers the absorbed energy to an activator that emits the desired light. Generally, there are four basic mechanisms for the energy transfer from a sensitizer to an activator (Fig. 2).^{81,82}

- I). Resonant radiative energy transfer, i.e., the emission of the sensitizer is reabsorbed by the activator;
- II). Resonant non-radiative energy transfer between sensitizer and activator;
- III). Multi-phonon assisted non-radiative energy transfer process; and
- IV). Cross-relaxation between two identical ions.

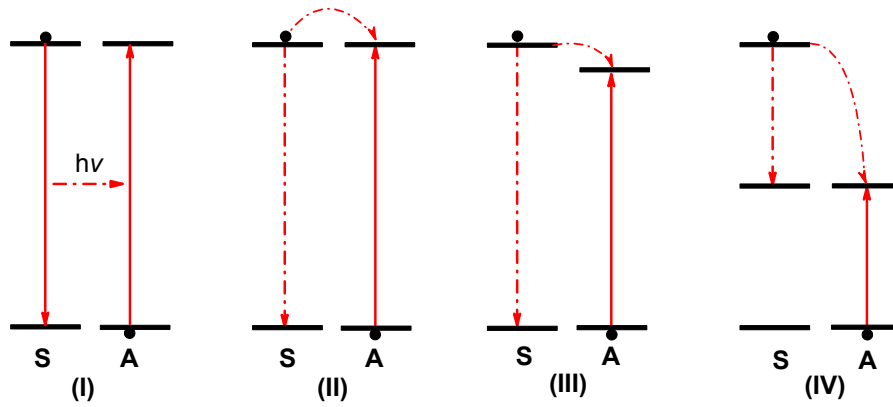


Fig. 2. Four basic mechanisms for the energy transfer from a sensitizer to an activator. (I) Resonant radiative; (II) resonant non-radiative; (III) multiphonon assisted non-radiative; and (IV) cross-relaxation energy transfer. S: Sensitizer and A: Activator.

The η_{EQE} of the resonant energy transfer (I) depends strongly on how efficiently the activator emission is excited by the sensitizer emission. Therefore, a large overlap between the PL spectrum of the sensitizer and the PLE spectrum of the activator is required for (I). If the radiative energy transfer (I) dominates the energy transfer process, then the PL lifetime of the sensitizer does not change with the activator concentration. On the contrary, if the non-radiative energy transfer process (II) dominates the energy transfer process, the PL lifetime of the sensitizer strongly decreases upon increasing the activator concentration. Most Tb^{3+} doped phosphors used in fluorescent lamps are sensitized by Ce^{3+} via an energy transfer process (II).⁵⁸ Taking $\text{CaSO}_4:\text{Ce}^{3+},\text{Tb}^{3+}$ for example, Ce^{3+} efficiently absorbs the UV excitation energy, and then the absorbed energy is transferred to Tb^{3+} by non-resonant energy transfer, resulting in efficient green light-emission of Tb^{3+} .⁸³

1.3.2. Line-type $4f^n \rightarrow 4f^n$ PL

1.3.2.1. $4f^n \rightarrow 4f^n$ line-type PL in the visible region

Ln^{3+} doped phosphors are of great importance for the modern solid state lighting due to their efficient and abundant PL lines in the visible range. The main line-type PL bands of Ln^{3+} in the visible region are reviewed as follows:

Pr^{3+} ($4f^2$)

Pr^{3+} ion with an electronic configuration of $4f^2$ is an efficient red light-emitting activator. The PL lines of Pr^{3+} in the visible region cover a broad spectral region of 480–800 nm with green emission originating from $^3\text{P}_0$ excited state, i.e., $\text{Pr}^{3+}:^3\text{P}_0 \rightarrow ^3\text{H}_4$ (~500 nm) and $\text{Pr}^{3+}:^3\text{P}_0 \rightarrow ^3\text{H}_5$ (~550 nm), and with red emission arising from both $^3\text{P}_0$ and $^1\text{D}_2$ excited state, i.e., $\text{Pr}^{3+}:^3\text{P}_0 \rightarrow ^3\text{H}_6$ (~628 nm), $\text{Pr}^{3+}:^3\text{P}_0 \rightarrow ^3\text{F}_2$ (~667 nm), $\text{Pr}^{3+}:^3\text{P}_0 \rightarrow ^3\text{F}_3$ (~705 nm), $\text{Pr}^{3+}:^3\text{P}_0 \rightarrow ^3\text{F}_4$ (~745 nm), and $\text{Pr}^{3+}:^1\text{D}_2 \rightarrow ^3\text{H}_4$ (~612 nm) under intrinsic PLE line at ~440 nm ($\text{Pr}^{3+}:^3\text{H}_4 \rightarrow ^3\text{P}_0$) (Fig. 1a).²⁸ Normally the red PL line at ~610 nm ($\text{Pr}^{3+}:^3\text{P}_0 \rightarrow ^3\text{H}_6$) dominates the PL spectra of Pr^{3+} , e.g., in $\text{CaTiO}_3:\text{Pr}^{3+}$ ($\lambda_{\text{max}} = 613$ nm).²⁸

Sm^{3+} ($4f^5$)

Sm^{3+} with an electronic configuration of $4f^5$ exhibits the typical orange to red line-type emission with four individual lines centered at ~570, 610, 645 and 725 nm corresponding to the intra-configurational parity-forbidden $4f^5 \rightarrow 4f^5$ electronic transitions from $^4\text{G}_{5/2}$ to $^6\text{H}_{5/2}$, $^6\text{H}_{7/2}$, $^6\text{H}_{9/2}$ and $^6\text{H}_{11/2}$, respectively (Fig. 1a) under the intrinsic excitation line of Sm^{3+} at ~405 nm ($\text{Sm}^{3+}:^6\text{H}_{5/2} \rightarrow ^6\text{P}_{5/2}$). This has been reported by Jin *et al.* in $\text{MMoO}_4:\text{Sm}^{3+}$ (M = Ca, Ba, and Sr).⁸⁴ The red PL line at ~610 nm ($\text{Sm}^{3+}:^4\text{G}_{5/2} \rightarrow ^6\text{H}_{7/2}$) shows the strongest intensity. The quantum efficiency of Sm^{3+} doped phosphors has been rarely reported.

Eu^{3+} ($4f^6$)

Eu^{3+} with an electronic configuration of $4f^6$ has been proved to be an efficient red-emitting activator ion.^{34–38} One good example is the commercialized $\text{Y}_2\text{O}_3:\text{Eu}^{3+}$ phosphor that shows efficient red emission under UV light excitation, involving an extrinsic CT from O^{2-} to Eu^{3+} .³⁴ The intrinsic excitation bands of Eu^{3+} are located close to the maximum quantum efficiency of NUV- and blue-LEDs, thus representing potential candidates for pc-WLEDs. The PL spectrum of Eu^{3+} is characterized by a variety of sharp PL lines in the orange to red spectral region due to the intra-configurational parity-forbidden $4f^6 \rightarrow 4f^6$ electronic transitions from non-degenerate $^5\text{D}_0$ level to $^7\text{F}_{\text{J}(\text{J}=0, 1, 2, 3 \text{ and } 4)}$ levels of Eu^{3+} (Fig. 1a).^{34–38} In principle, the electric-dipole allowed transition of $\text{Eu}^{3+}:^5\text{D}_0 \rightarrow ^7\text{F}_2$ in the red region depends strongly on the symmetric environment around Eu^{3+} sites, whereas the magnetic-dipole allowed transition of $\text{Eu}^{3+}:^5\text{D}_0 \rightarrow ^7\text{F}_1$ in the orange region is independent on the local environment of Eu^{3+} sites.^{36,37} If the charge density distribution is symmetric, the orange line of $\text{Eu}^{3+}:^5\text{D}_0 \rightarrow ^7\text{F}_1$ dominates the Eu^{3+} PL. But if the charge density

distribution is asymmetric, the red line of $\text{Eu}^{3+}:^5\text{D}_0 \rightarrow ^7\text{F}_2$ dominates the Eu^{3+} PL. Thus, the relative PL intensity ratio R ($I_{\text{ED}}/I_{\text{MD}}$) of electric- and magnetic-dipole allowed transition, termed “the asymmetric ratio”, can serve as a site symmetric probe to evaluate the ligand symmetry of the Eu^{3+} sites.³⁸ Low value of R means high ligand symmetry and low bond covalence of Eu^{3+} sites. So far, the commercialized Eu^{3+} -based red phosphors such as $\text{Y}_2\text{O}_2\text{S}:\text{Eu}^{3+}$ are still insufficient for W-LED applications mainly because of their poor chemical and thermal stability, as well as their environmental unfriendliness.⁶⁹ So it is urgent to develop new kinds of Eu^{3+} activated inorganic red phosphors for W-LEDs combined with NUV- or blue-LED chips with high quantum efficiency, good color rendering and high photo-stability.

Tb^{3+} ($4f^8$)

Tb^{3+} doped inorganic phosphors are well-known for their intense blue or green light emission depending on the doping concentration of Tb^{3+} . The abundant line-type PL of Tb^{3+} arises mainly from the intra-configurational parity-forbidden $4f^8 \rightarrow 4f^8$ electronic transitions of $\text{Tb}^{3+}:^5\text{D}_3 \rightarrow ^7\text{F}_J$ ($J = 2, 3, 4, 5$ and 6) in the blue region and $\text{Tb}^{3+}:^5\text{D}_4 \rightarrow ^7\text{F}_J$ ($J = 3, 4, 5$ and 6) in the green region (Fig. 1b).^{85,86} For the phosphors doped with low Tb^{3+} concentration (< 1 mol%), the blue light of $\text{Tb}^{3+}:^5\text{D}_3 \rightarrow ^7\text{F}_J$ ($J = 2, 3, 4, 5$ and 6) dominates the emission spectra. Whereas, for the phosphors doped with high Tb^{3+} concentration (> 5 mol%), the cross relaxation of $^5\text{D}_3 \rightarrow ^5\text{D}_4$ occurs with increase of Tb^{3+} doping concentration, due to the interaction between Tb^{3+} ions, resulting in the dominant green emission of $\text{Tb}^{3+}:^5\text{D}_4 \rightarrow ^7\text{F}_J$ ($J = 3, 4, 5$ and 6).⁸⁷⁻⁸⁹ For example, depending on the doping concentration of Tb^{3+} , both $\text{Li}(\text{Y},\text{Gd})(\text{PO}_3)_4:\text{Tb}^{3+}$ and $\text{Ca}_6\text{Ln}_{2-x}\text{Tb}_x\text{Na}_2(\text{PO}_4)_6\text{F}_2:\text{Tb}^{3+}$ ($\text{Ln} = \text{Gd},\text{La}$) phosphors show tunable blue-green emission color.⁸⁷⁻⁸⁹ Among the PL lines from the $^5\text{D}_4$ state, the magnetic dipole allowed transition ($\Delta J = 1$) $^5\text{D}_4 \rightarrow ^7\text{F}_5$ at ~ 544 nm is more intense than the other green PL lines of Tb^{3+} . As mentioned before, Ce^{3+} ion is normally used as sensitizer because of the relatively weak absorption intensity of Tb^{3+} .

Dy^{3+} ($4f^9$)

The tunable line-type PL of Dy^{3+} in the visible region mainly consists of two parts, the $\text{Dy}^{3+}:^4\text{F}_{2/9} \rightarrow ^6\text{H}_{13/2}$ transition in the yellow to orange region (550–600 nm) and the $\text{Dy}^{3+}:^4\text{F}_{2/9} \rightarrow ^6\text{H}_{15/2}$ transition in the blue region (460–500 nm) together with some weak lines at longer wavelengths (Fig. 1b).^{86,90,91} The yellow emission of $\text{Dy}^{3+}:^4\text{F}_{2/9} \rightarrow ^6\text{H}_{13/2}$ belongs to the hypersensitive transition with $\Delta J = 2$, and is an electric-dipole transition strongly influenced by the ligand field environment of Dy^{3+} , whereas the blue emission of $\text{Dy}^{3+}:^4\text{F}_{2/9} \rightarrow ^6\text{H}_{15/2}$ is a magnetic-dipole transition independent on the ligand field environment. Consequently, like the aforementioned emission intensity ratio

($^5D_0 \rightarrow ^7F_2/^5D_0 \rightarrow ^7F_1$) of Eu^{3+} , the intensity ratio ($^4F_{2/9} \rightarrow ^6H_{13/2}/^4F_{2/9} \rightarrow ^6H_{15/2}$) of Dy^{3+} can also be used as environmental probe to detect the local symmetry.⁹⁰ Interestingly, Dy^{3+} can emit white light with suitable blue to yellow intensity ratio by tuning the Dy^{3+} doping concentration and the ligand field of the host materials.^{86,90,91}

Tm^{3+} ($4f^{12}$)

The Tm^{3+} ion with an electronic configuration of $4f^{12}$ shows efficient blue light-emission. The line-type PL of Tm^{3+} is located at ~ 455 nm in the blue region owing to the $^1D_2 \rightarrow ^3F_4$ transition of Tm^{3+} together with some weak PL lines in the red region (at ~ 650 , 700 , and 775 nm, attributed to the $\text{Tm}^{3+}:^1G_4 \rightarrow ^3F_4$, $\text{Tm}^{3+}:^3F_3 \rightarrow ^3H_6$, and $\text{Tm}^{3+}:^1G_4 \rightarrow ^3H_5$ transitions, respectively) under the excitation of the intrinsic PLE line at ~ 360 nm ($\text{Tm}^{3+}:^3H_6 \rightarrow ^1D_2$), which matches the NUV-LEDs (Fig. 1b).⁹² One good example is $\text{LaOCl}:\text{Tm}^{3+}$.⁹² The blue emission of Tm^{3+} with appropriate lifetime and color-rendering properties suggests its potential applications in modern lighting and displays. However, the quantum efficiency of Tm^{3+} for the blue emission is normally low due to competing infrared emitting decay paths.

1.3.2.2. $4f^n \rightarrow 4f^n$ line-type PL in the NIR region

In modern telecommunication system, information is transmitted by light, which is guided by silica optical fibers. The light is attenuated over the distance, and thus amplifiers in wavelength division multi-plexing (WDM) network system are required.⁹³ The attenuation and dispersion of silica optical fibers strongly depend on the optical wavelength, and is caused by a combination of material absorption, Rayleigh scattering, Mie scattering and connection losses.⁹⁴⁻⁹⁷ Nowadays, the pressing requirements for high speed data transmission of telecommunication networks stimulate the development of amplifiers, splitters, couplers and multi-plexers. The six weakest attenuation bands have been standardized (so-called transmission windows) as the O-band (1260–1360 nm), E-band (1360–1460 nm), S-band (1460–1530 nm), C-band (1530–1565 nm), L-band (1565–1625 nm) and the U-band (1625–1675 nm). Due to their abundant energy levels, Ln^{3+} ions show many NIR PL bands, which fall in the aforementioned transmission windows, endowing their applications in optical amplifiers for telecommunications. For instance, PL of Pr^{3+} ($4f^2$), Nd^{3+} ($4f^3$) and Dy^{3+} ($4f^9$) at ~ 1.3 μm , Tm^{3+} ($4f^{12}$) at ~ 1.47 μm , and Er^{3+} ($4f^{11}$) at ~ 1.55 μm allow their applications in O-, S-, and C-band amplifiers, respectively.⁹⁴⁻⁹⁷

Pr^{3+} ($4f^2$)

In 1962, Yariv *et al.*⁹⁵ reported the first Pr³⁺ laser based on CaWO₄ crystalline phosphors, operating at 1.0468 μm (Pr³⁺:¹G₄ → ³H₄). Besides, the Pr³⁺ ion also shows efficient NIR emissions at 0.9 μm (Pr³⁺:³P₀ → ¹G₄) and 1.35 μm (Pr³⁺:¹G₄ → ³H₅) (Fig. 1b).^{98,99} Over the last two decades, Pr³⁺ doped fluoride glasses and fibers have drawn great attentions due to the emission at 1.35 μm for possible application in amplifiers.

Nd³⁺ (4f³)

The Nd³⁺ ion with an electronic configuration of 4f³ has turned out to be the most efficient Ln³⁺ ion for NIR solid state lasers due to its efficient and versatile PL at ~0.9 μm (Nd³⁺:⁴F_{3/2} → ⁴I_{9/2}), 1.06 μm (Nd³⁺:⁴F_{3/2} → ⁴I_{11/2}) and 1.35 μm (Nd³⁺:⁴F_{3/2} → ⁴I_{13/2}), as shown in (Fig. 1b).^{94,95,100} Practically, the intense absorption band of Nd³⁺:⁴I_{9/2} → ⁴F_{5/2} at ~800 nm matches the commercial laser diodes (LDs). Furthermore, the Nd³⁺:⁴F_{3/2} → ⁴I_{11/2} emission at ~1.06 μm of Nd³⁺ doped glasses has been demonstrated for the high peak power and high energy laser applications.⁹⁴ For crystalline materials, Nd³⁺-YAG is the most frequently used solid state laser operating at 1.0641 μm.⁹⁴ The Nd³⁺:⁴F_{3/2} → ⁴I_{13/2} emission at ~1.3 μm of Nd³⁺ doped glass fibers has other potential applications in optical fiber communication systems.^{95,100}

Sm³⁺ (4f⁵)

The trivalent Sm³⁺ presents three weak NIR PL bands at ~1.08, 1.24 and 1.49 μm due to the transitions of Sm³⁺:⁶F_{J(J=11/2, 9/2 and 7/2)} to their lower level.¹⁰¹

Ho³⁺ (4f¹⁰)

The Ho³⁺ ion exhibits three weak NIR PL bands at ~0.97, 1.2, and 1.46 μm due to the transition of Ho³⁺:⁵F₅ → ⁵I₇, Ho³⁺:⁵I₆ → ⁵I₈, and Ho³⁺:⁵F₅ → ⁵I₆, respectively.⁹⁵

Er³⁺ (4f¹¹)

Er³⁺ doped inorganic materials are of interest for optical telecommunication due to the broadband NIR PL of Er³⁺ at ~1.55 μm, which is located in the range of the optical communication window of C-band (Fig. 1b). The NIR emission of Er³⁺ is attributed to the intra-configurational transition from the first excited level ⁴F_{2/13} to the ground state ⁴F_{2/15} of Er³⁺ with a FWHM > 50 nm and a long lifetime of ~10 ms (the exact value depends on the host and co-dopants).⁹⁵ Er³⁺ doped silica fiber for telecommunications with emission at 1.536 μm was first reported by Mears *et al.* in 1987.¹⁰² Erbium doped fiber amplifiers (EDFAs) have become the key component towards the WDM system.⁴ Due to the weak absorption and the low pumping efficiency of the Er³⁺:⁴I_{11/2} level at 980 nm, Yb³⁺ is usually used as sensitizer for Er³⁺. The absorption cross-section of Yb³⁺ is ~10 times stronger than that of Er³⁺ at 980 nm, and the Yb³⁺:²F_{5/2} level and Er³⁺:⁴I_{11/2} are nearly resonant in energy.¹⁰³

Yb³⁺ (4f¹³)

Yb³⁺ with an electronic configuration of 4f¹³ has the simplest energy level scheme among all Ln³⁺ ions, i.e., it is composed of only two levels, the excited state Yb³⁺:²F_{5/2} and the ground state Yb³⁺:²F_{7/2} (Fig. 1b).⁷⁸ This simple energy level scheme makes it possible to avoid up-conversion and ESA processes. Accordingly, efficient PL at ~1 μm can be observed in Yb³⁺ doped materials. For instance, the Yb³⁺ doped silicate glass fibers show the highest reported value of output power at ~1 μm with an efficiency of ~80%.¹⁰⁴ Additionally, the Yb³⁺ ion shows high absorption cross-section at 980 nm, nicely matching commercial LDs at 980 nm. Accordingly, it is frequently used as sensitizer for the other Ln³⁺ ions. For instance, it frequently finds use as sensitizers for up-conversion phosphors, which can be used for applications in transparent displays.⁸² The up-conversion process will be discussed later in 1.6.2.

1.3.2.3. 4fⁿ → 4fⁿ line-type PL in the MIR region

MIR lasers from 2–8 μm have potential environmental and military applications including trace gas monitoring, remote sensing, ophthalmology, neurosurgery, soft tissue medicine and urology.^{105–108} The low loss Ln³⁺ doped silica fiber lasers and silica Raman lasers are limited to the 1–2 μm region due to their high intrinsic absorption beyond ~2.4 μm and high phonon energy of silica (~1100 cm⁻¹), which strongly quenches the MIR PL of Ln³⁺.¹⁰⁶

For fiber lasers 2–3.5 μm, fluoride and tellurite glasses might be the best choice for the following reasons. Tellurite glasses exhibit the lowest phonon energy among all conventional oxide glasses (~650–800 cm⁻¹), have the moderate transmission bandwidth in MIR region up to ~5 μm, and show good chemical and thermal stability.¹⁰⁸ Besides, high doping level of RE ions, up to ~10²¹ ion/cm³ can be achieved in tellurite glasses without clustering. However, the relatively high price of tellurite glasses somehow limits their applications. Fluoride glasses have relatively low phonon energy (~500–650 cm⁻¹) and moderate IR cutoff wavelength up to ~6 μm. ZBLAN glass with an atomic% composition of 56ZrF₄–19BaF₂–6LaF₃–4AlF₃–15NaF is the most widely used fluoride glass. However, its complex fabrication processes and poor stability limit its applications.¹⁰⁹

Beyond 3.5 μm, chalcogenide glasses composed of S, Se or Te are the most suitable candidates due to their high IR transparency up to 12 μm, low phonon energy (~300–450 cm⁻¹), and relatively good chemical and mechanical stability.¹⁰⁶ According to the Dieke diagram, Ln³⁺ ions such as Er³⁺, Ho³⁺, Tm³⁺ and Dy³⁺ possess numerous 4fⁿ → 4fⁿ

transitions in the 2–8 μm region, which is suitable for the MIR fiber lasers and amplifiers.⁷⁸

Emission at $\sim 2 \mu\text{m}$ from Tm^{3+} and Ho^{3+} ions doped silicate and tellurite glasses and fibers has frequently been reported.^{107–109} For example, Tm^{3+} doped fibers can be tuned over the widest range from 1.65 to 2.1 μm arising from the transition of $\text{Tm}^{3+}:^3\text{F}_4 \rightarrow ^3\text{H}_6$, depending on the host glasses.^{107,108} Recently, an output power of 1kW operating at 2.045 μm in Tm^{3+} doped silica fiber has been demonstrated.¹⁰⁷ The emission of Ho^{3+} with a maximum at $\sim 2.1 \mu\text{m}$ attributed to the transition of $\text{Ho}^{3+}:^5\text{I}_7 \rightarrow ^5\text{I}_8$ overlaps with an important atmospheric transmission window.¹⁰⁷ However, the Ho^{3+} ion is not suitable for the commercial LDs pumping according to its absorption spectra. Thus Er^{3+} , Tm^{3+} and Yb^{3+} ions are used as sensitizers for 2.0 μm emission of Ho^{3+} .¹⁰⁷

For emission of $\sim 2\text{--}3.5 \mu\text{m}$, Tm^{3+} ($\sim 2.3 \mu\text{m}$, $\text{Tm}^{3+}:^3\text{H}_4 \rightarrow ^3\text{H}_5$), Er^{3+} ($\sim 2.7 \mu\text{m}$, $\text{Er}^{3+}:^4\text{I}_{11/2} \rightarrow ^4\text{I}_{13/2}$), Ho^{3+} ($\sim 2.9 \mu\text{m}$, $\text{Ho}^{3+}:^5\text{I}_6 \rightarrow ^5\text{I}_7$), Dy^{3+} ($\sim 2.9 \mu\text{m}$, $\text{Dy}^{3+}:^6\text{H}_{11/2} \rightarrow ^6\text{H}_{15/2}$), Ho^{3+} ($\sim 3.3 \mu\text{m}$, $\text{Ho}^{3+}:^5\text{S}_2 \rightarrow ^5\text{F}_5$) and Er^{3+} ($\sim 3.45 \mu\text{m}$, $\text{Er}^{3+}:^4\text{F}_{9/2} \rightarrow ^4\text{I}_{11/2}$) doped tellurite and fluoride glasses and fibers have been widely reported.^{110,111}

For emission beyond 3.5 μm , Dy^{3+} ($\sim 4.3 \mu\text{m}$, $\text{Dy}^{3+}:^6\text{H}_{13/2} \rightarrow ^6\text{H}_{15/2}$), Tb^{3+} ($\sim 4.8 \mu\text{m}$, $\text{Tb}^{3+}:^7\text{F}_4 \rightarrow ^7\text{F}_6$) and Tb^{3+} ($\sim 8 \mu\text{m}$, $\text{Tb}^{3+}:^7\text{F}_4 \rightarrow ^7\text{F}_5$) doped chalcogenide glasses have been reported.^{106,107} One example is the emission of Dy^{3+} at 4.3 μm which has been firstly reported by Heo *et al.* in Dy^{3+} doped As_2S_3 glass.¹¹² Another example is the emission of Tb^{3+} at $\sim 8 \mu\text{m}$ in Tb^{3+} ($\text{Tb}^{3+}:^7\text{F}_4 \rightarrow ^7\text{F}_5$) doped chalcogenide glass, which is the longest MIR emission in glasses to date.¹⁰⁶

1.3.3. Band-type $4f^{n-1}5d \rightarrow 4f^n$ PL

Phosphors containing Ce^{3+} and Ln^{2+} ions such as Sm^{2+} , Eu^{2+} , Tm^{2+} and Yb^{2+} activated phosphors exhibit tunable broad band-type PL. The $4f^{n-1}5d$ level of Ln^{2+} is located at lower energies than the corresponding Ln^{3+} ($4f^n$) with the same electronic configuration. Thus intense band-type PL from NUV to NIR is expected in Ce^{3+} and Ln^{2+} activated phosphors.^{113,114} Unlike the 4f electrons, the outer 5d electron is not completely shielded by the surrounding ligands, and the position and width of the PLE and PL band (allowed by Laporte parity selection rule) is strongly dependent on the host lattices. For a host with strong crystal-field strength and high degree of covalence, the lowest $4f^{n-1}5d$ level is lower than the lowest excited state of $4f^n$, resulting in a band-type PL arising from the transition of $\text{Ln}^{2+}:4f^{n-1}5d \rightarrow 4f^n$. Whereas, in the case of a host with weak crystal-field strength and low degree of covalence, intra-configurational $4f^n \rightarrow 4f^n$ line-type PL of Ln^{3+} can also be

observed.¹¹⁴

Lanthanide oxides exist as trivalent ions in nature. The reduction of Ln^{3+} to Ln^{2+} has been a hot research topic over the last two decades. Generally, there are four reported routes which describe how to reduce Ln^{3+} to Ln^{2+} :¹¹⁵

I) by preparing the material in a strongly reducing atmosphere, such as N_2/H_2 , H_2 , CO gas or carbon;

II) by extrinsically reducing the polyvalent species in an as-prepared material, e.g., by high-energy photoreduction, such as UV light, γ -rays or X-rays, or by thermal treatment in a reducing atmosphere, such as N_2/H_2 , H_2 , CO gas or carbon;

III) by providing a sufficiently acidic host environment, where the reduced species can be obtained even if they are synthesized under air condition, e.g., the reduction of Eu^{3+} to Eu^{2+} during high temperature melting without any reducing treatment in europium doped $\text{ZnO-B}_2\text{O}_3\text{-P}_2\text{O}_5$ glasses;¹¹⁶

IV) by promoting an intrinsic reduction process under air or O_2 atmosphere condition at high temperature, e.g., by initiating structural rearrangements in a frozen-in system.

For environmental, technological and cost-related reasons, the latter two methods are the most attractive, but they can only be applied to a limited number of chemical systems.

1.3.3.1. Ce^{3+} ($4f^1$)

Cerium is the most abundant and least expensive among all RE elements. It is widely used as polishing agent for glasses. More importantly, it is also an efficient emission activator. The ground state of Ce^{3+} splits into $^2F_{7/2}$ excited state and $^2F_{5/2}$ ground state multiplet with an energy separation of $\sim 2000 \text{ cm}^{-1}$.⁷⁸ The band-type emission of Ce^{3+} covers a wide region from NUV to red. It is composed of overlapped asymmetric doublet bands due to the electric dipole allowed transitions from $5d^1$ to two spin-orbit splitting of the $4f^1$ ground state of Ce^{3+} (Fig. 1a).¹¹⁷ The PLE spectrum of Ce^{3+} is composed of up to five distinguishable PLE bands due to the crystal field splitting of the excited $5d^1$ state. The position of the lowest $5d^1$ excited band of Ce^{3+} is sensitive to the crystal field and covalence. As a result, Ce^{3+} doped phosphors show a broad absorption band in the UV to Vis spectral region and a broad emission band from 400 to 600 nm with relatively short lifetime of $\sim 50\text{--}100 \text{ ns}$ and FWHM $\sim 100 \text{ nm}$.^{118,119} Therefore, a lot of Ce^{3+} activated phosphors (e.g., oxides, fluorides, oxyfluorides, nitrides, and oxynitrides) have been thoroughly studied in the past decades, including $\text{NaSrBO}_3:\text{Ce}^{3+}$ (400 nm)¹²⁰, $\text{Ca}_{5.45}\text{Li}_{3.55}(\text{SiO}_4)_3\text{O}_{0.45}\text{F}_{1.55}$ (470 nm)¹²¹ for blue light-emission, $\text{Sr}_{2.975}\text{Ce}_{0.025}\text{Al}_{1-}$

$x\text{Si}_x\text{O}_{4+x}\text{F}_{1-x}$ (474–537 nm)¹²² for blue to green light-emission, YAG:Ce³⁺ (536–558 nm)¹²³ for yellow light-emission, and Y₂O₂S:Ce³⁺ (660 nm)¹²⁴ for red light-emission, etc.

Additionally, Ce³⁺ ions are frequently used as sensitizers for the other Ln³⁺ ions (e.g., Eu³⁺, Yb³⁺ and Tb³⁺) and TM ions (e.g., Mn²⁺) to enhance their absorption and thus emission efficiency. Besides, the peak position of Ce³⁺:5d → 4f PL in a specific matrix is helpful to estimate the energy levels for the other RE ions in the same host.¹²⁵

1.3.3.2. Sm²⁺ (4f⁶)

The 4f⁶ energy scheme of Sm²⁺ is spectroscopically similar to that of Eu³⁺. The lowest 4f⁵5d¹ level of Sm²⁺ is strongly ligand field dependent. For most of the crystals, the lowest 4f⁵5d¹ level is located at higher position than the lowest excited ⁵D_J level of 4f⁶ configuration, even in hosts with relatively strong crystal-field strength.¹¹⁴ As a result, in most crystals Sm²⁺ shows typical line-type PL due to the transition from ⁵D₀ level to the multiplet ground state ⁷F_J. For example, the lowest 4f⁵5d¹ level of Sm²⁺ is higher than ⁵D₀ level of Sm²⁺ in SrZnCl₄ crystal, thus line-type PL of Sm²⁺ arising from the transition from ⁵D₀ to the multiplet ground state ⁷F_J can be observed.¹¹⁴ However, for hosts with very strong crystal-field strength, the lowest 4f⁵5d level is located at lower position than the lowest excited ⁵D_J level of 4f⁶ configuration. Thus band-type PL of Sm²⁺ (4f⁵5d → 4f⁶) can be observed in this case. For example, the lowest 4f⁵5d¹ level is lower than ⁵D₀ level of Sm²⁺ in CaF₂ crystal, thus CaF₂:Sm²⁺ shows band-type PL peaked at ~740 nm due to the transition of 4f⁵5d → 4f⁶ at room temperature.¹²⁶

1.3.3.3. Eu²⁺ (4f⁷)

The 4f⁷ energy scheme of Eu²⁺ is spectroscopically similar to that of trivalent Gd³⁺ (4f⁷). The energy gap between the first excited state ⁶P_{7/2} and the ground state ⁸S_{7/2} of Eu²⁺ is comparatively large. The 4f⁶5d¹ level of Eu²⁺ is lower than the lowest excited level ⁶P_{7/2} in a material with strong crystal-field strength and high degree of host lattice covalence. As a result, the band-type PL occurs with a typical FWHM of ~50–100 nm and lifetime of ~1 μs, due to the spin-allowed inter-configurational transition of Eu²⁺:4f⁶5d¹(T_{2g}) → 4f⁷(⁸S_{7/2}).⁴¹ The position and width of the PLE and PL band of Eu²⁺ are strongly dependent on the type of host lattices. The broad PLE spectra of Eu²⁺ vary from X-ray to the blue region, and the corresponding PL spectra tune largely from NUV to red in different hosts in which Eu²⁺ ions are incorporated. In the same host materials, the PL peak position of Eu²⁺ red shifts

compared to that of Ce^{3+} . Besides, the 5d level of Eu^{2+} can split into different numbers depending on the local symmetry around the Eu^{2+} ions. For instance, in O_h symmetry the 5d orbitals of Eu^{2+} are split into two levels (i.e., T_{2g} and E_g).⁴² Normally, Eu^{2+} ions in large crystal field splitting environment and high host lattice covalence show long wavelength emissions. For example, in the case of $\text{MSi}_2\text{O}_2\text{N}_2:\text{Eu}^{2+}$ phosphors, the PL peak red shifts from ~ 498 nm for $\text{BaSi}_2\text{O}_2\text{N}_2:\text{Eu}^{2+}$ to ~ 560 nm for $\text{CaSi}_2\text{O}_2\text{N}_2:\text{Eu}^{2+}$, which can be explained by the stronger ligand field splitting of Ca^{2+} than that of Ba^{2+} .⁴¹ Similarly, oxynitrides and nitrides, which feature higher covalence metal-nitrogen bond and larger crystal field splitting effect of the N^{3-} anion, show absorption and emission of longer wavelength in comparison with oxides.^{43,44} Likewise, sulfide based phosphors show emission with longer wavelength as a result of the smaller electronegativity and better polarizability of S than that of O, and thus the larger nephelauxetic effect in sulfides based phosphors than that in oxide based phosphors.⁸¹ Eu^{2+} activated phosphors with different PL colors have been applied in the field of lighting and display backlights.⁴⁴ For instance, Eu^{2+} activated $\text{BaMgAl}_{10}\text{O}_{17}$ ¹²⁷/ $\text{Ca}_2\text{PO}_4\text{Cl}$ ¹²⁸, $\text{BaZrSi}_3\text{O}_9$ ¹²⁹, $\text{Na}_2\text{CaPO}_4\text{F}$ ¹³⁰/ $\text{CaLaGa}_3\text{S}_7$ ¹³¹, $\text{Sr}_8\text{ZnSc}(\text{PO}_4)_7$ ¹³² and CaAlSiN_3 ¹³³/ $(\text{Ca},\text{Sr},\text{Ba})_2\text{Si}_5\text{N}_8$ ¹³⁴ phosphors show blue, cyan, green, yellow and red emissions, respectively.

On the other hand, $4f \rightarrow 4f$ line-type PL of Eu^{2+} can be observed due to the transitions from $\text{Eu}^{2+} : ^6\text{P}_{7/2} \rightarrow ^8\text{S}_{7/2}$ in materials with weak crystal-field strength and low degree of covalence of the host lattice.¹¹⁴

1.3.3.4. Tm^{2+} ($4f^{13}$)

The $4f^{13}$ energy scheme of Tm^{2+} is spectroscopically similar to that of Yb^{3+} , leading to a $^2\text{F}_{7/2}$ ground state and a $^2\text{F}_{5/2}$ excited state. Compared to Yb^{3+} , the 4f electrons of Tm^{2+} show a reduced Coulomb attraction from the nucleus.¹³⁵ As a result, the $4f \rightarrow 4f$ NIR PL peak position of Tm^{2+} red shifts from ~ 1000 nm in Yb^{3+} to ~ 1150 nm in Tm^{2+} . For example, the emission peak position of $\text{CsCaI}_3:\text{Tm}^{2+}$ and $\text{RbCaI}_3:\text{Tm}^{2+}$ is located at ~ 1139 and 1138 nm, respectively.¹³⁵ Besides, it also shows a visible PL band due to the $4f^{12}5d \rightarrow 4f^{13} (^2\text{F}_{7/2})$ transition of Tm^{2+} . For instance, Tm^{2+} activated SrCl_2 ¹³⁶ and SrB_4O_7 ¹³⁷ show a broad band-type red PL at ~ 720 and 610 nm respectively, with a FWHM of more than 100 nm and a PL lifetime of ~ 220 μs .

1.3.3.5. Yb^{2+} ($4f^{14}$)

Yb^{2+} with an electronic configuration of $4f^{14}$ has a completely filled 4f shell. $4f^{14}$ configuration of Yb^{2+} only has a $^1\text{S}_0$ ground state of free ion and no other $4f^{14}$ levels exist. Band-type PL of Yb^{2+} from UV to red can be observed when the lowest $4f^{13}5d$ level is lower than the conduction band. Like Eu^{2+} ion, a stronger crystal field splitting strength and a higher degree of environmental covalence lead to longer PL wavelength. For example, the PL peak of $\text{MgF}_2:\text{Yb}^{2+}$ is located at relatively longer wavelength at ~ 480 nm.¹³⁸

1.4. Transition metal ions

The 3d TM ions are located in the 4th period of the periodic table, from Sc (element number 21) to Zn (element number 30) with electronic configuration of $3d^n 4s^2$ ($1 \leq n \leq 10$). The electrons in the partially filled 3d orbitals are responsible for their special optical properties. Inorganic materials doped with TM ions exhibit PL from visible to the MIR region. Accordingly, TM ions are frequently used as activators in phosphors and in tunable solid state lasers.^{1,3,80,139,140} It is highly desirable to explore and develop novel inorganic materials doped with TM ions, due to their low fabrication cost and the conservation of RE resources. Unlike Ln^{3+} ions, the 3d orbitals of the TM ions are not shielded by outer shells, thereby their spectral properties are strongly influenced by the surrounding ligand field or coordination environment. Both band-type ($S > 0$) and line-type ($S \approx 0$) PL can be observed in TM ions.^{80,139,140}

The energy level schemes of the TM ions are well described by standard Tanabe-Sugano diagrams, in which the sequence of energy levels of the TM ions depends on the symmetry of ion sites, the crystal-field strength $10 D_q$, and the inter-electronic interactions as described by the Racah parameters B and C.^{141,142} The energy level of a $3d^n$ ion in octahedral coordination is analogous to that of a $3d^{10-n}$ ion in tetrahedral coordination. The electronic transitions of $3d^n$ ions in octahedral coordination strictly follow Laporte rule, whereas for the electronic transitions of $3d^n$ ions in tetrahedral coordination the rule is weakened due to the lack of inversion center, which leads to an admixture of levels of different parity.^{140,143} In general, TM ions show a higher transition probability at a non-centrosymmetric site in comparison with a centrosymmetric site, due to the static admixture of odd-parity states. The PL properties of TM ions in octahedral and tetrahedral environments are reviewed as follows.

1.4.1. Octahedrally coordinated TM ions

1.4.1.1. 3d¹ configuration: ^{VI}Ti³⁺ and ^{VI}V⁴⁺

The 3d¹ configuration represents the simplest energy level among all 3dⁿ configurations, i.e., it consists of two energy levels, ²E and ²T₂.⁸⁰ ²E and ²T₂ levels serve as the lower energy for octahedral and tetrahedral coordination, respectively. Ti³⁺, V⁴⁺, Cr⁵⁺ and Mn⁶⁺ ions show a 3d¹ configuration. But Cr⁵⁺ and Mn⁶⁺ are only observed in tetrahedral coordination.

^{VI}Ti³⁺

Octahedrally coordinated ^{VI}Ti³⁺ shows a broad deep red to NIR emission from ~670 to 1100 nm with a FWHM of ~220 nm due to the spin-allowed transition of ^{VI}Ti³⁺:²T₂ → ²E. Tunable solid state Ti³⁺:Al₂O₃ lasers with a wide tuning range of ~660–1100 nm and with large gain cross-section in laser spectroscopy have great potential to replace the dye lasers.^{144,145}

^{VI}V⁴⁺

Octahedrally coordinated ^{VI}V⁴⁺ ion shows a broad absorption and PL band in the visible spectral region. Compared to ^{VI}Ti³⁺, the PL band of ^{VI}V⁴⁺ blue shifts to lower wavelengths, due to the higher valence and thus higher crystal field strength of V⁴⁺. Meyn *et al.*¹⁴⁶ investigated the PL properties of ^{VI}V⁴⁺ doped Al₂O₃, YAlO₃ and Y₃Al₅O₁₂, which show broad PL band peaking at ~650 nm with a HWHM of ~3500 cm⁻¹ and a PL lifetime of ~1–10 μs arising from the spin-allowed transition of ^{VI}V⁴⁺:²T₂ → ²E.¹⁴⁶

1.4.1.2. 3d³ configuration: ^{VI}V²⁺, ^{VI}Cr³⁺ and ^{VI}Mn⁴⁺

The position of the first excited state of 3d³ configuration is strongly dependent on the crystal field strength, i.e., ⁴T₂ (V²⁺ and Cr³⁺ in a low crystal field) and ²E (Cr³⁺ in a strong crystal field and Mn⁴⁺) is the first excited state, respectively.⁸⁰ As a result, both band-type spin-allowed transition of ⁴T₂ → ⁴A₂ (weak field) and line-type spin-forbidden transition of ²E → ⁴A₂ (strong field) can be observed for 3d³ ions, depending on the ligand field strength of the host materials and ion species.

^{VI}V²⁺

The PL band of octahedrally coordinated ^{VI}V²⁺ covers a broad range of ~1.0–1.75 μm with a FWHM > 1000 cm⁻¹ and a lifetime of ~2 μs due to the spin-allowed transition of ^{VI}V²⁺:⁴T₂(4F) → ⁴A₂(4F).^{147,148} Three absorption bands of ^{VI}V²⁺ can be observed arising

from the spin allowed transitions from the ground state ${}^4A_2(F)$ to the excited states ${}^4T_2(4F)$, ${}^4T_1(4F)$ and ${}^4T_1(4P)$. For instance, the emission peak of ${}^{VI}V^{2+}$ doped $KMgF_3$ is located at ~ 1100 nm with a FWHM of 1350 cm^{-1} , PL lifetime of $1.2\ \mu\text{s}$, and a quantum efficiency of 87% at room temperature.¹⁴⁸

${}^{VI}Cr^{3+}$

Octahedrally coordinated ${}^{VI}Cr^{3+}$ has been extensively investigated due to its broadband NIR PL from ~ 700 to 1800 nm with a lifetime of $\sim 100\ \mu\text{s}$, originating from the spin-allowed transition from the first excited state to the ground state of ${}^{VI}Cr^{3+}: {}^4T_2/{}^2E \rightarrow {}^4A_2$.^{149,150} The band-type NIR PL of ${}^{VI}Cr^{3+}$ is responsible for its tunable laser oscillation. The broad PL band of ${}^{VI}Cr^{3+}$ strongly depends on the ligand field strength and excitation wavelength. For example, ${}^{VI}Cr^{3+}$ doped Sc_2O_3 shows a broad PL band from 750 to 1100 nm (short wavelength emission) pumped by a 670 nm LD, while the PL band red shifts to 1050 – 1800 nm (long wavelength emission) when pumped by an 808 nm LD.¹⁴⁹ To date, ${}^{VI}Cr^{3+}$ doped crystals (e.g., Al_2O_3 , MgO , Sc_2O_3 etc.) have been commercially used for continuous-wave (CW) lasers in the range of 670 – 1100 nm. For instance, the first working solid state laser was reported on ${}^{VI}Cr^{3+}$ doped α - Al_2O_3 crystal operating at ~ 694 nm.¹⁵⁰

${}^{VI}Mn^{4+}$

${}^{VI}Mn^{4+}$ ion in octahedral environment offers a strong crystal field due to the high charge number. Thus the first quartet 4T_2 state is located above the 2E state. As a result, it shows a sharp R-line-type emission in the spectral range of 650 – 730 nm arising from the spin-forbidden transition of ${}^{VI}Mn^{4+}: {}^2E \rightarrow {}^4A_2$ under a blue or NUV light excitation. The PLE band of ${}^{VI}Mn^{4+}$ matches the blue- or NUV LEDs for the future warm W-LEDs applications.^{151–153} Correspondingly, two intense absorption bands peaking at ~ 460 and 360 nm are attributed to ${}^{VI}Mn^{4+}: {}^4A_2 \rightarrow {}^4T_2$ and ${}^{VI}Mn^{4+}: {}^4A_2 \rightarrow {}^4T_1$ transitions. The spin-forbidden transition of ${}^{VI}Mn^{4+}: {}^2E \rightarrow {}^4A_2$ shows longer PL lifetime in ms range.¹⁵³

1.4.1.3. $3d^4$ configuration: ${}^{VI}Cr^{2+}$, ${}^{VI}Mn^{3+}$ and ${}^{VI}Fe^{4+}$

In octahedral environment, the ground state 5D of $3d^4$ configuration splits into the higher 5E and the lower 5T_2 levels. Based on the Tanabe–Sugano diagram, the positions of ground and excited state strongly depend on the ligand field strength of the host materials. For low crystal field strength, the 5E serves as the ground state for $D_q/B < 2.5$. Meanwhile, for $D_q/B < 1.2$, 5T_2 is the lowest excited state and emission of ${}^5T_2 \rightarrow {}^5E$ is spin

allowed.^{80,139,140} Until now, there is no PL reported until now for octahedrally coordinated $^{VI}Cr^{2+}$ and $^{VI}Fe^{4+}$.

$^{VI}Mn^{3+}$

The emission band of $^{VI}Mn^{3+}$ covers a broadband of 550–1300 nm due to the spin allowed transition of $^{VI}Mn^{3+}:^5T_2 \rightarrow ^5E$. For instance, Mn^{3+} doped YAG shows doublet PL bands centered at 620 and 758 nm at room temperature.¹⁵⁴ Additionally, weak NIR emission at ~1150 nm can be also observed due to the transition of $Mn^{3+}:^1T_2 \rightarrow ^3T_1$.¹⁵⁴

1.4.1.4. $3d^5$ $^{VI}Mn^{2+}$

Manganese is the 12th most abundant element in the earth's crust (950 ppm). As one of the most important dopants, Mn^{2+} activated inorganic materials show a broad PL band varying from deep green to far red due to the parity-forbidden $3d \rightarrow 3d$ transition from the lowest excitation of $Mn^{2+}:^4T_1(^4G)$ to the ground state $Mn^{2+}:^6A_1(^6S)$.^{20–22} The position of the lowest excitation state $Mn^{2+}:^4T_1(^4G)$ is strongly dependent on the crystal field environment of the host lattices. In general, octahedrally coordinated Mn^{2+} (strong crystal field, $^{VI}Mn^{2+}$) shows orange to red PL, while tetrahedrally coordinated Mn^{2+} (weak crystal field, $^{IV}Mn^{2+}$) presents green PL.²² This enables tuning of the PL properties through CN of Mn^{2+} and local ligand field.

Although the excitation scheme of Mn^{2+} spans a broad spectral range of ~320 to 550 nm, the intrinsic $3d$ - $3d$ absorption transition of Mn^{2+} is hard to pump because of its characteristic spin- and parity-forbidden electric dipole transitions. Thus a sensitizer is necessary to improve the absorption and PL efficiency of Mn^{2+} . For instance, a Zn_2SiO_4 host is one of the most efficient sensitizers for $^{IV}Mn^{2+}$. And $Zn_2SiO_4:Mn^{2+}$ is the commercial green phosphor for PDPs.²⁰ In addition, the long decay time of Mn^{2+} emission (~10 ms) can result in saturation in high flux devices.³⁹

1.4.1.5. $3d^7$ ions $^{VI}Co^{2+}$

In octahedral symmetry, the ground state of $Co^{2+}:^4F$ splits into three levels, i.e., 4A_2 , 4T_1 , and 4T_2 with the 4T_1 state as the lowest. $^{VI}Co^{2+}$ shows tunable NIR emission from 1.5–2.5 μm with a FWHM of > 200 nm due to the transition of $^{VI}Co^{2+}:^4T_2(^4F) \rightarrow ^4T_2(^4F)$.^{155,156} Normally, two intense absorption bands at ~500 and 1200 nm can be observed and assigned to the transitions of $^{VI}Co^{2+}:^4T_1(^4F) \rightarrow ^4T_1(^4P)$ and $^{VI}Co^{2+}:^4T_1(^4F) \rightarrow ^4T_2(^4F)$, respectively. For example, the commercially available CW laser $MgF_2:Co^{2+}$ operates at

$\sim 1.6\text{--}2.1\ \mu\text{m}$.¹⁵⁷ The NIR emission from ${}^{\text{VI}}\text{Co}^{2+}:{}^4\text{T}_2({}^4\text{F}) \rightarrow {}^4\text{T}_2({}^4\text{F})$ is greatly quenched in intensity at room temperature compared to that at low temperature, which greatly limits its application.

1.4.1.6. $3d^8$ configuration: ${}^{\text{VI}}\text{Ni}^{2+}$, ${}^{\text{VI}}\text{Cu}^{3+}$

Both Cu^{3+} and Ni^{2+} ions have a $3d^8$ configuration. Due to its low stability, Cu^{3+} was reported only in a few crystals. Over the last decades, the spectroscopic properties of Ni^{2+} doped glasses, glass ceramics and single crystals have drawn great attention for potential applications in tunable lasers and optical amplifiers because of their broad band-type NIR PL.^{26,48} Broadband NIR PL of ${}^{\text{VI}}\text{Ni}^{2+}$ strongly depends on its CN. In general, there are three different coordination states for Ni^{2+} in nature: tetrahedral (fourfold, ${}^{\text{IV}}\text{Ni}^{2+}$), trigonal (fivefold, ${}^{\text{V}}\text{Ni}^{2+}$) and octahedral (sixfold, ${}^{\text{VI}}\text{Ni}^{2+}$). Only ${}^{\text{VI}}\text{Ni}^{2+}$ has been known to provide efficient NIR emission from ~ 1.0 to $1.8\ \mu\text{m}$ with a lifetime of hundreds of μs .^{26,48} The PL position of ${}^{\text{VI}}\text{Ni}^{2+}$ can be finely tuned by changing the ligand field strength around Ni^{2+} . There are three spin-allowed transitions in ${}^{\text{VI}}\text{Ni}^{2+}$, i.e., ${}^3\text{T}_{1g}({}^3\text{F}) \rightarrow {}^3\text{T}_{1g}({}^3\text{P})$, ${}^3\text{T}_{1g}({}^3\text{F}) \rightarrow {}^3\text{A}_{2g}({}^3\text{F})$ and ${}^3\text{T}_{1g}({}^3\text{F}) \rightarrow {}^3\text{T}_{2g}({}^3\text{F})$. They are located in the spectral range of $\sim 900\text{--}1100\ \text{nm}$, $600\text{--}800\ \text{nm}$ and $300\text{--}500\ \text{nm}$, respectively. The first tunable CW laser was reported in 1963 on ${}^{\text{VI}}\text{Ni}^{2+}:\text{MgF}_2$, operating from $1350\text{--}2000\ \text{nm}$ peaked at $\sim 1.6\ \mu\text{m}$ (${}^{\text{VI}}\text{Ni}^{2+}:{}^3\text{T}_2 \rightarrow {}^3\text{A}_2$).²⁵

1.4.2. Tetrahedrally coordinated TM ions

1.4.2.1. $3d^1$ configuration: ${}^{\text{IV}}\text{V}^{4+}$, ${}^{\text{IV}}\text{Cr}^{5+}$ and ${}^{\text{IV}}\text{Mn}^{6+}$

For tetrahedrally coordinated $3d^1$ ions, the energy gap between the excited state ${}^2\text{T}_2$ and the ground state ${}^2\text{E}$ is smaller than for those with octahedral coordination, due to the stronger crystal field strength. Broad PL band occurs in the NIR region. No emission is observed for tetrahedrally coordinated ${}^{\text{IV}}\text{V}^{4+}$ even at low temperature due to strong non-radiative decay process.

${}^{\text{IV}}\text{Cr}^{5+}$

${}^{\text{IV}}\text{Cr}^{5+}$ can be stabilized in phosphates, vanadates and arsenates, where Cr^{5+} substitutes the lattice position of P^{5+} , V^{5+} and As^{5+} . The absorption bands of ${}^{\text{IV}}\text{Cr}^{5+}:{}^2\text{E} \rightarrow {}^2\text{T}_2$ cover a broad range from ~ 520 to $1000\ \text{nm}$. The emission spectra of ${}^{\text{IV}}\text{Cr}^{5+}$ consist of two partially overlapping bands due to the transition from ${}^2\text{T}_2$ to two crystal split ground state of ${}^2\text{E}$. For

example, in $^{IV}\text{Cr}^{5+}$ doped $\text{Sr}_2\text{VO}_4\text{Cl}$, two overlapped emission bands are located at 1080 and 1250 nm.¹⁵⁸ However, the NIR PL of $^{IV}\text{Cr}^{5+}$ is very weak, with a quantum efficiency lower than 1% at room temperature.¹⁵⁹

$^{IV}\text{Mn}^{6+}$

$^{IV}\text{Mn}^{6+}$ shows a broad PL band from 900 to 1600 nm due to the transition of $^{IV}\text{Mn}^{6+}:^2\text{T}_2 \rightarrow ^2\text{E}$. For instance, $^{IV}\text{Mn}^{6+}$ doped BaSO_4 shows a broad NIR PL from 900 to 1600 nm with a quantum efficiency of ~60% at room temperature.¹⁶⁰ It has potential application in tunable and short pulse lasers in the NIR spectral region.

1.4.2.2. $3d^2$ configuration: $^{IV}\text{V}^{3+}$, $^{IV}\text{Cr}^{4+}$, $^{IV}\text{Mn}^{5+}$ and $^{IV}\text{Fe}^{6+}$

The absorption spectra of $3d^2$ ions in tetrahedral environment are dominated by triplet-triplet transitions, and the lowest excited state of $3d^2$ ions is strongly dependent on the ligand field, i.e., $^3\text{T}_2$ for V^{3+} and Cr^{4+} , and ^1E for Mn^{5+} and Fe^{6+} . Both broad band-type emission ($^3\text{T}_2 \rightarrow ^3\text{A}_2$) with relatively short lifetime and narrow line-type emission ($^1\text{E} \rightarrow ^3\text{A}_2$) with relatively long lifetime can be observed for $3d^2$ ions in tetrahedral environment.

$^{IV}\text{V}^{3+}$

Tetrahedrally coordinated $^{IV}\text{V}^{3+}$ exhibits a relatively weak NIR PL peaking at ~1.6 μm from 1.4 to 2.0 μm due to the spin-allowed transition of $^{IV}\text{V}^{3+}:^3\text{T}_2(\text{F}) \rightarrow ^3\text{A}_2(\text{F})$.^{143,161} For instance, the emission peaks of $^{IV}\text{V}^{3+}:\text{GaAs}$, $^{IV}\text{V}^{3+}:\text{LiGa}_2\text{O}_4$, $^{IV}\text{V}^{3+}:\text{LiAl}_2\text{O}_4$ and $^{IV}\text{V}^{3+}:\text{ZnS}$ are located at 1.6, 1.65, 1.73 and 1.75 μm , respectively.¹⁴³

$^{IV}\text{Cr}^{4+}$

Tetrahedrally coordinated $^{IV}\text{Cr}^{4+}$ is interesting because of the broad band-type NIR PL from 1.13–1.63 μm due to the spin-allowed transition of $^{IV}\text{Cr}^{4+}:^3\text{T}_2 \rightarrow ^3\text{A}_2$ with a lifetime of a few μs .^{162–164} For instance, $^{IV}\text{Cr}^{4+}$ doped YAG shows tuned NIR emission from 1332 to 1554 nm.^{162–164} $^{IV}\text{Cr}^{4+}$ has three absorption bands at ~460, 740 and 800–1150 nm, which can be assigned to the transitions of $^{IV}\text{Cr}^{4+}:^3\text{A}_2 \rightarrow ^3\text{T}_{1b}$, $^{IV}\text{Cr}^{4+}:^3\text{A}_2 \rightarrow ^3\text{T}_{1a}$ and $^{IV}\text{Cr}^{4+}:^3\text{A}_2 \rightarrow ^3\text{T}_2$, respectively.¹⁶⁴ $^{IV}\text{Cr}^{4+}$ doped crystals are suitable for tunable CW laser and femtosecond pulse operation in the NIR region between ~1.1–1.7 μm , e.g., $\text{Cr}^{4+}:\text{MgSiO}_4$ (from ~1.1 to 1.7 μm).¹⁶⁵

$^{IV}\text{Mn}^{5+}$

Mn^{5+} mainly exists in a tetrahedral environment. Due to the high charge number of Mn^{5+} , it presents a high crystal field with ^1E as its first excited state. Depending on the ligand field, $^{IV}\text{Mn}^{5+}$ exhibits narrow line-type emission from 1 to 1.5 μm , arising from the spin-

forbidden transition of ${}^{\text{IV}}\text{Mn}^{5+}:{}^1\text{E} ({}^1\text{D}) \rightarrow {}^3\text{A}_2({}^3\text{F})$ with a lifetime of hundreds of μs .¹⁶⁶ The first laser oscillation of Mn^{5+} was reported on ${}^{\text{IV}}\text{Mn}^{5+}$ doped $\text{Ba}_3(\text{VO}_4)_2$ and $\text{Sr}_3(\text{VO}_4)_2$ by Merkle *et al.* Under pulsed 592 nm excitation, the output laser operates at 1.181 μm with a threshold of 0.3 J/cm² and a PL lifetime of 0.43 ms at room temperature.¹⁶⁶

${}^{\text{IV}}\text{Fe}^{6+}$

Like ${}^{\text{IV}}\text{Mn}^{5+}$, the ${}^{\text{IV}}\text{Fe}^{6+}$ ion shows line-type PL at ~ 1600 nm due to the spin-forbidden transition of ${}^{\text{IV}}\text{Fe}^{6+}:{}^1\text{E} ({}^1\text{D}) \rightarrow {}^3\text{A}_2({}^3\text{F})$ with a lifetime of hundreds μs at room temperature. For instance, ${}^{\text{IV}}\text{Mn}^{6+}$ doped K_2CrO_4 shows line-type PL with a maximum at 1600 nm and a lifetime of 0.6 ms.¹⁶⁷

1.4.2.3. $3d^4$ configuration: ${}^{\text{IV}}\text{Cr}^{2+}$

In tetrahedral environment, the free ion electronic term ${}^5\text{D}$ of ${}^{\text{IV}}\text{Cr}^{2+}$ ($3d^4$ configuration) splits into ${}^5\text{T}_2$ ground state and ${}^5\text{E}$ first excited state. ${}^{\text{IV}}\text{Cr}^{2+}$ ion shows a broadband MIR emission in 2–3 μm region due to the spin-allowed transition of ${}^{\text{IV}}\text{Cr}^{2+}:{}^5\text{E} \rightarrow {}^5\text{T}_2$.^{168,169} For instance, MIR CW lasers of ${}^{\text{IV}}\text{ZnSe}:\text{Cr}^{2+}$ and ${}^{\text{IV}}\text{ZnS}:\text{Cr}^{2+}$ (${}^5\text{E} \rightarrow {}^5\text{T}_2$) operate in the 2–3 μm region upon excitation at 680 nm (${}^{\text{IV}}\text{Cr}^{2+}:{}^5\text{T}_2({}^5\text{D}) \rightarrow {}^4\text{A}_2({}^3\text{H})$).¹⁶⁹

1.4.2.4. $3d^6$ configuration: ${}^{\text{IV}}\text{Fe}^{2+}$

Tetrahedrally coordinated ${}^{\text{IV}}\text{Fe}^{2+}$ doped binary (e.g., such as ZnSe, ZnS and ZnTe) and ternary (e.g., CdMnTe, CdZnTe and ZnSSe) chalcogenide crystals show extra broad band-type emission in the MIR range from ~ 3.5 to 5.1 μm , with output powers exceeding 10 W and an efficiency up to 70% due to the transition of ${}^5\text{E} \rightarrow {}^5\text{T}_2$.¹⁷⁰ ${}^{\text{IV}}\text{Fe}^{2+}$ doped chalcogenide crystals are frequently used as MIR tunable lasers over a very broad range of 3.5–5 μm .

1.4.2.5. $3d^8$ configuration: ${}^{\text{IV}}\text{Ni}^{2+}$

Tetrahedrally coordinated ${}^{\text{IV}}\text{Ni}$ shows MIR PL at 2.6 μm at low temperatures due to the transition of ${}^3\text{T}_2(\text{F}) \rightarrow {}^3\text{T}_1(\text{F})$. This MIR PL can only be observed at very low temperature because of the strong non-radiative decay, e.g., in ${}^{\text{IV}}\text{Ni}^{2+}:\text{ZnSe}$.¹⁷¹

1.4.3. Other TM ion: V^{5+} ($3d^0$)

In inorganic oxide matrices, vanadium usually exists in three different oxidation states, i.e., V^{3+} ([Ar] 3d²), V^{4+} ([Ar] 3d¹) and V^{5+} ([Ar]), whereby the trivalent ion is readily oxidized to a higher valence. The PL of V^{5+} ion covers a broadband ranging from 400 to 700 nm due to the relaxation of $\equiv V-O^-$ to $\equiv V=O$.^{23,24} The corresponding excitation band lies in the UV range (200–400 nm) arising from an energy transfer process from O^{2-} to V^{5+} that occurs intrinsically in the vanadyl group. The PLE bands of V^{5+} match the NUV LED chips.²³ However, the knowledge on the optoelectronic properties of vanadium ions is still relatively limited.

1.5. White light-emitting diodes

A light emitting diode (LED) is an electronic device based on semiconductors, which generate light by injecting electrons from the valence band into the conduction band and create a light corresponding to the energy gap. Thanks to the breakthroughs in LED chips in the last two decades, the next-generation solid state lighting in the form of W-LEDs are attracting attention. They have longer working times (> 100,000 hrs), improved rendering index, higher brightness, lower power consumption, smaller size, faster switching and environmental friendliness in comparison with the traditional incandescent light sources. This is why W-LEDs have a wide application range: from full color displays and backlights to devices indicators and automobile headlights.^{172–176} Consequently, they are potential candidates to substitute the widely used conventional incandescent and fluorescent light sources for general lighting applications in future.^{172–176} If all conventional white light sources in the world were substituted by energy efficient LED light sources, ~1000 TW hrs in electricity could be saved every year.

Generally, white light is characterized by: the Commission International d'Eclairage (CIE) chromaticity color coordinates, color temperature and CRI. High quality white light-emission requires a source with CIE color coordinates of (0.333, 0.333), color temperature in the range of 2500–6500 K, and CRI above 80%.⁷⁴ As an inorganic semiconductor light source, the LED chips currently available feature in the wavelength range of UV-Vis-NIR with high brightness. Especially, gallium nitride (GaN)- and indium gallium nitride (InGaN)-based blue-LED chips, and AlGaN-, AlGaInN-based NUV-LED chips show high efficiency.

In principle, there are three different methods to generate white light-emission combining LED chips:^{175,176}

I) RGB-LEDs

The first technique is directly mixing multi-color white LEDs (bi-, tri- and tetrachromatic W-LEDs), i.e., combining two, three or four different monochromatic LEDs to generate the white light-emission. However, the applications of the multi-color W-LEDs are severely limited, mainly due to the fact that different LEDs possess slightly different emission patterns, resulting in variations of the color in regard to direction and poor temperature stability (i.e., the emission efficiency of multi-color LEDs drops exponentially with rising temperature). In addition, it is the most expensive among the three methods.¹⁷⁷

II) Quantum dots converted LEDs

In the second method, differently sized quantum dots are used to down convert higher energy light from NUV- and blue-LEDs to white light. The emitting color of quantum dots can be tuned finely from visible to NIR range by controlling their sizes.

III) pc-WLEDs

The third method is represented by phosphors converted white LEDs (pc-WLEDs), in which one or more visible light emitting phosphors are used to down convert monochromatic light from a NUV- or blue- LED to white light. For pc-WLEDs based blue-LED chips, pc-WLEDs are designed to leak some blue light from the pump blue LED to generate the blue part of the white light. Whereas, for the pc-WLEDs based NUV-LEDs, none of the harmful NUV light from the pumped LEDs is allowed to leak.

In general, the phosphor approach is the most promising, due to high efficiency, long lifetime, low cost, physical robustness, mercury-free design and color stability. As a matter of fact, pc-LEDs have turned out to be the most efficient approach for white light-emission.^{178,179}

Usually, the commercially available pc-WLEDs are a combination of a blue-emitting InGaN-based LED chip (450–470 nm) with a complimentary yellow-emitting phosphor, such as cerium doped yttrium aluminum garnet ($Y_3Al_5O_{12}:Ce^{3+}$).^{180,181} Although these exhibit high luminescence efficiency (> 90%) exceeding that of fluorescent lamps, and they are inexpensive, their applications are limited especially in the area of residential and medical lighting, due to its poor CRI ≈ 70 –80 and a high correlated temperature (CCT ≈ 7750 K) from the color deficiency in the red region and blue-yellow color separation.^{180,181} Besides, the high degradation of the luminescent efficiency at relatively high temperature (strong thermal quenching) and input power dependent emission color also limit their applications. The white light-emission requires improvements in the red light region.

On the other hand, AlGaN- and AlGaInN-based NUV-LED chips have higher intrinsically efficiency than InGaN-based blue-LED chips.¹⁸² Accordingly, an alternative

phosphor approach to get white light is to combine a NUV-LED chip (370–410 nm) with red-, green- and blue-emitting phosphors, due to their super color uniformity, excellent CRI > 90, high luminous efficiency, tunable color temperature and good light color stability. Red-emitting phosphors are still commercially limited to sulfide-based phosphors, such as CaS:Eu²⁺, SrY₂S₄:Eu²⁺, Y₂O₂S:Eu³⁺ and ZnCdS:Cu,Al.¹⁸³ But the poor chemical and thermal stability (and thus short lifetime), severe moisture sensitivity and environmental unfriendliness of these materials limit their applications.⁶⁹ On the other hand, nitrides- and oxynitrides-based phosphors show high chemical stability, but the severe synthesis conditions and high patent licensing costs greatly limit their applications.⁴⁴ Therefore, the development of novel oxide phosphors with low costs, good chemical stability, environmental friendliness and simple synthesis is urgently required to meet the requirements of solid state lighting.

To date, the powdered phosphors are normally embedded in organic epoxy resins in LED devices. But the big difference between of refractive index the phosphors and the organic resins causes a high ratio of light scattering and poor heat resistance, leading to a degradation of luminous intensity and a change of emission color over time. Additionally, the aging of organic epoxy resins under the long-term irradiation of UV light may shorten the lifetime of the LEDs.^{45–47} Glasses and glass ceramics doped with RE and TM ions were reported as good alternatives owing to their easy formability into plate-like shapes (which ensures direct encasement of the NUV-LED chips), excellent chemical and thermal stability, better heat resistance with respect to organic resins, and lower porosity comparing with sintered ceramics.^{37–37}

1.6. Solar cells

Sunlight is not only free, but also extremely abundant. It has been reported that the energy of sunlight irradiated on the Earth's surface is ~10,000 times as much as what we consume currently.¹⁰ Therefore, solar cells which convert sunlight to electricity are prime candidates to solve the upcoming energy crisis. Although the solar cell industry has experienced great development over the last decades, the conversion efficiency of the commercialized single-junction crystalline silicon (c-Si) solar cells is still low (~15%), resulting in high cost per kilowatt-hour.^{49–52} Based on the standard AM1.5 spectrum (Fig. 3), the sunlight irradiated onto the Earth's surface spans a wide range from NUV to MIR (280–2500 nm, 0.5–4.4 eV), but only a small fraction of the sunlight can be effectively used by the solar cells (Fig. 3). According to the Shockley-Queisser limit, the theoretical maximum conversion

efficiency of the single junction crystalline silicon (c-Si) with a band gap energy (E_g) of 1.12 eV is $\sim 30\%$. The other 70% of the energy is lost due to the aforementioned spectral mismatch: low energy photons ($< E_g = 1.12$ eV) are not absorbed (sub-band gap transmission loss), while the excess energy of the high energy photons ($> E_g$) is lost as ‘hot’ electron-hole pairs (lattice thermalization loss).^{66,184,185}

In general, there are two approaches to break the Shockley-Queisser limit. The first method is to develop a novel solar cell, the so called “third generation solar cell”, which can utilize the solar spectrum in a better way. The most promising approach is represented by multi-junction (“tandem”) solar cells of amorphous silicon or gallium arsenide with a smaller band gap. Green *et al.* estimated that the theoretical efficiency of an “infinity-layer” could get to 68% under the radiation of un-concentrated sunlight. However, the large scale applications of tandem solar cells are limited by their complex fabrication and high price.⁹

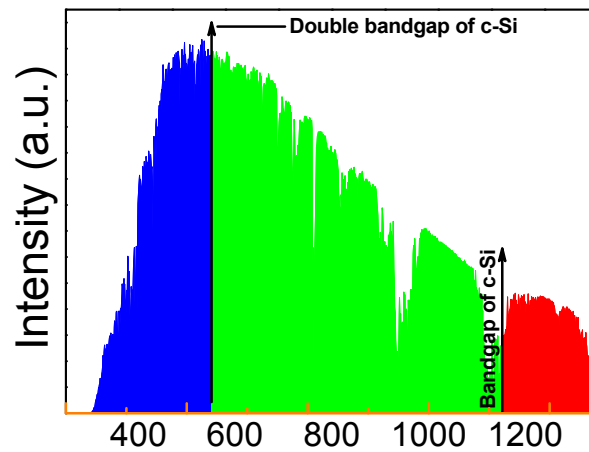


Fig. 3 Standard solar spectrum for air mass 1.5. Raw data was derived from ASTM G173-03 Reference Spectra.

The second route based on the modification of the solar spectrum to better match the solar cells. In general, there are three possible luminescent approaches to adapt the solar spectrum, reduce the loss due to spectral mismatch and enhance the quantum efficiency of the solar cells, i.e., down-shifting, up-conversion and down-conversion (Fig. 4a–4f). The rich energy levels of RE ions make them as ideal ions for aforementioned spectral conversion processes.^{49–52}

1.6.1. Down-shifting

Down-shifting is a one photon to one photon PL process (Fig. 4a), thus the η_{IQE} is smaller than or equal to unit. Even though it cannot exceed the Shockley-Queisser limit, it can raise the conversion efficiency of the solar cells by shifting one high energy photon from the UV-green region into a low energy photon in longer wavelength, which can be better absorbed by the solar cells.⁵² Up- and down-conversion can enhance the efficiency of the solar cells beyond the Shockley-Queisser limit and they will be discussed in the following paragraphs.

1.6.2. Up-conversion

Up-conversion is a non-linear process. Two (or more) sub-bandgap low-energy photons in the NIR region (which cannot be absorbed by the solar cells) are combined into one supra-bandgap high-energy photon in the visible region (which can be utilized by the solar cells). Up-conversion is an anti-Stokes process. According to the Richards' report,⁵⁴ ~35% of the sunlight can be used for up-conversion. Based on the Trupke *et al.*¹⁸⁵ report, the theoretical maximum conversion efficiency can be improved up to 40% by combining a single junction c-Si solar cell with an ideal up-converter layer under un-concentrated sunlight. Since the first report of up-conversion on $\text{CaWO}_4:\text{Yb}^{3+}/\text{Er}^{3+}$ by Auzel *et al.* in 1966, Ln^{3+} ions and pairs have been frequently reported for up-conversion, including Er^{3+} , Ho^{3+} , $\text{Yb}^{3+}/\text{Tm}^{3+}$, $\text{Yb}^{3+}/\text{Er}^{3+}$, $\text{Yb}^{3+}/\text{Ho}^{3+}$ and $\text{Yb}^{3+}/\text{Eu}^{3+}$.^{49,50,82}

In the case of ESA, the excitation photons are successively absorbed by a single active center (Fig. 4d). ESA is independent on dopant concentration. ETU is an energy transfer process involving two neighboring ions. Both neighboring ions absorb a pump photon that populates the metastable state E1. Then one of the two ions transfers the excited energy E1 to the excited state E1 of the other, which is excited to the upper excited state E2 (Fig. 4e). Unlike the ESA process, the ETU up-conversion process is strongly dependent on dopant concentration. PA processes are the combination of both ESA and ETU processes. In PA processes, the E2 states are populated by successively weak non-resonant GSA and ESA of E1. The subsequent cross relaxation (CR) between two neighboring ions leads to the fact that both ions possess the intermediate excited state E1. Circularly, these two ions can populate back to E2 by ESA, resulting in a strong up-conversion PL (Fig. 4f). The PA up-conversion is sensitive to the input power, requiring a pump intensity that exceeds a certain threshold value.⁵⁰

For up-conversion three mechanisms are possible: excited state absorption (ESA), energy transfer up-conversion (ETU) and photon avalanche (PA) (Fig. 4).⁵⁰

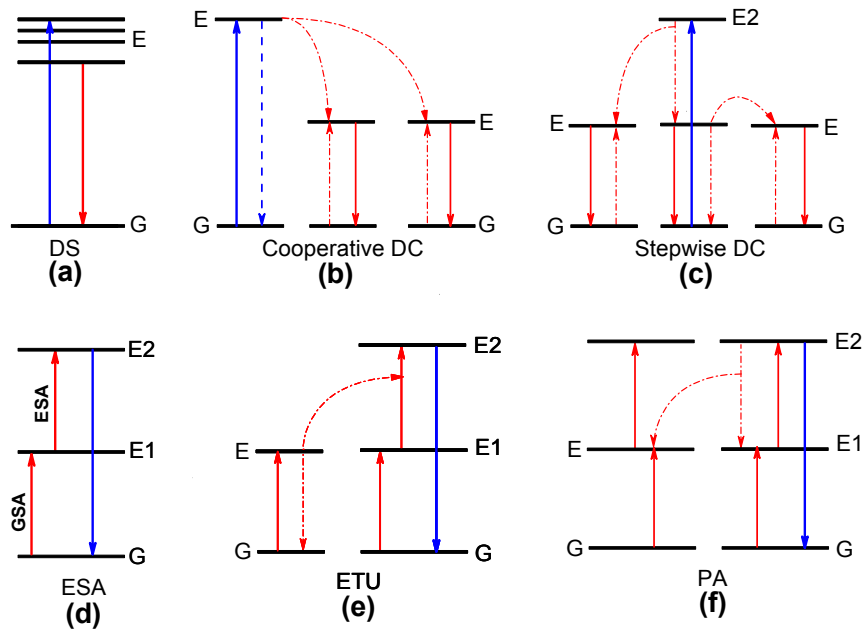


Fig. 4 (a) down-shifting, (b) cooperative down-conversion, (c) stepwise down-conversion, (d) excited state absorption (ESA), (e) energy transfer up-conversion (ETU), and, (f) photon avalanche (PA).

However, the conversion efficiency of the up-conversion solar cells is extremely low. This can be explained by the following reasons. Firstly, up-conversion is a non-linear process, thus a high excitation density is required to achieve high conversion efficiency. Secondly, the absorption efficiency of the Ln^{3+} ions is weak in a narrow spectral window, resulting in the conversion of only an extremely small fraction of sunlight in the NIR region. The highest reported quantum efficiency for up-conversion phosphors are $\sim 4\%$ and 8% for $\text{YF}_3:\text{Yb}^{3+}/\text{Er}^{3+}$ and $\text{KY}_3\text{F}_{10}:\text{Yb}^{3+}/\text{Tm}^{3+}$, respectively.⁵⁶

1.6.3. Down-conversion

Contrary to the up-conversion process, down-conversion is a quantum cutting process with a theoretical quantum efficiency higher than a unit. In this process one incident high-energy photon (NUV to visible) splits into two or more emitting low-energy photons (NIR), which consequently can be absorbed efficiently by the solar cells. Furthermore, it can also minimize the energy loss due to the thermalization of the hot charge carriers which are generated by the excess of high-energy photons ($> E_g$). According to the Richards' report,¹⁸⁴ $\sim 32\%$ of excess energy of UV-Vis photons, which are initially lost as heat, can

be utilized for down-conversion. As reported by Trupke *et al.*¹⁸⁶, the theoretical conversion efficiency of the single junction solar cell with a bandgap of 1.1 eV can be enhanced by up to ~39% upon applying an ideal layer of down-conversion materials on the top of the solar cell. Since the first demonstration of down-conversion in the deep blue region for YF₃:Pr³⁺ by Piper in 1963, wide attention has been devoted to the development of new type of high efficient down-conversion materials, especially to the development of solar cell technology.^{9,10}

According to the Dieke diagram (Fig. 1b), Yb³⁺ has only a single excited state ²F_{5/2} ~10,000 cm⁻¹ above the ground state ²F_{7/2}, which allows Yb³⁺ to pick up energy packages of ~10,000 cm⁻¹ from the other sensitizer ions emitting phonons at a wavelength of ~1000 nm, which falls in the range of the highest spectral response of the single junction c-Si solar cells.⁷⁸ However, the Yb³⁺ ion itself cannot absorb the high energy light in the UV-Vis region. As a consequence, a sensitizer with an energy level ~20,000 cm⁻¹ and capacity to absorb high energy photons in the spectral region at 280–550 nm is required to obtain an efficient down-conversion PL of Yb³⁺.

For the NIR down-conversion PL, two different types of sensitizers are available: a first order stepwise and a second order cooperative energy transfer from the sensitizer to Yb³⁺ (Fig. 4c and 4b, respectively). The Ln³⁺ ions with an intermediate energy level of ~10,000 cm⁻¹ have been reported for the stepwise energy transfer. Among them, Pr³⁺, Er³⁺, Nd³⁺, Ho³⁺ and Dy³⁺ ions are assigned to a two steps resonant first order energy transfer process (Fig. 4c).^{9,10} For example, a Pr³⁺/Yb³⁺ co-doped transparent YF₃ glass ceramic shows optimum quantum efficiency close to 200% by the first order stepwise energy transfer.¹⁸⁷ In contrast to the resonant energy transfer, an intermediate energy level of ~10,000 cm⁻¹ is normally missing in the cooperative energy transfer process (Fig. 4b). Ln³⁺ (e.g., Ce³⁺, Tm³⁺, Tb³⁺ and Pr³⁺) and Ln²⁺ ions (e.g., Eu²⁺ and Yb²⁺) belong to this type.^{9,10} Besides, Bi³⁺, Mn²⁺ and host combination (e.g., VO₄³⁻ and ZnO) are also responsible for this type.^{188,189}

1.7. Glasses and glass ceramics

1.7.1. Glasses

Glass, which was discovered as early as 3500 BCE in Mesopotamia, has been widely used as a major building and optical material for thousands of years.^{15,190} Unlike crystalline materials, it does not have a clear melting temperature, but exhibits a glass transition

temperature. Glasses possess only short range order structure and lack any long range periodicity.^{15,190}

The inorganic glasses can be divided into oxide, fluoride, chalcogenide, and chalcogen halide glasses. Among them, oxide glasses have been thoroughly investigated and are widely used. According to the type of glass forming oxide which make up the glass structure, they can be further classified into silicate, phosphate, borate, germanate and tellurite glasses.¹⁹⁰

Glasses are mainly produced by melting and quenching method. Their properties are strongly dependent on the chemical composition. In general, glasses possess high transparency, high mechanical strength, gas and liquid impermeability, easy formability into various shapes, high chemical durability, easy mass production, compositional variety and biocompatibility. Consequently, they are widely used in many areas including building, communication, medicine and environment.^{15,190,191}

1.7.2. Glass ceramics

Glass ceramics are two phases containing polycrystalline materials formed by the controlled crystallization of glasses. In general, there are three principle routes available to produce glass ceramics: (I) glass ceramic route, (II) sintered route, and (III) sol-gel route.¹⁹²

I). The traditional approach is the glass ceramic route. Here, glass ceramics are prepared by the controlled crystallization of the base glass at temperatures above T_g .¹⁹² Crystallization can be divided into two subsequent stages: nucleation and crystal growth stage. The first stage is holding the base glass at a relatively low temperature T_1 (nucleation temperature) to form a high density of nuclei or to promote phase separation. The second stage is carried out at a higher heat treatment temperature T_2 (crystal growth temperature) to induce the growth of the nuclei at a reasonable rate.¹⁵ Considering energy effectiveness, single heat treatments can also be applied to some glass systems presenting an extensive overlap of the nucleation rate and crystal growth rate in a certain temperature range.

II). Glass ceramics prepared by sintered route were proposed by Sack in 1965.¹⁹³ In this case, glass frits are sintered and surface crystallized. This method could utilize surface imperfections in quenched frits as nucleation sites. The biggest advantage of this method is that glass ceramics can be coated on metals or other ceramics.¹³

III). Glass ceramics can be synthesized by sol-gel route at far lower temperatures than those of the conventional melting and quenching method. Sol-gel glasses can avoid many processing problems, such as phase separation and uncontrolled crystallization occurring during high temperature melting process. Additionally, it is possible to encapsulate organic compounds or metal complexes in the sol-gel glass.¹⁹⁴ Furthermore, the gels can be formed in different shapes.

The properties of the glass ceramics are mainly determined by the crystalline phases precipitated in the base glass, and by their microstructure, which can be tailored by crystallizing glasses with appropriate chemical compositions, and controlling the crystal nucleation and growth steps. The volume nucleation of crystalline phases in glasses can occur from two mechanisms, i.e., homogeneous and heterogeneous nucleation. During homogeneous nucleation, the nuclei develop from their own composition, while nuclei arise from foreign boundaries in the case of heterogeneous nucleation.¹⁹⁵

Some glass compositions are nucleated homogeneously. But to enhance the internal nucleation rate and phase separation process, nucleating agents are commonly added to base glass compositions. Oxides (e.g., TiO₂, ZrO₂, Cr₂O₃, NiO, WO₃, MoO₃, P₂O₅ and V₂O₅), metallic colloids (e.g., Cu, Au, Ag, Ru and Pt) and F⁻ ions are normally used as nucleating agents.¹³

Based on the Stookey's fundamental studies, the first commercial glass ceramic was produced by Corning Glass Works in 1957.^{15,196,197} Since then a wide range of glass ceramics have been developed and played an important role in our daily life. The commercial glass ceramics are generally based on silica-containing glasses, including silicates, aluminosilicates, and fluorosilicates. Silicate glass ceramics are mainly comprised of alkali and alkaline earth silicate crystals, such as lithium silicate (Li₂SiO₃ and Li₂Si₂O₅), magnesium metasilicate (MgSiO₃), calcium-magnesium metasilicate (CaMgSi₂O₆) and calcium metasilicate (CaSiO₃). To date, aluminosilicate glass ceramics are the most successful developed and commercialized glass ceramics. Li₂O–Al₂O₃–SiO₂ (LAS), MgO–Al₂O₃–SiO₂ (MAS), ZnO–Al₂O₃–SiO₂ (ZAS) are the most studied systems. Accordingly, transparent β-quartz-, mullite-, spinel-based oxide glass ceramics have been developed and found applications in many areas.¹⁹⁷ Fluorosilicate glass ceramics show unique mechanical properties due to highly anisotropic crystals. Mica and chain silicates based glass ceramics are good examples. Mica glass ceramics present mechanical machinability, while chain silicates based glass ceramics display extreme strength and toughness. The sheet and chain structures of mica and chain silicates based glass ceramics are both stabilized by the F⁻ ion.¹⁹⁶

Meanwhile, transparent oxyfluoride glass ceramics, first reported by Wang and Ohwaki in 1993, were investigated extensively over the last two decades.^{198–200} They combine the advantages of both fluoride crystals (low phonon energy $\sim 500\text{--}650\text{ cm}^{-1}$, high level RE ions solubility and large transmission window up to $\sim 6\text{ }\mu\text{m}$) and glasses (e.g., broad compositional flexibility, high homogeneity, and easy fabrication such as fibers and large size plates). Up to now, many kinds of oxyfluoride glass ceramics have been developed, including BaF_2 , SrF_2 , CaF_2 , MgF_2 , PbF_2 , CdF_2 , NaYF_4 , LaF_3 , and YF_3 .^{199,200}

Normally, glass ceramics with crystalline volume fraction of $\sim 50\text{--}95\text{ vol}\%$ are not fully crystallized. One or more crystalline phases may appear during heat treatment. The composition of the crystalline phases and of the residual glass can differ from that of the precursor glass.²⁰¹ During the heat treatment process, the RE and TM ions can be selectively incorporated into the newly formed crystal phases. If the RE and TM ions can be incorporated into the crystalline phases after crystallization of the precursor glass, the combination of the excellent optical properties of poly-crystal and manipulation of the oxide glass is obtained.

Glass ceramic is a new material class with some special properties, which have not been totally known to date. Unlike the conventional ceramics, glass ceramics have almost no pores, because no pressing and sintering are needed for the glass ceramics fabrication. Since a glass ceramic consists of both ordered crystalline regions and disordered amorphous regions, it combines the advantages of both non-crystalline glasses (e.g., well-controlled dopant concentration and easy fabrication such as fibers and large size plates) and crystalline ceramics (e.g., optical activity, and excellent capability to host dopants).^{6,13} These properties allow glass ceramics to be used in a wide range of applications in many areas of science and technology.²⁰²

2. Cumulative summary

Most of the data in this thesis have been published in peer reviewed journals. Thus, the results and discussion part of the thesis will be presented in the form of a collection of publications in the peer reviewed journals.

2.1. Enhanced photoluminescence from mixed-valence Eu-doped nanocrystalline silicate glass ceramics

Both Eu^{3+} and Eu^{2+} ions can be stabilized in $\text{BaAl}_2\text{Si}_2\text{O}_8/\text{LaBO}_3$ glass ceramic. The incorporation of Eu^{3+} ions on La^{3+} sites in LaBO_3 crystalline phase after crystallization results in the improved PL properties of Eu^{3+} . Besides, Eu^{3+} ions can be partially reduced to Eu^{2+} owing to the incorporation of Eu^{3+} on Ba^{2+} sites in $\text{BaAl}_2\text{Si}_2\text{O}_8$ crystalline phase after crystallization. The first paper presents these results in detail.

G. Gao, N. Da, S. Reibstein and L. Wondraczek, *Opt. Express* 2010, **18**, A576–A583. -
Reproduced by permission of The Optical Society of America.

<http://www.opticsinfobase.org/oe/abstract.cfm?uri=oe-18-S4-A575>

Enhanced photoluminescence from mixed-valence Eu-doped nanocrystalline silicate glass ceramics

Guojun Gao, Ning Da, Sindy Reibstein, and Lothar Wondraczek*

Department of Materials Science, University of Erlangen-Nuremberg, 91058 Erlangen, Germany

*lothar.wondraczek@ww.uni-erlangen.de

Abstract: Intense photoluminescence was observed from mixed-valence Eu-doped nanocrystalline $\text{BaAl}_2\text{Si}_2\text{O}_8/\text{LaBO}_3$ glass ceramics. For preparation in air, the ratio between Eu^{3+} and Eu^{2+} luminescence depends on synthesis temperature. XRD, TEM and IR absorption spectra were employed to characterize the crystallization process and structural properties of the precursor glass and corresponding glass ceramics. When annealed at 950 °C, the material exhibited photoluminescence more than ten times stronger than was found in its glassy state. Spectroscopic data indicate that during such a heat treatment, even in air, a significant part of the Eu^{3+} ions is reduced to Eu^{2+} . Lifetime of the $^5\text{D}_0$ state of Eu^{3+} increases with increasing heat treatment temperature. Eu^{3+} species are largely incorporated on La^{3+} sites in LaBO_3 crystallites whereas Eu^{2+} locates on Ba^{2+} sites in the hexacelsian phase. A mechanism for the internal reduction of Eu^{3+} to Eu^{2+} is proposed. Spectroscopic properties of the material suggest application in additive luminescent light generation.

© 2010 Optical Society of America

OCIS codes: (160.4670) Optical materials; (140.3380) Laser materials; (160.2540) Fluorescent and luminescent materials; (140.4480) Optical amplifiers;

References and links

1. C. Ronda, ed., *Luminescence: From Theory to Applications* (Wiley-VCH, 2008).
2. K. K. Mahato, S. B. Rai, and A. Rai, "Optical studies of Eu^{3+} doped oxyfluoroborate glass," *Spectrochim. Acta A Mol. Biomol. Spectrosc.* **60**(4), 979–985 (2004).
3. S. S. Babu, K. Jang, E. J. Cho, H. Lee, and C. K. Jayasankar, "Thermal, structural and optical properties of Eu^{3+} -doped zinc-tellurite glasses," *J. Phys. D Appl. Phys.* **40**(18), 5767–5774 (2007).
4. S. Balaji, P. A. Azeem, and R. R. Reddy, "Absorption and emission properties of Eu^{3+} ions in Sodium fluoroborate glasses," *Physica B* **394**(1), 62–68 (2007).
5. W. Höland, and G. H. Beall, *Glass ceramic technology* (American Ceramic Society, 2002).
6. M. Peng, B. Sprenger, M. A. Schmidt, H. G. Schwefel, and L. Wondraczek, "Broadband NIR photoluminescence from bismuth-doped $\text{Ba}_2\text{P}_2\text{O}_7$ crystals: Insights into the nature of NIR-emitting Bismuth centers," *Opt. Express* **18**(12), 12852–12863 (2010).
7. N. Da, M. Peng, S. Krolkowski, and L. Wondraczek, "Intense red photoluminescence from Mn^{2+} -doped (Na^+ , Zn^{2+}) sulfophosphate glasses and glass ceramics as LED converters," *Opt. Express* **18**(3), 2549–2557 (2010).
8. S. Schweizer, L. Hobbs, M. Secu, J. Spaeth, A. Edgar, G. V. M. Williams, and J. Hamlin, "Photostimulated luminescence from fluorochlorozirconate glass ceramics and the effect of crystallite size," *J. Appl. Phys.* **97**(8), 083522 (2005).
9. K. Driesen, V. K. Tikhomirov, and C. Görrler-Walrand, " Eu^{3+} as a probe for rare-earth dopant site structure in nano-glass-ceramics," *J. Appl. Phys.* **102**(2), 024312 (2007).
10. B. Zhu, S. Zhang, S. Zhou, N. Jiang, and J. Qiu, "Enhanced upconversion and luminescence of transparent Eu^{3+} -doped glass-ceramics containing nonlinear optical microcrystals," *Opt. Lett.* **32**(6), 653–655 (2007).
11. Q. Luo, X. Fan, X. Qiao, H. Yang, M. Wang, and X. Zhang, " Eu^{2+} -Doped Glass Ceramics Containing BaF_2 Nanocrystals as a Potential Blue Phosphor for UV-LED," *J. Am. Ceram. Soc.* **92**(4), 942–944 (2009).
12. M. Nogami, T. Kawaguchi, and A. Yasumori, "Spectral hole burning of Eu^{3+} -doped Al_2O_3 - SiO_2 glass prepared by melt quenching," *Opt. Commun.* **193**(1-6), 237–244 (2001).
13. C. Wang, M. Peng, N. Jiang, X. Jiang, C. Zhao, and J. Qiu, "Tuning the Eu luminescence in glass materials synthesized in air by adjusting glass compositions," *Mater. Lett.* **61**(17), 3608–3611 (2007).

14. Q. Zhang, Y. Qiao, B. Qian, G. Dong, J. Ruan, X. Liu, Q. Zhou, Q. Chen, J. Qiu, and D. Chen, "Luminescence properties of the Eu-doped porous glass and spontaneous reduction of Eu^{3+} to Eu^{2+} ," *J. Lumin.* **129**(11), 1393–1397 (2009).
15. C. Zhang, J. Yang, C. Lin, C. Li, and J. Lin, "Reduction of Eu^{3+} to Eu^{2+} in $\text{MAl}_2\text{Si}_2\text{O}_8$ ($\text{M}=\text{Ca}, \text{Sr}, \text{Ba}$) in air condition," *J. Solid State Chem.* **182**(7), 1673–1678 (2009).
16. M. Peng, Z. Pei, G. Hong, and Q. Su, "The reduction of Eu^{3+} to Eu^{2+} in $\text{BaMgSiO}_4:\text{Eu}$ prepared in air and the luminescence of BaMgSiO_4 phosphor," *J. Mater. Chem.* **13**(5), 1202–1205 (2003).
17. M. Peng, and G. Hong, "Reduction from Eu^{3+} to Eu^{2+} in $\text{BaAl}_2\text{O}_4:\text{Eu}$ phosphor prepared in an oxidizing atmosphere and luminescence properties of $\text{BaAl}_2\text{O}_4:\text{Eu}$," *J. Lumin.* **127**(2), 735–740 (2007).
18. M. P. Saradhi, and U. V. Varadaraju, "Photoluminescence studies on Eu^{2+} -Activated $\text{Li}_2\text{SrSiO}_4$ -a Potential Orange-Yellow Phosphor for Solid-State Lighting," *Chem. Mater.* **18**(22), 5267–5272 (2006).
19. A. Kremenović, P. Norby, R. Dimitrijević, and V. Dondur, "Time-temperature resolved synchrotron XRPD study of the hexacelsian $\alpha \rightarrow \beta$ polymorph inversion," *Solid State Ion.* **101–103**(1-2), 611–618 (1997).
20. R. Böhlhoff, H. U. Bambauer, and W. Hoffmann, "Hochtemperatur-Lanthanborat," *Naturwissenschaften* **57**(3), 129 (1970).
21. n.n., Natl. Buro Standards US monograph No. 25 (1), p. 20 (1962).
22. K. El-Egili, "Infrared studies of $\text{Na}_2\text{O}-\text{B}_2\text{O}_3-\text{SiO}_2$ and $\text{Al}_2\text{O}_3-\text{Na}_2\text{O}-\text{B}_2\text{O}_3-\text{SiO}_2$ glasses," *Physica B* **325**, 340–348 (2003).
23. L. Stoch, and M. Sroda, "Infrared spectroscopy in the investigation of oxide glasses structure," *J. Mol. Struct.* **511–512**(1-3), 77–84 (1999).
24. M. Arora, S. Baccaro, G. Sharma, D. Singh, K. S. Thind, and D. P. Singh, "Radiation effects on $\text{PbO}-\text{Al}_2\text{O}_3-\text{B}_2\text{O}_3-\text{SiO}_2$ glasses by FTIR spectroscopy," *Nucl. Instrum. Methods Phys. Res. B* **267**(5), 817–820 (2009).
25. F. Wang, A. Stamboulis, D. Holland, S. Matsuya, and A. Takeuchi, "Solid state MAS-NMR and FTIR study of barium containing aluminosilicate glasses," *Key Eng. Mater.* **361–363**, 825–828 (2008).
26. P. Pernice, S. Esposito, A. Aronne, and V. N. Sigaev, "Structure and crystallization behavior of glasses in the $\text{BaO}-\text{B}_2\text{O}_3-\text{Al}_2\text{O}_3$ system," *J. Non-Cryst. Solids* **258**(1-3), 1–10 (1999).
27. Y. Chen, H. Xiao, S. Chen, and B. Tang, "Structure and crystallization of $\text{B}_2\text{O}_3-\text{Al}_2\text{O}_3-\text{SiO}_2$ glasses," *Physica B* **404**(8-11), 1230–1234 (2009).
28. H. Giesber, J. Ballato, G. Chumanov, J. Kolis, and M. Dejneka, "Spectroscopic properties of Er^{3+} and Eu^{3+} doped acentric LaBO_3 and GdBO_3 ," *J. Appl. Phys.* **93**(11), 8987–8994 (2003).

1. Introduction

Over the last few decades, optical properties of rare-earth (RE) ions doped into various host materials have been studied extensively, mainly with respect to potential application in solid state lighting, displays, lasers, optical amplifiers, sensors, etc [1]. Of the various RE species, europium is traditionally occupying a dominant role. The electronic configuration of Eu is $[\text{Xe}]4f^75d^06s^2$. In oxide matrices, it is usually incorporated as Eu^{3+} or Eu^{2+} . Depending on valence state, its red (Eu^{3+}) or bluish (Eu^{2+}) luminescence is widely known and made use of in various applications. In the case of Eu^{3+} , photoluminescence typically originates from $f-f$ transitions which are practically independent of ligand field strength. The corresponding emission spectrum comprises relatively narrow bands, in glasses usually dominated by the ${}^5\text{D}_0 \rightarrow {}^7\text{F}_2$ transition at a wavelength of about 612 nm. On the other hand, for Eu^{2+} , photoluminescence evolves from $f-d$ relaxation. In this case, corresponding emission bands are typically rather broad and strongly field-dependent (e. g. [2–4]).

Doping Eu^{3+} into glass ceramics may be motivated by various aspects. Most importantly, compared to conventional solid-state reactions, the glass ceramic route enables to benefit from all the advantages of glass processing. That is, glasses with very broad compositional flexibility, very high homogeneity and well-controlled dopant concentration may be prepared (and recycled) by conventional melting, and can, in principal, be processed almost universally [5]. In a second step of thermal annealing, one or more crystalline phases are then precipitated from the glass, preferably by internal nucleation without affecting macroscopic geometry of the as-processed body. The structure of the precipitated crystallite species is typically controlled by composition and annealing procedure. Depending on the availability of sufficiently large (or small) lattice sites, the dopant will at least partially enter (or not enter) the crystalline phase [6]. As a consequence, the spectroscopic properties of the material change. For instance, if the dopant does not enter the crystalline phase, it will ultimately be enriched in the residual glass phase and, e.g., concentration quenching may be observed. Alternatively, emission intensity may be increased as a result of multiple scattering at the

newly developed glass-crystal interfaces [7]. Multiple scattering may also occur in the contrary case, if the dopant enters the crystalline phase. As a result of the changing ligand field, distinct changes may occur in the emission spectrum as well as in the lifetime of the excited states. Internal QE may be affected by a change in the phonon-electron interaction and, hence, the probability of non-radiative transfer. Additionally, a change in the absorption cross section may further lead to increasing emission intensity. Often, it is thus highly desirable to, via developing glass ceramics, combine advantages of glasses and polycrystalline materials. From a standpoint of optical application, it is usually even more desirable to prepare glass ceramics with high crystallite number density and low crystallite size. Such nanocrystalline glass ceramics, suitable as host material of Eu-dopants, can be obtained only from a rather limited number of chemical systems [8–11].

Usually, in order to stabilize Eu^{2+} , synthesis of the doped material requires a reducing atmosphere (e.g. H_2 or CO). However, it has been shown that in relatively acidic glasses such as Al_2O_3 - SiO_2 [12], alkaline earth borate [13] or infiltrated nanoporous silica [14], the redox equilibrium can be pushed towards Eu^{2+} even for melting in oxidizing atmosphere. Similarly, various polycrystalline materials, typically prepared via solid state reaction, are now known where Eu^{2+} can be stabilized even when synthesizing in air, e.g. alkaline earth aluminosilicates [15], BaMgSiO_4 [16], BaAl_2O_4 [17], and $\text{Li}_2\text{SrSiO}_4$ [18]. However, little attention has been paid in this respect to Eu-doped glass ceramics. The present work therefore focuses on a novel mixed-valence Eu-doped nanocrystalline glass ceramic material in which, after synthesis in air, the luminescence ratio of $\text{Eu}^{2+}/\text{Eu}^{3+}$ can be controlled by the temperature of annealing and the degree of crystallization.

2. Experimental

Samples of nominal composition (mol.%) 33.3SiO_2 - $10\text{Al}_2\text{O}_3$ - $16.7\text{B}_2\text{O}_3$ - 35BaO - $5\text{La}_2\text{O}_3$ - $0.2\text{Eu}_2\text{O}_3$ (SABBL) were prepared by conventional melting and quenching from a 100 g batch of analytical grade reagents SiO_2 , Al_2O_3 , H_3BO_3 , BaCO_3 , La_2O_3 and Eu_2O_3 . Melting was performed in alumina crucibles at 1600 °C for 2 hours. Glass slabs were obtained after pouring the melts into preheated (500 °C) graphite moulds and annealing for 2 h. From these slabs, disks of $10 \times 10 \times 1 \text{ mm}^3$ were cut and polished (SiC/water). Subsequently, samples were heat-treated on an alumina substrate at temperatures between 800 °C and 950 °C (step size 50 °C) for 2 hours in ambient atmosphere. During this procedure, glasses were transformed into translucent glass ceramics. Structural characterization was performed by X-ray diffractometry (XRD, Siemens Kristalloflex D500, Bragg-Brentano, 30 kV/30 mA, Cu $\text{K}\alpha$) and infrared (IR) absorption spectroscopy (FTIR spectroscopy, Pekin-Elmer 1600) in the wave number range of 400 - 2000 cm^{-1} with a resolution of 2 cm^{-1} . Photoluminescence was studied with a high-resolution spectrofluorometer and by single photon counting (Horiba Jobin Yvon Fluorolog-3), using a static Xc lamp (450 W) and a Xc flashlamp (75 W) as excitation sources, respectively. All spectroscopic analyses were performed at room temperature. Transmission electron microscopy (TEM) was performed on a Philips CM30 at 300kV. For that, samples were cut in slices, polished, dimpled and subsequently ion-thinned and coated with a thin carbon layer.

3. Results and discussion

3.1 Structural characterization

XRD patterns of Eu-doped SABBL samples are shown in Fig. 1. The as-melted specimen does not exhibit any discrete diffraction peaks, confirming its amorphous nature. Annealing resulted in the gradual precipitation of hexacelsian [19], $\text{BaAl}_2\text{Si}_2\text{O}_8$, (JCPDS card no. 00-012-0725), first observed after heat-treating for 2 h at 850 °C. Subsequently, after treatment at 950 °C, an orthorhombic high-temperature polymorph of lanthanum orthoborate can be observed (JCPDS card no. 00-012-0762). The latter is assumed to be a result of lattice

distortion in monoclinic LaBO_3 ([20], JCPDS card no. 00-073-1149) due to the incorporation of impurities such as, eventually, Eu-ions [21]. Both phases can readily be observed by TEM (Fig. 1, right).

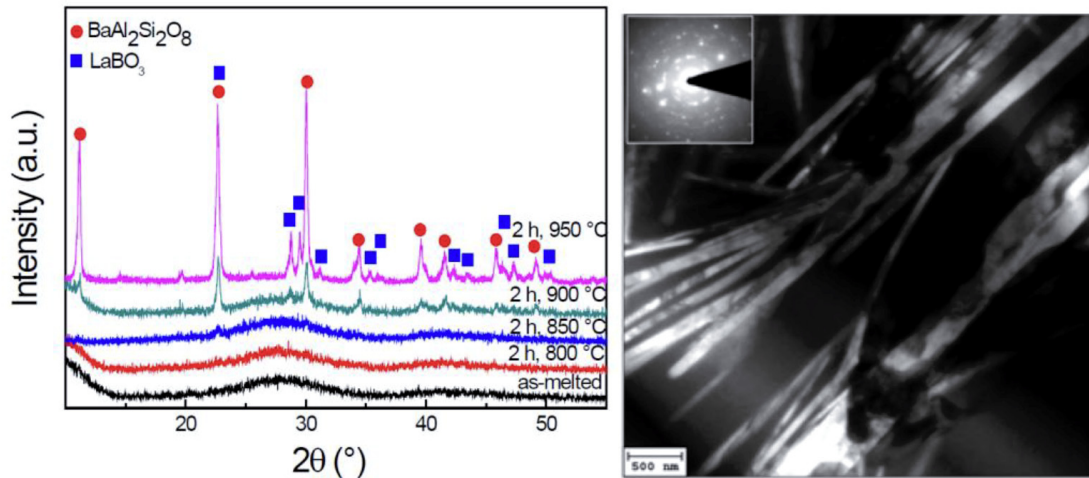


Fig. 1. XRD pattern of as-made Eu-doped SABBL and corresponding samples after annealing at various temperatures (left). Right: Bright field image showing diffraction contrast of needle-shaped hexacelsian and globular LaBO_3 crystallites. Inset: Corresponding diffraction pattern, resulting from contributions of several crystals with different orientation.

Corresponding FTIR absorption spectra are presented in Fig. 2. Spectra were normalized to the intensity of the peak at around 960 cm^{-1} . In Fig. 2(a), the deconvolution of the spectrum of the as-made glass into eight individual peaks is shown. These are attributed to Si-O-Si asymmetric bending of SiO_4 tetrahedra ($\sim 450\text{ cm}^{-1}$ [22]), due to the impact of the Ba^{2+} network modifier ion deconvoluted into two peaks at 441 cm^{-1} and 481 cm^{-1} [12], the B-O-B bending vibration in trigonal BO_3 , overlapped by vibrations of the AlO_6 -group at 702 cm^{-1} [23,24], B-O-B stretching in tetrahedral BO_4 , overlapped by vibrations of Si-O⁻ non-bridging oxygen at $\sim 950\text{ cm}^{-1}$ [13], the Si-O-Si asymmetric stretching vibration at 1052 cm^{-1} [25], asymmetric stretching of the B-O⁻ non-bridging oxygen at 1233 cm^{-1} and 1395 cm^{-1} [13,26] and boroxol rings at 1306 cm^{-1} [27]. Upon transition to the glass ceramic [Fig. 2(b)], distinct sharpening and splitting of these bands can be observed. I. e., splitting of the Si-O-Si asymmetric bending increases. At the same time, the B-O-B bending vibration of trigonal BO_3 shifts to higher energy and decreases in intensity, and a new band evolves at $\sim 650\text{ cm}^{-1}$. Also the broad resonance at around 960 cm^{-1} sharpens, shifts towards higher energy and, upon crystallization, deconvolutes further into at least three distinct bands. The intensity ratio of the bands at $\sim 960\text{ cm}^{-1}$ and $\sim 700\text{ cm}^{-1}$ increases with increasing crystallization progress, indicating a transition in boron coordination from trigonal to tetrahedral. Consequently, also the resonances of the asymmetric stretching vibrations of non-bridging oxygen sharpen, and the band centered at $\sim 1233\text{ cm}^{-1}$ (B-O⁻ of BO_4) increases in intensity.

3.2 Photoluminescence from Eu^{3+} centers

As noted before, it is well known that in a solid matrix, photoluminescence from Eu^{2+} is dominated by the $4f^65d \rightarrow 4f^7$ transition, while emission from Eu^{3+} ions results from $^5\text{D}_0 \rightarrow ^7\text{F}_J$ ($J = 0-4$). Both species can thus be unambiguously distinguished by luminescence spectroscopy.

Room temperature excitation spectra of Eu^{3+} (monitoring the 612 nm emission) in Eu-doped SABBL glass and glass ceramics are shown in Fig. 3(a). Broad excitation peaks correspond to Eu^{3+} transitions from the ground state ($^7\text{F}_0$) to the indicated excited levels. The most intense excitation peak corresponds to the $^7\text{F}_0 \rightarrow ^5\text{L}_6$ transition at 393 nm and was used in

the following for recording Eu^{3+} emission spectra [Fig. 3(b), relaxation from $^5\text{D}_0$ to the indicated states]. As visible from Fig. 3(b), upon heat-treatment, the luminescence properties of Eu^{3+} ions undergo significant changes. That is, firstly, upon crystallization, intensity of all excitation and emission peaks increases notably. In principle, this may be a result of either multiple scattering, increasing absorption cross section or increasing quantum efficiency, eventually caused by the incorporation of Eu^{3+} in a crystalline environment. In a more detailed consideration, it further becomes visible that particularly the emission bands of $^5\text{D}_0 \rightarrow ^7\text{F}_1$ (587 nm), $^5\text{D}_0 \rightarrow ^7\text{F}_3$ (648 nm) and $^5\text{D}_0 \rightarrow ^7\text{F}_4$ at (702 nm) become sharpen and that, relative to the overall increase, their intensity increase is stronger (i.e., the intensity ratio of these peaks to the 612 nm - peak increases). This change is most prominent when the annealing temperature reaches 950 °C and is taken as a clear indicator that at this temperature, Eu^{3+} species are incorporated into one of the crystalline phases.

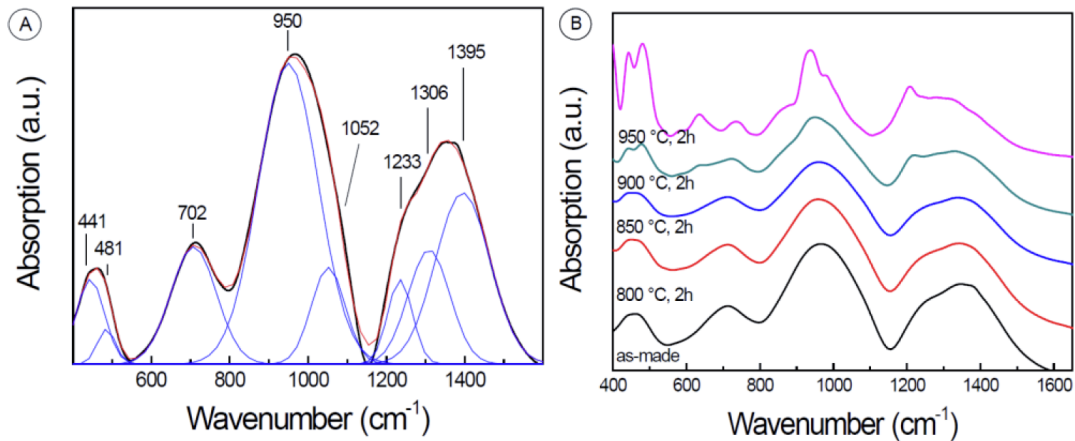


Fig. 2. FTIR absorption spectra of SABBL samples. In (A) the deconvolution of the spectrum of the as-made glass is shown. (B) shows spectra of samples after annealing at different temperatures.

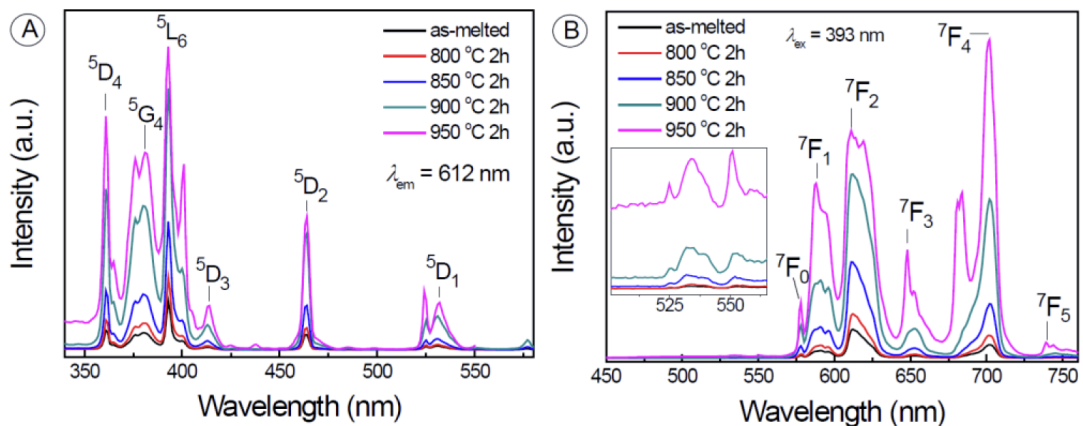


Fig. 3. Eu^{3+} -excitation (A) and emission (B) spectra of as-melted glass and SABBL samples after annealing at various temperatures. Inset of (B): Zoom at the spectral region of 500-570 nm.

The $^5\text{D}_0 \rightarrow ^7\text{F}_2$ transition is electric-dipole allowed and, hence, the intensity of the corresponding photoemission depends strongly on the symmetry of the Eu^{3+} environment. Contrary, $^5\text{D}_0 \rightarrow ^7\text{F}_1$ is magnetic-dipole allowed and is independent of local symmetry [9]. As a result, the ratio R of the emission intensities of $^5\text{D}_0 \rightarrow ^7\text{F}_2$ and $^5\text{D}_0 \rightarrow ^7\text{F}_1$ can be taken as a probe of the ligand asymmetry in the vicinity of Eu^{3+} ions. High values of R indicate low ligand symmetry and high bond covalency. For the present case, R is plotted as a function of the annealing temperature in Fig. 4. Its value decreases with increasing annealing temperature

from about 3.8 to 1.30. Hence, with higher heat treatment temperature, Eu^{3+} locates in an increasingly symmetric environment of less covalent character.

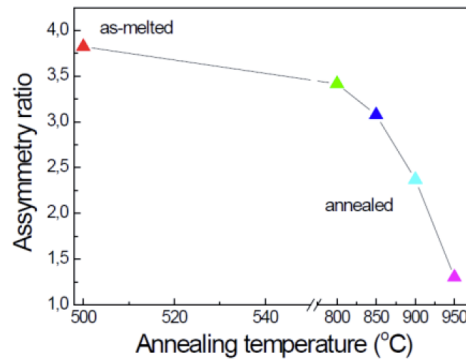


Fig. 4. Asymmetry ratio of the emission intensities of Eu^{3+} transitions of ${}^5\text{D}_0 \rightarrow {}^7\text{F}_2$ and ${}^5\text{D}_0 \rightarrow {}^7\text{F}_1$ for as-melted as well as annealed (2h) SABBL samples for different annealing temperatures.

For the glass ceramic, the emission bands of ${}^5\text{D}_0 \rightarrow {}^7\text{F}_1$ and ${}^5\text{D}_0 \rightarrow {}^7\text{F}_2$ exhibit strong Stark splitting into two or three, respectively, distinct bands. For the as-melted glass, splitting of the ${}^5\text{D}_0 \rightarrow {}^7\text{F}_1$ transition into three peaks indicates the low symmetry of the Eu^{3+} environment. Upon crystallization, these split bands become sharper and gradually overlap. This is a further indicator of the increasing symmetry of the Eu^{3+} environment. A similar conclusion can be drawn from the evolution of the split emission bands of ${}^5\text{D}_0 \rightarrow {}^7\text{F}_3$ and ${}^5\text{D}_0 \rightarrow {}^7\text{F}_4$.

Typically, photoluminescence from Eu^{3+} ions doped into glasses always results from ${}^5\text{D}_0$, regardless of which was the highest excitation band. The reason for this is the occurrence of fast non-radiative relaxation of the ${}^5\text{D}_{J(1-3)}$ states by multiphonon interaction. In the spectral range of 550 to 570 nm, photoemission (from ${}^5\text{D}_{J(1-3)}$) is therefore very improbable. However, as shown in the inset of Fig. 3(b), for the crystallized samples, photoluminescence from higher lying excited levels ${}^5\text{D}_1 \rightarrow {}^7\text{F}_{1,2,3,4}$, peaking at 525, 535, 551, 560 nm can indeed be observed and the intensity of these bands increases with increasing crystallization. As will be discussed in the following, the reason for this is the lower maximum phonon energy in the vicinity of Eu^{3+} species embedded in the crystalline phase, resulting in less-likely non-radiative energy transfer (see also Fig. 2).

Considering charge and ionic radius, it appears highly probable that the incorporation of Eu^{3+} occurs via substitution of La^{3+} in LaBO_3 [28]. This is further confirmed by the transformation of monoclinic LaBO_3 into an orthorhombic polymorph, $\text{La}_x\text{Eu}_{1-x}\text{BO}_3$, which appears, as already discussed, related to the presence of a stabilizing impurity species (i.e., in the present case, Eu^{3+}). In the consequence, photoluminescence from Eu^{3+} centers is strongly enhanced. Dynamic emission data for the ${}^5\text{D}_0 \rightarrow {}^7\text{F}_2$ and ${}^5\text{D}_0 \rightarrow {}^7\text{F}_1$ transitions of Eu^{3+} , respectively, are shown in Fig. 5(a) and 5(b). For all samples, the observed decay curves follow a single exponential equation. Corresponding emission lifetimes were found to increase from 1.81 to 2.56 ms (${}^5\text{D}_0 \rightarrow {}^7\text{F}_2$) and 1.95 to 2.63 ms (${}^5\text{D}_0 \rightarrow {}^7\text{F}_1$), respectively, from glass to glass ceramic. Longer emission lifetimes as observed for the crystallized specimens indicate lower probability of non-radiative energy transfer. This may originate from the lower maximum phonon energy of XBO_3 which lies within the range of 1296 cm^{-1} ($\text{X} = \text{La}$) and 1040 cm^{-1} ($\text{X} = \text{Eu}$) [28].

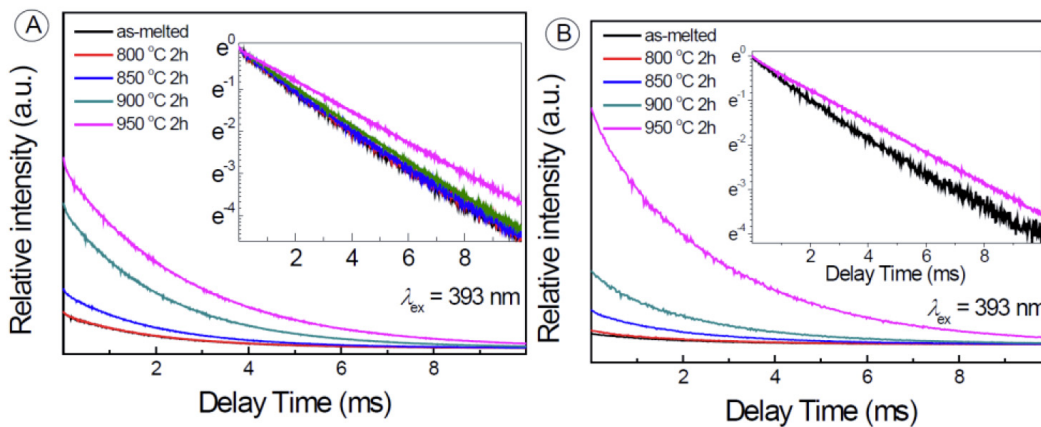


Fig. 5. Luminescence decay curve of Eu^{3+} emission resulting from ${}^5\text{D}_0 \rightarrow {}^7\text{F}_2$ (A) and ${}^5\text{D}_0 \rightarrow {}^7\text{F}_1$ (B) in as-melted Eu-doped SABBL and after annealing at various temperatures. Inset: Exponential plot of the same data, shown for clarity.

3.3 Photoluminescence from Eu^{2+} centers

Monitoring photoemission at 450 nm, a different set of excitation spectra of Eu-doped SABBL glass and glass ceramics is shown in Fig. 6(a). The strong excitation band peaking at 350 nm is assigned to the $4f^7 \rightarrow 4f^6 5d^1$ transition of Eu^{2+} . Corresponding emission spectra (excited at 350 nm) are shown in Fig. 6(b). Emission bands in the spectral range of 570 to 670 nm clearly belong to the already-discussed transitions from ${}^5\text{D}_0$ to ${}^7\text{F}_J$ ($J = 0, 1, 2, 3$ and 4) of Eu^{3+} . However, in samples which were annealed at 800 °C or higher, additional broad emission bands appear at around 400 and 510 nm. These are readily assigned to the transition $4f^6 5d \rightarrow 4f^7$ of Eu^{2+} ions (noteworthy, blank reference samples of SABBL glass and glass ceramics did not exhibit any photoluminescence in the considered spectral range). Interestingly, the quantity of divalent europium ions appears to be affected by the annealing temperature: For the temperature regime of 800-900 °C, Eu^{2+} -related emission intensity only slightly increases with increasing annealing temperature (whereby the as-melted glass sample did not show any photoluminescence in this spectral range). When treated at 950 °C for 2 h, a sudden and strong jump is observed in the emission intensity from Eu^{2+} centers. Although while at the same time, photoluminescence intensity from Eu^{3+} centers, as well, increases, the ratio of $\text{Eu}^{3+}/\text{Eu}^{2+}$ -related emission intensity strongly decreases with increasing annealing temperature. This is interpreted as a redox transition from Eu^{3+} to Eu^{2+} , caused by the annealing process. Hence, the quantity of Eu^{2+} emission centers increases with increasing annealing temperature.

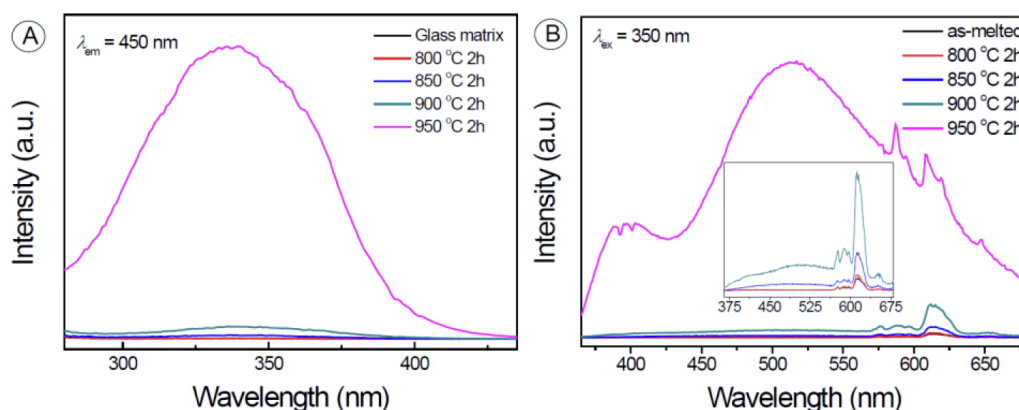


Fig. 6. Eu^{2+} -excitation (A) and emission (B) spectra of as-melted glass and SABBL samples after annealing at various temperatures. Inset of (B): Zoom at the spectral region of 375-675 nm.

The decay curve of the Eu^{2+} -related photoemission from a crystallized sample of SABBL (950 °C, 2h), monitored at 450 nm, is shown in Fig. 7. An effective non-exponential emission lifetime of 29.3 μs is obtained from these data. The decay curve can best be fit by a second-order exponential decay function, resulting in two distinct emission lifetimes, i.e. 17.6 and 34.5 μs . This is taken as further evidence for the present of at least two types of Eu^{2+} -emission sites.

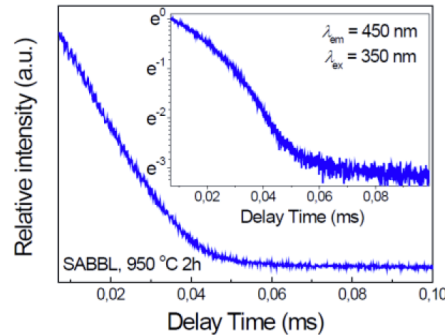
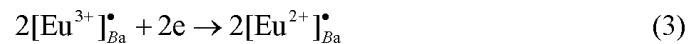
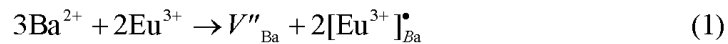


Fig. 7. Luminescence decay curve of Eu^{2+} emission from SABBL after annealing for 2 h at 950 °C. Inset: Exponential plot of the same data, shown for clarity.

In the following, a possible mechanism for the internal reduction of Eu^{3+} to Eu^{2+} is proposed on the basis of charge compensation [4,18–20]. Firstly, it is assumed that Eu^{2+} is incorporated on Ba^{2+} sites in the $\text{BaAl}_2\text{Si}_2\text{O}_8$ hexacelsian phase. While in principle, considering ionic radius alone, Eu^{2+} could readily be incorporated on the relatively large interstitials as well as on either of the cationic sites, this assumption is based on charge and coordination equivalence. In order to incorporate Eu -species in this lattice, for reasons of charge balance, two Eu^{3+} ions are needed to substitute for three Ba^{2+} ions, resulting in the formation of one barium vacancy. This vacancy then acts as the donor of electrons to Eu^{3+} . The whole process is presented in the following equations:



Only a comparably small number of Eu^{3+} species enters the hexacelsian phase where it is reduced to Eu^{2+} . There, it may be present on one of the two differently coordinated (sixfold and eightfold, respectively) Ba^{2+} sites, what gives rise to the occurrence of the distinct emission bands [Fig. 6(b)] and the fact that the decay curve (Fig. 7) does not follow a single exponential equation. Compared with the Ba^{2+} site in $\text{BaAl}_2\text{Si}_2\text{O}_8$, the La^{3+} site in LaBO_3 represents an highly suitable host for Eu^{3+} dopants [28].

Hence, the evolution of luminescence properties with increasing degree of crystallization can be understood as follows: For annealing at ~ 850 °C, the onset of hexacelsian precipitation can be observed (Fig. 1, left). In this temperature range, however, crystallization kinetics appear rather slow. Crystallization is promoted by increasing the annealing temperature. During hexacelsian precipitation, the composition of the residual glass phase shifts towards higher molar content of B_2O_3 and La_2O until at ~ 950 °C, crystalline LaBO_3 precipitates as the secondary crystalline phase. In accordance to this assumption, TEM indicates precipitation of LaBO_3 primarily at the glass- $\text{BaAl}_2\text{Si}_2\text{O}_8$ interface (Fig. 1, right). During this process, Eu^{3+} species are first partly incorporated into the hexacelsian phase, where they are immediately reduced to Eu^{2+} , occupying one of the two available distinct Ba^{2+} -sites. With the subsequent precipitation of LaBO_3 , another part of the Eu^{3+} ions is incorporated on La^{3+} sites, leading to the formation of orthorhombic $(\text{La}_{1-x}, \text{Eu}_x)\text{BO}_3$ [21,28]. Consequently,

photoluminescence occurs simultaneously for Eu^{2+} and Eu^{3+} species. The whole process is overlapped by additional changes in the extent of multiple scattering, especially with the occurrence of the secondary crystalline phase at 950 °C.

4. Conclusions

In summary, the photoluminescence properties of Eu-doped SABBL glasses and glass ceramics were studied. XRD, FTIR and TEM analyses indicate the formation of hexacelsian $\text{BaAl}_2\text{Si}_2\text{O}_8$ and monoclinic LaBO_3 after annealing at ≥ 850 °C and ≥ 950 °C, respectively. While no Eu^{2+} species are present in the as-melted glass, upon annealing, Eu^{3+} ions are partly incorporated into the hexacelsian phase. There, they are immediately reduced to Eu^{2+} . The reduction process may be understood on the basis of a charge compensation model. In the hexacelsian environment, Eu^{2+} ions occupy the two distinct Ba^{2+} sites. LaBO_3 precipitates as secondary crystalline phase and provides a further host for Eu^{3+} species. Their incorporation leads to the stabilization of an orthorhombic polymorph of LaBO_3 , and simultaneous photoemission from Eu^{2+} as well as Eu^{3+} centers can be observed. At the same time, Eu^{3+} - related photoemission strongly intensifies. The lifetime of the excited state of $^5\text{D}_0$ increases as a result of decreasing phonon energy. Spectroscopic properties of the material suggest application in additive luminescent light generation.

Acknowledgement

The authors would like to acknowledge the funding of the Deutsche Forschungsgemeinschaft (DFG) through the Cluster of Excellence Engineering of Advanced Materials.

2.2. Tunable dual-mode photoluminescence from nanocrystalline Eu-doped $\text{Li}_2\text{ZnSiO}_4$ glass ceramic phosphors

Eu^{2+} ions can be stabilized in $\text{Li}_2\text{ZnSiO}_4$ glass ceramic. During the controlled nucleation and crystallization processes, Eu^{3+} ions are partially incorporated into $\text{Li}_2\text{ZnSiO}_4$ crystalline phases, and are gradually reduced to Eu^{2+} . The resulting PL color ranging from orange/red to blue can be tuned by adjusting the annealing temperature.

G. Gao, S. Reibstein, M. Peng and L. Wondraczek, *J. Mater. Chem.* 2011, **21**, 3156–3161.
-Reproduced by permission of The Royal Society of Chemistry.

<http://pubs.rsc.org/en/Content/ArticleLanding/2011/JM/c0jm03273e>

Tunable dual-mode photoluminescence from nanocrystalline Eu-doped $\text{Li}_2\text{ZnSiO}_4$ glass ceramic phosphors

Guojun Gao, Sindy Reibstein, Mingying Peng† and Lothar Wondraczek*

Received 29th September 2010, Accepted 9th December 2010

DOI: 10.1039/c0jm03273e

We report on tunable photoluminescence from mixed-valence Eu-doped nanocrystalline $\text{Li}_2\text{ZnSiO}_4$ glass ceramics. After preparation of the precursor glass in air, gradual reduction of Eu^{3+} to Eu^{2+} occurs intrinsically during thermal annealing and precipitation of crystalline $\text{Li}_2\text{ZnSiO}_4$. Dual-mode photoemission can be generated for exciting at a wavelength of about 360 nm. The resulting colour of luminescence, ranging from orange/red to blue, can be controlled by adjusting the annealing temperature and, hence, the degree of crystallization: with increasing annealing temperature, the ratio of luminescence intensities related to Eu^{3+} and Eu^{2+} species, respectively, varies as a result of increasing degree of Eu^{3+} -reduction as well as distinct changes in the optical scattering behaviour of the obtained glass ceramic. At the same time, the bandwidth of Eu^{2+} -related photoemission increases from 87 to 154 nm. The underlying mechanisms of photoemission and energy transfer from Eu^{2+} to Eu^{3+} are discussed on the basis of dynamic emission spectroscopy and structural considerations, and a description of the internal reduction process is given.

Introduction

Inorganic phosphor materials based on lanthanide-doped oxides and mixed-anion species are receiving great attention for potential applications in solid state lighting, display technology and various other areas.^{1–4} Among the various dopant species, europium in divalent or trivalent oxidation state is traditionally occupying a dominant role. The electronic configuration of Eu is $[\text{Xe}]4f^75d^06s^2$. Photoluminescence from Eu^{3+} -doped matrices is characterized by a series of sharp emission bands which are located in the red spectral region. They can be assigned to the electronic transitions ${}^3\text{D}_0 \rightarrow {}^7\text{F}_J$ ($J = 0, 1, 2, 3, 4$) and, hence, their position is practically independent on ligand field strength whereas their intensity ratio is partly related to ligand symmetry.⁵ For Eu^{2+} , photoemission occurs as a result of $4f^65d^1(\text{T}_{2g}) \rightarrow 4f^7({}^8\text{S}_{7/2})$. In this case, the active electronic level is not shielded against the surrounding ligands and position and width of the emission band are strongly dependent on the host lattice.^{6–9}

In oxide matrices, particularly when employing Eu_2O_3 as raw material, europium is usually incorporated in its trivalent form. In order to obtain Eu^{2+} -doped materials, one of four general reduction strategies can typically be applied: (i) to prepare the material in a strongly reducing atmosphere, *e.g.* H_2 or CO (*e.g.* ref. 10), (ii) to extrinsically reduce the polyvalent species in an as-prepared material, *e.g.* by high-energy photoreduction or

thermal treatment in a reducing atmosphere (*e.g.* ref. 11–13), (iii) to provide a sufficiently acidic environment in which the reduced species can be obtained even for synthesis in air,^{14–21} or (iv) to promote an intrinsic reduction process, *e.g.* by initiating a structural rearrangement in a frozen-in system.^{22,23} For environmental, technological and cost-related reasons, the latter two methods are the most attractive, but can be applied only to a limited number of chemical systems.

Compared to conventional solid-state reaction, the glass ceramic route (preparation of a precursor glass and recrystallization of this glass to a dense and homogeneous polycrystalline material²⁴) provides various technological and property-related advantages (*e.g.* ref. 25–28). Specific to the present case, it enables an attractive strategy to generate Eu^{2+} and mixed-valence Eu-doped materials *via* path (iv).²³ Nanocrystalline Eu-doped $\text{Li}_2\text{ZnSiO}_4$ glass ceramics are therefore introduced as such a material. Based on structural considerations as well as dynamic and static spectroscopic data, it is shown in the present report how the ratio between divalent and trivalent europium dopants and, hence, the colour of photoluminescence can be finely tuned from blue to orange and red by controlling the annealing and crystallization process, and how dual-band photoemission can be achieved.

Experimental

Zinc silicate glasses represent a classical candidate for the precipitation of nanocrystals after annealing. In particular, on the zinc-rich side, nanocrystalline β -willemitte (Zn_2SiO_4) glass ceramics can readily be obtained.²⁹ If crystalline $\text{Li}_2\text{ZnSiO}_4$ is

Department of Materials Science, University of Erlangen-Nuremberg, Erlangen, 91058, Germany. E-mail: lothar.wondraczek@ww.uni-erlangen.de; Fax: +49 (0)9131 28311; Tel: +49 (0)9131 85 27553

† Present address: Institute of Optical Communication Materials, South China University of Technology, Guangzhou, 510641, China.

precipitated, it is expected that aliovalent substitution of Zn^{2+} by Eu^{3+} can take place. In other matrix materials, such aliovalent substitution has been suggested as the primary driving force for intrinsic reduction of Eu^{3+} to Eu^{2+} , even in oxidizing atmosphere.^{10,14,18,31} It should hence enable a facile route for the simultaneous stabilization of Eu^{3+} and Eu^{2+} in a non-toxic matrix material. To study this hypothesis, precursor glasses with nominal composition (mol%) $48\text{SiO}_2\text{-}24\text{Li}_2\text{O-}16\text{ZnO-}8\text{Al}_2\text{O}_3\text{-}3\text{K}_2\text{O-}1\text{P}_2\text{O}_5\text{-}0.2\text{Eu}_2\text{O}_3$ (SLZAKP) were prepared by conventional melting and quenching from a batch (100 g) of analytical grade reagents SiO_2 , Li_2CO_3 , ZnO , Al_2O_3 , K_2CO_3 , $\text{NH}_4\text{H}_2\text{PO}_4$ and Eu_2O_3 . Melting was performed in alumina crucibles at $1600\text{ }^\circ\text{C}$ for 2 hours. Glass slabs were obtained after pouring the melts into preheated ($400\text{ }^\circ\text{C}$) graphite moulds and annealing for 2 h at $450\text{ }^\circ\text{C}$. From these slabs, disks of $10 \times 10 \times 1\text{ mm}^3$ were cut and polished. Subsequently, individual samples were placed on alumina substrates and annealed for 2 h at 550 , 600 , 650 , 700 and $750\text{ }^\circ\text{C}$, respectively, in ambient atmosphere. Annealing temperatures were chosen on the basis of previous high-temperature X-ray diffraction experiments and differential thermo-analyses. During the annealing procedure, glasses transformed into opalescent glass ceramics *via* precipitation of a homogeneously distributed nanocrystalline phase. These glass ceramics were first analyzed by X-ray diffractometry (XRD Siemens Kristalloflex D500, Bragg-Brentano, $30\text{ kV}/30\text{ mA}$, $\text{Cu K}\alpha$). Subsequently, photoluminescence was studied with a high-resolution spectrofluorometer and by time correlated single photon counting (TCSPC, Horiba Jobin Yvon Fluorolog FL3-22), using a static Xe lamp (450 W), a Xe flashlamp (75 W) and a ps-LED-source at 370 nm (nanoLED), respectively, as excitation sources. For detection, a Peltier-cooled photomultiplier tube (Hamamatsu PMT 925) was used. Excitation curves were corrected over the lamp intensity with a silicon photodiode. External quantum efficiency (eQE) of each sample was obtained from four individual measurements, using a BaSO_4 -coated integration sphere, *i.e.* by recording absorption and emission spectra of the sphere with and without sample. CIE color coordinates were subsequently determined by integrating the emission spectrum. Photographs of the samples were taken under 40 W UV-A broadband illumination. All spectroscopic analyses were performed at room temperature.

Results and discussion

X-Ray diffraction

XRD patterns of SLZAKP samples are depicted in Fig. 1. The as-melted specimen does not exhibit any discrete diffraction peaks, confirming its amorphous nature. After annealing at various temperatures, samples initially remain fully transparent before (for annealing temperatures $\geq 650\text{ }^\circ\text{C}$) starting to turn increasingly translucent, what empirically indicates precipitation of a nanocrystalline secondary phase. For annealing within ~ 550 to $700\text{ }^\circ\text{C}$, XRD patterns suggest assignment to $\text{Li}_2\text{ZnSiO}_4$ (JCPDS card no. 00-024-0682) as the sole crystalline species. $\text{Li}_2\text{ZnSiO}_4$ (monoclinic, space group $Pmn2_1$, $a = 0.613\text{ nm}$, $b = 0.537\text{ nm}$, $c = 0.494\text{ nm}$ ³⁰) is structurally related to Li_3PO_4 , where all cations are fourfold coordinated. Minor amounts of willemite (Zn_2SiO_4) may be present in samples which were annealed at

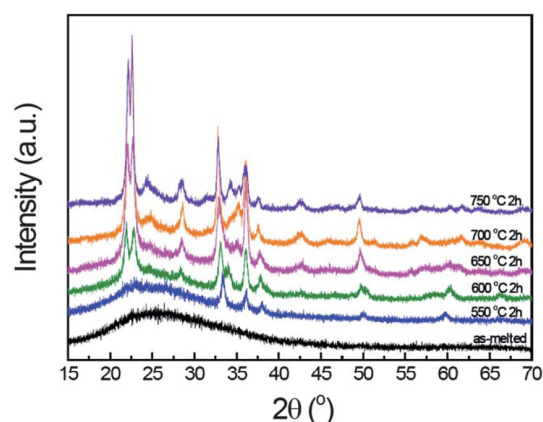


Fig. 1 XRD patterns of as-melted SLZAKP glass and corresponding glass ceramics for different annealing temperatures.

higher temperature.²⁹ With increasing annealing temperature, diffraction peaks increase in intensity and become sharper. In a first consideration, the observed peak shift is taken as a result of lattice distortion due to the assumed incorporation of relatively large Eu^{2+} -ions (1.25 \AA) on Zn^{2+} -sites (0.60 \AA).

Eu^{3+} -luminescence

Fig. 2 shows Eu^{3+} -related excitation and emission spectra of as-made SLZAKP and after annealing at various temperatures. The relatively broad excitation bands can readily be assigned to transitions from the ground state (${}^7\text{F}_0$) to the indicated excited levels.²³ The most intense excitation peak, located at 393 nm , corresponds to the transition ${}^7\text{F}_0 \rightarrow {}^5\text{L}_6$. In the following, this peak was used to record Eu^{3+} emission spectra (Fig. 2B, electronic dipole relaxation from ${}^5\text{D}_0$ to the indicated states). Here, for the as-made glass, the strongest emission is observed at 612 nm (${}^5\text{D}_0 \rightarrow {}^7\text{F}_2$). Thermal annealing results in significant changes of photoemission as well as in the excitation schemes. Generally, all emission bands attain a maximum for samples which were heat-treated at $600\text{ }^\circ\text{C}$ (*e.g.*, a fourfold increase in emission intensity was observed for the 612 nm band as compared to that of the as-made glass). While for higher annealing temperatures, emission intensity decreased somewhat, even for the glass ceramic which was heat-treated at $750\text{ }^\circ\text{C}$, it is still higher than that for the as-made glass. A parallel change can be observed in the excitation spectra (Fig. 2A). At this point, a possible explanation may be that up to a temperature of $600\text{ }^\circ\text{C}$, Eu^{3+} -ions are partly incorporated into the freshly formed crystalline phase.

As noted previously,^{5,23} the intensity ratio R of the electric and magnetic dipole allowed transitions, respectively, of ${}^5\text{D}_0 \rightarrow {}^7\text{F}_2$ and ${}^5\text{D}_0 \rightarrow {}^7\text{F}_1$ which provides a means to assess ligand symmetry of the Eu^{3+} -site. Because ${}^5\text{D}_0 \rightarrow {}^7\text{F}_2$ is dependent on ligand symmetry and ${}^5\text{D}_0 \rightarrow {}^7\text{F}_1$ is not, high values of R typically indicate low ligand symmetry and high bond covalency. In Fig. 3, obtained values of R are given as a function of annealing temperature. Generally, a decrease of R is observed with increasing annealing temperature, *i.e.* from a value of about 3.2 to 1.5. This observation is taken as evidence for the

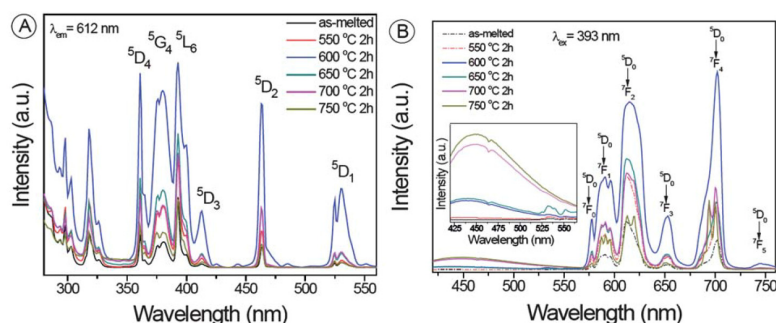


Fig. 2 Eu^{3+} -excitation (A) ($\lambda_{\text{em}} = 612 \text{ nm}$) and emission (B) ($\lambda_{\text{ex}} = 393 \text{ nm}$) spectra of SLZAKP glass and corresponding glass ceramics (labels: annealing temperatures). Inset of (B): zoom at the spectral region of 420–570 nm.

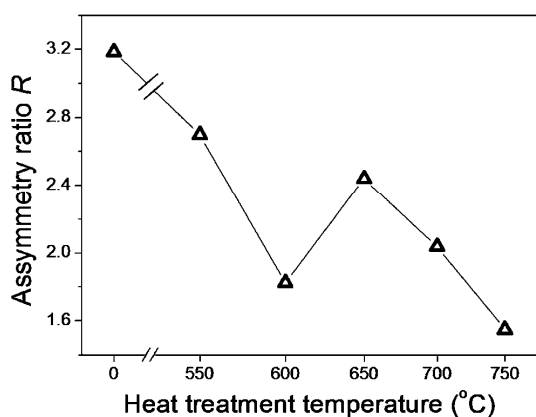


Fig. 3 Asymmetry ratio of the emission intensities of Eu^{3+} transitions of ${}^5\text{D}_0 \rightarrow {}^7\text{F}_2$ and ${}^5\text{D}_0 \rightarrow {}^7\text{F}_1$ for SLZAKP glass and corresponding glass ceramics.

incorporation of Eu^{3+} species into a more symmetric environment of less covalent character, presumably the crystalline phase of $\text{Li}_2\text{ZnSiO}_4$. Noteworthy, the discontinuity in the 600–700 °C range of annealing temperatures, as will be discussed in the following paragraphs, may be interpreted as a result of competition between internal reduction (decreasing amount of Eu^{3+} centers) and crystal precipitation. Accordingly, Stark-splitting of the major emission bands (${}^5\text{D}_0 \rightarrow {}^7\text{F}_1$, ${}^5\text{D}_0 \rightarrow {}^7\text{F}_2$ and ${}^5\text{D}_0 \rightarrow {}^7\text{F}_4$, up to three individual side-bands can be identified, Fig. 2B) significantly increases during crystallization of the samples.

Dynamic emission data for the ${}^5\text{D}_0 \rightarrow {}^7\text{F}_2$ and ${}^5\text{D}_0 \rightarrow {}^7\text{F}_1$ transitions of Eu^{3+} , respectively, are shown in Fig. 4A and B. At least two individual decay processes can be identified, *i.e.* a fast one with a lifetime of about 0.5–1 ms and a slow one with a lifetime of about 2–3 ms. With increasing annealing temperature, the effective lifetime decreases from 2.18 to 0.97 ms (${}^5\text{D}_0 \rightarrow {}^7\text{F}_2$) and 2.55 to 0.49 ms (${}^5\text{D}_0 \rightarrow {}^7\text{F}_1$), respectively. The two decay regimes are assigned to Eu^{3+} species in the glassy and in the crystalline phase, respectively. Upon crystallization, the fast decay process becomes dominant. At the same time, external quantum efficiency decreases from 10.9% to 2.5%, what confirms the increasing occurrence of fast, non-radiative relaxation processes.

Eu^{2+} -luminescence

Optical excitation and emission spectra of Eu^{2+} centers in SLZAKP glass and glass ceramics are shown in Fig. 5. In the as-melted glass, practically no Eu^{2+} -related optical activity could be detected, indicating that only Eu^{3+} is present. The broad UV-blue excitation band that can be observed with increasing intensity for increasing annealing temperature corresponds to the $4f^7 \rightarrow 4f^65d^1$ transition of Eu^{2+} . With increasing annealing temperature, its position blue-shifts from 337 to 307 nm (Fig. 5A). Corresponding emission spectra (excited at 350 nm) are shown in Fig. 5B. They comprise a broad emission band spanning the range of 350 to 650 nm ($4f^65d^1(T_{2g}) \rightarrow 4f^7({}^8S_{7/2})$; noteworthy, undoped samples did not exhibit any photoluminescence for 350 nm excitation). Clearly, as a result of annealing, Eu^{3+} is transformed to Eu^{2+} to an increasing extent. Reflected by the increase in Eu^{2+} -emission intensity, the quantity of divalent europium ions appears to be affected by the heat treatment temperature or by the degree of crystallization. The position of the emission peak red-shifts with increasing annealing temperature, *i.e.* from 420 to 430 nm. This is understood as a result of distortion of the $\text{Li}_2\text{ZnSiO}_4$ lattice with the incorporation of an increasing amount of relatively large Eu^{2+} ions (Fig. 1).

The $4f^65d^1(T_{2g}) \rightarrow 4f^7({}^8S_{7/2})$ emission band can also be observed for excitation at 393 nm (Fig. 2B), although with a much lower intensity (393 nm lies on the red tail of the excitation spectrum, Fig. 5A). Intensities of Eu^{3+} and Eu^{2+} emission bands change oppositely with increasing annealing temperature, what directly illustrates the gradual conversion of Eu^{3+} to Eu^{2+} species.

Interestingly in Fig. 5B, two weak holes can be observed in the emission band, *i.e.* at 393 and 464 nm. Similarly, the excitation band (Fig. 5A) exhibits four weak holes at 298, 318, 361 and 393 nm. The position of these spectral holes corresponds to the luminescence properties of Eu^{3+} and, hence, indicates energy transfer from the 5d level of Eu^{2+} to the 4f levels of Eu^{3+} . This energy transfer results from the overlap between Eu^{2+} -related photoemission at 393 and 464 nm and the ${}^7\text{F}_0 \rightarrow {}^5\text{L}_6$ and ${}^7\text{F}_2 \rightarrow {}^5\text{D}_2$ transition of Eu^{3+} , respectively. That is, from Fig. 2B, it is obvious that Eu^{3+} can practically not be excited at 350 nm. Then, the emission peak which is seen in Fig. 5B at 612 nm (${}^5\text{D}_0 \rightarrow {}^7\text{F}_2$) is a clear reflection of this energy transfer. Again, the decrease in the ratio between the intensities of the bands at

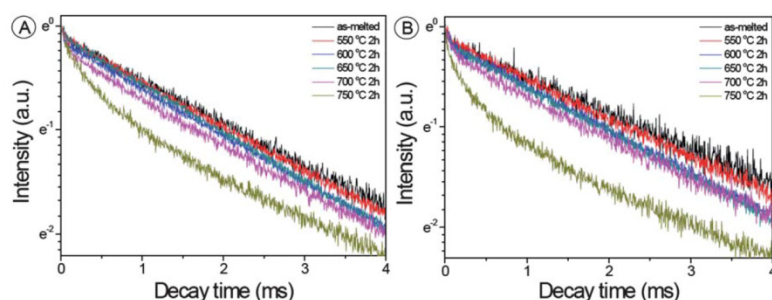


Fig. 4 Luminescence decay curve of Eu^{3+} emission resulting from ${}^3\text{D}_0 \rightarrow {}^7\text{F}_2$ (A) and ${}^3\text{D}_0 \rightarrow {}^7\text{F}_1$ (B) in SLZAKP glass and glass ceramics (labels: annealing temperatures).

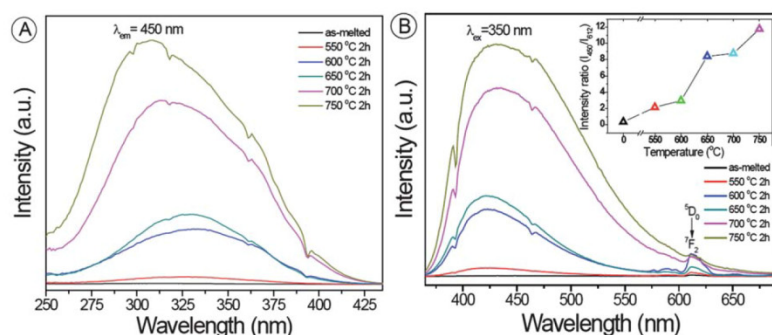


Fig. 5 Eu^{2+} -excitation (A) ($\lambda_{\text{em}} = 450 \text{ nm}$) and emission (B) ($\lambda_{\text{ex}} = 350 \text{ nm}$) spectra of SLZAKP glass and glass ceramics. Inset of (B): emission intensity ratio of Eu^{2+} at 450 nm and Eu^{3+} at 612 nm (labels: annealing temperatures).

450 nm (Eu^{2+}) and 612 nm (Eu^{3+}) with increasing degree of crystallization reflects the reduction of Eu^{3+} to Eu^{2+} . Maximum energy transfer appears to occur in the sample which was annealed at 600 °C.

Noteworthy, also the width of the Eu^{2+} -related emission band increases with increasing annealing temperature, *i.e.* from 87 nm to 154 nm.

Luminescence decay curves of the $4f^65d^1({}^2\text{T}_{2g}) \rightarrow 4f^7({}^8\text{S}_{7/2})$ band are shown in Fig. 6 (no data were plotted for the as-melted glass and the sample which was annealed at 550 °C because of the, in those cases, too low emission intensity). Again, especially for the samples which were annealed at relatively low temperature, decay appears to not follow a single exponential equation, indicating interaction of at least two distinct emission centers. With increasing heat treatment temperature, the effective lifetime increases from 11.4 to 46.9 μs . In accordance with the observed broadening of the excitation spectrum with increasing degree of crystallization (Fig. 5A), for higher degrees of crystallization, decay appears to be dominated by a somewhat slower relaxation process. This is taken as another evidence that Eu^{2+} is present in the crystalline phase and is attributed to the fact that $\text{Li}_2\text{ZnSiO}_4$ crystals exhibit a lower phonon energy than the glass and that, hence, the probability of fast non-radiative relaxation is reduced. Consequently, the observed external quantum efficiency increases from about 0.3% (550 °C sample) to about 8.5% (750 °C sample).

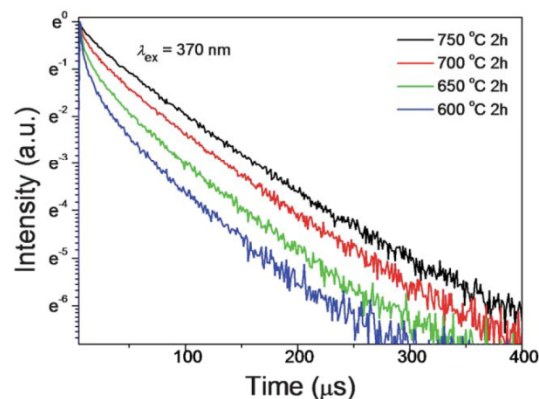


Fig. 6 Luminescence decay curve of Eu^{2+} emission from SLZAKP glass and glass ceramics (labels: annealing temperatures).

Dual-mode luminescence from Eu^{2+} and Eu^{3+} centers

The strongest overlap between the excitation spectra of Eu^{3+} and Eu^{2+} centers exists at 361 nm (Fig. 2A and 5A). As shown in Fig. 7, simultaneous emission from both species can therefore best be obtained when exciting at this wavelength. It becomes clearly visible how, by changing the annealing temperature

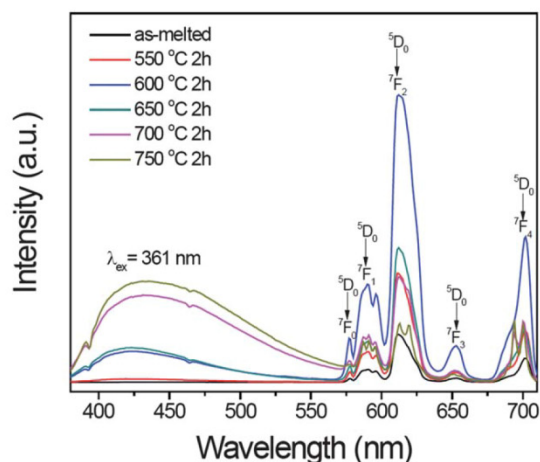


Fig. 7 Eu^{2+} - and Eu^{3+} -emission spectra ($\lambda_{\text{ex}} = 361$ nm) of SLZAKP glass and glass ceramics (labels: annealing temperatures).

during sample synthesis, the ratio between Eu^{2+} and Eu^{3+} -related photoemission can be varied almost continuously. Accordingly, the colour of luminescence can be tuned in this way. Corresponding colour coordinates (Commission internationale de l'éclairage, CIE) are summarized in Fig. 8, together with photographs of the samples (photographs taken under UV-A broadband excitation). Chromaticity can be controlled from about (0.63, 0.35) to (0.22, 0.17), *i.e.* from orange *via* red and violet to blue. This suggests various applications of the material. For example, if combined with a green phosphor, white light can be obtained and finely adjusted with respect to color temperature whereby all advantages of a glass ceramic can be made use of.

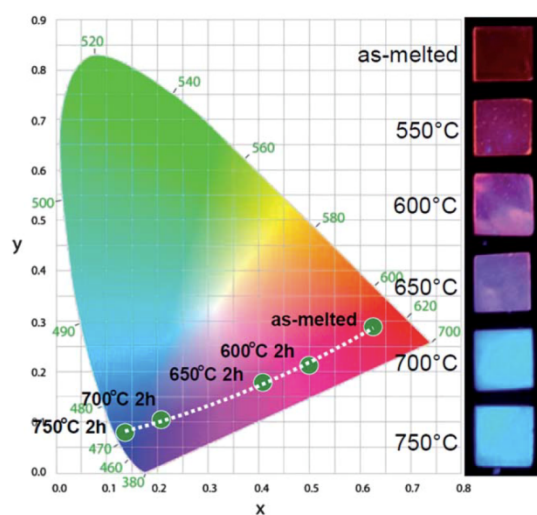


Fig. 8 CIE chromaticity diagram for SLZAKP glass and glass ceramics (labels: annealing temperatures) and photographs of corresponding samples as taken under UV-A broadband illumination.

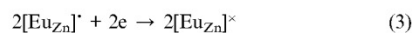
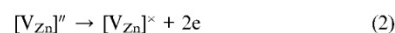
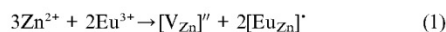
Table 1 Relative difference in ionic radii (D_r , %) between matrix cations, Eu^{2+} and Eu^{3+} (data on effective ionic radii taken from ref. 32)^a

Dopant	Radius/Å (CN)	$D_r = 100 \times [R_m(\text{CN}) - R_d(\text{CN})]/R_m(\text{CN})$		
		Li^+ 0.59 (4)	Zn^{2+} 0.60 (4)	Si^{4+} 0.26 (4)
Eu^{3+}	0.947(6)	-60.51	-57.83	-264.23
Eu^{2+}	1.17(6)	-98.31	-95.00	-350.00

^a CN = coordination number.

Europium reduction mechanism

A possible mechanism for the intrinsic reduction of Eu^{3+} to Eu^{2+} can be formulated on the basis of charge compensation,^{10,23,31} considering the aliovalent substitution of available matrix cations by Eu^{3+} . In principle, Eu^{3+} ions could be incorporated on either of the three cation sites, *i.e.* Zn^{2+} (ionic radius of 0.60 Å), Li^+ (0.59 Å) and Si^{4+} (0.26 Å) (ionic radii from ref. 32 and Table 1). The effective ionic radius of Eu^{3+} ions is 0.947 Å (for sixfold coordinated Eu^{3+} ; data on fourfold coordination are presently not available). Comparison of ionic radii and charge mismatch, however, points to Zn^{2+} -sites as the most probable host for Eu^{3+} . In order to maintain charge balance, two Eu^{3+} ions are needed to substitute three Zn^{2+} ions. Therefore, two defects $[\text{Eu}_{\text{Zn}}]'$, each bearing one positive charge, and one Zn^{2+} vacancy $[\text{V}_{\text{Zn}}]''$ with two negative charges will be created simultaneously during substitution of every two Eu^{3+} ions. By continuous thermal stimulation, electrons of the vacancies of $[\text{V}_{\text{Zn}}]''$ would be released and then trapped by Eu^{3+} ions, reducing them to Eu^{2+} , what can be explicitly written in Kroger–Vink notation:



This reaction is controlled by the degree of incorporation of Eu^{3+} into the $\text{Li}_2\text{ZnSiO}_4$ phase, *i.e.* the degree of crystallization and, hence, the employed annealing temperature.

Conclusions

In summary, we reported on tunable photoluminescence from mixed-valence Eu-doped nanocrystalline $\text{Li}_2\text{ZnSiO}_4$ glass ceramics. The precipitation of crystalline $\text{Li}_2\text{ZnSiO}_4$ was controlled *via* a process of thermal annealing of the as-melted Eu-doped precursor glass in air. During this process, a significant amount of Eu^{3+} ions was incorporated into the crystalline phase. For reasons of charge compensation, Eu^{3+} was subsequently intrinsically reduced to Eu^{2+} . Simultaneous photoemission from both Eu-species could be obtained by exciting at a wavelength of 361 nm. Depending on the employed annealing temperature and, hence, the degree of crystallization, the resulting colour of luminescence could be finely tuned from orange *via* red and violet to blue. Energy transfer was observed from Eu^{2+} to Eu^{3+} . Evidence for the incorporation of both species into the crystalline

environment was given on the basis of XRD, lifetime analyses, experimental quantum efficiency and spectral sensitivity.

Acknowledgements

The authors would like to acknowledge funding of the Deutsche Forschungsgemeinschaft (DFG) through the Cluster of Excellence "Engineering of Advanced Materials—EAM".

References

- 1 V. Mahalingam, F. Vetrone, R. Naccache, A. Speghini and A. Capobianco, Colloidal $\text{Tm}^{3+}/\text{Yb}^{3+}$ -doped LiYF_4 nanocrystals: multiple luminescence spanning the UV to NIR regions via low-energy excitation, *Adv. Mater.*, 2009, **21**, 4025–4028.
- 2 Y. Liu, D. Tu, H. Zhu, R. Li, W. Luo and X. Chen, A strategy to achieve efficient dual-mode luminescence of Eu^{3+} in lanthanides doped multifunctional NaGdF_4 nanocrystals, *Adv. Mater.*, 2010, **22**, 3266–3271.
- 3 *Luminescence: from Theory to Applications*, ed. C. Ronda, Wiley-VCH, 2008.
- 4 J. Bünzli, Europium in the limelight, *Nat. Chem.*, 2010, **2**, 696.
- 5 K. Driesen, V. K. Tikhomirov and C. Görrler-Walrand, Eu^{3+} as a probe for rare-earth dopant site structure in nano-glass-ceramics, *J. Appl. Phys.*, 2007, **102**, 024312.
- 6 P. Ptacek, H. Schäfer, K. Kömpe and M. Haase, Crystal phase control of luminescing $\text{NaGdF}_4:\text{Eu}^{3+}$ nanocrystals, *Adv. Funct. Mater.*, 2007, **17**, 3843–3848.
- 7 K. Kwon, W. Im, H. Jang, H. Yoo and D. Jeon, Luminescence properties and energy transfer of site-sensitive $\text{Ca}_{6-x-y}\text{Mg}_{x-z}(\text{PO}_4)_4:\text{Eu}^{2+}, \text{Mn}^{2+}$ phosphors and their application to near-UV LED-based white LEDs, *Inorg. Chem.*, 2009, **48**, 11525–11532.
- 8 M. Peng, J. Qiu, L. Yang and C. Zhao, Observation of $\text{Eu}^{3+} \rightarrow \text{Eu}^{2+}$ in barium hexa-aluminates with β' or β alumina structure prepared in air, *Opt. Mater.*, 2004, **27**, 591–595.
- 9 S. Schweizer, L. Hobbs, M. Secu, J. Spaeth, A. Edgar, G. V. M. Williams and J. Hamlin, Photostimulated luminescence from fluorochlorozirconate glass ceramics and the effect of crystallite size, *J. Appl. Phys.*, 2005, **97**, 083522.
- 10 M. Peng, Z. Pei, G. Hong and Q. Su, The reduction of Eu^{3+} to Eu^{2+} in $\text{BaMgSiO}_4:\text{Eu}$ prepared in air and the luminescence of BaMgSiO_4 phosphor, *J. Mater. Chem.*, 2003, **13**, 1202–1205.
- 11 M. Peng, Q. Zhao, J. Qiu and L. Wondraczek, Generation of emission centers for broadband NIR luminescence in bismuthate glass by femtosecond laser irradiation, *J. Am. Ceram. Soc.*, 2009, **92**, 542–544.
- 12 E. Malchukova and B. Boizot, Reduction of Eu^{3+} to Eu^{2+} in aluminoborosilicate glasses under ionizing radiation, *Mater. Res. Bull.*, 2010, **45**, 1299–1303.
- 13 M. Peng, B. Sprenger, M. A. Schmidt, H. Schwefel and L. Wondraczek, Broadband NIR photoluminescence from bismuth-doped $\text{Ba}_2\text{P}_2\text{O}_7$ crystals: insights into the nature of NIR-emitting Bismuth centers, *Opt. Express*, 2010, **18**, 12852–12863.
- 14 M. Peng and G. Hong, Reduction from Eu^{3+} to Eu^{2+} in $\text{BaAl}_2\text{O}_4:\text{Eu}$ phosphor prepared in an oxidizing atmosphere and luminescence properties of $\text{BaAl}_2\text{O}_4:\text{Eu}$, *J. Lumin.*, 2007, **127**, 735–740.
- 15 M. Peng and L. Wondraczek, Bi^{2+} -doped strontium borates for white light emitting diodes, *Opt. Lett.*, 2009, **34**, 2885–2887.
- 16 C. Wang, M. Peng, N. Jiang, X. Jiang, C. Zhao and J. Qiu, Tuning the Eu luminescence in glass materials synthesized in air by adjusting glass compositions, *Mater. Lett.*, 2007, **61**, 3608–3611.
- 17 Q. Zhang, Y. Qiao, B. Qian, G. Dong, J. Ruan, X. Liu, Q. Yhou, Q. Chen, J. Qiu and D. Chen, Luminescence properties of the Eu-doped porous glass and spontaneous reduction of Eu^{3+} to Eu^{2+} , *J. Lumin.*, 2009, **129**, 1393–1397.
- 18 M. Peng, Z. Pei, G. Hong and Q. Su, Study on the reduction of $\text{Eu}^{3+} \rightarrow \text{Eu}^{2+}$ in $\text{Sr}_4\text{Al}_{14}\text{O}_{25}$, *Chem. Phys. Lett.*, 2003, **371**, 1–6.
- 19 C. Chang and T. Chen, White Light generation under violet-blue excitation from tunable green-to-red emitting $\text{Ca}_2\text{MgSi}_2\text{O}_7:\text{Eu}$, Mn through energy transfer, *Appl. Phys. Lett.*, 2007, **90**, 161901.
- 20 M. P. Saradhi and U. V. Varadaraju, Photoluminescence studies on Eu^{2+} -activated $\text{Li}_2\text{SrSiO}_4$ —a potential orange-yellow phosphor for solid-state lighting, *Chem. Mater.*, 2006, **18**, 5267–5272.
- 21 M. Peng and L. Wondraczek, Photoluminescence of $\text{Sr}_2\text{P}_2\text{O}_7:\text{Bi}^{2+}$ as red phosphor for additive light generation, *Opt. Lett.*, 2010, **35**, 2544–2546.
- 22 M. Peng, C. Zollfrank and L. Wondraczek, Origin of broad NIR photoluminescence in bismuthate glass and Bi-doped glasses at room temperature, *J. Phys.: Condens. Matter*, 2009, **21**, 285106.
- 23 G. Gao, N. Da, S. Reibstein and L. Wondraczek, Enhanced photoluminescence from mixed-valence Eu-doped nanocrystalline silicate glass ceramics, *Opt. Express*, 2010, **18**, A575–A583.
- 24 W. Höland and G. H. Beall, *Glass Ceramic Technology*, American Ceramic Society, 2002.
- 25 N. Da, M. Peng, S. Krolkowski and L. Wondraczek, Intense red photoluminescence from Mn^{2+} -doped ($\text{Na}^+, \text{Zn}^{2+}$) sulfophosphate glasses and glass ceramics as LED converters, *Opt. Express*, 2010, **18**, 2549–2557.
- 26 L. Wondraczek, S. T. Mixture, J. Deubener and R. Knitter, Crystallization kinetics of lithium orthosilicate glasses, *J. Am. Ceram. Soc.*, 2006, **89**, 1342–1346.
- 27 B. Zhu, S. Zhang, S. Zhou, N. Jiang and J. Qiu, Enhanced upconversion and luminescence of transparent Eu^{3+} -doped glass-ceramics containing nonlinear optical microcrystals, *Opt. Lett.*, 2007, **32**, 653–655.
- 28 Q. Luo, X. Fan, X. Qiao, H. Yang, M. Wang and X. Zhang, Eu^{2+} -Doped glass ceramics containing BaF_2 nanocrystals as a potential blue phosphor for UV-LED, *J. Am. Ceram. Soc.*, 2009, **92**, 942–944.
- 29 D. Ehrh, H. T. Vu, A. Herrmann and G. Völksch, Luminescent $\text{ZnO}-\text{Al}_2\text{O}_3-\text{SiO}_2$ glasses and glass ceramics, *Adv. Mater. Res. (Berlin, Ger.)*, 2008, **39–40**, 231–236.
- 30 P. Tarte and R. Cahay, Chimie Physique. Synthèse et structure d'une nouvelle famille de composés $\text{Li}_2\text{X}^2\text{SiO}_4$ et $\text{Li}_2\text{X}^2\text{GeO}_4$ structurellement apparentés à Li_3PO_4 , *C. R. Seances Acad. Sci., Ser. C*, 1970, **271**, 777–779.
- 31 C. Zhang, J. Yang, C. Lin, C. Li and J. Lin, Reduction of Eu^{3+} to Eu^{2+} in $\text{MgAl}_2\text{Si}_2\text{O}_8$ ($\text{M} = \text{Ca}, \text{Sr}, \text{Ba}$) in air condition, *J. Solid State Chem.*, 2009, **182**, 1673–1678.
- 32 R. Shannon, Revised effective ionic radii and systematic studies of interatomic distances in halides and chalcogenides, *Acta Crystallogr., Sect. A: Cryst. Phys., Diffraction, Theor. Gen. Crystallogr.*, 1976, **32**, 751–767.

2.3. Enhanced broadband green and red photoluminescence from transparent Mn²⁺-doped nanocrystallized silicate glass ceramics

The CN and thus emission color of Mn²⁺ can be well tailored in SLZAKP glass and corresponding Li_{4-2(x+y)}Zn_xMn_ySiO₄ glass ceramic. The Mn²⁺ ion is octahedrally coordinated in the precursor glass and gives rise to the broad orange to red emission. During the controlled crystallization process, Mn²⁺ is partially incorporated into the crystalline phase offering tetrahedral sites to Mn²⁺ species, which leads to the green emission of ^{IV}Mn²⁺.

G. Gao, S. Reibstein, M. Peng and L. Wondraczek, *Phys. Chem. Glass - Euro. J. Glass Sci. Tech. Part B* 2011, **52**, 59–63. -Reproduced by permission of German Society of Glass Technology (DGG).

<http://www.ingentaconnect.com/content/sgt/pcg/2011/00000052/00000002/art00004>

Dual-mode photoluminescence from nanocrystalline Mn²⁺-doped Li,Zn-aluminosilicate glass ceramics

Guojun Gao, Sindy Reibstein, Mingying Peng¹ & Lothar Wondraczek*

Department of Materials Science, University of Erlangen-Nuremberg, Martensstrasse 5, 91058 Erlangen, Germany

Manuscript received 9 November 2010
Revised version received 23 December 2010
Accepted 23 December 2010

We report on the photoluminescence (PL) of Mn²⁺-doped (Li, Zn²⁺) aluminosilicate glasses and glass ceramics. Glass ceramics are fabricated by controlled crystallization of as-melted precursor glasses. X-ray diffraction (XRD), electron spin resonance (ESR) and PL analyses indicate precipitation of Li_{1-2(x+y)}Zn_xMn_ySiO₄ with relatively low x and y values during the earlier phase of crystallization and x → 1 in the later phase. During the crystallization process, Mn²⁺ ions, octahedrally coordinated in the precursor glass, partially precipitate on tetrahedral Zn²⁺ sites. This gives rise to the simultaneous occurrence of green and red luminescence, respectively, due to spin-allowed ⁴T₁(G) → ⁶A₁(S) and spin-forbidden ⁴T₁(G) → ⁶A₁(S) in ^{IV}Mn²⁺ and ^{VI}Mn²⁺. Accordingly, the amount of ^{IV}Mn²⁺ species, the ratio of ^{IV}Mn²⁺/^{VI}Mn²⁺ and, hence, the ratio between green and red photoemission bands can be controlled by the temperature at which the glass ceramics are produced. FWHM of the resulting emission spectrum can be increased from about 100 000 to about 50 000 cm⁻¹. In parallel, as a result of multiple scattering, emission intensity appears to generally increase with increasing degree of crystallization.

Introduction

As for most *d-d* transitions in transition metal ions,⁽¹⁾ photoluminescence from Mn²⁺-centres ([Xe]3d⁵) is strongly dependent on ligand field strength and may occur over the spectral range from deep green to far red.^(2–8) The corresponding excitation scheme spans the spectral range of about 300 to 500 nm. Distinct excitation bands are typically located at ~350, ~360, ~410, ~420 and ~500 nm, corresponding to the transitions of ⁶A₁(S) → ⁴E(D), ⁶A₁(S) → ⁴T₂(D), ⁶A₁(S) → ⁴A₁(G), ⁴E(G), ⁶A₁(S) → ⁴T₂(G) and ⁶A₁(S) → ⁴T₁(G), respectively. Hence, Mn²⁺-doped phosphors have a long tradition in various types of luminescent light sources, e.g. ultraviolet (UV)-blue LED-based systems, fluorescent tubes or compact fluorescent lamps (CFLs). Although photoemission spectra are usually characterized by one broad peak which can be, to a large extent, shifted towards either blue or red, two principal cases may generally be distinguished: if Mn²⁺ ions are incorporated on tetrahedral lattice sites (^{IV}Mn²⁺) photoemission typically occurs in the green spectral range; when their coordination environment is octahedral (^{VI}Mn²⁺), photoemission lies in the orange or red spectral regime. Consequently, for matrices within which Mn²⁺ can precipitate simultaneously on both types of lattice sites, dual-mode luminescence⁽⁹⁾ can be generated and the resulting emission spectrum spans the spectral range from about 500–700 nm. If, in this case, the ratio of [^{IV}Mn²⁺]/[^{VI}Mn²⁺] can be adjusted in a controlled way, the emission colour can be tuned to generate, e.g. warm white or yellow light of high

colour quality. This would offer an interesting alternative to rare-earth doped materials (e.g. Refs 9, 10).

While over several decades, the optoelectronic properties of Mn²⁺ species have been studied for numerous glassy and (poly)crystalline matrix materials, related knowledge on Mn²⁺-doped glass ceramics in which both [^{IV}Mn²⁺] and [^{VI}Mn²⁺] can be generated simultaneously is still limited.⁽⁹⁾ In comparison to conventional polycrystalline phosphors, such glass ceramics, *per se*, offer several technological advantages. In particular, they enable facile production of luminescent microbeads by conventional melt processing.⁽¹¹⁾ When the colour of photoemission is not controlled by distinct combinations of multiple optically active dopant species but by the process of crystallization, they further enable straightforward recycling by simple remelting.

In the present paper, it is shown how such dual-mode luminescence can be obtained and controlled in Mn²⁺-doped Li₂ZnSiO₄ glass ceramics. Optoelectronic properties will be discussed in relation to microstructure.

Experimental procedures

Samples with nominal composition 48SiO₂·24Li₂O·15·8ZnO·8Al₂O₃·3K₂O·1P₂O₅·0·2MnO (SLZAKP^(10,12)) (mol%) were prepared by conventional melting and quenching from a 100 g batch of analytical grade reagents SiO₂, Li₂CO₃, ZnO, Al₂O₃, K₂CO₃, NH₄H₂PO₄ and MnCO₃. Melting was performed in alumina crucibles at 1550°C for 2 h. Subsequently, melts were poured into preheated graphite moulds and annealed for 2 h at 450°C. From the obtained glass slabs, individual

* Corresponding author. Email lothar.wondraczek@ww.uni-erlangen.de
¹ Now with South China University of Technology, Guanzhou, China

specimens $10 \times 10 \times 1$ mm in size were cut and polished. The glasses exhibit a pale violet tint, originating from an absorption band at ~ 490 nm which can readily be assigned to traces of Mn^{3+} , $3d^4$; ${}^5E \rightarrow {}^5T_2$ (Mn^{3+} does not exhibit optical emission in the 600 nm spectral range). Samples were then transformed into glass ceramics via a single step heat treatment process of 2 h at 500, 600, 650 and 750°C (heating at 4 K/min), respectively. The crystallization process was characterized by differential scanning calorimetry (DSC, Netzsch, Ar atmosphere) and x-ray diffractometry (XRD, Siemens Kristalloflex D500, Bragg-Brentano, 30 kV/30 mA, Cu K_α). Static and dynamic photoluminescence (PL) were studied with a high resolution spectrofluorometer and by single photon counting (Horiba Jobin Yvon Fluorolog-3), respectively, using a static Xe lamp (450 W) and a Xe flashlamp (75 W) as excitation sources. All spectroscopic analyses were performed at room temperature. Electron spin resonance spectra (ESR) were recorded on an X-band microwave spectrometer at a frequency of 9.7 GHz (Bruker ESR 300E).

Results and discussion

When annealed, samples initially remain transparent but start to turn opalescent for heat treatment at $>700^\circ\text{C}$. This empirically indicates precipitation of a sub-microscopic secondary phase by internal nucleation. For a heating rate of 20 K/min, DSC experiments (inset of Figure 1) reveal a glass transition temperature of $531 \pm 0.5^\circ\text{C}$ and the onset of crystallization at $592 \pm 0.5^\circ\text{C}$. XRD patterns of SLZAKP samples after isothermal heat treatment at various temperatures are depicted in Figure 1. As expected, the as-melted specimen does not exhibit any discrete diffraction peaks. For annealing at 500°C or higher, XRD patterns suggest assignment^(14,11) to orthorhombic Li_2ZnSiO_4 (non-indexed JCPDS card no. 00-024-0681) as the sole crystalline species. The peak arrangement appears to match that of orthorhombic $Li_{3.8}Zn_{1.2}P_{1.8}Si_{0.2}O_8$, notwithstanding the clear discrepancy in chemistry. Both Li_2ZnSiO_4 and $Li_{3.8}Zn_{1.2}P_{1.8}Si_{0.2}O_8$ are structurally related to low- Li_3PO_4 (JCPDS card no. 01-084-0003). Here, as will be discussed later, we interpret the observed patterns as a reflection of the formation of a solid solution of $Li_{4-2(x+y)}Zn_xMn_ySiO_4$. The values of x and y appear to be dependent on heat treatment temperature, and, hence, the progress of crystallization.

The evolution of excitation and emission spectra of Mn^{2+} -doped SLZAKP with increasing isothermal heat treatment temperature is shown in Figure 2. In accordance with the previous discussion, observed excitation peaks can readily be assigned to transitions from the ground state of Mn^{2+} to the indicated levels. With increasing heat treatment temperature and, hence, increasing degree of crystallization, distinct changes occur in excitation and, particularly, emission

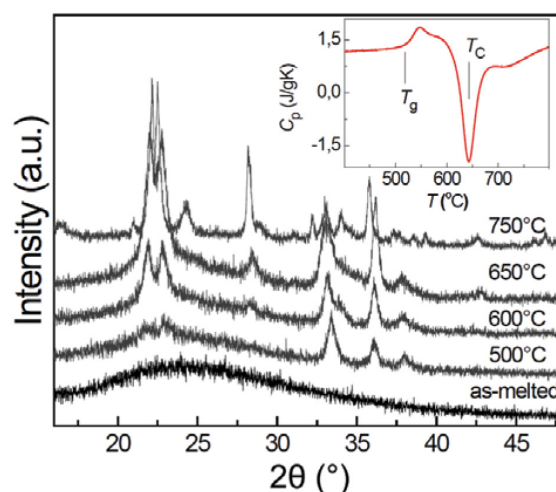


Figure 1. XRD patterns of Mn^{2+} doped SLZAKP glass and glass ceramics after heat treatments at various temperatures (labels). Inset: DSC scan of SLZAKP glass

spectra of SLZAKP (noteworthy, un-doped glass and glass ceramics did not exhibit any photoluminescence for 315 nm excitation, indicating that Zn^{2+} ions do not contribute to the observed luminescence):

(i) For samples which were heat treated in the temperature regime of 500–600°C, the intensity of the emission peak at 620 nm increases by a factor of 6. This observation is interpreted as a result of multiple scattering, increasing absorption cross section and, hence, increasing total excitation efficiency. Interestingly, although XRD clearly indicated crystal precipitation already occurring in this temperature regime, besides a relatively weak red-shift of the emission peak, no further changes occur in the emission spectra. While such changes could be taken as evidence for the incorporation of Mn^{2+} into the evolving crystal phase, their absence leads to the assumption that at this stage, Mn^{2+} species remain in the residual glass phase. The red-shift is then attributed to two parallel effects: increasing interaction between neighbouring Mn^{2+} -centres because of volumetric enrichment in the residual glass phase and, secondly, compositional changes of the residual glass phase with increasing precipitation of Li_2O and ZnO .

(ii) When glass ceramics are produced at higher heat treatment temperatures, i.e. between 650 and 750°C, a relatively sharp secondary emission band appears in the green spectral range (centred at ~ 532 nm). Its position is practically not affected by the heat treatment temperature. On the contrary, the lower emission band strongly red-shifts with increasing heat treatment temperature due to Mn–Mn interactions.⁽¹⁵⁾ For increasing degree of crystallization, as with the samples which were heat treated at $<650^\circ\text{C}$, the observed emission intensity increases by a factor of about 6–8. In parallel, the overlapping pairs of excitation bands of ${}^6A_1(S) \rightarrow {}^4E(D)$ and ${}^6A_1(S) \rightarrow {}^4T_2(D)$, and

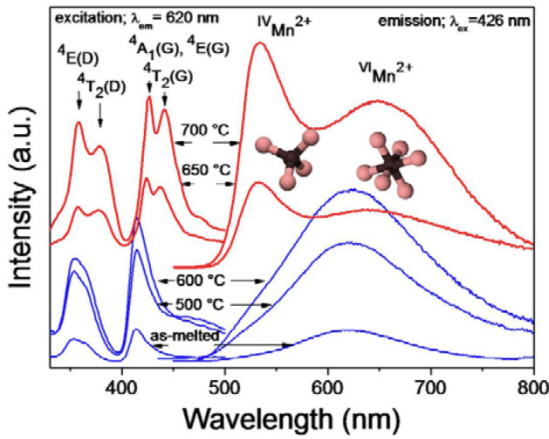


Figure 2. Excitation and emission spectra of as-melted SLZAKP glass and corresponding glass ceramic. Labels indicate heat treatment temperatures

${}^6A_1(S) \rightarrow {}^4A_1(G)$, 4E and ${}^6A_1(S) \rightarrow {}^4T_2(G)$, respectively, sharpen notably, and all excitation bands are red-shifted.⁽³⁾ In order to exclude anything other than divalent manganese species as emission centres for the green emission peak, additional excitation spectra were recorded for an excitation wavelength of 358 nm (not shown). In these spectra, the red emission peak of ${}^{VI}Mn^{2+}$ was found to exhibit a distinct shoulder in the green spectral range for samples which were heat treated at 500–600°C, indicating that the appearance of the secondary green emission peak occurs indeed gradually with increasing annealing temperature, and that it is related to Mn^{2+} species.

Time resolved emission spectra are shown in Fig-

ures 3 and 4, as exemplars for the as-melted glass and the glass ceramic which was produced by isothermal heat treatment at 750°C. The effective lifetime (i.e. the time after which luminescence intensity decayed to $1/e$ times of its initial value) of the emission band at 620 nm (Figure 3, left) decreases with increasing degree of crystallization, i.e. from 17.8 ms (as-made glass) to 8.5 ms (glass ceramic produced at 750°C). The lifetime of the red emission in glass is slightly smaller than that of Mn^{2+} doped zinc aluminosilicate glass.⁽¹³⁾ Lifetime of the 532 nm emission (Figure 4, left), on the contrary, appears to be less affected by the degree of crystallization. It varies from 9.7 ms (as-melted glass: NB this value is obtained at a very low emission intensity) to 8.6 ms (glass ceramic produced at 600°C) to 7.8 ms (glass ceramic produced at 750°C). The lifetime of green emission in the glass ceramic heat treated at 750°C is smaller than that of Mn^{2+} doped $Zn_2SiO_4/ZnAl_2O_4$ glass ceramics.⁽¹⁶⁾ In both cases, the decay curves appear to deviate from a single exponential equation. This indicates the contribution of at least two different emission centres to the observed emission dynamics. For a clearer view, spectral decay curves were recorded. As shown in Figures 3–4, the peak of the 531 nm emission band does not change with delay time, while for the 620 nm emission band, a red-shift is observed for a delay time of >30 ms. Seemingly, in the later stage, luminescence is dominated by emission from a centre in a somewhat stronger crystal field (or from interacting Mn^{2+} species, Figure 3, right).

A more detailed view at the immediate structural environment of Mn^{2+} can be obtained by ESR spectroscopy (Figure 5).^(17–19) For all samples, spectra ex-

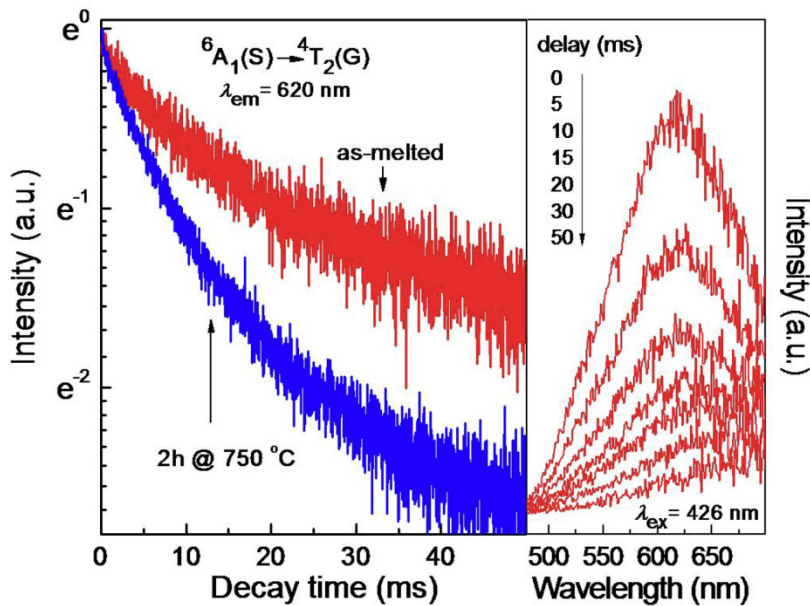


Figure 3. Luminescence decay (left) and time resolved emission spectra (right) of ${}^{VI}Mn^{2+}$ species in as-melted SLZAKP glass and corresponding glass ceramic

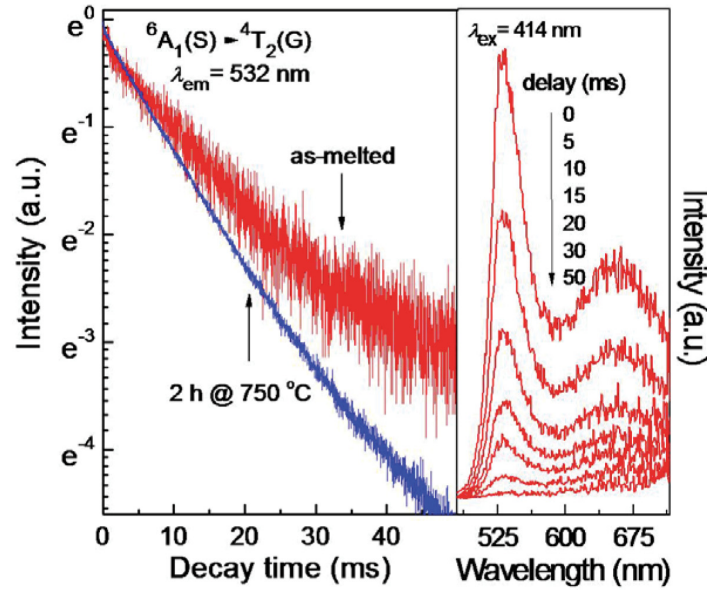


Figure 4. Luminescence decay (left) and time resolved emission spectra (right) of $^{IV}Mn^{2+}$ species in as-melted SLZAKP glass and corresponding glass ceramic

hibit two distinct resonances which can be assigned to Mn^{2+} species: a broad signal at ~ 1600 G ($g \approx 4.27$) and a well-resolved sextet hyperfine line structure at ~ 3400 G ($g \approx 2.01$) (NB both resonances were absent in blank reference samples). The two resonances can readily be attributed to Mn^{2+} ions in undistorted octahedral ($g \approx 2.01$) and distorted tetragonal ($g \approx 4.3$) sites, respectively.⁽¹⁷⁾ With increasing degree of crystallization, the intensity of the sextet fingerprint (obtained from the product of quadratic width and peak-to-peak height) and the degree of hyperfine splitting (the ratio of HFS intensity of each sextet signal over the overall $g \approx 2.01$ singlet intensity) decrease. This indicates increasing interaction between neighbouring Mn^{2+} -species,

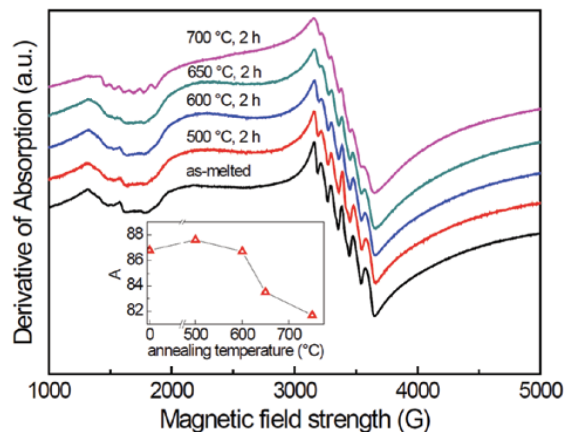


Figure 5. Normalized ESR spectra of Mn^{2+} doped SLZAKP glass and corresponding glass ceramics. Inset: Evolution of hyperfine splitting constant A with heat treatment temperature. Labels: heat treatment temperatures

which could be attributed to chemical changes and Mn^{2+} -enrichment in the residual glass phase. For heat treatment temperatures below $700^\circ C$, no significant variation can be observed in the $^{IV}Mn^{2+}$ -related resonance ($g \approx 4.3$). However, a clear sextet structure was recorded for the glass ceramic which was produced at $750^\circ C$, indicating a significant increase in the amount of isolated tetragonal distorted Mn^{2+} sites for this heat treatment temperature. The hyperfine splitting constant A (calculated from $H_m = H_0 - Am_l - A^2[(35 - m_l^2)/8H_0]$ where $H_0 = hv/g_0\beta$ and $m_l = -2/5, -2/3, -1/2, 1/2, 3/2, 5/2$, g_0 is the isotropic g factor⁽²⁰⁾), provides a measure of covalency and coordination number of Mn^{2+} ions. The smaller the value of A , the more covalent is the bond character of the anion, and the smaller is the coordination number of Mn^{2+} ions.^(11,21) The evolution of A with annealing temperature is shown in the inset of Figure 5. For the temperature regime of 500 – $600^\circ C$, A remains practically constant. However, for a further increase in annealing temperature, it decreases gradually from 87 to 81, which means that octahedrally coordinated Mn^{2+} ions were partly converted into tetrahedrally coordinated Mn^{2+} ions over this temperature regime.

Luminescence and ESR-data consistently reveal the simultaneous presence of $^{IV}Mn^{2+}$ and $^{VI}Mn^{2+}$ after crystallization. The as-melted glass, on the other hand, contains only octahedrally coordinated Mn^{2+} . Consequently, the as-melted glass exhibits only red luminescence (due to spin-forbidden $^4T_{1g}(G) \rightarrow ^6A_{1g}(S)$ in the $3d^5$ level of $^{VI}Mn^{2+}$), whereas the emission spectrum of the glass ceramic is strongly broadened by the simultaneous occurrence of green emission from $^{IV}Mn^{2+}$.^(2,4) The degree of crystallization, controlled

by the temperature of the isothermal heat treatment, appears to be the key parameter for controlling the amount of tetrahedrally coordinated Mn²⁺. That is, during crystal precipitation, Mn²⁺-species appear to partially enter the crystalline phase on tetrahedral lattice sites. Significant amounts of ^{IV}Mn²⁺ could be detected for heat treatment temperatures of 650°C or higher. Mn²⁺ (0.66 Å) is assumed to be incorporated on Zn²⁺ sites (0.60 Å). The observed deviation between the progress of crystallization and Mn²⁺-incorporation is interpreted as a result of differing mobility of Li⁺ and Zn²⁺ (Mn²⁺) species during the crystallization process. It is assumed that crystals are precipitated as a solid solution of (Li_{4-2(x+y)}Zn_xMn_y)SiO₄. In the initial phase of crystallization, *x* and *y* are relatively low whereas in the later crystallization process, crystallite composition shifts towards Li₂ZnSiO₄.

Conclusions

In summary, we have reported on the photoluminescence of Mn²⁺-doped SLZAKP glasses and glass ceramics. Li₂ZnSiO₄:Mn²⁺ glass ceramics were fabricated by controlled crystallization of as-melted precursor glasses. XRD, ESR and PL analyses indicated precipitation of Li_{4-2(x+y)}Zn_xMn_ySiO₄, with relatively low *x* and *y* during the earlier phase of crystallization (heat treatment temperature <700°C) and *x*→1 in the later phase (heat treatment temperature >700°C). Mn²⁺ species are assumed to be incorporated in the crystal phase on tetrahedral Zn²⁺ sites. Accordingly, the amount of ^{IV}Mn²⁺ species, the ratio of ^{IV}Mn²⁺/^{VI}Mn²⁺ and, hence, the ratio between green and red photoemission bands could be controlled by the temperature at which the as-melted glasses were transformed into glass ceramics. FWHM of the resulting emission spectrum increased from 84700 to 53100 cm⁻¹. In parallel, as a result of multiple scattering, emission intensity was found to generally increase

with increasing degree of crystallization. Tunability of luminescence colour from red to green suggests applications as a versatile primary or secondary phosphor in solid state lighting devices.

Acknowledgement

The authors gratefully acknowledge funding from the German Science Foundation (DFG) through the Cluster of Excellence "Engineering of Advanced Materials - EAM".

References

- Herrmann, A. & Ehr, D. *Glass Sci. Technol.*, 2005, **78**, 99.
- Reisfeld, R., Kisilev, A. & Jorgensen, C. K. *Chem. Phys. Lett.*, 1984, **111**, 19.
- Da, N., Peng, M., Krolkowski S. & Wondraczek, L. *Opt. Express*, 2010, **18**, 2549.
- Won, Y., Jang, H., Im, W. & Jeon, D. *Appl. Phys. Lett.*, 2006, **89**, 231909.
- Kawano, M., Takebe, H. & Kuwabara, M. *Opt. Mater.*, 2009, **32**, 277.
- Machado, I. E. C., Prado, L., Gomes, L., Prizon, J. M. & Martinelli, J. R. *J. Non-Cryst. Solids*, 2004, **348**, 113.
- Martín-Rodríguez, R., Valiente, R. & Bettinelli, M. *Appl. Phys. Lett.*, 2009, **95**, 091913.
- Yan, Q., Liu, Y., Chen, G., Da, N. & Wondraczek, L. *J. Am. Ceram. Soc.*, 2011, **94**, 660.
- Gao, G., Da, N., Reibstein, S. & Wondraczek, L. *Opt. Express*, 2010, **18**, A557.
- Gao, G., Reibstein, S., Peng, M. & Wondraczek, L. *J. Mater. Chem.*, 2011, **21**, 3156.
- Wondraczek, L., Misture, S. T., Deubener, J. & Knitter, R. *J. Am. Ceram. Soc.*, 2006, **89**, 1342.
- Kea, Z. B., Lub, A. X. & Huang, G. F. *Adv. Mater. Res.*, 2006, **10-12**, 205.
- Faber, A. J., van Die, A., Blasse, G. & van der Weg, F. *Phys. Chem. Glasses*, 1987, **28**, 150.
- Lu, A. X., Ke, Z. B., Xiao, Z. H., Zhang, X. F. & Li, X. Y. *J. Non-Cryst. Solids*, 2007, **353**, 2692.
- Sanada, T., Yamamoto, K., Wada, N. & Kojima, K. *Thin Solid Films*, 2006, **496**, 176.
- Ehr, D. *Mater. Sci. Eng.*, 2009, **2**, 012001
- Wieringen, J. S. V. *Discuss. Faraday Soc.*, 1955, **19**, 118.
- Reddy, M. S., Krishna, G. M. & Veeraiah, N. *J. Phys. Chem. Solids*, 2006, **67**, 789.
- Konidakis, I., Varsamis, C. E., Kamitsos, E. I., Möncke, D. & Ehr, D. *J. Phys. Chem. C*, 2010, **114**, 9125.
- Murali, A., Chakradhar, R. P. S. & Rao, J. L. *Physica B*, 2005, **358**, 22.
- Šimánke, E. & Müller, K. A. *J. Phys. Chem. Solids*, 1970, **31**, 1027.

2.4. Broadband UV-to-green photoconversion in V-doped lithium zinc silicate glasses and glass ceramics

V^{5+} ions can be stabilized in both SLZAKP glass and corresponding Li_2ZnSiO_4 glass ceramic. The V^{5+} ions show a broad green PL band from 400 to 700 nm due to the relaxation of $\equiv V-O^-$ to $\equiv V=O$. The corresponding excitation band covers the complete UV-B to UV-A spectral region. Crystallization leads to enhanced emission intensity of V^{5+} .

G. Gao, R. Meszaros, S. Reibstein and L. Wondraczek, *Opt. Express* 2011, **19**, A312–A318. -Reproduced by permission of The Optical Society of America.

<http://www.opticsinfobase.org/oe/abstract.cfm?uri=oe-19-s3-a312>

Broadband UV-to-green photoconversion in V-doped lithium zinc silicate glasses and glass ceramics

Guojun Gao,¹ Robert Meszaros,¹ Mingying Peng,^{1,2} and Lothar Wondraczek^{1,*}

¹Department of Materials Science, University of Erlangen-Nuremberg, 91058 Erlangen, Germany

²Institute of Optical Communication Materials, South China University of Technology, Guangzhou 510641, China

*lothar.wondraczek@ww.uni-erlangen.de

Abstract: We report on photoluminescence of vanadium-doped lithium zinc silicate glasses and corresponding nanocrystalline Li₂ZnSiO₄ glass ceramics as broadband UV-to-VIS photoconverters. Depending on dopant concentration and synthesis conditions, VIS photoemission from [VO₄]³⁻ is centered at 550-590 nm and occurs over a bandwidth (FWHM) of ~250 nm. The corresponding excitation band covers the complete UV-B to UV-A spectral region. In as-melted glasses, the emission lifetime is about 34 μs up to a nominal dopant concentration of 0.5 mol%. In the glass ceramic, it increases to about 45 μs. For higher dopant concentration, a sharp drop in emission lifetime was observed, what is interpreted as a result of concentration quenching. Self-quenching is further promoted by energy transfer to V⁴⁺ centers (²Γ₁₄ → ²Γ₁₃). Partitioning of vanadium into V⁵⁺ and V⁴⁺ was examined by electron paramagnetic resonance and X-ray photoelectron spectroscopy. Suppression of V⁵⁺-reduction requires careful adjustment of the optical basicity of the host glass and/or synthesis conditions.

© 2011 Optical Society of America

OCIS codes: (160.4670) Optical materials; (140.3380) Laser materials; (160.2540) Fluorescent and luminescent materials; (140.4480) Optical amplifiers.

References and links

1. Y. Fujimoto, F. Tanno, K. Izumi, S. Yoshida, S. Miyazaki, M. Shirai, K. Tanaka, Y. Kawabe, and E. Hanamura, "Vanadium-doped MgAl₂O₄ crystals as white light source," *J. Lumin.* **128**(3), 282–286 (2008).
2. J. El Ghoul, C. Barthou, M. Saadoun, and L. El Mir, "Optical characterization of SiO₂/Zn₂SiO₄:V nanocomposite obtained after the incorporation of ZnO:V nanoparticles in silica host matrix," *J. Phys. Chem. Solids* **71**(3), 194–198 (2010).
3. M. Anpo, I. Tanahashi, and Y. Kubokawa, "Photoluminescence and photoreduction of V₂O₅ supported on porous vycor glass," *J. Phys. Chem.* **84**(25), 3440–3443 (1980).
4. S. Dzwigaj, M. Matsuoka, M. Anpo, and M. Che, "Evidence of three kinds of tetrahedral vanadium (V) species in VSi₃ zeolite by diffuse reflectance UV-Visible and photoluminescence spectroscopies," *J. Phys. Chem. B* **104**(25), 6012–6020 (2000).
5. M. Morita, S. Kajiyama, T. Kai, D. Rau, and T. Sakurai, "Physicochemical control of valence in luminescence of Cr(III) and V (III, IV) complexes embedded in xero-gel and sol-gel SiO₂ glasses," *J. Lumin.* **94–95**, 91–95 (2001).
6. S. Dzwigaj, J. Krafft, M. Che, S. Lim, and G. L. Haller, "Photoluminescence study of the introduction of V in Si-MSM-41: role of surface defects and their associated SiO⁻ and SiOH groups," *J. Phys. Chem. B* **107**(16), 3856–3861 (2003).
7. D. C. Yu, S. Ye, M. Y. Peng, Q. Y. Zhang, J. R. Qiu, J. Wang, and L. Wondraczek, "Efficient near-infrared downconversion in GdVO₄:Dy³⁺ phosphors for enhancing the photo response of solar cells," *Sol. Eng. Mat. Sol. Cell* (2011), doi:10.1016/j.solmat.2011.01.004.
8. W. Höland and G. H. Beall, *Glass Ceramic Technology* (American Ceramic Society, 2002).
9. G. Gao, N. Da, S. Reibstein, and L. Wondraczek, "Enhanced photoluminescence from mixed-valence Eu-doped nanocrystalline silicate glass ceramics," *Opt. Express* **18**(S4 Suppl 4), A575–A583 (2010).
10. G. Gao, S. Reibstein, M. Peng, and L. Wondraczek, "Tunable dual-mode photoluminescence from nanocrystalline Eu-doped Li₂ZnSiO₄ glass ceramics phosphors," *J. Mater. Chem.* **21**(9), 3156–3161 (2011).

11. A. R. West and F. P. Glasser, "Preparation and crystal chemistry of some tetrahedral Li_3PO_4 -type compounds," *J. Solid State Chem.* **4**(1), 20–28 (1972).
12. N. Da, M. Peng, S. Krolikowski, and L. Wondraczek, "Intense red photoluminescence from Mn^{2+} -doped (Na^+ , Zn^{2+}) sulfophosphate glasses and glass ceramics as LED converters," *Opt. Express* **18**(3), 2549–2557 (2010).
13. Z. B. Kea, A. X. Jub, and G. F. Huang, "Effect of K_2O addition on crystallization and microstructure of Li_2O - ZnO - Al_2O_3 - SiO_2 system glass-ceramics," *Adv. Mater. Res.* **11-12**, 205–208 (2006).
14. Y. Zhuang, Y. Teng, J. Luo, B. Zhu, Y. Chi, E. Wu, H. Zeng, and J. Qiu, "Broadband optical amplification in silicate glass ceramics containing $\text{Li}_2\text{ZnSiO}_4\text{:Cr}^{4+}$ nanocrystals," *Appl. Phys. Lett.* **95**(11), 111913 (2009).
15. C. K. Jorgensen, S. Döger, M. Frydman, and L. G. Sillén, "Comparative ligand field studies IV. vanadium (IV), titanium (III) and other systems with one d-electron," *Acta Chem. Scand.* **11**, 73–85 (1957).
16. C. J. Ballhausen and H. B. Gray, "The electronic structure of the vanadyl ion," *Inorg. Chem.* **1**(1), 111–122 (1962).
17. W. D. Johnston, "Optical spectra of the various valence states of vanadium in $\text{Na}_2\text{O}\cdot 2\text{SiO}_2$ glass," *J. Am. Ceram. Soc.* **48**(12), 608–611 (1965).
18. M. Shareefuddin, M. Jamal, G. Ramadevudu, M. Lakshmi pati Rao, and M. N. Chary, "Electron paramagnetic resonance spectra of VO^{2+} ions in $\text{NaI}\text{-Na}_2\text{O}\text{-K}_2\text{O}\text{-B}_2\text{O}_3$ mixed alkali glasses," *J. Non-Cryst. Solids* **255**(2-3), 228–232 (1999).
19. L. D. Bogomolova, A. N. Khabarova, E. V. Klimashina, N. A. Krasil'nikova, and V. A. Jachkin, "EPR of V^{4+} ions in silica glass, 20," *J. Non-Cryst. Solids* **103**(2-3), 319–324 (1988).
20. H. Farah, "An EPR characterization of vanadium in CaO and Na_2O based Al_2O_3 - SiO_2 glasses," *J. Alloy. Comp.* **453**(1-2), 288–291 (2008).
21. T. Srikumar, C. Srinvasa Rao, Y. Gandhi, N. Venkatramaiah, V. Ravikumar, and N. Veeraiah, "Microstructure, dielectric and spectroscopic properties of $\text{Li}_2\text{O}\text{-Nb}_2\text{O}_5\text{-ZrO}_2\text{-SiO}_2$ glass system crystallized with V_2O_5 ," *J. Phys. Chem. Solids* **72**(3), 190–200 (2011), doi:10.1016/j.jpcs.2010.12.009.
22. J. A. Duffy, "A review of optical basicity and its applications to oxidic systems," *Geochim. Cosmochim. Acta* **57**(16), 3961–3970 (1993).
23. H. Bach, F. G. K. Baucke, and D. Krause, *Electrochemistry of Glasses and Glass Melts, Including Glass Electrodes* (Springer-Verlag, 2001), p. 293.
24. Z. Cheng, R. Xing, Z. Hou, S. Huang, and J. Lin, "Patterning of light-emitting $\text{YVO}_4\text{:Eu}^{3+}$ thin films via inkjet printing," *J. Phys. Chem. C* **114**(21), 9883–9888 (2010).
25. C. Hsu and R. C. Powell, "Energy transfer in europium doped yttrium vanadate crystals," *J. Lumin.* **10**(5), 273–293 (1975).
26. A. X. Lu, Z. B. Ke, Z. H. Xiao, X. F. Zhang, and X. Y. Li, "Effect of heat-treatment condition on crystallization behavior and thermal expansion coefficient of $\text{Li}_2\text{O}\text{-ZnO}\text{-Al}_2\text{O}_3\text{-SiO}_2\text{-P}_2\text{O}_5$ glass-ceramics," *J. Non-Cryst. Solids* **353**(28), 2692–2697 (2007).

1. Introduction

Broadband conversion of ultraviolet (UV) radiation to visible (VIS) light is highly desirable in a variety of applications, ranging from solar energy harvesting (UV-A and UV-B conversion), luminescent lighting, UV-detection and imaging to, e.g., agricultural lighting. Thereby, the converter may either be used to directly emit VIS radiation or as a sensitizer for a secondary conversion or energy transfer process. In principle, a large variety of optically active materials can be employed for this purpose. However, several limiting factors have to be considered, such as low excitation bandwidth, high Stokes shift, photostability or, for example, undesired excitation in the blue spectral region. In this respect, knowledge on the optoelectronic properties of vanadium ions is still relatively limited. In inorganic oxide matrices, vanadium is usually present in three different oxidation states, V^{3+} ($[\text{Ar}] 3d^3$), V^{4+} ($[\text{Ar}] 3d^1$) and V^{5+} ($[\text{Ar}]$), whereby the trivalent ion is readily oxidized to higher valence. Photoluminescence is attributed to the presence of V^{5+} ions and covers a broad band ranging from 400 to 700 nm [1–7]. Excitation ($\sim 200\text{-}400$ nm) may be understood as an energy transfer process from O^{2-} to V^{5+} which occurs intrinsically in the vanadyl group. Emission then results from relaxation of $\equiv\text{V}\text{-O}^\cdot$ to $\equiv\text{V}=\text{O}$.

Generally, synthesis of vanadium-bearing materials on the melting route offers unique advantages with respect to dopant concentration, chemical homogeneity and compositional versatility. It provides several tools to adjust the equilibrium between V^{5+} and V^{4+} . Moreover, it enables facile fabrication of specific geometries such as fiber and/or fleeces, microspheres, sheet, tape etc. In this respect, vanadium has a long tradition in melt-processed glasses, where it may be present in quantities of several tens of ppm (e.g. as coloring agent) to up to tens of mol% (e.g. in electron-conducting vanadate glasses). By choosing a suitable matrix

composition and, eventually, employing agents for heterogeneous nucleation, glasses can subsequently be converted into glass ceramics with controlled crystallite size and volume fraction [8]. In this way, a crystalline environment can be provided that may at least partially host the dopant species [9–12]. At the same time, all advantages of glass processing can be made use of. However, comparably little is known on the luminescence of V-doped glasses and, in particular, V⁵⁺-doped glass ceramics. Here, we report on luminescence and vanadium partitioning in a V-doped zinc silicate model glass and the corresponding nanocrystalline Li₂ZnSiO₄ glass ceramic.

2. Experimental

In accordance with previous work, lithium zinc silicate glasses were chosen as a model system due to their facile convertibility into Li₂ZnSiO₄ glass ceramics [10,11,13,14]. The availability of relatively large tetrahedral Zn²⁺ lattice sites (ionic radius $r \sim 0.60 \text{ \AA}$) and the proximity of mobile Li⁺ for eventual charge compensation appear favorable for the incorporation of various dopant species [11]. Samples with nominal composition (mol%) 48SiO₂-24Li₂O-16ZnO-8Al₂O₃-3K₂O-1P₂O₅-xV₂O₅ (SLZAKP, $x = 0, 0.1, 0.2, 0.5, 1, 2$ and 4) were prepared by conventional melting and quenching of a 100 g batch of analytical grade reagents SiO₂, Li₂CO₃, ZnO, Al₂O₃, K₂CO₃, NH₄H₂PO₄ and V₂O₅. Melting was performed in alumina crucibles at 1550 °C for 2 hours. Glass slabs were obtained after pouring the melts into preheated graphite moulds and annealing for 2 h at 450 °C. From these slabs, disks of 10 × 10 × 2 mm³ were cut and polished (SiC/water). Conversion into glass ceramics was done via a single-step heat treatment for 2 h at a temperature between 550 and 700 °C (in steps of 50 °C) in air (applying a heating rate of 3 K/min). Density before and after crystallization was determined by the Archimedes method. The crystallization process was characterized by X-ray diffractometry (XRD Siemens Kristalloflex D500, Bragg-Brentano, 30 kV/30 mA, Cu K α). UV-NIR absorption spectra were recorded with a double-beam photospectrometer, using a 150 mm integration sphere and a PbS detector (PerkinElmer Lambda 950). Room-temperature photoluminescence and fluorescence decay kinetics were studied with a spectrofluorometer equipped with double monochromators (Czerny-Turner) in excitation and emission (Fluorolog-3, Horiba Jobin Yvon), using a 400 W Xe-lamp for static and a 75 W Xe-flashlamp for dynamic analyses, respectively, as excitation sources. Electron paramagnetic resonance spectra (EPR) were taken on an X-band microwave spectrometer operated at a frequency of 9.7 GHz (Bruker ESR 300E). XPS spectra were acquired using a PHI 5600 spectrometer with a 450 W Al K α X-ray source. Wide scans were made at 300 W source power and a emission angle to the specimen of 45° in a binding energy range of 0 - 1200 eV and pass energy of 187.85 eV. The C1s, O1s and the V2p core levels were recorded with a step of 0.2 eV and pass energy of 23.50 eV, whereby the levels for V₂O₅ were recorded simultaneously. Binding energies of the photoelectron lines of the sample were charge referenced to the C1s line of adventitious hydrocarbon at 284.80 eV. Background subtraction was made using a Shirley function. O1s and V2p signals were fitted to Gaussian peak functions.

3. Results and discussion

Depending on nominal vanadium concentration, as-melted glasses exhibited greenish to brown coloration (the un-doped glass was completely colorless). Corresponding absorption spectra are shown in Fig. 1(A). The dominating absorption bands are located at 1065, 615 and 450 nm. These are assigned to the presence of V⁴⁺ ions and correspond to the electronic transitions of ${}^2\Gamma_{t4} \rightarrow {}^2\Gamma_{t5}$, ${}^2\Gamma_{t4} \rightarrow {}^2\Gamma_{t3}$, and ${}^2\Gamma_{t4} \rightarrow {}^2\Gamma_{t1}$, respectively [15,16]. The spectra further indicate that no V³⁺ [17] is present in the as-melted glasses. The absorption bands of V⁵⁺ lie in the UV spectral range and can, in a first consideration, not unambiguously be extracted from Fig. 1. With increasing dopant concentration, the UV cut-off is shifted to longer wavelength.

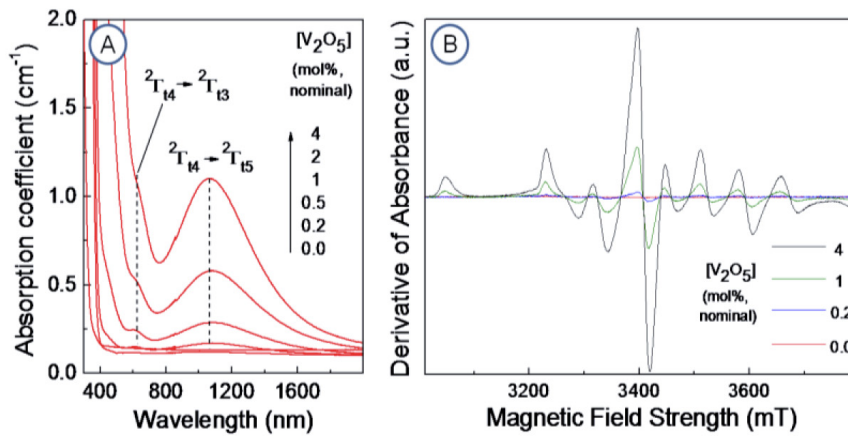


Fig. 1. UV-NIR absorption spectra (A) and EPR spectra (B) of SLZAKP for different nominal dopant concentration, expressed as V_2O_5 .

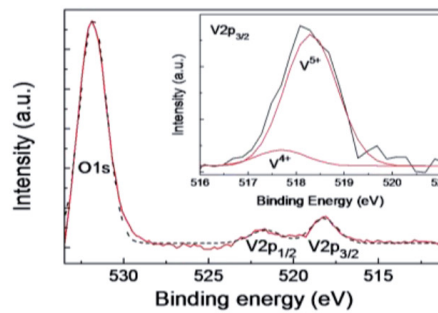


Fig. 2. XPS spectra of as-melted SLZAKP with different nominal vanadium concentration (labels). The inset depicts a zoom at the $V2p_{3/2}$ signal.

In silicate glasses, V^{4+} ions are typically present in the form of a VO^{2+} complex [18]. Due to the unpaired d-electron of the V^{4+} ion, this complex exhibits characteristic electron paramagnetic resonance. Corresponding EPR spectra comprise a well-resolved hyperfine structure (located around $g \sim 2.0$) which is associated with the ^{51}V nucleus ($I = 7/2$) [19–21]. EPR spectra of as-melted SLZAKP with different nominal vanadium content are shown in Fig. 1(B). In accordance with optical absorption data, the presence of an increasing amount of VO^{2+} with increasing total vanadium concentration is clearly confirmed (noteworthy, resonances were absent in blank reference samples). The resonance intensity is used as an indicator for the relative amount of VO^{2+} -species. It increases almost linearly with increasing total vanadium content. Hence, it may be assumed that in the considered compositional range, the ratio of V^{4+}/V^{5+} remains untouched by the total vanadium concentration.

The optical basicity A of the glass provides a way to estimate the location of the redox equilibrium between V^{4+} and V^{5+} [22]. It is obtained via a linear mixing approach, taking into account the molar fraction X_i and the partial molar basicity A_i of each component i ,

$$A = \sum_i X_i \times A_i \quad (1)$$

The optical basicity of the employed SLZAKP glass is 0.63. From this value, the ratio of V^{4+}/V^{5+} can be estimated according to the empirical equation [23]

$$\log \frac{V^{4+}}{V^{5+}} = 4 - 8A \quad (2)$$

From Eq. (2), a value of 0.1 was obtained for the ratio of V^{4+}/V^{5+} . Hence, it may be assumed that vanadium is present dominantly in the form of V^{5+} . Since visible luminescence arises from V^{5+} and the absorption band of ${}^2\Gamma_{t4} \rightarrow {}^2\Gamma_{t3}$ of V^{4+} strongly interferes with photoemission, this is the desired case. XPS analyses were conducted to directly assess partitioning of vanadium into V^{4+} and V^{5+} species (Fig. 2). Since the overall vanadium concentration is relatively small, however, XPS can only yield a coarse estimated of V^{4+}/V^{5+} and only samples with nominal $V_2O_5 \geq 1$ mol% were examined. For the analyses, the $V2p_{3/2}$ resonance was deconvoluted into V^{5+} and V^{4+} signals at 518.3 and 517.7 eV, respectively (best-fit data). The ratio of the areas of both peaks was used to estimate the ratio of V^{4+}/V^{5+} , and a value of ~ 0.2 was obtained, what is in relatively good accordance with the previous estimate from the optical basicity.

Optical excitation and emission spectra are given in Fig. 3(A). All doped samples show a broad excitation band, ranging from 250 to 400 nm. The excitation band comprises two individual peaks, i.e. at about 275 and 320 nm. These peaks are assigned to the already noted charge transfer reaction in $[VO_4]^{3-}$ groups [24,25]. Interestingly, the position of the higher-lying excitation band remains unchanged with increasing vanadium concentration whereas the low-lying band appears to red-shift from 313 to 336 nm as the vanadium concentration (V_2O_5) is increased from 0.1 to 4.0 mol%. Emission spectra were recorded by exciting on the lower-lying band. Emission occurs over a broad asymmetric band ranging from 400 to 800 nm with a maximum at 580 nm. Its position and FWHM do not vary with increasing dopant concentration. Emission intensity reaches a maximum for a nominal V_2O_5 concentration of about 1 mol%. For higher dopant concentration, the emission intensity drops sharply, indicating concentration quenching and/or increasing interference of V^{4+} -species. In the considered spectral range, for excitation at 315 nm, blank samples of SLZAKP did not show any photoluminescence. Figure 3(B) represents the dependence of emission lifetime (time within which the luminescence intensity decays to $1/e$ times of its initial value) on nominal vanadium concentration (expressed as V_2O_5). Generally, luminescence decay follows a single exponential equation (inset of Fig. 3(B), shown exemplarily for $[V_2O_5] = 0.1$ mol%), indicating that only a single type of emission centers is present. For a concentration of up to about 0.5 mol%, lifetime remains practically concentration-independent (~ 34 μ s). At higher dopant concentration, it decreases notably, i.e. to 22.4 μ s for $[V_2O_5] = 4.0$ mol%. This decrease is attributed to increasing interaction between neighboring V-species and, hence, increasing probability of fast non-radiative decay. The observed lifetime is comparable to that of crystalline V-MgAl₂O₄ (13.7 μ s) [1], much larger than that of V-doped SiO₂/Zn₂SiO₄ composites (13 ns) [2] and significantly below the value observed in C-V_{0.05}Si β (88 ms) [4].

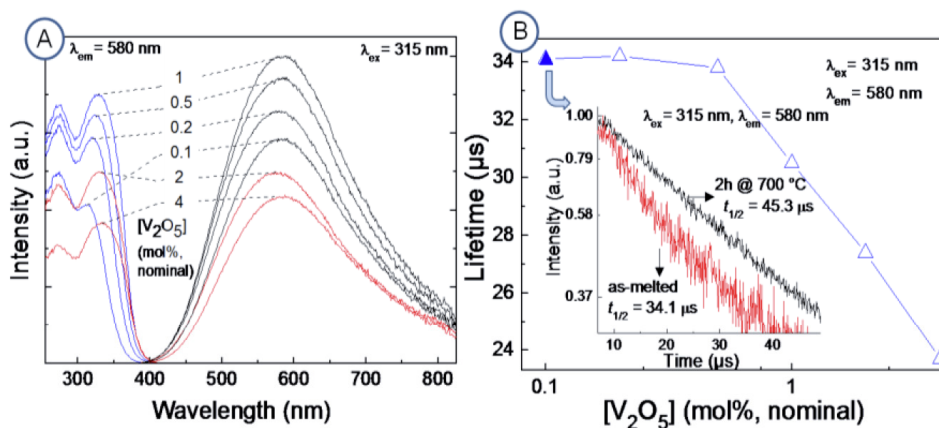


Fig. 3. Static photoluminescence (A) and luminescence lifetime (B) of SLZAKP for different nominal vanadium concentration (labels). The inset of (B) shows the decay kinetics of an as-melted specimen and a crystallized sample (both doped with 0.1 mol% V_2O_5).

Upon annealing at ≥ 550 °C, the samples partially crystallize (Fig. 4(A)). Crystallization occurs by internal nucleation homogeneously over the bulk of the sample. In accordance with previous observations [10,11,14], XRD data confirm precipitation of a nanocrystalline phase and suggest assignment to the orthorhombic polymorph of $\text{Li}_2\text{ZnSiO}_4$ (JCPDS card no. 00-024-0682) [11,26]. However, it must be noted that the phase is presently not indexed. The peak arrangement matches that of orthorhombic $\text{Li}_{3.8}\text{Zn}_{1.2}\text{P}_{1.8}\text{Si}_{0.2}\text{O}_8$, notwithstanding the clear discrepancy in chemistry. Both phases are structurally related to low- Li_3PO_4 (JCPDS card no. 01-084-0003). We therefore interpret the observed patterns as a reflection of the formation of a solid solution of $\text{Li}_{4-2x}\text{Zn}_x\text{SiO}_4$, eventually incorporating or being nucleated by minor amounts of PO_4^{3-} [11]. In accordance with [11], XRD spectra indicate a phase transition in the temperature range of 600-650 °C. During crystallization, density of the samples does not change significantly (as-made SLZAKP-0.1 mol% V_2O_5 : $2,721 \pm 0.005$ g/cm³; after annealing for 2 h at 700 °C: $2,735 \pm 0.005$ g/cm³). The crystal volume fraction V_c was estimated from the relative area of all diffraction peaks. Calculated values are noted in Fig. 4(A). V_c is limited by the amount of ZnO. A simple consideration of glass composition and stoichiometry indicates a theoretical maximum of V_c of 45-50 vol.%, provided that stoichiometric $\text{Li}_2\text{ZnSiO}_4$ is the single crystalline phase. Such a degree of crystallization is achieved after treatment for 2 h at 700 °C. Traces of Zn^{2+} -depleted crystallite species, appearing especially in the later stages of crystallization, may be a result of ZnO depletion and higher mobility of Li^+ -ions, and may explain the difficulties in assigning the obtained XRD patterns. The residual glass phase is an aluminosilicate glass with reduced optical basicity. Photoluminescence spectra of exemplary SLZAKP glass ceramics ($[\text{V}_2\text{O}_5] = 0.1$ mol%) are shown in Fig. 4(B). Upon crystallization and as a function of annealing temperature (i.e., degree of crystallization), the relative emission intensity increases up to tenfold for the sample which was annealed for 2 h at 700 °C as compared to the as-melted glass. In a first consideration, this increase is at least partly attributed to multiple scattering of incident and luminescent light in the glass ceramic. On the other hand, the position of the emission band blue-shifts with increasing annealing temperature, i.e. from 580 nm (as-melted glass) to 546 nm (glass ceramic after 2 h at 700 °C), what indicates that the active vanadyl groups undergo a change in ligand field strength. This observation is in accordance with the significant increase which is observed in emission lifetime: as shown in Fig. 3(B), upon crystallization, lifetime increases from 34.1 to 45.3 μs , what is a clear indicator for the reduction of non-radiative relaxation and, hence, an increase in quantum efficiency. In the present case, it is also taken as strong evidence for the effective incorporation of V^{5-} emission centers into the crystalline phase for the following reason: if vanadyl groups would not partition into the crystalline phase, they would enrich in the residual glass phase. That is, for V_c of ~48 vol.%, V_2O_5 concentration in the residual glass phase would double to about 0.2 mol%. As shown in Fig. 3(B) for the as-melted glasses, at this dopant concentration, lifetime is still about 34 μs . Taking into account the change in chemical composition of the residual glass phase due to selective precipitation of Li_2O , ZnO and SiO_2 in the crystalline phase (resulting in lower optical basicity), one would expect an increase in the amount of V^{4+} (Eq. (2)). This would result in additional quenching of photoluminescence due to ${}^2\Gamma_{14} \rightarrow {}^2\Gamma_{13}$ (what is not the case, here).

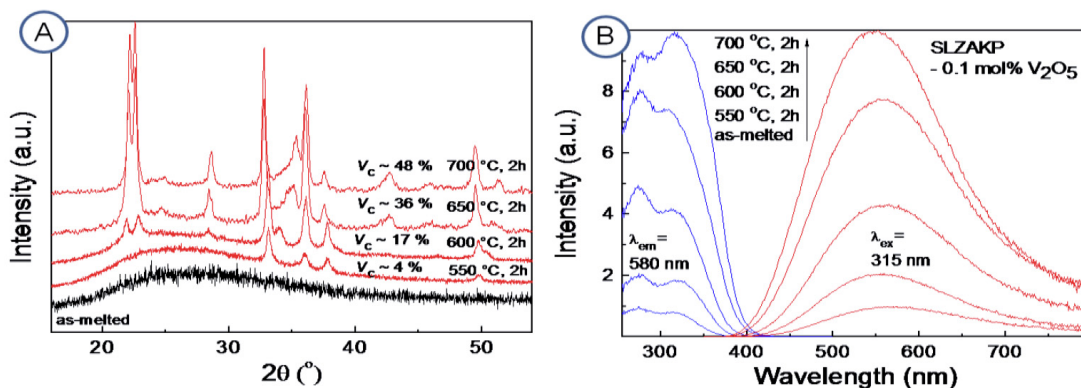


Fig. 4. (A): *Ex situ* XRD patterns of as-melted SLZAKP and samples which were annealed for 2 h at different temperatures ($[V_2O_5] = 0.1 \text{ mol}\%$). The labels indicate the calculated crystal volume fraction. (B): Photoexcitation (right) and emission (left) spectra of crystallized SLZAKP for various annealing temperatures.

4. Conclusions

Photoluminescence of vanadium-doped lithium zinc silicate glasses and corresponding nanocrystalline Li_2ZnSiO_4 glass ceramics was studied. Depending on dopant concentration and synthesis conditions, VIS photoemission from $[VO_4]^{3-}$ centers peaks at 550-590 nm and occurs over a bandwidth (FWHM) of ~ 250 nm. While within the considered range of dopant concentrations, the emission band position remains unaffected by dopant concentration, a notable blue-shift occurs after crystallization. The corresponding excitation band covers the complete UV-B to UV-A spectral region. Here, the excitation peak at about 315 nm remains unaffected by crystallization, but red-shifts when the dopant concentration is increased. Both observations are attributed to the nature of photoemission in the considered system. That is, photoemission occurs as a result of relaxing charge transfer in vanadyl groups. This process is strongly affected by the ligand field strength, and also by interference of V^{4+} species and oxygen vacancies, respectively. Partitioning of vanadium into V^{5+} and V^{4+} was examined by EPR and XPS. Due to the very high absorption cross section of ${}^2\Gamma_{t4} \rightarrow {}^2\Gamma_{t3}$, even small amounts of V^{4+} strongly interfere with photoluminescence. In as-melted glasses, the emission lifetime is about 34 μs . After crystallization, it increases to about 45 μs . With respect to concentration quenching, the optimal dopant concentration was found at about 0.5 mol% V_2O_5 . Crystallization was observed to result in a tenfold increase of emission intensity, what is attributed to multiple scattering and the incorporation of V^{5+} species into the crystal phase.

Acknowledgment

The authors gratefully acknowledge funding from the German Excellence Initiative within the cluster "Engineering of Advanced Materials".

2.5. Broadband NIR photoluminescence from Ni²⁺-doped nanocrystalline Ba–Al titanate glass ceramics

The CN of Ni²⁺ is well controlled by the crystallization process in nanocrystalline Ba–Al titanate glass ceramics. Ni²⁺ ions are tetrahedrally coordinated in precursor glasses, whereas Ni²⁺-species are incorporated into the crystalline environment in octahedral coordination, which gives rise to the broadband NIR PL of ^{VI}Ni²⁺. Decay kinetics as well as position and shape of the emission band are adjusted by dopant concentration and synthesis conditions.

G. Gao, S. Reibstein, E. Spiecker, M. Peng and L. Wondraczek, *J. Mater. Chem.* 2012, **22**, 2582–2588. -Reproduced by permission of The Royal Society of Chemistry.

<http://pubs.rsc.org/en/Content/ArticleLanding/2012/JM/c1jm14292e>

Broadband NIR photoluminescence from Ni²⁺-doped nanocrystalline Ba–Al titanate glass ceramics

Guojun Gao,^a Sindy Reibstein,^a Erdmann Spiecker,^b Mingying Peng^c and Lothar Wondraczek^{*a}

Received 31st August 2011, Accepted 21st November 2011

DOI: 10.1039/c1jm14292e

Nanocrystalline Ba–Al titanate precipitates from supercooled TiO₂–BaO–SiO₂–Al₂O₃ melts by catalyzed volume nucleation in the presence of Ni²⁺, forming a BaAl₂Ti₆O₁₆ hollandite-type lattice. Ni²⁺-species are incorporated into the crystalline environment in octahedral coordination. Hollandite formation is accompanied by precipitation of tetrahedrally distorted BaTiO₃ as a secondary crystal phase, where crystal species and habitus can be clearly distinguished by dark-field transmission electron microscopy. Resulting photoluminescence due to spin-allowed relaxation of ³T_{2g}(³F) to ³A_{2g}(³F) in ^{VI}Ni²⁺ occurs from three distinct emission centers. It spans the spectral range of 1.0 to 1.6 μm and exhibits a lifetime of about 60 μs, which suggests applications in tunable lasers and broadband optical amplifiers. Besides red and IR laser excitation, NIR photoemission can be excited with conventional near UV light sources, *i.e.* in the spectral range of 350–420 nm. Decay kinetics as well as position and shape of the emission band can be adjusted by dopant concentration and synthesis conditions.

Introduction

Due to broad photoemission bands in the near infrared (NIR), 3d transition metal ions such as Ni²⁺, Co²⁺ and Cr³⁺ are receiving significant and continuous attention for potential applications in tunable lasers and optical amplifiers.^{1–6} However, the 3d electronic configuration is typically very sensitive to the ligand situation within the employed host material. That is, in oxide matrices, NIR luminescence is typically observed only when a specific coordination is provided, *e.g.* tetrahedral for Cr⁴⁺ and Co²⁺, and octahedral for Ni²⁺.^{1–11} For Co²⁺, reported NIR emission intensity is mostly very low which, at present, appears to rule out any concrete application.¹² Chromium ions usually partition in mixed valence, Cr³⁺, Cr⁴⁺ and Cr⁶⁺, but Cr³⁺ and Cr⁶⁺ can quench NIR luminescence from ^{IV}Cr⁴⁺. There is no practical way for avoiding the presence of Cr³⁺ and Cr⁶⁺ in most host candidates. In contrast, nickel ions which, in oxide hosts, typically reside solely as Ni²⁺ provide an interesting alternative. Consequently, the spectroscopic properties of Ni²⁺ doped glasses, glass ceramics and single crystals have attracted much attention over the last decade.^{3–11,13–15} As mentioned before, the coordination state in which Ni²⁺ is incorporated into the host lattice is

one of the key factors for achieving specific spectroscopic properties. The most frequently observed environments of Ni²⁺ in solid matrices are tetrahedral (fourfold coordination, ^{IV}Ni²⁺), trigonal bipyramidal (fivefold, ^VNi²⁺) and octahedral (sixfold, ^{VI}Ni²⁺), respectively. In most oxide glasses, Ni²⁺ favors fivefold coordinated sites. For such ^VNi²⁺ species, no or very weak NIR luminescence can be observed due to predominance of non-radiative relaxation. Significant radiative relaxation at room temperature and, hence, high NIR quantum efficiency are known only for ^{VI}Ni²⁺, *e.g.* in single-crystalline LiGa₅O₈ : Ni²⁺.⁴ Major limitations of single-crystalline materials lie, however, in the complexity of their fabrication processes which may lead to low degrees of freedom in composition (dopant and co-dopant concentrations) as well as specimen shape (fiber, large-scale). In principle, this drawback can be overcome by fabricating a glass ceramic material, where a crystalline species is precipitated from a supercooled melt by controlled nucleation and crystallization.^{16–19} In this way, conventional glass processing techniques (*e.g.*, melt casting, fiber drawing, extrusion, *etc.*) can be employed to obtain at least some of the properties of a crystalline host material. As a prerequisite, however, Ni²⁺ species must actually precipitate into the crystalline phase rather than remain in the residual glass phase.³ Secondly, crystal growth must be limited to not more than several tens of nanometres in order to ensure optical transparency while, at the same time, a high crystallite volume fraction (crystallite number density) must be achieved. With these objectives, *e.g.*, NIR-luminescent nanocrystalline LiGa₅O₈ : Ni²⁺ glass ceramics were prepared from Li₂O–Ga₂O₃–SiO₂ glasses by Suzuki *et al.*,⁴ and β-Ga₂O₃ : Ni²⁺ glass ceramics from Na₂O–Al₂O₃–Ga₂O₃–SiO₂ glasses by Zhou *et al.*^{10,20} In both materials, Ni²⁺ coordinates on octahedral sites, but besides

^aInstitute of Glass and Ceramics, Department of Materials Science, University of Erlangen-Nuremberg, Martensstrasse 5, Erlangen, D-91058, Germany. E-mail: lothar.wondraczek@www.uni-erlangen.de; Fax: +49 (0)9131 28311; Tel: +49 (0)9131 85 27553

^bCenter for Nanoanalysis and Electron Microscopy (CENEM), Department of Materials Science, University of Erlangen-Nuremberg, 91058, Germany

^cInstitute of Optical Communication Materials & State Key Laboratory of Luminescent Materials and Devices, South China University of Technology, Guangzhou, 510641, China

the proof of principle, actual applicability is questionable because of the presence of Ga₂O₃ as a rather rare raw material, relatively low quantum yield as well as unfavorable processing properties.

There are three spin-allowed transitions in ^{VI}Ni²⁺, ³T_{1g}(³F) → ³T_{1g}(³P), ³T_{1g}(³F) → ³A_{2g}(³F) and ³T_{1g}(³F) → ³T_{2g}(³F). They locate in the spectral range of about 900–1100 nm, 600–800 nm and 300–500 nm, respectively. Accordingly, NIR photoemission should be expected for excitation to any of the upper levels, ³T_{1g}(P), ³A_{2g}(F), and T_{2g}(F). At present, however, NIR emission from Ni²⁺ doped glass ceramics has been reported primarily for excitation with 800 and 980 nm laser diodes (LDs). On the other hand, making available the broad absorption band in the 300–500 nm spectral range for near-ultraviolet (NUV) excitation would be highly desirable.²¹

In the present study, we consider hollandite-type crystallites of the general composition A_x(B,C)₈O₁₆ as a matrix material for NIR luminescent Ni²⁺ species. The crystal lattice of hollandite is depicted in Fig. 1b. It comprises a channel structure, formed by double strings of [(B,C)O]₆ octahedra. The channels are occupied by large A cations. Our specific interest in this crystal phase results from the possibility to incorporate a very large variety of dopant species, if desired also in large concentration (a property which is being made use of for, e.g., the immobilization of radioactive wastes in “Synroc”, a “synthetic rock” comprising a significant amount of hollandite-type crystals).²² Besides crystal structure, the stoichiometric variety is enabled by the very broad extension of the phase field where almost complete solubility exists between various end members, e.g. A = {Ba⁺, Ca⁺}; B = {Ti³⁺, Al³⁺, Ni²⁺, Mn²⁺, Fe³⁺, Cu²⁺, Co²⁺}; and C = {Ti⁴⁺, Si⁴⁺, Sn⁴⁺}. Hence, we can expect great potential to also incorporate optically active species on octahedral lattice sites. This requires, however, fabrication of an optically transparent composite material comprising nanocrystalline hollandite.

Here, we demonstrate that this can be achieved in supercooled TiO₂–BaO–SiO₂–Al₂O₃–NiO melts, from which nanocrystalline Ba_{1.24}(Al_{2.48}Ti_{5.52})O₁₆ : Ni²⁺ can be precipitated. We then discuss in detail how controlling the coordination state of Ni²⁺ can be used to tune the spectroscopic properties of the material, especially broadband NIR photoemission.

Experimental

Precursor glasses were prepared by conventional melting of 50 g batches of nominal composition (mol%) 30TiO₂–30BaO–

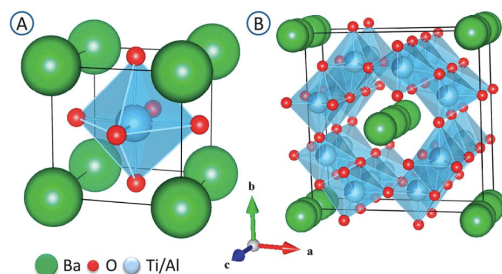


Fig. 1 Crystal structure of tetrahedral BaTiO₃ (a) and Ba–Al hollandite (b).

30SiO₂–10Al₂O₃–*x*Ni (TBSA, *x* = 0, 0.05, 0.1, 0.2, 0.4 and 0.8, sample nomenclature is TBSA*x*Ni, e.g. TBSA005Ni for a dopant concentration of 0.05 mol%). As raw materials, analytical grade reagents SiO₂, TiO₂, BaCO₃, Al₂O₃ and NiO were employed. Melting was performed at 1550 °C for 2 hours in alumina crucibles. Glass slabs were obtained after pouring the melt into a preheated (400 °C) graphite mould and subsequent annealing for 2 h at 500 °C. From these slabs, disks of 15 × 15 × 2 mm³ were cut and polished on both sides.

The crystallization process of each specimen was first analyzed by non-isothermal differential scanning calorimetry (DSC, Netzsch, Ar atmosphere) at heating rates of 5, 10 and 20 K min^{−1}. Subsequently, individual samples were placed on alumina substrates and isothermally annealed for 2 hours at 750, 800, 850 and 900 °C, and at 850 °C for 0, 1, 2, 8 and 32 hours in air. During the annealing procedure, glasses transformed into transparent glass ceramics *via* precipitation of homogeneously distributed nanocrystalline phases. Except for the sample which was annealed at 900 °C for 2 hours, visual inspection did not reveal any indication of surface crystallization. In order to avoid experimental artifacts which might have resulted from surface effects, annealed samples were polished a second time before further analyses. The density before and after crystallization was determined with an Archimedes balance. To identify and describe crystalline phases, X-ray diffractometry (XRD, Siemens Kristalloflex D500, Bragg-Brentano, 30 kV/30 mA, Cu Kα) and transmission electron microscopy (TEM, Philips CM30 at 300 kV) were used. For TEM, specimens were produced by slicing thin disks from each sample. These were then mechanically polished, dimpled and Ar⁺ ion-thinned to obtain electron transparent samples. During ion thinning, the samples were cooled to liquid nitrogen temperature in order to suppress irradiation damage of the material. To also characterize the occurrence of surface crystallization, powdered TBSA01Ni glass was studied during heating by *in situ* high temperature XRD (see above).

UV-VIS-NIR absorption spectra were recorded from 300 to 2200 nm with a double-beam photospectrometer equipped with a 150 mm integration sphere and a PbS detector (Perkin-Elmer Lambda 950). IR transmittance spectra were recorded on a Perkin-Elmer 1600 FTIR spectrometer in the wavenumber range of 400–4000 cm^{−1} with a resolution of 2 cm^{−1}. Static and dynamic photoluminescence was studied with a high-resolution spectrofluorometer and time correlated single photon counting (TCSPC, Horiba Jobin Yvon Fluorolog FL3-22), using a static Xe lamp (450 W) and a ps-LED-source at 370 nm (nano-LED), respectively, as excitation sources, and mechanical double monochromators in emission and excitation channels. NIR emission was observed with a high-sensitivity thermoelectrically cooled InP/InGaAs-photomultiplier tube (NIR-PMT, Hamamatsu H10330A-75). Excitation curves were corrected over the lamp intensity with a silicon photodiode. Emission curves were corrected by the spectral response of the NIR-PMT detector. All analyses were performed at room temperature.

Results and discussion

Crystal precipitation

Fig. 2 exemplarily shows DSC curves of un-doped TBSA, TBSA01Ni and TBSA08Ni for heating rates of 5, 10 and

20 K min⁻¹ after baseline correction. The onset of glass transition, T_g , was found at 747 ± 0.5 °C and is, within the considered regime, independent of the dopant concentration. In contrast, the crystallization peak temperature T_c is strongly influenced by the content of NiO. While between TBSA and TBSA01Ni, it varies only slightly, it decreases from 864 ± 0.5 °C for TBSA to 828 ± 0.5 °C for TBSA08Ni. In a first consideration, the presence of NiO facilitates crystallization.

Fig. 3 represents X-ray diffraction patterns of samples of TBSA01Ni after *ex situ* annealing at temperatures between 750 °C and 900 °C for 2 h. Consistent with DSC data, first diffraction peaks can be detected after annealing at 750–800 °C, whereby, however, phase assignment is complicated by small crystallite size and large overlap with the amorphous hump. For higher annealing temperature, sharper peaks indicate crystal growth (although at a low level). Phase assignment was performed by indexing the spectrum which was obtained after annealing at 900 °C/2 h. It indicated the presence of at least two phases: tetragonal barium titanate, Ba(TiO₃) (JCPDS card no. 81-2202),²³ and Ba–Al hollandite, Ba_{1.24}(Al_{2.48}Ti_{5.52})O₁₆ (JCPDS card no. 78-0013).²⁴ For a rough estimate of crystallite size, the Debye–Scherrer formula may be consulted. In the present case, however, formal calculation is subject to a large error because of the low crystallite size and volume fraction and, hence, rather broad diffraction peaks. For the Ba(TiO₃) phase, we find that only the peak at $2\theta = 66^\circ$ may be used. For the sample annealed at 900 °C, it indicates an average Ba(TiO₃) crystallite size of about 30 ± 10 nm. The density of the samples increases with annealing temperature (*i.e.*, as-made TBSA01Ni: 3.690; 750 °C/2 h: 3.792; 800 °C/2 h: 3.846; 850 °C/2 h: 3.868 and 900 °C/2 h: 3.900 ± 0.005 g cm⁻³), reflecting the increase in crystal volume fraction.

Both titanate phases precipitate by volume crystallization. Additional surface crystallization was observed for temperatures above 875 °C by analyzing powder and unpolished samples, respectively. In these cases, the major crystalline phase is hexacelsian, BaAl₂Si₂O₈ (JCPDS card no. 770185).²⁵

To clarify the nature and distribution of crystallite phases as a function of annealing conditions, TEM analyses were performed. For that, two samples of TBSA01Ni (850 °C/8 h and 900 °C/2 h) were considered. Bright field (BF) images, electron diffraction patterns and selected dark field (DF) images are shown in Fig. 4 and 5. In BF images, dark areas (large Bragg

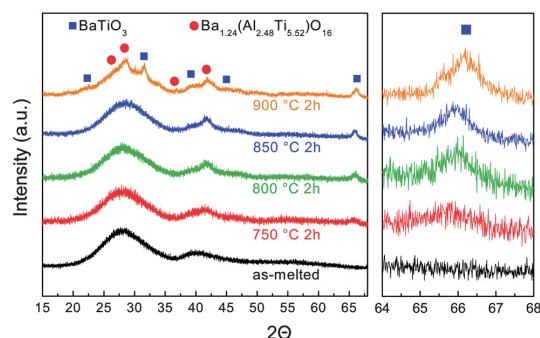


Fig. 3 *Ex situ* XRD patterns of individual TBSA01Ni samples taken after annealing for 2 h at the indicated annealing temperature.

contrast) indicate size and shape of the crystalline phases. For the 850 °C/8 h sample, observed crystals are practically isometric and exhibit a mean size of about 30 nm, consistent with XRD data (Fig. 4). In contrast, the 900 °C/2 h sample appears to contain at least two different types of crystals. They can be revealed separately by hollow-cone dark field (DF01, DF02) imaging, where the objective aperture is placed on the optical axis and the incident electron beam rotates around the optical axis at a specific tilt angle corresponding to a diffraction ring obtained by conventional electron diffraction. By integrating over the whole diffraction ring, a hollow-cone DF image reveals more crystallites than a conventional DF image formed with fixed incident beam direction. However, one has to keep in mind that still not all the crystallites of the selected phase are met. In Fig. 5, the selected rotational angles are indicated by a blue and green ring, respectively. According to the previous XRD analyses, these rings reflect the Ba–Al hollandite (DF02) and the barium titanate (DF01) phase, respectively. Then, for TBSA/900 °C/2 h, barium titanate crystals appear isometric with a mean size of about

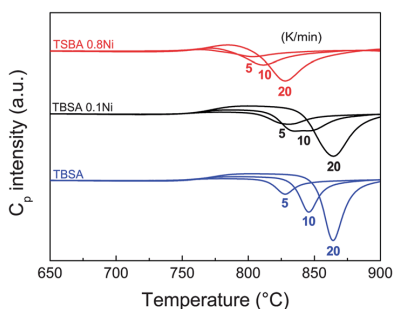


Fig. 2 DSC scans of undoped TBSA, TBSA01Ni and TBSA08Ni for various heating rates (labels), taken on bulk samples.

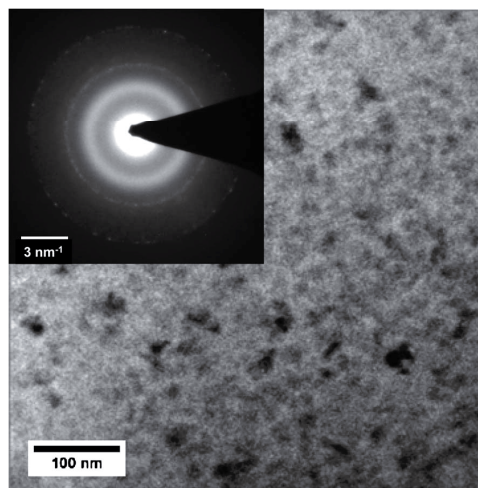


Fig. 4 Bright field TEM micrographs and corresponding electron diffraction pattern of TBSA01Ni after annealing for 8 h at 850 °C.

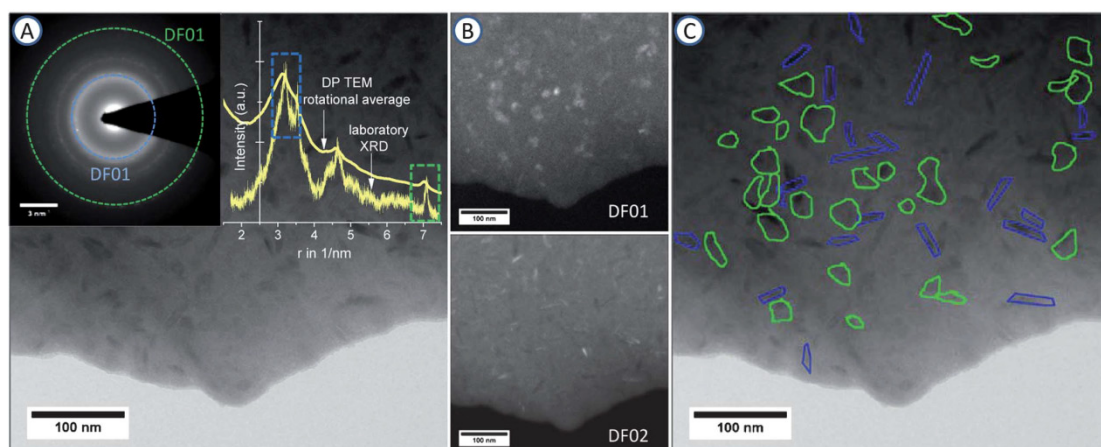


Fig. 5 TEM bright field (BF) image (a), corresponding electron diffraction pattern (inset of (a), DP) and selected hollow-cone dark field images (DF01 and DF02) (b) of TBSA01Ni after annealing for 2 h at 900 °C. The hollow cone dark field images DF01 and DF02 were formed with electrons scattered into diffraction angles marked green and blue in (a), respectively. For comparison, laboratory XRD and TEM diffraction patterns are shown (inset of a). DF01 and DF02 were overlaid to visualize the distribution of BaTiO₃ (green) and Ba–Al hollandite (blue) crystallites in the considered sample (c).

40 nm, somewhat larger than the estimate which was obtained from the Debye–Scherrer equation. Barium hollandite crystals are elongated in one direction with prismatic cross-sections and an aspect ratio of ~ 5 . In the hollow cone dark field image DF02, some of the elongated crystals appear dark rather than bright. This can be explained by the fact that for these crystals, the Bragg condition is not met (see above) so that they basically represent missing volume of the glass phase which contributes as background to the dark-field image.

In accordance with DSC data, also XRD and TEM results indicate a significant effect of NiO on crystal growth. Intermediate concentration of NiO resulted in the preferred precipitation of Ba(TiO₃) whereas higher NiO content tends to stabilize the Ba_{1.24}(Al_{2.48}Ti_{5.52})O₁₆ phase. Exact evaluation of crystallite stoichiometry, however, is not possible because of the low crystallite size, high volume fraction of residual glass phase and unavailability of appropriate reference data.

UV-VIS optical absorption and Ni²⁺ coordination

As-melted TBSA01Ni glass exhibits a characteristic reddish-brown color. During crystallization, its coloration changes to green, but samples remain visually transparent (inset of Fig. 6). Fig. 6a and b represent the optical absorption spectra of un-doped TBSA and TBSA01Ni glass and corresponding glass ceramics. Un-doped TBSA glass exhibits a UV cutoff λ_0 at about 350 nm, probably due to charge transfer reactions associated with the high molar content of Ti⁴⁺. No further absorption peaks are visible in the spectrum of TBSA. Crystallization of un-doped TBSA results in a red-shift of the absorption edge and the appearance of a shoulder in the green spectral region, both presumably related to charge transfer reactions and optical scattering. Introduction of Ni²⁺ yields three additional absorption bands, spanning the spectral ranges of ~ 1200 to 2000 nm (peaking at ~ 1740 nm), ~ 700 to 1100 nm (896 nm) and ~ 400 to

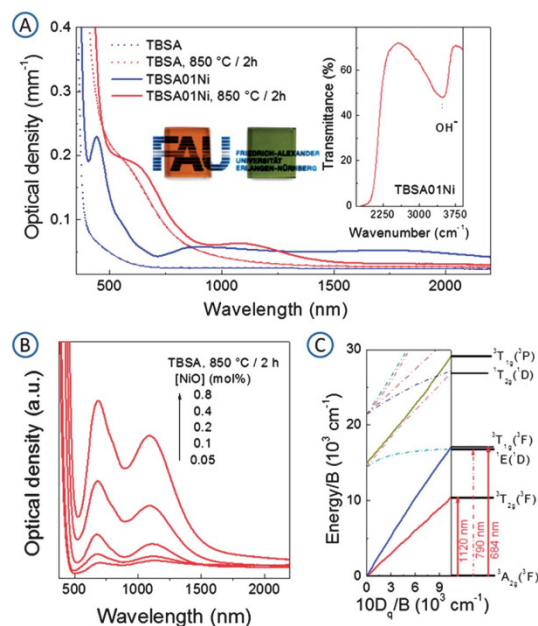


Fig. 6 (a) Optical absorption spectra of un-doped TBSA and TBSA01Ni glasses and glass ceramics (850 °C/2 h). Inset I: photograph of corresponding TBSA01Ni glass (left) and glass ceramic (right). Inset II: FTIR optical transmission spectrum of TBSA01Ni. (b) Residual optical absorption spectra of TBSA glass ceramics (850 °C/2 h) as a function of absolute NiO concentration (labels) after subtracting the absorption spectrum of the un-doped TBSA glass ceramic. (c) d⁵-Tanabe–Sugano and energy level diagram of ⁶Ni²⁺ in TBSA glass ceramics (solid lines: spin-allowed transitions; dashed lines: spin-forbidden transitions).

600 nm (443 nm), respectively. These bands can readily be assigned to the transitions of ${}^3E_{1g}({}^3F) \rightarrow {}^3E_{1g}({}^1F)$, ${}^3E_{1g}({}^3F) \rightarrow {}^3A_{2g}({}^3F)$ and ${}^3E_{1g}({}^3F) \rightarrow {}^3A_{2g}({}^3P)$, respectively, in ${}^VI\text{Ni}^{2+}$.¹⁵ After thermal annealing, position and shape of the bands change significantly: they are essentially replaced by two new bands ranging from ~ 500 to 800 nm (684 nm) and ~ 900 to 1400 nm (1122 nm), where the absorption band at 684 nm is the primary reason for the observed green coloration of the glass ceramic. The two new bands are ascribed to spin-allowed d–d transitions from the ${}^3A_2({}^3F)$ ground state to ${}^3T_{1g}({}^1F)$ and ${}^3T_{2g}({}^3F)$, respectively, in ${}^VI\text{Ni}^{2+}$.¹⁵ The weak shoulder which is located at around 790 nm originates from spin-forbidden ${}^3A_{2g}({}^3F) \rightarrow {}^1E({}^1D)$, also in ${}^VI\text{Ni}^{2+}$.¹⁵

On the basis of optical absorption data, the ligand field and Racah parameters D_q and B were calculated by fitting to the Tanabe–Sugano diagram of the d^8 complex (exemplarily shown for TBSA01Ni 850 °C/2 h in Fig. 6c). Obtained values are $D_q = 891 \text{ cm}^{-1}$ and $B = 857 \text{ cm}^{-1}$. The splitting field strength acting on ${}^VI\text{Ni}^{2+}$ in TBSA01Ni glass ceramics is hence somewhat larger than in $(\text{Ga}_2\text{O}_3)_3(\text{GeO}_2)_2$ glass ceramics (870 cm^{-1}),⁵ but smaller than in LiGa_5O_8 glass ceramics (974 cm^{-1}).⁴

Above observations clearly show that with crystallization, the Ni^{2+} ion at least partly undergoes a coordination change from fivefold to octahedral, which is a strong indicator for its incorporation into the crystalline phase. Both available titanate phases, $\text{Ba}(\text{TiO}_3)$ and Ba–Al hollandite, provide octahedral sites for the incorporation of Ni^{2+} : as observed by XRD, $\text{Ba}(\text{TiO}_3)$ forms a tetragonally distorted perovskite lattice,²³ where three different atom sites can be distinguished: Ba^{2+} at the corners, Ti^{4+} in the center and O^{2-} on the faces (Fig. 1a). Hence, Ba^{2+} and Ti^{4+} are twelvefold and sixfold coordinated, respectively. The ionic radii mismatch between ${}^VI\text{Ni}^{2+}$ (69 pm) and ${}^VI\text{Ti}^{4+}$ (60.5 pm) is about 12%.²⁶ This would generally allow for ${}^VI\text{Ti}^{4+}$ substitution by ${}^VI\text{Ni}^{2+}$.²⁷ Charge compensation can be achieved by, e.g., the formation of one oxygen vacancy.²⁸ As noted before, hollandite-type $\text{Ba}_{1.24}(\text{Al}_{2.48}\text{Ti}_{5.52})\text{O}_{16}$ (Fig. 1b) offers edge-sharing $[(\text{Ti,Al})\text{O}_6]$ octahedra²⁴ where Ni can substitute either Ti or Al species. This lets us expect the presence of up to three optically active ${}^VI\text{Ni}^{2+}$ species.

Static NIR photoluminescence

Static photoemission and excitation data of TBSA glasses and corresponding glass ceramics are summarized in Fig. 7. The dependence of NIR luminescence on annealing temperature is illustrated in Fig. 7a; while expectedly, in as-melted TBSA01Ni no NIR luminescence can be detected for any excitation wavelength, crystallization results in the evolution of distinct excitation and emission spectra. Excitation spectra comprise two individual bands which are located at about 365 nm and 650 nm, and a shoulder at about 420 nm. These excitation bands are assigned to spin-allowed ${}^3T_1({}^3P) \rightarrow {}^3A_2({}^3F)$, ${}^3T_2({}^1D) \rightarrow {}^3A_2({}^3F)$ and spin-forbidden ${}^3T_1({}^3F) \rightarrow {}^3A_2({}^3F)$, respectively, in ${}^VI\text{Ni}^{2+}$. The most intense excitation band (${}^3T_1({}^3P) \rightarrow {}^3A_2({}^3F)$) was initially used for recording the NIR emission spectra. Then, a very broad emission band (~ 1050 to 1600 nm) is detected with a maximum at ~ 1370 nm (emission was recorded up to a maximum wavelength of 1600 nm; above this wavelength, the sensitivity of the employed NIR-PMT detector sharply

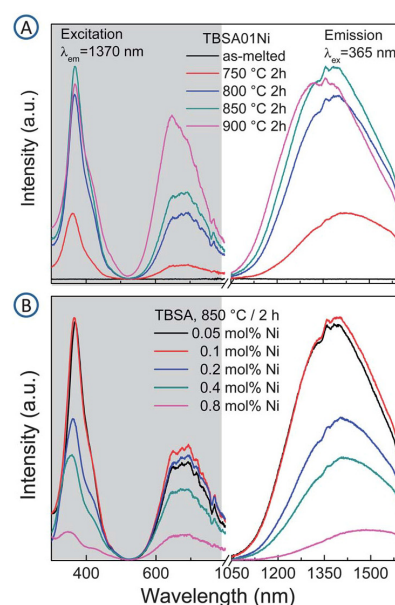


Fig. 7 Excitation and emission spectra of TBSA glass and corresponding glass ceramics (a) with 0.1 mol% NiO as a function of annealing temperature (2 h, labels) and (b) after annealing at 850 °C for 2 h as a function of NiO content.

decreases). The broad emission band corresponds to the spin-allowed relaxation of ${}^3T_{2g}({}^3F) \rightarrow {}^3A_{2g}({}^3F)$ in ${}^VI\text{Ni}^{2+}$ and can be used as a general confirmation of Ni^{2+} partitioning on octahedral lattice sites. The experimental data are best reproduced by fitting to three overlapping Gaussian functions. In the case of TBSA01Ni 850 °C/2 h (Fig. 7c), this yields three peaks at 1264, 1419 and 1570 nm. Beyond sample quality, absolute emission intensity is influenced by various factors, *i.e.* emission site concentration, internal and external quantum efficiency and multiple scattering.^{17,29} By examining samples with constant dopant concentration (TBSA01Ni), it first increases with annealing temperature up to 850 °C and apparently decreases with higher annealing temperatures (Fig. 7a). This increase is interpreted as a joint result of increasing ${}^VI\text{Ni}^{2+}$ species with increasing crystallinity and multiple scattering of the excitation light, where, as already discussed, density, XRD and TEM data show that the crystallite size and crystallinity increase with increasing annealing temperature. Both effects result in higher emission intensity.

While the shape of the excitation spectrum remains practically unaffected by annealing temperature, the emission band clearly blue-shifts with increasing annealing temperature, *i.e.* from about 1430 nm to 1330 nm. As already noted, the energy gap of d–d transitions is highly sensitive to crystal field splitting and, hence, the local ligand situation. The blue-shift of the corresponding NIR emission band is therefore caused by changes in the local environment at the responsible ${}^VI\text{Ni}^{2+}$ luminescence centers, but also by surface effects and the size of the crystallites.³⁰ That is, the mean Ni–O distance is lower in Ba–Al hollandite, resulting in stronger crystal field splitting and, hence,

higher emission energy (see also Fig. 6c). The blue shift then reflects a transition from the predominance of ${}^{\text{VI}}\text{Ni}^{2+}$ centers in BaTiO_3 to ${}^{\text{VI}}\text{Ni}^{2+}$ in Ba–Al hollandite.^{23,24} The bandwidth of NIR emission (full width at half maximum, FWHM) reaches its maximum of about 353 nm when annealing at 750–850 °C. This is several times broader than the bandwidth of conventional Er^{3+} -doped glasses used as optical amplifiers for wavelength division multiplexing,³¹ and is comparable to previous findings in $(\text{Ga}_2\text{O}_3)_3(\text{GeO}_2)_2 : \text{Ni}^{2+}$ glass ceramics.⁵

The dependence of static spectroscopic properties on dopant concentration is shown in Fig. 7b for samples which were annealed at 850 °C for 2 hours. Emission as well as excitation intensity increase with dopant concentration to reach their maximum at a NiO content of about 0.1 mol%. Beyond this value, they drop significantly. In addition, with increasing NiO concentration, the NIR emission peak red-shifts significantly from 1365 nm to 1470 nm, while the dominant excitation peak blue-shifts from 366 nm to 347 nm. Both observations are related to an increasing extent of self-quenching with increasing total NiO content. Aside the previous comments, the observed intensity behaviour indicates concentration quenching for absolute NiO concentrations larger than 0.1 mol%. At this point, it must be noted that Ni^{2+} species do not completely precipitate in the crystal phase. A certain fraction must be assumed to remain as ${}^{\text{VI}}\text{Ni}^{2+}$ in the residual glass phase, although it cannot be detected by UV-VIS spectroscopy (Fig. 6). Considering the approximate crystal volume fraction (Fig. 5), structural properties of hollandite and especially the broad solid solubility, we may assume, however, that within the regime of comparably low NiO concentration we are considering here, partitioning occurs linearly with NiO concentration, and that the ratio between ${}^{\text{VI}}\text{Ni}^{2+}$ and ${}^{\text{V}}\text{Ni}^{2+}$ remains, on a high level, independent of the absolute amount of NiO.

It should be noted that NIR transmittance and, hence, photoemission may be affected significantly by the presence of water. Essentially dry raw materials were employed for glass preparation, but no further precautions were taken to avoid the incorporation of water during the melting process. This lets us expect a molar water content of several hundred ppm. In this concentration regime, water is present primarily in the form of hydroxyl ions (OH^-). Conformingly, the FTIR spectrum reveals the typical absorption band at about 2.7–2.8 μm which can be related to stretching vibrations of OH^- (inset II of Fig. 6a). Harmonics and overtones of this band occur, at around 1.4 μm , 1.25 μm and 0.95 μm . These could interfere directly with photoemission from ${}^{\text{VI}}\text{Ni}^{2+}$, especially in glass fiber. They, however, cannot be detected for the relatively low absorption path length as considered in the present case. We assume that a further increase in emission efficiency may be obtained when the water content of the material is specifically reduced.

Dynamic NIR photoluminescence

Fig. 8 represents luminescence decay curves of ${}^{\text{VI}}\text{Ni}^{2+}$ in TBSA glass ceramics for excitation of ${}^3\text{T}_1({}^3\text{P}) \rightarrow {}^3\text{A}_2({}^3\text{F})$. Within the examined regime of dopant concentration, best fit of the experimental data is obtained by a third-order exponential decay equation (inset). This reflects an overlay of two fast (τ_{fast}) and one slow (τ_{slow}) decay processes, and suggests the presence of

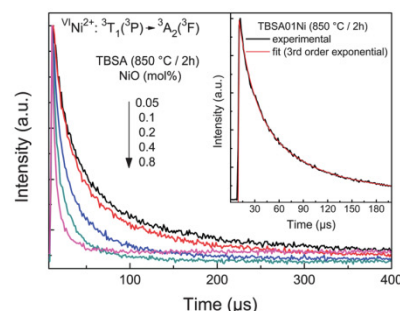


Fig. 8 Luminescence decay curves of Ni^{2+} -doped TBSA glass ceramics (annealed at 850 °C/2 h; monitoring photoemission at 1370 nm after excitation at 370 nm) for various Ni^{2+} -concentrations (labels). The inset exemplarily represents the fit of a third-order exponential function to the decay curve of TBSA01Ni/850 °C/2 h.

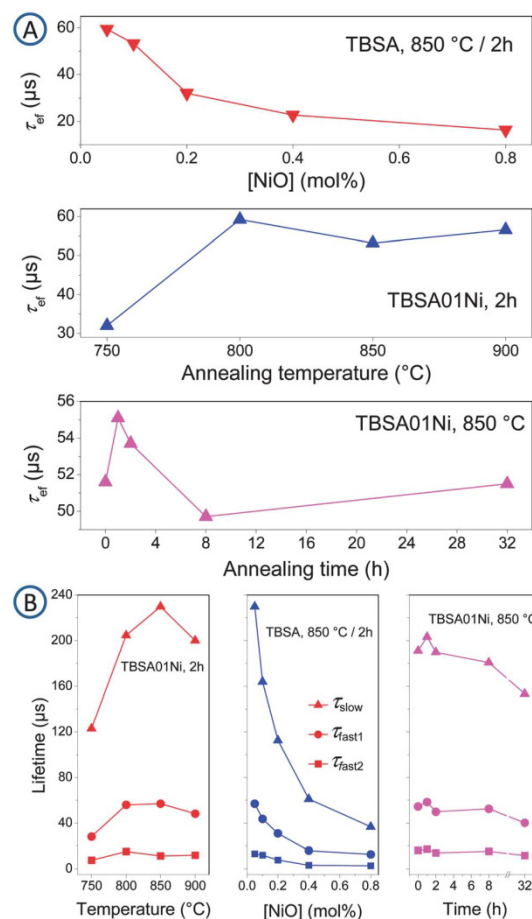


Fig. 9 Effective fluorescence lifetime (a) and deconvoluted lifetimes for the three individual decay processes (b) as a function of dopant concentration, annealing time and annealing temperature.

three different ${}^{\text{VI}}\text{Ni}^{2+}$ species, consistent with previous arguments. Lifetime values were obtained from the best fit. The effective lifetime τ_{ef} is the time after which the emission intensity decreases to $1/e$ of its initial value. Data on τ_{ef} are summarized in Fig. 9a. In summary, τ_{ef} reaches its maximum value for annealing at 800 °C and remains unchanged for higher annealing temperature. It further reaches a maximum for a NiO content of 0.05 mol% and decreases strongly with increasing dopant concentration. There is no clear trend in the dependence on annealing time, although it appears that the optimal annealing time is in the range of 1–2 h. Deconvoluting the data into the three individual decay processes reveals exactly the same trend (Fig. 9b). Generally, the excited state lifetime reflects the probability of (fast) non-radiative decay. Longer lifetime hence indicates higher quantum efficiency, whereas shorter lifetime indicates quenching. In accordance with static emission data as well as structural considerations, we can therefore conclude that there are three ${}^{\text{VI}}\text{Ni}^{2+}$ emission centers in the material, that these emission centers are subject to approximately the same quantitative quenching effects, and that the optimal quantum efficiency is obtained for an absolute NiO concentration of 0.05–0.1 mol% in TBSA after annealing for 1–2 h at 800–850 °C. Higher NiO concentration, higher annealing temperature and longer annealing time lead to increasing interaction between ${}^{\text{VI}}\text{Ni}^{2+}$, the surrounding lattice and neighboring Ni^{2+} species,¹⁸ respectively. The slow decay process ($\tau_{\text{slow}} \approx 230 \mu\text{s}$) is similar to that of the NIR luminescence decay in $(\text{Ga}_2\text{O}_3)_3(\text{GeO}_2)_2:\text{Ni}^{2+}$ glass ceramics ($\tau \approx 254 \mu\text{s}$),⁵ interestingly even when exciting with a UV light source at 365 nm. This means that NIR luminescence can be initiated with near-ultraviolet LED chips with emissions at 350–420 nm.²¹

Conclusions

In summary, we have demonstrated precipitation of nano-crystalline Ba–Al titanates from supercooled $\text{TiO}_2\text{–BaO–SiO}_2\text{–Al}_2\text{O}_3\text{–NiO}$ melts. Volume crystallization occurs sequentially in BaTiO_3 and Ba–Al hollandite-type crystallites, where NiO facilitates crystal nucleation and growth. The typical crystallite size is ~ 30 nm. During crystallization, Ni^{2+} species undergo a coordination change from fivefold to sixfold. This is caused by incorporation of Ni^{2+} into the crystalline environment on three distinct octahedral lattice sites. Resulting photoluminescence due to spin-allowed relaxation of ${}^3\text{T}_{2g}({}^3\text{F})$ to ${}^3\text{A}_{2g}({}^3\text{F})$ in ${}^{\text{VI}}\text{Ni}^{2+}$ accordingly occurs from three distinct emission centers. It spans the spectral range of 1.0 to 1.6 μm and exhibits an effective lifetime of about 60 μs and FWHM of ~ 350 nm, suggesting applications in tunable lasers and broadband optical amplifiers. Interestingly, NIR emission can be excited with conventional NUV light sources, i.e. in the spectral regime of 350–420 nm. Decay kinetics, and position and shape of the emission band can be adjusted by dopant concentration and synthesis conditions. Optimal luminescence efficiency is found for an absolute NiO concentration of 0.05–0.1 mol% and crystallization at 800–850 °C for 1–2 h. The onset of crystallization was observed at ~ 750 °C.

Acknowledgements

The authors gratefully acknowledge financial support by the Deutsche Forschungsgemeinschaft (DFG) through the Cluster of Excellence “Engineering of Advanced Materials—EAM” and the Chinese Fundamental Research Fund for the Central Universities (grant no. 2011ZZ0001).

References

- C. Batchelor, W. J. Chung, S. Shen and A. Jha, *Appl. Phys. Lett.*, 2003, **82**, 4035–4037.
- N. V. Kuleshov, V. P. Mikhailov, V. G. Scherbitsky, P. V. Prokoshin and K. V. Yumashev, *J. Lumin.*, 1993, **55**, 265–269.
- B. N. Samson, L. R. Pinckney, J. Wang, G. H. Beall and N. F. Borrelli, *Opt. Lett.*, 2002, **27**, 1309–1311.
- T. Suzuki, G. S. Murugan and Y. Ohishi, *Appl. Phys. Lett.*, 2005, **86**, 131903–131904.
- S. Zhou, N. Jiang, B. Wu, J. Hao and J. Qiu, *Adv. Funct. Mater.*, 2009, **19**, 2081–2088.
- H. Shigemura, M. Shojiya, R. Kanno, Y. Kawamoto, K. Kadono and M. Takahashi, *J. Phys. Chem. B*, 1998, **102**, 1920–1925.
- D. Deng, H. Ma, S. Xu, Q. Wang, L. Huang, S. Zhao, H. Wang and C. Li, *J. Non-Cryst. Solids*, 2011, **357**, 1426–1429.
- S. Khonthon, S. Morimoto and Y. Ohishi, *J. Solid Mech. Mater. Eng.*, 2007, **1**, 439–446.
- B. Wu, J. Ruan, J. Ren, D. Chen, C. Zhu, S. Zhou and J. Qiu, *Appl. Phys. Lett.*, 2008, **92**, 041110–041113.
- S. Zhou, G. Feng, B. Wu, N. Jiang, S. Xu and J. Qiu, *J. Phys. Chem. C*, 2007, **111**, 7335–7338.
- B. Wu, S. Zhou, J. Ruan, Y. Qiao, D. Chen, C. Zhu and J. Qiu, *Opt. Express*, 2008, **16**, 2508–2513.
- T. C. Brunold, H. U. Gudel and E. Cavalli, *Chem. Phys. Lett.*, 1996, **252**, 112–120.
- C. Jiang, *Opt. Express*, 2009, **17**, 6759–6769.
- H.-T. Sun, F. Shimaoka, J. Ruan, Y. Miwa, M. Fujii, J. Qiu, M. Mizuhata, S. Deki and S. Hayashi, *J. Non-Cryst. Solids*, 2009, **355**, 2425–2428.
- T. Suzuki, Y. Arai and Y. Ohishi, *J. Lumin.*, 2008, **128**, 603–609.
- G. Gao, S. Reibstein, M. Peng and L. Wondraczek, *Phys. Chem. Glasses: Eur. J. Glass Sci. Technol. B*, 2011, **52**(2), 59–63.
- G. Gao, N. Da, S. Reibstein and L. Wondraczek, *Opt. Express*, 2010, **18**, A575–A583.
- G. Gao, R. Meszaros, M. Peng and L. Wondraczek, *Opt. Express*, 2011, **19**, A312–A318.
- G. Gao, S. Reibstein, M. Peng and L. Wondraczek, *J. Mater. Chem.*, 2011, **21**, 3156–3161.
- S. F. Zhou, N. Jiang, K. Miura, S. Tanabe, M. Shimizu, M. Sakakura, Y. Shimotsuna, M. Nishi, J. R. Qiu and K. Hirao, *J. Am. Chem. Soc.*, 2010, **132**, 17945–17952.
- S. Yuan, Y. Yang, X. Zhang, F. Tessier, F. Cheviré, J.-L. Adam, B. Moine and G. Chen, *Opt. Lett.*, 2008, **33**, 2865–2867.
- A. E. Ringwood, S. E. Kesson, N. G. Ware, W. Hibberson and A. Major, *Nature*, 1979, **278**, 219–223.
- G. H. Kwei, A. C. Lawson, S. J. L. Billinge and S. W. Cheong, *J. Phys. Chem.*, 1993, **97**, 2368–2377.
- R. Cheary, *Acta Crystallogr., Sect. B: Struct. Sci.*, 1987, **43**, 28–34.
- Y. Takéuchi, *Mineral. J.*, 1958, **2**, 311–332.
- R. Shannon, *Acta Crystallogr., Sect. A: Cryst. Phys., Diffr., Theor. Gen. Crystallogr.*, 1976, **32**, 751–767.
- M. Y. Peng, B. Sprenger, M. A. Schmidt, H. G. L. Schwefel and L. Wondraczek, *Opt. Express*, 2010, **18**, 12852–12863.
- M. T. Buscaglia, V. Buscaglia, M. Viviani, P. Nanni and M. Hanuskova, *J. Eur. Ceram. Soc.*, 2000, **20**, 1997–2007.
- N. Da, M. Y. Peng, S. Krolkowski and L. Wondraczek, *Opt. Express*, 2010, **18**, 2549–2557.
- S. Zhou, N. Jiang, H. Dong, H. Zeng, J. Hao and J. Qiu, *Nanotechnology*, 2008, **19**, 015702.
- J. Yang, S. Dai, Y. Zhou, L. Wen, L. Hu and Z. Jiang, *J. Appl. Phys.*, 2003, **93**, 977–983.

2.6. Temperature dependence and quantum efficiency of ultrabroad NIR photoluminescence from Ni²⁺ centers in nanocrystalline Ba–Al titanate glass ceramics

From the former paper, the optimal sample for the broadband NIR PL of ^{VI}Ni²⁺ is TBSA glass doped with 0.1 mol% Ni²⁺ and crystallized at 850 °C for 32 hrs. The low temperature static and dynamic emission properties are performed on the optimal sample. From these data, η_{IQE} , stimulated emission cross-section, σ_{em} , and practical figure of merit, $\sigma_{\text{em}}^* \tau$, are calculated.

G. Gao, M. Peng and L. Wondraczek, *Opt. Lett.* 2012, **37**, 1166–1168. -Reproduced by permission of The Optical Society of America.

<http://www.opticsinfobase.org/ol/abstract.cfm?uri=ol-37-7-1166>

Temperature dependence and quantum efficiency of ultrabroad NIR photoluminescence from Ni²⁺ centers in nanocrystalline Ba-Al titanate glass ceramics

Guojun Gao,¹ Mingying Peng,² and Lothar Wondraczek^{1,*}

¹Department of Materials Science, University of Erlangen-Nuremberg, Erlangen 91058, Germany

²Institute of Optical Communication Materials & State Key Laboratory of Luminescent Materials and Devices, South China University of Technology, Guangzhou 510641, China

*Corresponding author: lothar.wondraczek@ww.uni-erlangen.de

Received January 19, 2012; revised January 25, 2012; accepted January 25, 2012;
posted January 27, 2012 (Doc. ID 161633); published March 23, 2012

Ultrabroad near-infrared (NIR) photoluminescence from Ni²⁺-centers in nanocrystalline Ba-Al titanate glass ceramics was studied by temperature-dependent static and dynamic photoluminescence spectroscopy in the regime of 10 to 300 K. Photoluminescence covers the spectral range of about 1100 nm to >1600 nm with a typical bandwidth (FWHM) greater than 300 nm. For UV-LED excitation at 352 nm, an internal quantum efficiency of 65% is obtained. The excited state lifetime τ at room temperature is 39 μ s. The stimulated emission cross section σ_{em} is 8.5×10^{-20} cm², resulting in a practical figure of merit, $\sigma_{em} \tau$, of 3.3×10^{-24} cm²s at room temperature. These properties suggest suitability as a broadband gain medium for tunable lasers and optical amplifiers. © 2012 Optical Society of America

OCIS codes: 160.2540, 160.2750, 160.4670, 160.6990, 300.6280.

3d transition metal ions such as Ni²⁺, Co²⁺, and Cr⁴⁺ doped into inorganic matrices have been a subject of interest for many years due to their broadband near-infrared (NIR) photoluminescence (PL). In such materials, NIR PL arises from d-d transitions and is hence strongly dependent on ligand field and coordination [1–5]. While various efforts have been undertaken to make use of this property in next-generation broadband optical amplifiers for telecommunication and other applications, especially with Co²⁺ and Cr⁴⁺, any breakthrough has so far been prevented by difficulties in stabilizing the specific valence and coordination state in a suitable matrix material [1,2]. From a practical point of view, Ni²⁺ species seem the most promising choice to approach this problem. In an inorganic matrix, they may be present in three different coordination states, tetrahedral (fourfold, ^{IV}Ni²⁺), trigonal (fivefold, ^VNi²⁺) and octahedral (sixfold, ^{VI}Ni²⁺). Only ^{VI}Ni²⁺ has been known to provide efficient NIR emission [3–5]. Consequently, ^{VI}Ni²⁺-containing glass ceramics and single crystalline materials have drawn continuous attention over the last decade [3–5]. Of these two materials classes, glass ceramics, produced by controlled nucleation and crystallization of a suitable precursor glass, combine the advantages of glasses and crystalline materials: depending on viscosity and crystallization temperature of the precursor glass, they can be processed into optical fiber, and depending on the type of precipitated crystal species, high quantum efficiency (QE) can be obtained [6–8]. As a prerequisite, however, crystal precipitation must occur in sufficiently high number density to ensure very low crystallite size and, hence, high optical transparency. In this setting, the number of available matrix candidates has been limited to only a few systems, which typically rely on rare raw materials or exhibit major process limitations (such as high liquidus temperature and high dynamic fragility).

Recently, we reported on glasses of the type 30TiO₂-30BaO-30SiO₂-10Al₂O₃ (TBSA, mol%) as a new matrix candidate [9]. In this system, nanocrystalline hol-

landite-type (BaAl₂Ti₆O₁₆, secondary BaTiO₃) Ba-Al titanates can be precipitated at high number density and crystal sizes of ~ 30 nm \pm 10 nm. Upon crystallization, added Ni²⁺ species undergo a coordination change from fivefold to sixfold due to incorporation into the crystalline environment. This was demonstrated to result in an intense NIR PL emission band spanning the spectral range of 1.0 to 1.6 μ m with a full width at half maximum (FWHM) of ~ 350 nm. Interestingly, it was shown that NIR PL can be induced with conventional near-UV (NUV) LEDs or other light sources and does not require laser excitation. In the present letter, we report on quantitative efficiency of photoemission from this material as a prerequisite for application as a gain medium in optical amplifiers. QE is obtained on the basis of low temperature static and dynamic PL spectroscopy, and stimulated emission cross section (σ_{em}) and figure of merit ($\sigma_{em}\tau$) are calculated.

A slab of ~ 50 g of TBSA precursor glass with a dopant concentration of 0.1 mol% (expressed as NiO) was prepared by conventional melting and quenching [9]. Melting was performed at 1550 °C for 2 hrs in alumina crucibles under ambient atmosphere. The melt was then poured into a preheated graphite mould and annealed for 2 h at 500 °C. Specimen of 15 \times 15 \times 2 mm³ were cut from the obtained glass and polished to optical quality for spectroscopic analyses. Optimal conditions for transferring the precursor glass into a transparent nanocrystalline glass ceramic were found for annealing at 850 °C for 2 h (ambient atmosphere) [9].

Temperature-dependent analyses (10 to 300 K) were performed in a closed-cycle liquid helium cryostat. Static excitation and emission spectra were recorded through optical windows with a high-resolution spectrofluorometer (Edinburgh Instruments FLSP 920) equipped with a 450 W steady-state xenon lamp and a pulsed 60 W Xe flashlamp as excitation sources. Decay curves were obtained by time-correlated single photon counting (TCSPC). A nitrogen-cooled NIR photomultiplier tube

(Hamamatsu R5509-72) was used for NIR PL detection with a response width of 800 ps. Excitation curves were corrected over the lamp intensity with a silicon photodiode. Emission curves were corrected over the spectral response of the NIR-PMT detector. The refractive index of the sample at 632 nm was measured on an ellipsometer (EL X-02C).

In Fig. 1(a), NIR PL and photoluminescence excitation (PLE) spectra of the Ni^{2+} -doped TBSA glass ceramic are illustrated as a function of temperature. Excitation spectra were obtained by monitoring PL at 1430 nm. The obtained PLE spectra consist of two bands and a shoulder with maxima at 352, 665, and 465 nm, respectively, which are readily assigned to spin-allowed ${}^3T_1({}^3P) \rightarrow {}^3A_2({}^3F)$, ${}^3T_2({}^1D) \rightarrow {}^3A_2({}^3F)$, and spin-forbidden ${}^3T_1({}^3F) \rightarrow {}^3A_2({}^3F)$ transitions of Ni^{2+} ions on octahedral sites (${}^VI\text{Ni}^{2+}$). Position and shape of the excitation peaks remain unchanged with increasing temperature. The most intense excitation band [${}^3T_1({}^3P) \rightarrow {}^3A_2({}^3F)$] spans the spectral range of 300 to 450 nm. It matches well emission from NUV LED chips (e.g., 350–420 nm). These can therefore be used as excitation sources. NIR PL spectra were recorded for monochromatic excitation at 352 nm. The resulting spectrum is dominated by a broad emission band (1100 to >1600 nm) which peaks at ~ 1430 nm. The width of this band (FWHM) exceeds 300 nm ($\sim 1545 \text{ cm}^{-1}$). NIR PL is ascribed to the spin-allowed relaxation of ${}^3T_{2g}({}^3F) \rightarrow {}^3A_{2g}({}^3F)$ in ${}^VI\text{Ni}^{2+}$ and covers the complete telecommunication window (O–L bands, 1260–1625 nm). The intensity of the emission band decreases gradually with increasing temperature [Fig. 1(b)]. However, unlike the sharp intensity decrease that was previously observed in Ni^{2+} -doped silicate glass [10], the intensity at 300 K is still about 40% as strong as that at 10 K, indicating significantly less thermal quenching at room temperature. The shape of NIR PL spectra remains

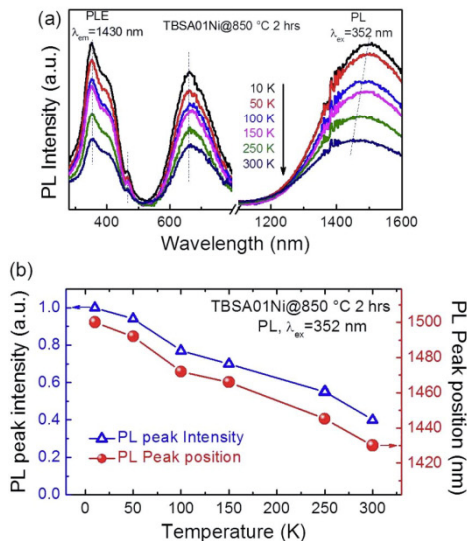


Fig. 1. (Color online) (a) Temperature-dependent NIR PL and PLE spectra of Ni^{2+} -doped TBSA glass ceramic. (b) Variation of band intensity, position, and shape as a function of temperature. Lines in (b) are guides for the eye.

practically unaffected by temperature, but a notable blue-shift occurs with increasing temperature, namely from about 1500 nm at 10 K to 1430 nm at 300 K [Fig. 1(b)]. Similar behavior was found in a $\text{Ni}^{2+}:\text{LiGa}_5\text{O}_8$ glass ceramic by Suzuki *et al.* [4]. Secondary features such as a zero-phonon line and phononic side bands could not be detected in the observed band structure, even at temperatures down to 10 K. This indicates the strong vibronic interaction in this system.

Normalized NIR PL decay data are shown in Fig. 2(a) as a function of temperature, recording emission intensity at 1430 nm after excitation at 352 nm. None of the decay curves appear to follow a single exponential equation, what confirms the interaction of at least two distinct ${}^VI\text{Ni}^{2+}$ emission centers [9]. The effective excited state lifetime $\tau_{1/e}$ (the time after which the emission intensity did decay to $1/e$ of its initial value) at 10 K was found at about 60 μs . Its value decreases with increasing temperature. With 39 μs at room temperature, however, it is still about 65% as compared to the value at 10 K. The decrease of PL lifetime at high temperature is primarily caused by temperature-dependent nonradiative relaxation of ${}^3T_{2g}({}^3F)$ to ${}^3A_{2g}({}^3F)$. The obtained lifetime at 300 K under NUV excitation is much longer than that of crystalline $\text{Cr}^{4+}:\text{Mg}_2\text{SiO}_4$ (3.87 μs) excited with a Nd:YAG 1.064 μm laser [2] but shorter than what has been observed in $\text{Ni}^{2+}:\text{LiGa}_5\text{O}_8$ glass ceramic (583 μs) excited with a 970 nm laser diode [4].

Figure 2(b) depicts NIR PL lifetime and internal QE (η) of Ni^{2+} -doped TBSA glass ceramic as a function of temperature. Experimental data were fit to a parabolic function and extrapolated to 0 K. From this extrapolation, a lifetime of about 60 μs was estimated for a temperature of

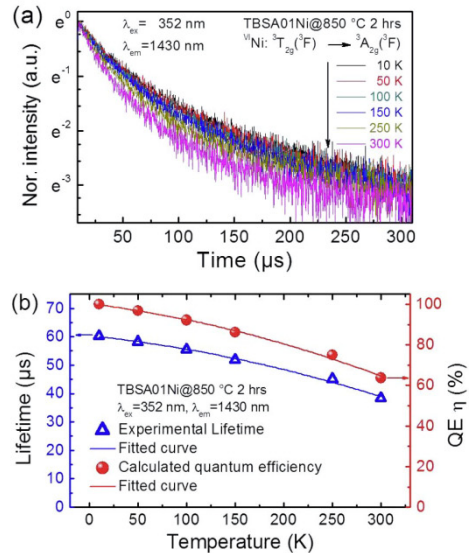


Fig. 2. (Color online) (a) Temperature-dependent NIR PL decay curves of Ni^{2+} -doped TBSA glass ceramic. (b) Variation of effective lifetimes of the excited state ($\tau_{1/e}$) and calculated internal QE (η) as a function of temperature, showing experimental (dotted line) and fitted (solid line, parabolic fit of experimental data) data.

5 K. Internal η of the NIR PL process at temperature $T = x$ was then obtained from $\eta_{T=x} = (\tau_x/\tau_{5\text{K}}) \times 100$, where τ_x is the experimental lifetime as obtained at temperature x and $\tau_{5\text{K}}$ is the extrapolated lifetime at 5 K [5]. For ambient temperature ($x = 300\text{ K}$), a value of $\eta = 65\%$ was obtained. This value significantly exceeds the one which has been observed previously in most other materials, such as $\text{Ni}^{2+}:\text{MgAl}_2\text{O}_4$ ($\eta = 20\%$) [11] and $\text{Ni}^{2+}:\text{Mg}_2\text{SiO}_4$ crystal ($\eta \sim 3\%$) [12]. It is also bigger than that of a $\text{Ni}^{2+}:\text{LiGa}_5\text{O}_8$ glass ceramic ($\eta \sim 60\%$) [4]. While the observed QE is still smaller than what has been found for $\text{Ni}^{2+}:\text{MgO}$ single crystals ($\eta \sim 80\%$) [13], the latter are not suitable for optical fiber production and, hence, would target different applications.

The stimulated emission cross section σ_{em} can be estimated with the Füchtbauer—Ladenburg equation by assuming a Gaussian-shaped emission band of FWHM $\Delta\nu_{1/2}$:

$$\sigma_{\text{em}} = \frac{\lambda_0^2 \eta}{4\pi c n^2 \tau \Delta\nu_{1/2}} \times \left(\frac{\ln 2}{\pi} \right)^{1/2}, \quad (1)$$

where λ_0 is the wavelength at band center, n is the refractive index of the host material, τ is the emission lifetime, and η is the quantum efficiency. For a band center at 1430 nm, a value of $8.5 \times 10^{-20}\text{ cm}^2$ (300 K, $\eta = 65\%$, $\tau = 39\text{ }\mu\text{s}$, $n = 1.8 \pm 0.02$, and $\Delta\nu_{1/2} = 1545\text{ cm}^{-1}$) is obtained. The product of σ_{em} and τ is considered as a figure of merit when characterizing the potential of prospective laser materials. This is because it is proportional to the amplification gain and inverse laser oscillation threshold. So, the higher the value of $\sigma_{\text{em}} * \tau$, the more interesting would be potential application as laser gain medium [14]. In the present case, a value of $3.3 \times 10^{-24}\text{ cm}^2\text{ s}$ is obtained (300 K). This compares to typical data of glasses and glass ceramics that have been considered for similar applications, such as $\text{Ni}^{2+}:\text{LiGa}_5\text{O}_8$ glass ceramic ($3.7 \times 10^{-24}\text{ cm}^2\text{ s}$) [4], Pr^{3+} -doped chalcogenide glasses ($4.8 \times 10^{-24}\text{ cm}^2\text{ s}$) [15], and $\text{Ti}^{3+}:\text{Al}_2\text{O}_3$ crystals ($1.4 \times 10^{-24}\text{ cm}^2\text{ s}$) [16], and Tm^{3+} -doped heavy metal oxide glasses ($\sim 9 \times 10^{-25}\text{ cm}^2\text{ s}$) [17]. The high value of $\sigma_{\text{em}} * \tau$ promises large amplification gain and low oscillation threshold, and hence suggests further studies with the objective of application of Ni^{2+} -doped TBSA glass ceramics as a broadband gain medium for tunable lasers and amplifiers.

In summary, we reported on highly efficient NIR PL from Ni^{2+} -doped nanocrystalline Ba-Al titanate glass

ceramics. The excited state lifetime of ${}^{\text{VI}}\text{Ni}^{2+}$ [${}^3\text{T}_{2g}({}^3\text{F})$] was found at $60\text{ }\mu\text{s}$ at 10 K and $39\text{ }\mu\text{s}$ at 300 K, from which an internal QE of $\sim 65\%$ at room temperature was calculated. The stimulated emission cross section (σ_{em}) and figure of merit for an optical gain medium ($\sigma_{\text{em}} * \tau$) were found at $8.5 \times 10^{-20}\text{ cm}^2$ and $3.3 \times 10^{-24}\text{ cm}^2\text{ s}$, respectively.

The authors gratefully acknowledge financial support by the Deutsche Forschungsgemeinschaft (DFG) through the Cluster of Excellence “Engineering of Advanced Materials,” and by the Chinese Fundamental Research Fund for Central Universities (grant no. 2011ZZ0001).

References

1. T. C. Brunold, H. U. Gudel, and E. Cavalli, *Chem. Phys. Lett.* **252**, 112 (1996).
2. A. Semnaroglu and B. Pekerten, *Opt. Lett.* **23**, 361 (1998).
3. S. Zhou, N. Jiang, K. Miura, S. Tanabe, M. Shimizu, M. Sakakura, Y. Shimotsuma, M. Nishi, J. Qiu, and K. Hirao, *J. Am. Chem. Soc.* **132**, 17945 (2010).
4. T. Suzuki, G. S. Murugan, and Y. Ohishi, *Appl. Phys. Lett.* **86**, 131903 (2005).
5. S. Zhou, H. Dong, G. Feng, B. Wu, H. Zeng, and J. Qiu, *Opt. Express* **15**, 5477 (2007).
6. G. Gao, N. Da, S. Reibstein, and L. Wondraczek, *Opt. Express* **18**, A575 (2010).
7. G. Gao, R. Meszaros, M. Peng, and L. Wondraczek, *Opt. Express* **19**, A312 (2011).
8. G. Gao, S. Reibstein, M. Peng, and L. Wondraczek, *J. Mater. Chem.* **21**, 3156 (2011).
9. G. Gao, S. Reibstein, E. Spiecker, M. Peng, and L. Wondraczek, *J. Mater. Chem.* **22**, 2582 (2012).
10. T. Suzuki and Y. Ohishi, *Appl. Phys. Lett.* **84**, 3804 (2004).
11. N. V. Kuleshov, V. G. Shcherbitsky, V. P. Mikhailov, S. Kück, J. Koetke, K. Petermann, and G. Huber, *J. Lumin.* **71**, 265 (1997).
12. G. Walker, B. Kamaluddin, T. J. Glynn, and R. Sherlock, *J. Lumin.* **60**, 123 (1994).
13. M. V. Iverson, J. C. Windscheif, and W. A. Sibley, *Appl. Phys. Lett.* **36**, 183 (1980).
14. J. H. Song, J. Heo, and S. H. Park, *J. Appl. Phys.* **93**, 9441 (2003).
15. K. Wei, D. P. Machewirth, J. Wenzel, E. Snitzer, and G. H. Sigel, *J. Non-Cryst. Solids* **182**, 257 (1995).
16. P. Albers, E. Stark, and G. Huber, *J. Opt. Soc. Am. B* **3**, 134 (1986).
17. D. Shi, Y. Zhao, Q. Qian, D. Chen, and Q. Zhang, *J. Alloys Compd.* **499**, 126 (2010).

2.7. Near-infrared downconversion in Pr³⁺/Yb³⁺ co-doped borosilicates glasses and LaBO₃ glass ceramics

Pr³⁺ ions act as sensitizers by absorbing 415–505 nm photons and transferring the absorbed energy to Yb³⁺ ions in a cooperative down-conversion process resulting in NIR emission at ~1000 nm. After crystallization, both Pr³⁺ and Yb³⁺ ions occupy the La³⁺ ion sites in the LaBO₃ crystal structure resulting in the improved PL properties.

G. Gao and L. Wondraczek, *Opt. Mater. Express* 2013, **3**, 633–644. -Reproduced by permission of The Optical Society of America.

<http://www.opticsinfobase.org/ome/abstract.cfm?uri=ome-3-5-633>

Near-infrared downconversion in Pr³⁺/Yb³⁺ co-doped boro-aluminosilicate glasses and LaBO₃ glass ceramics

Guojun Gao and Lothar Wondraczek*

Otto-Schott-Institute, University of Jena, 07743 Jena, Germany

*lothar.wondraczek@uni-jena.de

Abstract: We report on downconversion of one blue photon to two near-infrared (NIR) photons ($\sim 10000\text{ cm}^{-1}$) in Pr³⁺/Yb³⁺ co-doped SrO-La₂O₃-Al₂O₃-B₂O₃-SiO₂ glasses and LaBO₃ glass ceramics. The Pr³⁺ ions act as broadband spectral sensitizer in the spectral range of 415-505 nm. Energy transfer occurs subsequently from Pr³⁺ to Yb³⁺, followed by re-emission in the NIR spectral range. The transfer efficiency is indicated by the degree of decrease of Pr³⁺-related photoluminescence (PL) and PL lifetime of the ³P₀ and ¹D₂ levels with increasing Yb³⁺ concentration. For the present case, we find an optimum dopant concentration of Yb₂O₃ of ~ 0.5 mol % for a Pr₂O₃ concentration of 1.0 mol %. A theoretical maximum of quantum efficiency of 183% is reached for 5 mol % of Yb₂O₃. PL characteristics (absorption cross section and emission lifetime) are further improved upon precipitation of crystalline LaBO₃, where both Pr³⁺ and Yb³⁺ ions occupy La³⁺ sites with an assumedly statistical distribution and a high degree of partitioning.

© 2013 Optical Society of America

OCIS codes: (160.4670) Optical materials; (160.5690) Rare-earth-doped materials; (160.2540) Fluorescent and luminescent materials; (160.2750) Glass and other amorphous materials.

References and links

1. M. A. Green, K. Emery, Y. Hishikawa, W. Warta, and E. D. Dunlop, "Solar cell efficiency tables (version 39)," *Prog. Photovolt. Res. Appl.* **20**(1), 12–20 (2012).
2. J. J. Eilers, D. Biner, J. T. van Wijngaarden, K. Krämer, H.-U. Güdel, and A. Meijerink, "Efficient visible to infrared quantum cutting through downconversion with the Er³⁺-Yb³⁺ couple in Cs₃Y₂Br₉," *Appl. Phys. Lett.* **96**, 151106 (2010).
3. G. Gao and L. Wondraczek, "Near-infrared downconversion in Mn²⁺-Yb³⁺ co-doped Zn₂GeO₄," *J. Mater. Chem.* **1**(10), 1952–1958 (2013).
4. B. M. van der Ende, L. Aarts, and A. Meijerink, "Near-infrared quantum cutting for photovoltaics," *Adv. Mater.* **21**(30), 3073–3077 (2009).
5. B. M. van der Ende, L. Aarts, and A. Meijerink, "Lanthanide ions as spectral converters for solar cells," *Phys. Chem. Chem. Phys.* **11**(47), 11081–11095 (2009).
6. D. Chen, Y. Wang, Y. Yu, P. Huang, and F. Weng, "Near-infrared quantum cutting in transparent nanostructured glass ceramics," *Opt. Lett.* **33**(16), 1884–1886 (2008).
7. D. Yu, S. Ye, M. Peng, Q. Zhang, and L. Wondraczek, "Sequential three-step three-photon near-infrared quantum splitting in β -NaYF₄:Tm³⁺," *Appl. Phys. Lett.* **100**(19), 191911 (2012).
8. D. Yu, X. Huang, S. Ye, M. Peng, Q. Zhang, and L. Wondraczek, "Three-photon near-infrared quantum splitting in β -NaYF₄:Ho³⁺," *Appl. Phys. Lett.* **99**(16), 161904 (2011).
9. D. Yu, S. Ye, M. Peng, Q. Zhang, J. Qiu, J. Wang, and L. Wondraczek, "Efficient near-infrared downconversion in GdVO₄:Dy³⁺ phosphors for enhancing the photo-response of solar cells," *Sol. Energy Mater. Sol. Cells* **95**(7), 1590–1593 (2011).
10. S. Ye, J. Zhou, S. Wang, R. Hu, D. Wang, and J. Qiu, "Broadband downshifting luminescence in Cr³⁺-Yb³⁺ co-doped garnet for efficient photovoltaic generation," *Opt. Express* **21**(4), 4167–4173 (2013).
11. J. Zhou, Y. Teng, S. Ye, Y. Zhuang, and J. Qiu, "Enhanced downconversion luminescence by co-doping Ce³⁺ in Tb³⁺-Yb³⁺ doped borate glasses," *Chem. Phys. Lett.* **486**(4-6), 116–118 (2010).
12. S. Ye, N. Jiang, J. Zhou, D. Wang, and J. Qiu, "Optical property and energy transfer in the ZnO-LiYbO₂ hybrid phosphors under the indirect near-UV excitation," *J. Electrochem. Soc.* **159**(1), H11–H15 (2012).

13. J. Zhou, Y. Teng, X. Liu, S. Ye, Z. Ma, and J. Qiu, "Broadband spectral modification from visible light to near-infrared radiation using Ce³⁺-Er³⁺ co-doped yttrium aluminum garnet," *Phys. Chem. Chem. Phys.* **12**(41), 13759–13762 (2010).
14. J. de Wild, A. Meijerink, J. K. Rath, W. G. J. H. M. van Sark, and R. E. I. Schropp, "Upconverter solar cells: materials and applications," *Energy Environ. Sci.* **4**(12), 4835–4848 (2011).
15. H.-Q. Wang, M. Batentschuk, A. Osvet, I. Pinna, and C. J. Brabec, "Rare-earth ion-doped up conversion materials for photovoltaic applications," *Adv. Mater.* **23**(22-23), 2675–2680 (2011).
16. Z. Xia, Y. Luo, M. Guan, and L. Liao, "Near-infrared luminescence and energy transfer studies of LaOBr:Nd³⁺/Yb³⁺," *Opt. Express* **20**(Suppl 5), A722–A728 (2012).
17. M. Peng and L. Wondraczek, "Bismuth-doped oxide glasses as potential solar spectral converters and concentrators," *J. Mater. Chem.* **19**(5), 627–630 (2009).
18. B. S. Richards, "Enhancing the performance of silicon solar cells via the application of passive luminescence conversion layers," *Sol. Energy Mater. Sol. Cells* **90**(15), 2329–2337 (2006).
19. V. D. Rodríguez, V. K. Tikhomirov, J. Méndez-Ramos, A. C. Yanes, and V. V. Moshehalkov, "Towards broad range and highly efficient downconversion of solar spectrum by Er³⁺-Yb³⁺ co-doped nanostructured glass-ceramics," *Sol. Energy Mater. Sol. Cells* **94**(10), 1612–1617 (2010).
20. S. Ye, B. Zhu, J. Chen, J. Luo, and J. Qiu, "Infrared quantum cutting in Tb³⁺, Yb³⁺ co-doped transparent glass ceramics containing CaF₂ nanocrystals," *Appl. Phys. Lett.* **92**(14), 141112 (2008).
21. A. Guille, A. Pereira, C. Martinet, and B. Moine, "Quantum cutting in CaYAlO₄: Pr³⁺, Yb³⁺," *Opt. Lett.* **37**(12), 2280–2282 (2012).
22. Y. Xu, X. Zhang, S. Dai, B. Fan, H. Ma, J.-I. Adam, J. Ren, and G. Chen, "Efficient near-infrared downconversion in Pr³⁺-Yb³⁺ co-doped glasses and glass ceramics containing LaF₃ nanocrystals," *J. Phys. Chem. C* **115**(26), 13056–13062 (2011).
23. W. Höland and G. H. Beall, *Glass Ceramic Technology* (Am. Ceram. Soc., 2002).
24. W. Zhang, Q. Chen, J. Zhang, Q. Qian, Q. Zhang, and L. Wondraczek, "Enhanced NIR emission from nanocrystalline LaF₃:Ho³⁺ germanate glass ceramics for E-band optical amplification," *J. Alloy. Comp.* **541**, 323–327 (2012).
25. G. Gao, R. Meszaros, M. Peng, and L. Wondraczek, "Broadband UV-to-green photoconversion in V-doped lithium zinc silicate glasses and glass ceramics," *Opt. Express* **19**(Suppl 3), A312–A318 (2011).
26. G. Lakshminarayana and L. Wondraczek, "Photoluminescence and energy transfer in Tb³⁺/Mn²⁺ co-doped ZnAl₂O₄ glass ceramics," *J. Solid State Chem.* **184**(8), 1931–1938 (2011).
27. G. Gao, S. Reibstein, M. Peng, and L. Wondraczek, "Tunable dual-mode photoluminescence from nanocrystalline Eu-doped Li₂ZnSiO₄ glass ceramic phosphors," *J. Mater. Chem.* **21**(9), 3156–3161 (2011).
28. G. Gao, N. Da, S. Reibstein, and L. Wondraczek, "Enhanced photoluminescence from mixed-valence Eu-doped nanocrystalline silicate glass ceramics," *Opt. Express* **18**(Suppl 4), A575–A583 (2010).
29. K. L. Ley, M. Krumpelt, R. Kumar, J. H. Meiser, and I. Bloom, "Glass-ceramic sealants for solid oxide fuel cells: Par I. Physical properties," *J. Mater. Res.* **11**(06), 1489–1493 (1996).
30. R. Shannon, "Revised effective ionic radii and systematic studies of interatomic distances in halides and chalcogenides," *Acta Crystallogr. A* **32**(5), 751–767 (1976).
31. Q. Chen, W. Zhang, X. Huang, G. Dong, M. Peng, and Q. Zhang, "Efficient down- and up-conversion of Pr³⁺-Yb³⁺ co-doped transparent oxyfluoride glass ceramics," *J. Alloy. Comp.* **513**, 139–144 (2012).
32. D. K. Sardar and C. C. Russel III, "Optical transitions, absorption intensities, and inter-manifold emission cross section of Pr³⁺ (4I²) in Ca₅(PO₄)₃F crystal host," *J. Appl. Phys.* **95**(10), 5334–5339 (2004).
33. G. Gao, G. Wang, C. Yu, J. Zhang, and L. Hu, "Investigation of 2.0 μm emission in Tm³⁺ and Ho³⁺ co-doped oxyfluoride tellurite glass," *J. Lumin.* **129**(9), 1042–1047 (2009).
34. J. T. van Wijngaarden, S. Scheidelaar, T. J. H. Vlugt, M. F. Reid, and A. Meijerink, "Energy transfer mechanism for downconversion in the (Pr³⁺, Yb³⁺) couple," *Phys. Rev. B* **81**(15), 155112 (2010).
35. X. Chen, X. Huang, and Q. Zhang, "Concentration-dependent near-infrared quantum cutting in NaYF₄:Pr³⁺, Yb³⁺ phosphor," *J. Appl. Phys.* **106**(6), 063518 (2009).
36. E. van der Kolk, O. M. Ten Kate, J. W. Wiegman, D. Biner, and K. W. Krämer, "Enhanced ¹G₄ emission in NaLaF₄: Pr³⁺, Yb³⁺ and charge transfer in NaLaF₄: Ce³⁺, Yb³⁺ studied by Fourier transform luminescence spectroscopy," *Opt. Mater.* **33**(7), 1024–1027 (2011).
37. G. Gao, S. Reibstein, E. Spiecker, M. Peng, and L. Wondraczek, "Broadband NIR photoluminescence from Ni²⁺-doped nanocrystalline Ba–Al titanate glass ceramics," *J. Mater. Chem.* **22**(6), 2582–2588 (2012).
38. G. Gao, M. Peng, and L. Wondraczek, "Temperature dependence and quantum efficiency of ultra-broad NIR photoluminescence from Ni²⁺ centers in nanocrystalline Ba–Al titanate glass ceramics," *Opt. Lett.* **37**(7), 1166–1168 (2012).
39. G. Gao, S. Reibstein, M. Peng, and L. Wondraczek, "Dual-mode photoluminescence from nanocrystalline Mn²⁺-doped Li₂Zn-aluminosilicate glass ceramics," *Phys. Chem. Glasses* **52**, 59–63 (2011).
40. Q. Zhang, G. Yang, and Z. Jiang, "Cooperative downconversion in GdAl₃(BO₃)₄:RE³⁺, Yb³⁺ (RE = Pr, Tb, and Tm)," *Appl. Phys. Lett.* **91**(5), 051903 (2007).

41. A. Nakatsuka, O. Ohtaka, H. Arima, N. Nakayama, and T. Mizota, "Aragonite-type lanthanum orthoborate, LaBO₃," *Acta Crystallogr. Sect. E Struct. Rep. Online* **62**(4), i103–i105 (2006).
42. Y. Katayama and S. Tanabe, "Mechanism of quantum cutting in Pr³⁺-Yb³⁺ co-doped oxyfluoride glass ceramics," *J. Lumin.* **134**, 825–829 (2013).

1. Introduction

One of the reasons for the low theoretical quantum efficiency of silicon solar cells is related to the Shockley–Quaiasser limit, where due to the spectral mismatch between incident photons and the band-gap of crystalline silicon of ~1.1 eV, only about 32% of the solar spectrum can be used for the generation of photoelectrons. In addition, high energy photons are often lost due to recombination effects and/or active filtering to prevent photobleaching [1–3]. For these reasons, several ways have been explored to convert, by photoluminescence, parts of the solar spectrum to regions where the photovoltaic efficiency might be improved. These comprise three principle routes, i.e., downconversion [4–13] where a near-ultraviolet (NUV) to visible (Vis) photon is cut into two or more near infrared (NIR) photons, up-conversion [14,15], where the energy of two or three NIR photons is absorbed to emit one photon of higher energy, and down-shifting [16,17], where the energy of incident photons is shifted into wavelength regions which can be harvested more effectively. Downconversion provides the additional advantage that the energy loss due to the thermalization of hot charge carriers after absorption of a high-energy photon is minimized. A brief look at the solar irradiance spectrum reveals that, in principal, ~15% of excess energy, the UV-Vis part of the spectrum which would otherwise be lost as heat, is available for downconversion [18,19].

Considering the energy level of all lanthanides, Yb³⁺ has been recognized as the most suitable candidate for downconversion. That is, the Yb³⁺ ion has only a single excited state, ²F_{5/2} at ~10000 cm⁻¹, above the ground state of ²F_{7/2}. This means that Yb³⁺ centers may act as efficient recipients for energy quanta of ~10000 cm⁻¹ from any other co-dopant to emit photons with a wavelength of about ~1 μm [4,19]. To effectively sensitize Yb³⁺ to the UV-Vis spectral region, a donor ion with an energy level at ~20000 cm⁻¹ is necessary. For this, Pr³⁺, Er³⁺, Nd³⁺, Ho³⁺, Tm³⁺, Tb³⁺ or Ce³⁺ may be employed. In the present report, we focus on Pr³⁺ to sensitize Yb³⁺ because the absorption bands of Pr³⁺ cover a broad spectral window in the blue region due to the successive energy levels of Pr³⁺:³P_{J(J = 0, 1 and 2)} [Fig. 1(b)]. These absorption bands are located at approximately twice the band level of Yb³⁺:²F_{7/2} → ²F_{5/2} [20–22]. As host material, we chose a glass matrix which exhibits virtually universal forming capability and high compositional flexibility for well-controlled and homogeneous doping. To adjust the ligand symmetry and phonon energy, the glass composition may be selected so that in a subsequent annealing procedure, a crystalline species precipitates from the undercooled melt into which dopants are incorporated during crystallization [23–28]. Here we employ a glass of the composition 20 SrO-20 La₂O₃-10 Al₂O₃-40 B₂O₃-10 SiO₂ [29]. In this system, LaBO₃ crystallites can be precipitated by controlled nucleation in a heat treatment process. Due to the equivalent charge and similar ionic radii of La³⁺ (1.16 Å, CN = 8), Pr³⁺ (1.13 Å, CN = 8) and Yb³⁺ (0.99 Å, CN = 8), we expect that the dopant species can readily be incorporated into the lattice of crystalline LaBO₃ [30].

2. Experimental

Precursor glass samples with nominal composition (mol %) 20 SrO-(19-x) La₂O₃-10 Al₂O₃-40 B₂O₃-10 SiO₂-1 Pr₂O_{3-x} Yb₂O₃ (SLABS, x = 0, 0.1, 0.2, 0.5, 1, 2, and 5) were produced by conventional melting in alumina crucibles at 1400°C for 2 h (air). Glass slabs were obtained after pouring the melt into a preheated (500°C) graphite mold and subsequent annealing at 550°C for 2 h. From these slabs, disks of 20 × 20 × 3.0 mm³ were cut and polished on both sides. To obtain glass ceramic samples, individual specimen were placed on alumina substrates and isothermally annealed at 800°C for up to 32 h (air).

UV-VIS-NIR absorption spectra were recorded from 300 to 2500 nm with a double-beam photo-spectrometer equipped with a 150 mm integration sphere and a PbS detector (Perkin-Elmer Lambda 950). Static and dynamic photoluminescence (PL) were studied with a high-resolution spectrofluorometer and time correlated single photon counting (TCSPC, Horiba Jobin Yvon Fluorolog FL3-22) using a static Xe lamp (450 W) and a Xe flashlamp (75 W) as excitation sources. NIR PL was observed with a thermoelectrically cooled InP/InGaAs-based photomultiplier tube (Hamamatsu H10330A-75). Photoluminescence excitation (PLE) spectra were corrected over the lamp intensity with a silicon photodiode and PL spectra were corrected by the spectral response of the detector using correction spectra of the employed PMT. The crystallization process of each specimen was first analyzed by differential scanning calorimetry (DSC, Netzsch, Ar atmosphere) with a heating rate of 20 K min⁻¹. To identify the crystalline phases after heat treatment, X-ray diffractometry (XRD, Siemens Kristalloflex D500, Bragg-Brentano, 30 kV/30 mA, Cu K α) was performed with a step width of 0.02 $^\circ$ /s and a counting time of 10 s per step over the 2 θ range of 5-70 $^\circ$. All analyses were performed at room temperature.

3. Results and discussion

In Fig. 1 the effect of Yb₂O₃ concentration on optical absorption is shown. For Pr³⁺ singly doped SLABS glass, eight absorption peaks centered at 440, 471, 484, 591, 1003, 1416, 1515 and 1915 nm are ascribed to the inhomogeneously broadened 4f-4f transitions from the ground state ³H₄ to the excited states ³P₂, ³P₁, ³P₀, ¹D₂, ¹G₄, ³F₄, ³F₃ and ³F₂ of Pr³⁺ (labels in Fig. 1) [31]. As mentioned in the introduction section, three relatively strong and overlapping absorption bands (³H₄ → ³P_{1,2,3}) cover a large part of the blue wavelength range of 415-505 nm. For the Pr³⁺/Yb³⁺ co-doped samples, the additional absorption band with a maximum at 976 nm and a shoulder peak at ~935 nm is assigned to the transition from the ground state of Yb³⁺, ²F_{7/2}, to two different Stark levels of the excited state of ²F_{5/2}. As expected, the intensity of this NIR absorption band of Yb³⁺ increases linearly with increasing Yb³⁺ doping concentration.

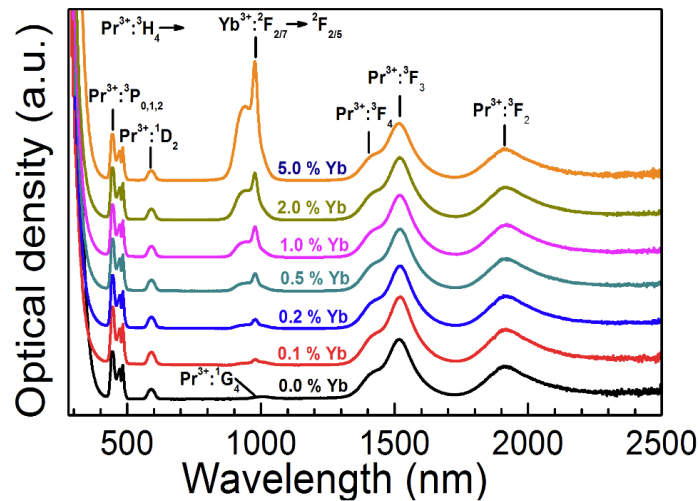


Fig. 1. Absorption spectra of the Pr³⁺/Yb³⁺ co-doped SLABS glasses dependent on Yb₂O₃ doping concentration.

Radiative transitions within the 4fⁿ configurations of trivalent rare earth ions can be predicted by the Judd-Ofelt (J-O) theory. The Judd-Ofelt parameters Ω_2 , Ω_4 and Ω_6 as obtained from the measured absorption spectra in Fig. 1 are calculated 1.10×10^{-20} , 1.06×10^{-20} and 0.87×10^{-20} cm² respectively [31–33]. Using these values, the radiative decay rate $A_{JJ'}$, the branching ratio $\beta_{JJ'}$ and the radiative emission lifetime τ_{rad} were estimated. Data are summarized in Table 1.

Table 1. Predicted Radiative Decay Rates ($A_{J,J'}$), Branching Ratio ($\beta_{J,J'}$) and Radiative Emission Lifetime (τ_{rad}) of Pr^{3+} in SLABS Glasses at 300 K

Transitions SLJ \rightarrow S'L'J'	Wavenumber (cm^{-1})	Wavelength (nm)	$A_{J,J'}$ (s^{-1})	$\beta_{J,J'}$
$^3\text{P}_0 \rightarrow ^1\text{D}_2$	3815	2621	2.67	0.00
$^1\text{G}_4$	10801	926	219.99	0.02
$^3\text{F}_4$	13789	725	881.50	0.09
$^3\text{F}_3$	14267	701	0	0
$^3\text{F}_2$	15562	642	3616.41	0.35
$^3\text{H}_6$	16516	605	802.18	0.08
$^3\text{H}_5$	18680	535	0	0
$^3\text{H}_4$	20747	482	4796.91	0.46
$A_{\text{T}}(^3\text{P}_0) = 10319.64 \text{ s}^{-1}$, $\tau_{\text{rad}}(^3\text{P}_0) = 66 \mu\text{s}$				
$^1\text{D}_2 \rightarrow ^1\text{G}_4$	6986	1431	88.76	0.10
$^3\text{F}_4$	9974	1003	400.35	0.43
$^3\text{F}_3$	10352	966	36.85	0.04
$^3\text{F}_2$	11747	851	105.51	0.11
$^3\text{H}_6$	12701	787	98.09	0.11
$^3\text{H}_5$	14865	673	5.15	0.01
$^3\text{H}_4$	16932	591	189.73	0.21
$A_{\text{T}}(^1\text{D}_2) = 924.43 \text{ s}^{-1}$, $\tau_{\text{rad}}(^1\text{D}_2) = 1081 \mu\text{s}$				
$^1\text{G}_4 \rightarrow ^3\text{F}_4$	2988	3347	4.64	0.02
$^3\text{F}_3$	3366	2971	0.66	0.00
$^3\text{F}_2$	4761	2100	0.77	0.00
$^3\text{H}_6$	5715	1750	46.48	0.22
$^3\text{H}_5$	9879	1012	155.79	0.72
$^3\text{H}_4$	9946	1005	9.73	0.04
$A_{\text{T}}(^1\text{D}_2) = 218.07 \text{ s}^{-1}$, $\tau_{\text{rad}}(^1\text{G}_4) = 4586 \mu\text{s}$				

PLE and PL spectra reveal direct evidence of energy transfer from Pr^{3+} to Yb^{3+} [Figs. 2(a)–2(d)]. Room temperature PLE spectra are shown for emission at 608 nm (Pr^{3+}) and 976 nm (Yb^{3+}), respectively. Consistent with the absorption spectra (Fig. 1), the PLE bands of Pr^{3+} comprise three characteristic peaks at 445, 471 and 483 nm, together with a relatively weak band at 591 nm. The former three bands exhibit similar intensity and strong overlap with each other, what lets expect a relatively high excitation efficiency in this spectral range. The PLE spectra of the $\text{Yb}^{3+}:^2\text{F}_{5/2} \rightarrow ^2\text{F}_{7/2}$ [Fig. 2(d)] are in full agreement with those of the Pr^{3+} -related PLE [Fig. 2(a)] and with the absorption spectra of Pr^{3+} (Fig. 1), what is taken as clear evidence for the sensitization of the Yb^{3+} emission center by Pr^{3+} donors in the NUV-Vis spectral range. In the following, the maximum PLE peak at 445 nm is selected to monitor the PL spectra as a function of Yb_2O_3 doping concentration.

The PL spectra of Pr^{3+} -related emission centers [Fig. 2(b)] consist of six characteristic bands which are located at 487, 530, 608, 646, 701 and 730 nm. Their designation is shown in the inset of Fig. 2(a) and labeled in Fig. 2(b) [34–36]. The PL spectra of all samples are dominated by the red band at ~ 608 nm which is attributed to the transition of $\text{Pr}^{3+}:^3\text{P}_0 \rightarrow ^3\text{H}_6$. The intensity of all bands of Pr^{3+} decreases gradually with increasing Yb^{3+} concentration over the whole range of observed concentrations [Figs. 2(b) and 2(c)]. Very sharp drop appears to occur in the sample with 5 mol% of Yb_2O_3 .

In Fig. 2(e), PL spectra of the NIR region are presented. For the Pr^{3+} singly-doped SLABS sample, the broad NIR PL band centered at ~ 1047 nm with a full width at half maximum (FWHM) of 73 nm and a shoulder centered at ~ 998 nm is ascribed to the transitions of $^1\text{D}_2 \rightarrow ^3\text{F}_4$ and $^1\text{D}_2 \rightarrow ^3\text{F}_3$ in Pr^{3+} , respectively. The relatively weak PL band at ~ 1475 nm is assigned to $^1\text{D}_2 \rightarrow ^1\text{G}_4$. The observation of three bands originating from $^1\text{D}_2$ implies that relaxation of the $^3\text{P}_{1,2,3}$ levels occurs via a multi-phonon relaxation to $^1\text{D}_2$. This indicates that $^1\text{D}_2$ is efficiently occupied [2]. After co-doping with a small amount of Yb^{3+} ($x = 0.1$), a sharp PL peak appears at 976 nm, accompanied by a broad shoulder at ~ 997 nm. These two bands are attributed to the transition of the lowest Stark level of $^2\text{F}_{5/2}$ in Yb^{3+} to two different Stark

levels of the ground state of ${}^2F_{7/2}$ [20]. The latter two overlap with the Pr^{3+} -related emission band at 1046 nm. To account for these three bands, all NIR PL spectra were deconvoluted into three Gaussian functions [Figs. 3(a)–3(f)]. Regarding the concentration of Yb^{3+} , the intensity of the emission bands at 976 and 997 nm increases for $x \leq 0.5$ and decreases sharply for higher amounts Yb^{3+} -doping. We conclude that this is caused by concentration quenching and that, in the present matrix material, $x = 0.5$ represents the optimal doping concentration. As already seen in the excitation spectra, also the decrease of the intensity of Pr^{3+} -related PL intensity after co-doping with a small amount of Yb^{3+} and the parallel occurrence of increasingly intense Yb^{3+} -related emission bands indicate energy transfer from Pr^{3+} to Yb^{3+} . Pr^{3+} acts as a sensitizer by absorbing NUV-Vis photons and partially transferring their energy to Yb^{3+} [Figs. 2(e) and 2(f)] [37–39]. Parallel to the intensity decrease of PL bands of Pr^{3+} in the visible range, also the PL intensity of $\text{Pr}^{3+}: {}^1D_2 \rightarrow {}^3F_4$ [1047 nm, Figs. 3(e) and 3(f)] and $\text{Pr}^{3+}: {}^1D_2 \rightarrow {}^1G_4$ [1475 nm, Fig. 2(e)] decrease gradually with increasing Yb^{3+} concentration. At the same time, the position of the $\text{Pr}^{3+}: {}^1D_2 \rightarrow {}^3F_3$ band red-shifts from 1047 to 1072 nm with increasing Yb^{3+} concentration [Fig. 3(e)], what is understood as another consequence of energy transfer from Pr^{3+} to Yb^{3+} .

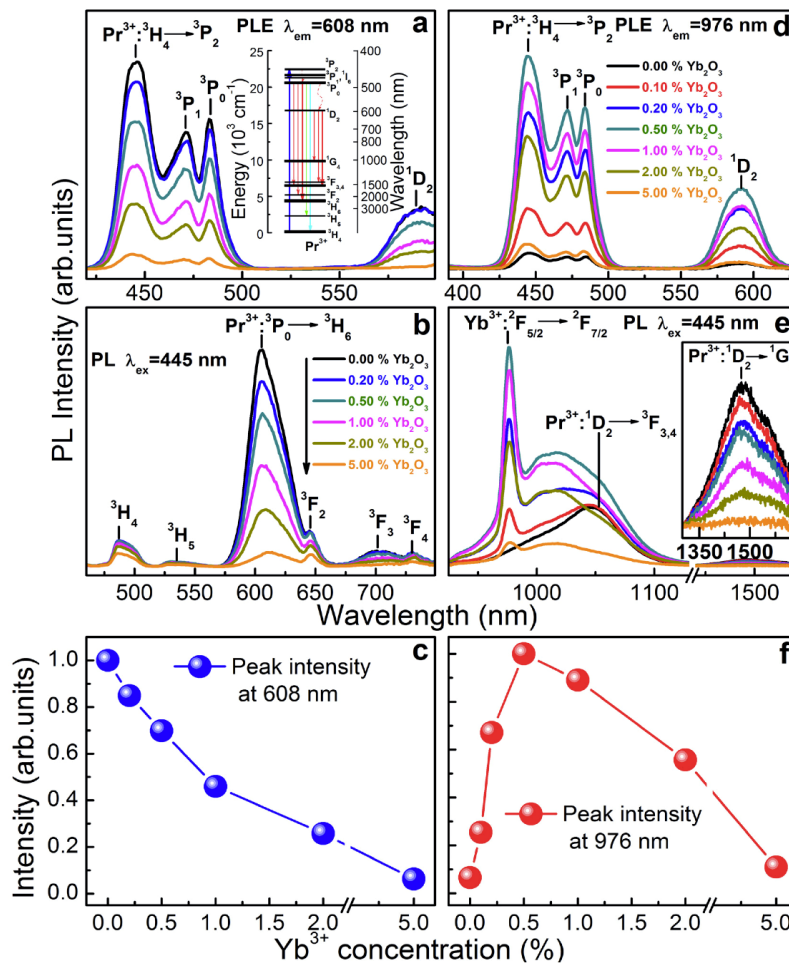


Fig. 2. Steady-state visible (a) PLE ($\lambda_{\text{em}} = 608$ nm) and (b) PL ($\lambda_{\text{exc}} = 445$ nm) spectra of Pr^{3+} , and NIR (d) PLE ($\lambda_{\text{exc}} = 976$ nm) and (e) PL ($\lambda_{\text{exc}} = 445$ nm) spectra of Yb^{3+} of the $\text{Pr}^{3+}/\text{Yb}^{3+}$ co-doped SLABS glasses as a function of Yb^{3+} doping concentration. (c) PL peak intensity of Pr^{3+} at 608 nm and (f) integrated PL intensity in the spectral range of 920–1200 nm as a function of Yb^{3+} doping concentration. Inset of (b): Energy levels of Pr^{3+} . Lines in (c) and (f) are guides for the eye.

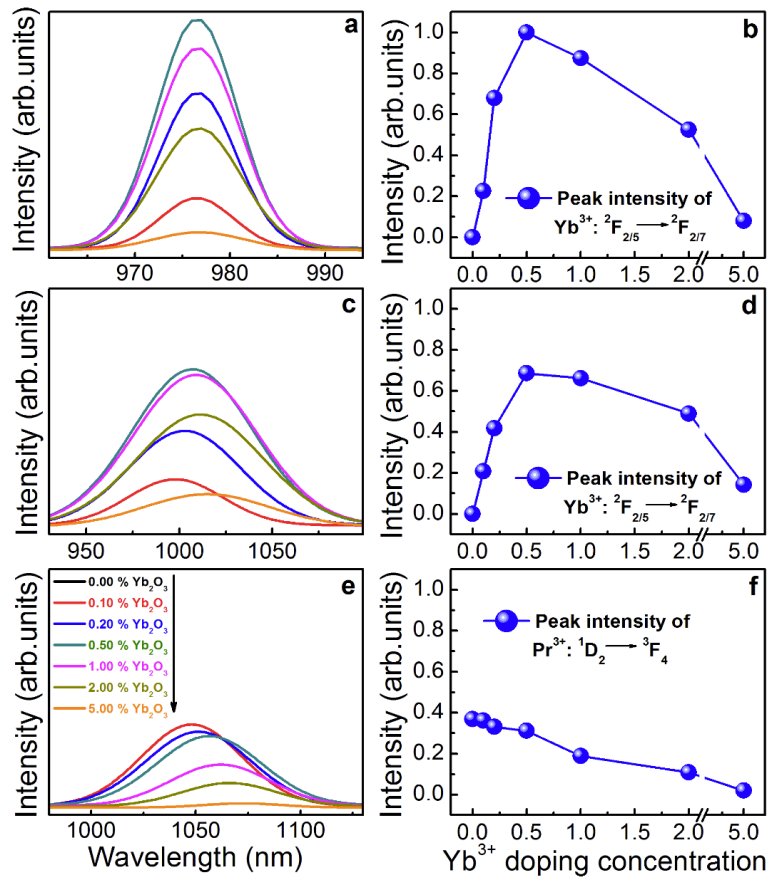


Fig. 3. Gaussian fitted PL spectra of the $\text{Pr}^{3+}/\text{Yb}^{3+}$ co-doped SLABS glasses in the NIR region as a function of Yb^{3+} doping concentration, (a) $\text{Yb}^{3+}: {}^2\text{F}_{7/2} \rightarrow {}^2\text{F}_{5/2}$ at 976 nm, (c) $\text{Yb}^{3+}: {}^2\text{F}_{7/2} \rightarrow {}^2\text{F}_{5/2}$ at 997 nm and (e) $\text{Pr}^{3+}: {}^1\text{D}_2 \rightarrow {}^3\text{F}_4$. (b), (d) and (f) corresponding PL intensity change of the $\text{Pr}^{3+}/\text{Yb}^{3+}$ co-doped SLABS glasses dependent on Yb_2O_3 doping concentration respectively. Lines in (b), (d) and (f) are guides for the eye.

Figures 4(a), 4(c), and 4(e) depict normalized PL decay curves for the Pr^{3+} -related transitions of ${}^3\text{P}_0 \rightarrow {}^3\text{H}_6$ (608 nm) and ${}^1\text{D}_2 \rightarrow {}^1\text{G}_4$ (1475 nm), and for the Yb^{3+} -related transition of ${}^2\text{F}_{5/2} \rightarrow {}^2\text{F}_{7/2}$ (976 nm) as a function of Yb^{3+} concentration after excitation at 445 nm. For $\text{Pr}^{3+}: {}^3\text{P}_0 \rightarrow {}^3\text{H}_6$, all decay curves exhibit multi-exponential behavior [Fig. 4(a)]. In the Pr^{3+} singly-doped sample, this may be due to cross-relaxation between Pr^{3+} ions, whereas in co-doped samples, this is caused by the increasingly faster depopulation of the $\text{Pr}^{3+}: {}^3\text{P}_0$ level due to energy transfer from ${}^3\text{P}_J$ of Pr^{3+} to ${}^2\text{F}_{5/2}$ of Yb^{3+} with increasing Yb^{3+} concentration [39]. The effective PL lifetime of the $\text{Pr}^{3+}: {}^3\text{P}_0$ state decreases from 7.2 to 1.2 μs when the Yb^{3+} concentration is increased to 5 mol % [Figs. 4(a) and 4(b)]. Similarly, also the effective PL lifetime of the $\text{Pr}^{3+}: {}^1\text{D}_2$ state decreases from 7.6 to 2.1 μs with increasing Yb^{3+} concentration [Figs. 4(c) and 4(d)]. This shows that both states contribute to the energy transfer process. The energy transfer from the ${}^3\text{P}_0$ level results in downconversion of one visible photon into two NIR photons whereas the energy transfer from the ${}^1\text{D}_2$ level results in down-shifting of one NIR photon into another NIR photon. A more detailed discussion will be presented in the following paragraphs. The energy transfer efficiency η_{ETE} is defined as the ratio between the number of depopulation events which result in energy transfer from donor to acceptor and the total population of the excited states in the donor. It can be calculated from the ratio of the lifetimes of the excited state(s) of the donor in the presence of the acceptor as compared to a specimen which contains only the donor species [6,38].

$$\eta_{ETE,x\%Yb} = 1 - \frac{\tau_{x\%Yb}}{\tau_{0\%Yb}} \quad (1)$$

Here, $\tau_{x\%Yb}$ is the lifetime a Pr^{3+} -related state after co-doping with x mol% Yb_2O_3 . For both levels, ${}^3\text{P}_0$ and ${}^1\text{D}_2$, the calculated values of η_{ET} increase with increasing Yb^{3+} concentration, i.e., from 11.5% and 9.8% for $x = 0.1$ to 83.0% and 88.1% for $x = 5.0$, respectively. The total theoretical quantum efficiency is then calculated as a function of Yb^{3+} concentration [6,40],

$$\eta = \eta_{\text{Pr}} (1 - \eta_{ETE,x\%Yb}) + 2\eta_{\text{Yb}}\eta_{ETE,x\%Yb} \quad (2)$$

where η_{Pr} and η_{Yb} are the quantum efficiencies for the Pr^{3+} and Yb^{3+} luminescence, respectively. To estimate the theoretical optimum, the latter two are set to unity. Then, if only the energy transfer from the ${}^3\text{P}_0$ level is considered, a total theoretical quantum efficiency of 183% is obtained for $x = 5.0$. This value is close to the upper limit of two-photon quantum cutting of 200%. The actual quantum efficiency, however, is significantly lower due to concentration quenching and other non-radiative decay processes.

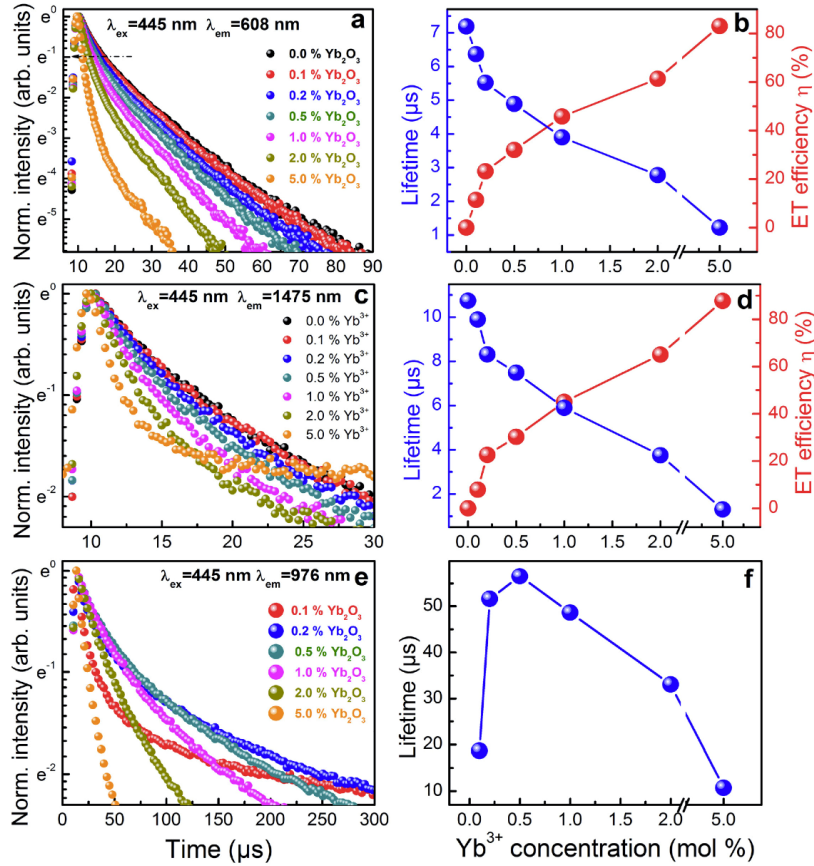


Fig. 4. (a) Normalized decay curves of the $\text{Pr}^{3+}/\text{Yb}^{3+}$ co-doped SLABS glasses dependent on Yb_2O_3 doping concentration under excitation at 445 nm by monitoring PL (a) at 608 nm ($\text{Pr}^{3+}: {}^3\text{P}_0 \rightarrow {}^3\text{H}_6$), (c) at 1475 nm ($\text{Pr}^{3+}: {}^1\text{D}_2 \rightarrow {}^1\text{G}_4$) and (e) at 976 nm ($\text{Yb}^{3+}: {}^2\text{F}_{5/2} \rightarrow {}^2\text{F}_{7/2}$). Yb^{3+} doping concentration dependent lifetimes of (b) Pr^{3+} PL at 608 nm, (d) Pr^{3+} PL at 1475 nm and (f) Yb^{3+} PL at 976 nm. Lines in (d), (e) and (f) are guides for the eye.

In agreement with the PL intensity change of $\text{Yb}^{3+}: {}^2\text{F}_{5/2} \rightarrow {}^2\text{F}_{7/2}$ (976 nm) upon Yb^{3+} concentration increase [Figs. 4(e) and 4(f)], also the effective lifetime of this emission band first increases up to $\sim 56.6 \mu\text{s}$ for $x = 0.5$ and subsequently decreases for higher x , i.e., to $10.7 \mu\text{s}$ for $x = 5.0$.

To evaluate the potential of further enhancement of the energy transfer efficiency, glass ceramic samples were considered where LaBO_3 crystallites were precipitated so that Pr^{3+} and Yb^{3+} are incorporated into the crystalline lattice on La^{3+} sites.

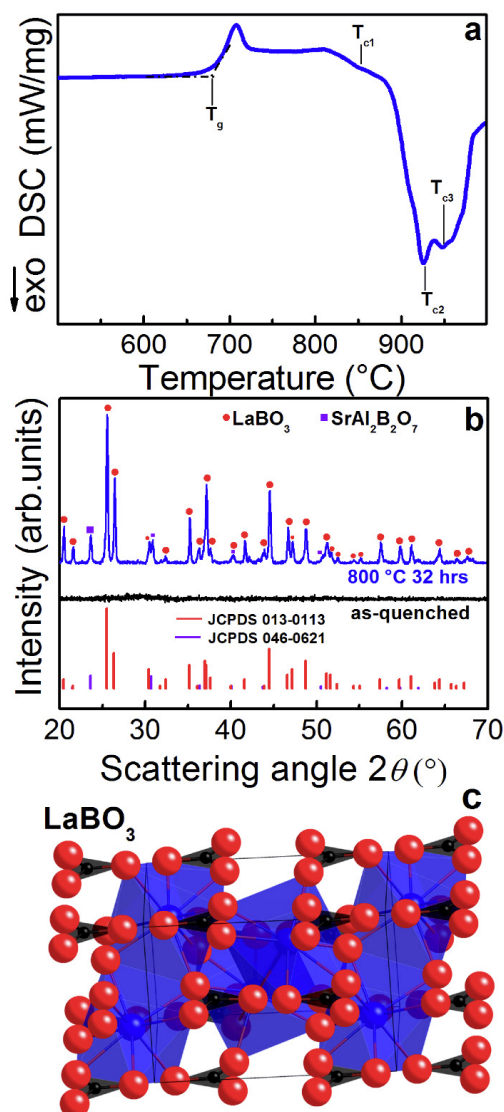


Fig. 5. (a) DSC curve of the SLABS glass sample. (b) *ex situ* XRD patterns of the $1\text{Pr}^{3+}/0.5\text{Yb}^{3+}$ co-doped SLABS glass and LaBO_3 glass ceramic annealed at 800 °C for 32 hrs. (c) Crystal structure of LaBO_3 . Blue, black and red full sphere illustrates La^{3+} , B^{3+} and O^{2+} respectively.

Figure 5(a) exemplarily shows a DSC curve of the SLABS glass sample with a heating rate of 20 K min^{-1} after baseline correction. The onset of glass transition T_g was observed at 679.5 ± 0.5 °C. Three crystallization peaks were found at 852, 926 and 948 ± 0.5 °C. Targeting the non-isothermal crystallization event at 852 °C, controlled crystallization was then performed isothermally at 800 °C for 32 h. XRD [Fig. 5(b)] of the untreated sample did not reveal any diffraction peaks, showing that the as-made glass was - within the accuracy of measurement - free of any crystalline phases. After thermal annealing, multiple intense diffraction peaks were found. These were indexed to the room-temperature orthorhombic phase of LaBO_3 (JCPDS card no. 00-013-0113). In addition, XRD patterns indicate the presence of at least one further, minor crystallite species which we assign as hexagonal $\text{SrAl}_2\text{B}_2\text{O}_7$ (JCPDS card no. 00-046-0621). For clarity, the tabulated diffraction patterns of both species are shown in Fig. 5(b). The lattice of LaBO_3 is illustrated in Fig. 5(c). It

comprises an orthorhombic aragonite-type structure and cell parameters of $a = 5.104 \text{ \AA}$, $b = 8.252 \text{ \AA}$, $c = 5.872 \text{ \AA}$, composed of LaO_9 polyhedra and BO_3 trigonal groups [41]. Due to the aforementioned similarity of ionic radii, Pr^{3+} and Yb^{3+} should readily be incorporated on La^{3+} -sites (for comparison, the radius of B^{3+} is about one third, i.e., 0.41 \AA , as compared to the three rare earth species) [30].

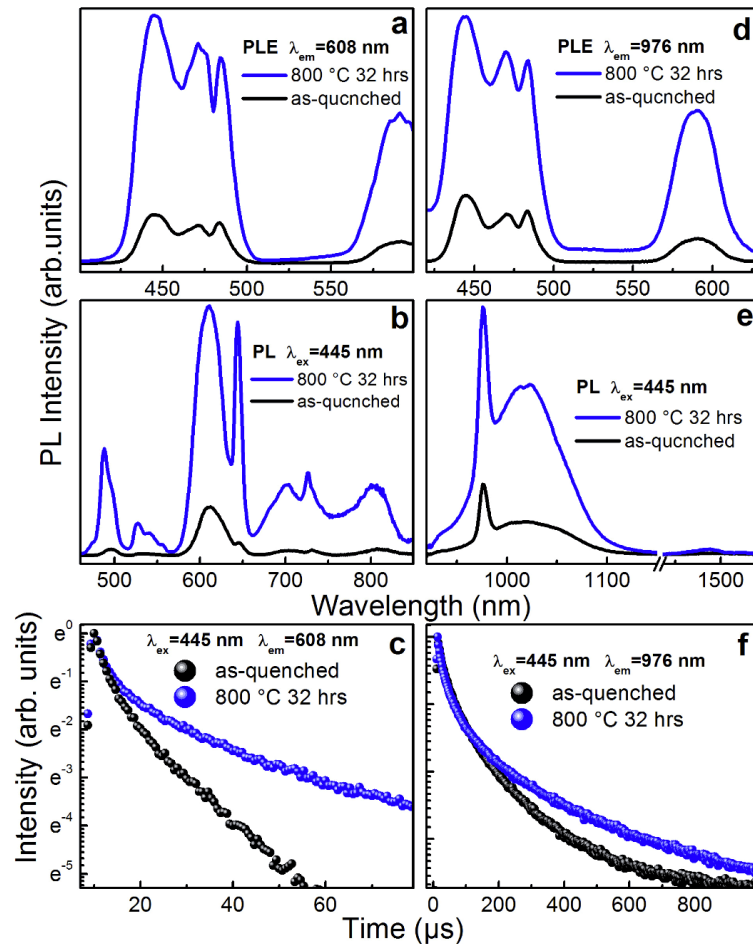


Fig. 6. Steady-state visible (a) PLE and (b) PL spectra of Pr^{3+} , and NIR (d) PLE and (e) PL spectra of Yb^{3+} of the $1\text{Pr}^{3+}/0.5\text{Yb}^{3+}$ co-doped SLABS glass and LaBO_3 glass ceramic annealed at $800 \text{ }^\circ\text{C}$ for 32 hrs. (c) Visible (Pr^{3+} PL at 608 nm ($^3\text{P}_0 \rightarrow ^3\text{H}_6$)) and (f) NIR (Yb^{3+} PL at 976 nm ($^2\text{F}_{5/2} \rightarrow ^2\text{F}_{7/2}$)) decay curves of the SLABS glass and glass ceramic annealed at $800 \text{ }^\circ\text{C}$ for 32 hrs excited at 445 nm monitoring PL at 608 nm of Pr^{3+} and 976 nm of Yb^{3+} respectively.

Figures 6(a) and 6(d) show PLE spectra (monitoring 608 nm PL from Pr^{3+} and 976 nm PL from Yb^{3+} , respectively) of the SLABS glass and glass ceramic for $x = 0.5$. After crystallization, the characteristic excitation bands of Pr^{3+} are clearly enhanced. Not surprisingly, annealing at elevated temperature leads to a great change in the PL spectra [Figs. 6(b) and 6(e)] and decay curves [Figs. 6(c) and 6(f)], as well. For Vis PL from Pr^{3+} [Fig. 6(b)], the peak intensity at 608 nm increased by a factor of ~ 5 after crystallization. Moreover, all PL bands apparently split and sharpen notably as a result of crystallization. The latter observations indicate that Pr^{3+} is indeed incorporated into the LaBO_3 crystal phase. A comparison of the decay curves of the $\text{Pr}^{3+}:^3\text{P}_0 \rightarrow ^3\text{H}_6$ PL band of the SLABS glass and the corresponding glass ceramic is shown in Fig. 6(c). Both curves can be best fit by second-order exponential equations, suggesting that in both cases a slow and a fast decay process contributes to PL. The lifetime values are obtained from the best fit. For both decay processes they increase after crystallization, i.e. from 2.4 to $7.1 \text{ } \mu\text{s}$ and from 11.9 to $52.3 \text{ } \mu\text{s}$, respectively. This is taken as further evidence for the incorporation of Pr^{3+} into the crystallite

phase. If Pr^{3+} is incorporated into the LaBO_3 lattice, we expect that Yb^{3+} would behave similarly. Otherwise, energy transfer between the two species would become highly unlikely due to their spatial and configurational separation. Examining the PL spectra of Yb^{3+} in the NIR range for the crystallized sample [Fig. 6(e)], a strongly enhanced intensity of the peak at 976 nm is visible as compared to the as-made glass. Additionally, the peak intensity ratio of the two peaks at 976 and 997 nm, I_{976}/I_{997} , decreases from 2.2 to 1.5 after crystallization. We attribute the latter observation to stronger Stark splitting of the ground state of Yb^{3+} , $^2\text{F}_{7/2}$, in the LaBO_3 crystalline environment. Analogous to the behavior in the as-made glass, and also similar to the behavior of Pr^{3+} in the LaBO_3 lattice, decay curves follow a second-order exponential equation [Fig. 6(f)]. After crystallization, the two resulting lifetime values increase from 28.7 to 35.3 μs and from 149.0 to 297.3 μs , respectively, for the fast and for the slow decay process. From these observations, we conclude that also Yb^{3+} is incorporated into the crystallite phase.

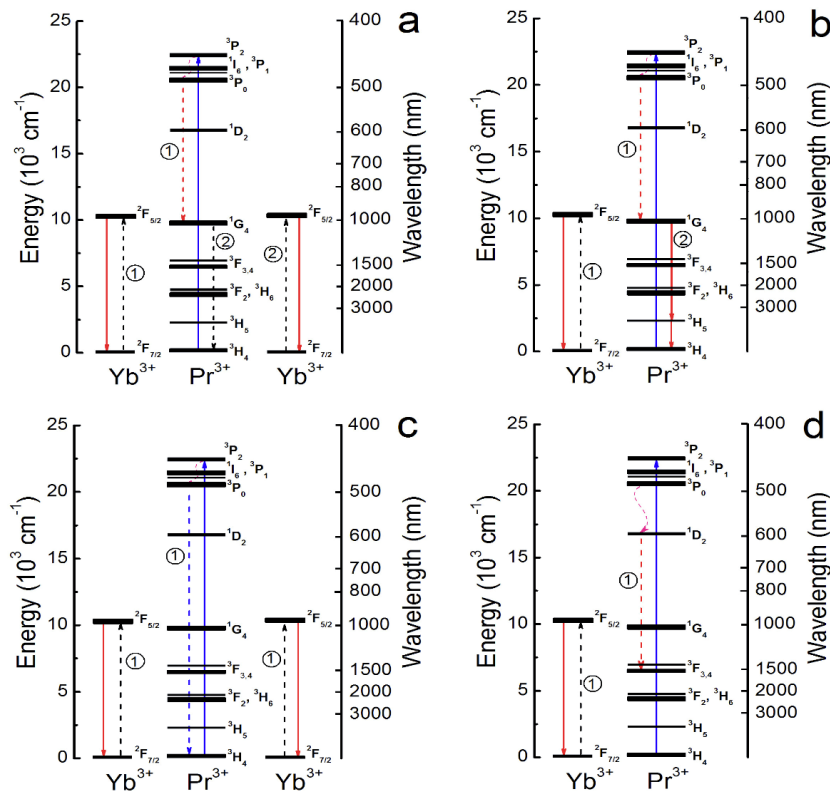


Fig. 7. Energy levels diagram of Pr^{3+} and Yb^{3+} , and possible energy transfer mechanism from Pr^{3+} to Yb^{3+} . (a) Resonant energy transfer from Pr^{3+} : $^3\text{P}_0$ and Pr^{3+} : $^1\text{G}_4$ levels to two Yb^{3+} : $^2\text{F}_{5/2}$ level. (b) One step first-order resonant energy transfer from Pr^{3+} : $^3\text{P}_0$ level to Yb^{3+} : $^2\text{F}_{5/2}$ and then a radiative relaxation from Pr^{3+} : $^1\text{G}_0$ level to Pr^{3+} : $^3\text{H}_4$ or Pr^{3+} : $^3\text{H}_5$ level. (c) Cooperative energy transfer from one Pr^{3+} : $^3\text{P}_0$ level to two neighboring Yb^{3+} : $^2\text{F}_{5/2}$ level. (d) The first-order resonant energy transfer from Pr^{3+} : $^1\text{P}_2$ level to Yb^{3+} : $^2\text{F}_{5/2}$.

Although on the first view, the presence of an intermediate level at about 10000 cm^{-1} in Pr^{3+} , suggest a relatively simple energy transfer process, at least four different ways may be considered for the pair of Pr^{3+} and Yb^{3+} , illustrated in Figs. 7(a)–7(d). These are

- two-step first-order resonant energy transfer from the $^3\text{P}_0$ and $^1\text{G}_4$ levels of Pr^{3+} to the $^2\text{F}_{5/2}$ level of Yb^{3+} , resulting in the generation of two NIR photons at $\sim 1\text{ }\mu\text{m}$ [4],
- single step first-order resonant energy transfer from $^3\text{P}_0$ of Pr^{3+} to $^2\text{F}_{5/2}$ of Yb^{3+} , and further relaxation of $^1\text{G}_0$ to $^3\text{H}_4$ or $^3\text{H}_5$ of Pr^{3+} , resulting in one photon at $\sim 1\text{ }\mu\text{m}$ and another one at $\sim 1\text{ }\mu\text{m}$ ($^3\text{H}_4$) or at $\sim 1.33\text{ }\mu\text{m}$ ($^3\text{H}_5$) [42],

- c) single step second-order cooperative energy transfer from the 3P_0 level of Pr^{3+} to two neighboring $Yb^{3+}:^2F_{5/2}$ levels, resulting in the emission of photons from Yb^{3+} centers with a wavelength of $\sim 1 \mu m$ [36], and
- d) non-radiative relaxation of 3P_0 to 1D_2 (Pr^{3+}), followed by first-order resonant energy transfer from $Pr^{3+}:^1D_2$ to $Yb^{3+}:^2F_{5/2}$, resulting in the emission of a single photon at $\sim 1 \mu m$.

All processes (a-d) require some extent of phonon interaction.

The first two mechanisms (a-b) appear rather unlikely due to the following reasons: firstly, the absence of Pr^{3+} PL bands from $^3P_0 \rightarrow ^1G_4$ (which should occur ~ 950 nm), from $^1G_4 \rightarrow ^3H_6$ (~ 1850 nm) and from $^1G_4 \rightarrow ^3H_5$ (~ 1330 nm), what indicates poor population of the 1G_4 level of Pr^{3+} . Secondly, the 1G_4 level of Pr^{3+} is $\sim 200 \text{ cm}^{-1}$ lower than the $^2F_{5/2}$ level of Yb^{3+} . This means that energy transfer should rather occur from Yb^{3+} to Pr^{3+} than vice versa. Thirdly, the absorption band which is assigned to the transition from the ground state of Pr^{3+} , 3H_4 , to the 1G_4 level is very weak (Fig. 1). Fourthly, the energy gap between the 1G_4 and the lower lying 3F_4 level is low ($\sim 3000 \text{ cm}^{-1}$) may lead to very high multi-phonon assisted non-radiative transition rates from the 1G_4 level. Finally, the branching ratio of the $^3P_0 \rightarrow ^1G_4$ radiative transition and the total radiative rates of the 3P_0 level are as low as ~ 0.06 and 218.07 cm^{-1} , respectively, resulting in a low population of the 1G_4 level (Table 1).

As briefly discussed in the previous chapters, the decrease in intensity of all PL bands of Pr^{3+} in the presence of Yb^{3+} [Figs. 2(a)–2(f)], and also of PL lifetime of the $Pr^{3+}:^3P_0$ and $Pr^{3+}:^1D_2$ levels [Figs. 4(a)–4(d)] suggests that energy transfer occurs through both the 3P_0 and 1D_2 levels of Pr^{3+} . The branching ratio of the $^3P_0 \rightarrow ^1D_2$ radiative transition is close to zero. This indicates the dominating multi-phonon assisted non-radiative transition of $^3P_0 \rightarrow ^1D_2$ (Table 1). The excitation efficiency of Yb^{3+} via the 3P_0 level of Pr^{3+} is 2.7 times higher than via the 1D_2 level [Fig. 2(e)]. This indicates that also energy transfer from the 3P_0 state is more efficient than from the 1D_2 state. Additionally, the total radiative rate of the 3P_0 level (10319.43 cm^{-1}) is much higher than that of the 1D_2 level (924.43 cm^{-1}) which confirms our conclusion (Table 1). The absence of $^3P_0 \rightarrow ^1G_4$ Pr^{3+} PL also indicates that the cooperative energy transfer process cannot be neglected [Fig. 7(c)].

4. Conclusions

In summary, NIR downconversion of one blue photon into two NIR photons ($\sim 10000 \text{ cm}^{-1}$) was observed in Pr^{3+}/Yb^{3+} co-doped SLABS glasses and corresponding $LaBO_3$ glass ceramics. The decrease of all Pr^{3+} -related PL bands in intensity and lifetime with increasing Yb^{3+} concentration along with the observation of typical Pr^{3+} PLE bands by monitoring Yb^{3+} -related PL at 976 nm indicated that energy transfer occurs through both the 3P_0 and the 1D_2 level of Pr^{3+} to Yb^{3+} . Thereby, transfer from $Pr^{3+}:^3P_0$ to Yb^{3+} occurs as a downconversion reaction where of one visible photon is cut into two NIR photons, whereas transfer from $Pr^{3+}:^1D_2$ to Yb^{3+} results in a down-shift of the energy of a single NIR. The transfer efficiency from the $Pr^{3+}:^3P_0$ level is higher as compared to that from the $Pr^{3+}:^1D_2$ level. A theoretical quantum efficiency of 183% was estimated for this process. In the present matrix material, the optimal doping concentration of Yb_2O_3 for downconversion is ~ 0.5 mol%. Crystallization of the as-made glass into a $LaBO_3$ glass ceramic leads to improved emission properties. Thereby, Pr^{3+} ions as well as Yb^{3+} ions enter the crystallite lattice, assumedly on La^{3+} sites.

Acknowledgment

The authors gratefully acknowledge financial support by the Deutsche Forschungsgemeinschaft (DFG) through the Cluster of Excellence “Engineering of Advanced Materials - EAM”.

2.8. Near-Infrared down-conversion in Mn^{2+} - Yb^{3+} co-doped Zn_2GeO_4

The intrinsic defect transitions of Zn_2GeO_4 lattice and Mn^{2+} ions act as broadband spectral sensitizers by absorbing UV-Vis (280–500 nm) photons. The absorbed energy is transferred to Yb^{3+} ions in a cooperative down-conversion process resulting in NIR emission ~1000 nm.

G. Gao and L. Wondraczek, *J. Mater. Chem. C* 2013, **1**, 1952–1958. -Reproduced by permission of The Royal Society of Chemistry.

<http://pubs.rsc.org/en/Content/ArticleLanding/2013/TC/c3tc00803g#!divCitation>

Near-infrared down-conversion in Mn^{2+} - Yb^{3+} co-doped Zn_2GeO_4 Cite this: *J. Mater. Chem. C*, 2013, 1, 1952Guojun Gao^{ab} and Lothar Wondraczek^{*a}

We report on near-infrared (NIR) down-conversion by energy transfer between Mn^{2+} and Yb^{3+} in crystalline $\text{Zn}_{1.96-x}\text{GeO}_{4+1/2x}\text{Mn}_{0.04}\text{Yb}_x$. In the Zn_2GeO_4 lattice, intrinsic defect transitions and Mn^{2+} ions act as broadband spectral sensitizers by absorbing UV-Vis (280–500 nm) photons and transferring the absorbed energy to Yb^{3+} centers in a cooperative down-conversion process. The Yb^{3+} acceptor is then the source of NIR emission at a wavelength of ~ 1000 nm. Efficient energy transfer is reflected by a sharp decrease in the excited state lifetime and green photoluminescence (PL) from tetrahedrally coordinated Mn^{2+} with increasing Yb^{3+} concentration. PL-excitation spectra of NIR luminescence from Yb^{3+} are identical to those of from $^{\text{IV}}\text{Mn}^{2+}$. A maximal energy transfer efficiency (ETE) from Mn^{2+} to Yb^{3+} and a total theoretical quantum efficiency of 63.8% and 163.8%, respectively, are estimated.

Received 6th December 2012
Accepted 10th January 2013

DOI: 10.1039/c3tc00803g

www.rsc.org/MaterialsC

1 Introduction

Solar spectral down-conversion of one UV-Vis photon of high energy into two or more near infrared (NIR) photons of lower energy has been proposed as a potential route to overcome the Shockley–Queisser limit of the spectral efficiency of solar cells.^{1–7} For example, for crystalline silicon (c-Si), about 32% of ~~the solar energy~~ is available in the UV-Vis part of the solar spectrum, which is usually lost by electronic recombination and thermal relaxation (see Fig. 1a). If this part of the incoming spectrum could effectively be converted to the NIR, the efficiency of a single junction c-Si solar cell could be enhanced up to 40%.^{8–11} Luminescence schemes, which could be employed towards this goal, are therefore being given significant attention since the 1990s.^{9–12} The Yb^{3+} ion has been identified as an almost ideal acceptor species for this purpose, as it possesses only a single excited state, $^2\text{F}_{7/5}$, which is located close to the maximum of the spectral efficiency of c-Si.^{13,14} Various rare earth (RE) ions have been considered as sensitizers for Yb^{3+} , *i.e.*, Pr^{3+} , Er^{3+} , Nd^{3+} , Ho^{3+} , Tm^{3+} and Tb^{3+} .^{15–20} However, these RE species typically exhibit relatively narrow absorption bands with low absorption efficiency due to their characteristic parity forbidden 4f-transitions. While this property makes them the material of choice for, *e.g.*, applications in optical amplifiers and lasers, for efficient spectral conversion, a broader absorption spectrum would be desirable.^{21–24} We therefore consider the 5d transition metal (TM) ion Mn^{2+} as a sensitizer for Yb^{3+} . As one of the most important class of inorganic phosphors, Mn^{2+} activated materials show a broad PL band varying from deep green to far red

due to the parity-forbidden d–d transition from the lowest excited level, $^4\text{T}_1(^4\text{G})$, to the ground state of $^6\text{A}_1(^6\text{S})$. The versatility of the Mn^{2+} center originates from the strong ligand dependence of the $^4\text{T}_1(^4\text{G})$ state (Fig. 3d),^{25,26} which typically leads to greenyellow or yellow-red photoemission from tetrahedral $^{\text{IV}}\text{Mn}^{2+}$ or octahedrally coordinated $^{\text{VI}}\text{Mn}^{2+}$, respectively.^{27,28} The line strength of the spin- and parity-forbidden

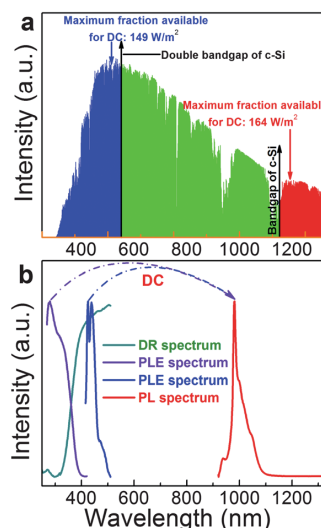


Fig. 1 (a) Standard solar spectrum for air mass 1.5. Raw data of (a) was derived from ASTM G173-03 reference spectra. (b) Diffuse reflectance (DR) spectra of ZGM-0Yb; PLE spectrum for greenish-white PL from the pure Zn_2GeO_4 host ($\lambda_{\text{em}} = 535$ nm); direct PLE spectrum for green PL from $^{\text{IV}}\text{Mn}^{2+}$ ($\lambda_{\text{em}} = 535$ nm) and the PL spectrum ($\lambda_{\text{em}} = 330$ nm) of Yb^{3+} in ZGM-0004Yb.

^aOtto-Schott-Institute, University of Jena, 07743 Jena, Germany^bDepartment of Materials Science, University of Erlangen-Nuremberg, 91058 Erlangen, Germany. E-mail: lothar.wondraczek@www.uni-erlangen.de

electric dipole transitions of Mn^{2+} is usually low,^{29,30} and sensitizers are often employed to improve the absorption efficiency. As one such, willemite-type zinc orthogermanate (Zn_2GeO_4), a wide-bandgap (4.68 eV) semiconductor, has received much attention.^{31–35} By itself, it exhibits bright white-blue PL from the recombination reactions of native donors (V_{O}^{\bullet} and Zn_i^{\bullet}) and acceptors (V_{Zn}'' and V_{Ge}').^{34,35} By doping with Mn^{2+} , it has been demonstrated as a highly efficient green-emitting phosphor due to energy transfer from the Zn_2GeO_4 host to Mn^{2+} on tetrahedral lattice sites.^{36–41} Its excitation (PLE) bands cover almost the whole spectral window from 250 to 500 nm (see Fig. 1b). The position of the active state of Mn^{2+} ; ${}^4\text{T}_2$ (${}^4\text{G}$) ($\sim 21\,000\text{ cm}^{-1}$) is approximately twice the absorption energy of Yb^{3+} ; ${}^2\text{F}_{2/7} \rightarrow {}^2\text{F}_{2/5}$ ($\sim 10\,200\text{ cm}^{-1}$).^{42–44} Energy transfer from Yb^{3+} to Mn^{2+} has therefore been studied for the up-conversion of NIR light.^{45,46} In this report, we focus on the alternative direction of energy transfer, *i.e.* from Mn^{2+} to Yb^{3+} as a potential way for spectral down-conversion. We show that Mn^{2+} is an efficient sensitizer for Yb^{3+} in $\text{Zn}_{1.96-x}\text{GeO}_{4+1/2x}\text{Mn}_{0.04}\text{Yb}_x$. Then, broadband cooperative down-conversion can be achieved by energy transfer from Mn^{2+} to Yb^{3+} and from Zn_2GeO_4 to Yb^{3+} *via* Mn^{2+} , respectively.

2 Experimental

Samples of $\text{Zn}_{1.96-x}\text{GeO}_{4+1/2x}\text{Mn}_{0.04}\text{Yb}_x$ ($x = 0, 0.004, 0.04$ and 0.4 , sample nomenclature: ZGM- $x\text{Yb}$, *e.g.* ZGM-0004Yb for $x = 0.004$) and pure Zn_2GeO_4 were synthesized in a conventional high-temperature solid state reaction from high purity ZnO (99.97%), GeO_2 (99.999%), MnCO_3 (99.9%) and Yb_2O_3 (99.999%). All ZGM- $x\text{Yb}$ samples were doped with the optimized nominal concentration of Mn (2 at.%) for obtaining green PL from ${}^{\text{IV}}\text{Mn}^{2+}$ in Zn_2GeO_4 .³⁶ Stoichiometric mixtures of raw materials were ground, pre-calcined at $900\text{ }^\circ\text{C}$ for 4 h in air, and again ground in an agate mortar. Sintering was then performed at $1300\text{ }^\circ\text{C}$ for 12 h in air.

The crystal structure of the synthesized samples was studied *ex situ* by powder X-ray diffractometry (XRD, Siemens Kristalloflex D500, Bragg-Brentano, 30 kV/30 mA, Cu K α) with a step width of 0.02° s^{-1} and a counting time of 10 s per step over a 2θ range of $10\text{--}70^\circ$. Diffuse reflectance (DR) spectra were recorded with a dual-beam photospectrometer equipped with a 150 mm integration sphere and a PbS detector (Perkin-Elmer Lambda 950). Static and dynamic PL were studied with a high-resolution spectrofluorometer and by time correlated single photon counting (TCSPC, Horiba Jobin Yvon Fluorolog FL3-22) using a 450 W static Xe lamp and a 75 W Xe flashlamp as excitation sources, and mechanical double monochromators in the emission and excitation channels. NIR PL was observed with an InP/InGaAs-based thermoelectrically cooled photomultiplier tube (NIR-PMT, Hamamatsu H10330A-75). Photoluminescence excitation (PLE) spectra were corrected over the lamp intensity with a silicon photodiode and PL spectra were corrected by the spectral response of the detector using the correction spectra of the employed PMT. The external quantum efficiency η_{EQE} of the PL in each sample was obtained from three individual measurements using a BaSO_4 -coated integration sphere, *i.e.*, by

recording the PL spectra of the sphere alone and with the sample, and the PLE spectra of the sphere alone. The value of η_{EQE} was then obtained from

$$\eta_{\text{EQE}} = (\int L_{\text{S}} - \int L_{\text{R}}) / \int E_{\text{R}} \quad (1)$$

where $\int L_{\text{S}}$ and $\int L_{\text{R}}$ represent the integral PL intensity with and without the sample, respectively, and $\int E_{\text{R}}$ is the integrated PL intensity which is obtained when exciting over the complete PLE spectrum of the sphere alone. All analyses were performed at room temperature.

3 Results and discussion

Fig. 2a shows *ex situ* powder XRD patterns of ZGM- $x\text{Yb}$ samples with various Yb^{3+} doping concentrations. For the samples doped with lower amounts of Yb^{3+} ($x \leq 0.04$), all diffraction peaks can readily be assigned to pure Zn_2GeO_4 (orthorhombic, JCPDS card no. 00-013-0687, tabulated diffraction pattern shown for reference). As displayed in Fig. 2b, willemite-type Zn_2GeO_4 belongs to the space group $R\bar{3}$ with a phenacite-like structure and cell parameters of $a = b = 14.231\text{ \AA}$, $c = 9.530\text{ \AA}$, $\alpha = \beta = 90^\circ$ and $\gamma = 120^\circ$. Its lattice is composed of corner sharing ZnO_4 and GeO_4 tetrahedra. Due to the closeness of the effective ionic radii and equivalent charge, Mn^{2+} (0.66 \AA in four-fold coordination) would preferably occupy the Zn^{2+} sites (0.60 \AA) as compared to Ge^{4+} sites (0.39 \AA).⁴⁷ No secondary crystal phases can be identified for the samples with $x \leq 0.04$, indicating that Mn^{2+} ions indeed completely dissolve in the Zn_2GeO_4 lattice. For the samples doped with higher Yb^{3+} concentration ($x \geq 0.04$), minor amounts of $\text{Yb}_2\text{Ge}_2\text{O}_7$ (tetragonal, JCPDS card no. 00-045-0531) and ZnO (hexagonal, JCPDS

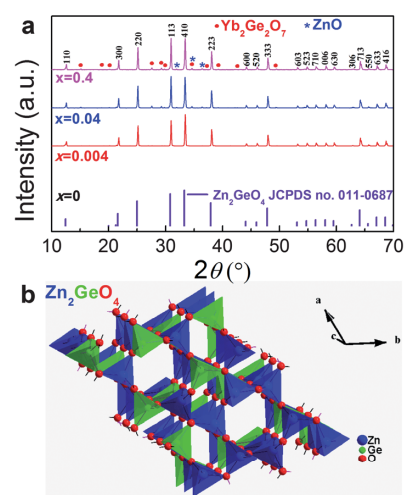


Fig. 2 (a) *Ex situ* powder XRD patterns of ZGM- $x\text{Yb}$ as a function of Yb^{3+} concentration. Diffraction patterns of $\text{Yb}_2\text{Ge}_2\text{O}_7$ and ZnO crystals are marked by filled circles and stars, respectively. Also shown in (a) is the tabulated diffraction pattern of Zn_2GeO_4 . (b) Schematic of the Zn_2GeO_4 crystallite lattice. Blue and green tetrahedra represent the ZnO_4 and GeO_4 groups, respectively.

card no. 00-075-0576) can also be indexed (Fig. 1a). With an effective ionic radius of Yb^{3+} of $\sim 0.87 \text{ \AA}$ (six-fold coordination), the radius difference between Yb^{3+} and Zn^{2+} or Ge^{4+} appears too large to allow for an immediate assignment of lattice sites in Zn_2GeO_4 .⁴⁷ Instead, at an elevated Yb^{3+} content, Yb^{3+} and Ge^{4+} partition into $\text{Yb}_2\text{Ge}_2\text{O}_7$ and leave residual ZnO . $\text{Yb}_2\text{Ge}_2\text{O}_7$ is composed of apex-sharing GeO_6 octahedra. Yb^{3+} is incorporated into the network voids between those octahedra where it forms scalenohedrons of YbO_8 which share edges with the GeO_6 groups.⁴⁸ Interestingly, the general pyrochlore structure of $\text{A}_2\text{B}_2\text{O}_6\text{X}$ offers a large chemical variety for the occupation of A and B sites.

All ZGM-xYb samples exhibit a wide and intense absorption band which covers the spectral range of 250 to 400 nm with peaks at $\sim 298 \text{ nm}$ and $\sim 255 \text{ nm}$ (Fig. 1b). The latter are attributed to matrix absorption of Zn_2GeO_4 .

As already mentioned, Zn_2GeO_4 is a self-activated phosphor. We therefore first consider the PL properties of pure Zn_2GeO_4 . As shown in Fig. 3b, it exhibits a broad PL band in the spectral range of 400–700 nm with a maximum at 505 nm and a full width at half maximum (FWHM) of $\sim 148 \text{ nm}$ (5609 cm^{-1}) under excitation at 307 nm. This band is attributed to the radiative recombination of a donor (V_{O}^{\bullet} and Zn_i^{\bullet}) and an acceptor defect (V_{Zn}^{\bullet} and V_{Ge}^{\bullet}).³⁵ The corresponding PLE spectrum (monitoring PL at 505 nm) is comprised of a broad band from 250 to 350 nm with two individual peaks at ~ 269 and $\sim 307 \text{ nm}$, consistent with the two absorption peaks in Fig. 1b and 3a. The PLE peak at 269 nm is ascribed to the transition from the valence band to the conduction band of the Zn_2GeO_4 host, whereas the origin of the PLE peak at 307 nm is not clear.⁴¹ The corresponding effective lifetime of PL is $< 3 \mu\text{s}$ (Fig. 3c, note that the pulse width of the employed Xe flash lamp is $3 \mu\text{s}$).

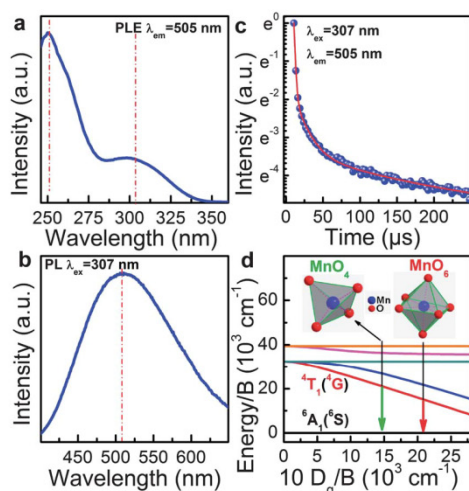


Fig. 3 Room temperature steady-state (a) PLE and (b) PL spectrum for greenish-white PL in pure Zn_2GeO_4 . (c) Corresponding room temperature decay curve. (d) Tanabe-Sugano diagram of $5d$ (Mn^{2+}). Arrows in (d) schematically indicate typical field strengths for Mn^{2+} in tetrahedral or octahedral coordination.

Fig. 4a and 5a display room temperature PLE spectra for the green PL from ${}^{\text{IV}}\text{Mn}^{2+}$ in ZGM-xYb . The spectra consist of two distinct parts, *i.e.*, an intense band ranging from 260–400 nm with two individual peaks centered at ~ 280 and $\sim 330 \text{ nm}$, and a weak band in the spectral range of 410–500 nm. High-energy excitation is related to the Zn_2GeO_4 matrix, where the first PLE peak at $\sim 280 \text{ nm}$ is attributed to the aforementioned transition between the valence and the conduction band, and the $\sim 330 \text{ nm}$ peak reflects the charge transfer transition from the ground state of ${}^{\text{IV}}\text{Mn}^{2+}$ (${}^6\text{A}_1({}^6\text{S})$) to the conduction band of Zn_2GeO_4 .⁴⁹ The comparably weaker PLE bands in the range of 410–500 nm (maxima at ~ 475 , 436 and 424 nm) arise from the d-d transitions of the ground state of Mn^{2+} (${}^6\text{A}_1({}^6\text{S})$) to the excited states as labeled in Fig. 5a. In the following, the 330 nm band was selected as the strongest of all to monitor the PL spectra of ${}^{\text{IV}}\text{Mn}^{2+}$ (Fig. 4b). For comparison, also the PL spectra of ${}^{\text{IV}}\text{Mn}^{2+}$ for excitation to ${}^4\text{A}_1({}^4\text{G}) + {}^4\text{E}({}^4\text{G})$ ($\sim 424 \text{ nm}$) are presented (Fig. 5b).

Intense characteristic PL from ${}^{\text{IV}}\text{Mn}^{2+}$ ($\sim 535 \text{ nm}$, Fig. 4b) is observed in both cases. The emission band spans the spectral range of 480–640 nm with a FWHM of $\sim 54 \text{ nm}$ (1836 cm^{-1}) and is attributed to the aforementioned parity-forbidden d-d transition from the lowest excited state ${}^4\text{T}_1({}^4\text{G})$ to the ground state ${}^6\text{A}_1({}^6\text{S})$ of ${}^{\text{IV}}\text{Mn}^{2+}$. The position of the PL band confirms relatively low crystal field splitting and, hence, tetrahedral coordination of Mn^{2+} in the Zn_2GeO_4 host. It is noteworthy that no bluish-white PL from the Zn_2GeO_4 host can be observed at this point, which indicates that energy transfer occurs from the

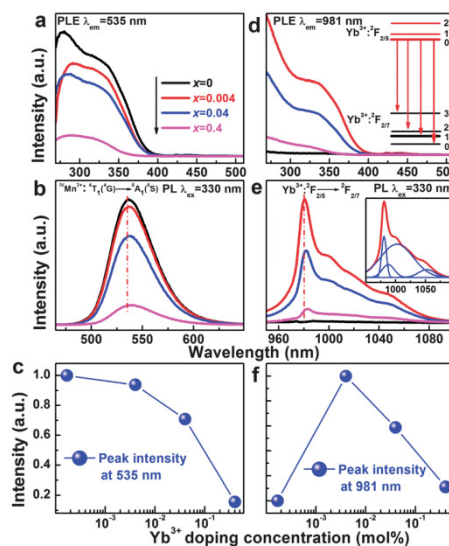


Fig. 4 Room temperature steady-state (a) PLE and (b) PL spectra of ${}^{\text{IV}}\text{Mn}^{2+}$ in ZGM-xYb , and (d) PLE and (e) PL spectra for NIR PL from Yb^{3+} in ZGM-xYb . The inset of (d) shows the Stark-split energy scheme of Yb^{3+} and the origin of the four NIR PL bands, and the inset of (e) shows a Gaussian deconvolution of the NIR PL spectrum of Yb^{3+} . (c) and (f) present the PL intensity of ${}^{\text{IV}}\text{Mn}^{2+}$ at 535 nm and Yb^{3+} at 981 nm, respectively, in ZGM-xYb phosphors in dependence of the Yb^{3+} concentration. Lines in (c) and (f) are guides to the eye.

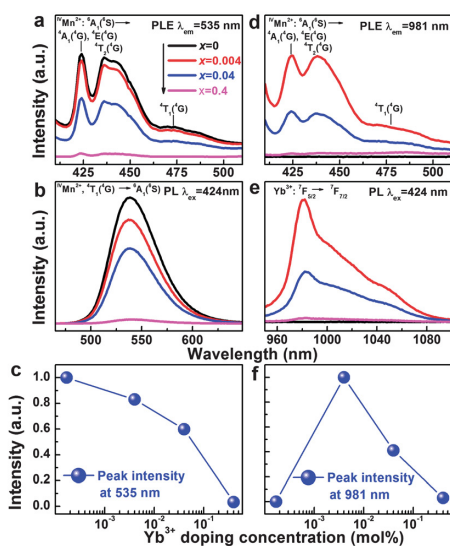


Fig. 5 Room temperature steady-state (a) PLE and (b) PL spectra for green PL of $^{IV}\text{Mn}^{2+}$, and (d) PLE and (e) PL spectra of Yb^{3+} in ZGM-xYb. (c) and (f) show the PL intensity of $^{IV}\text{Mn}^{2+}$ at 535 nm and Yb^{3+} at 981 nm, respectively, in ZGM-xYb in dependence of the Yb^{3+} concentration. Lines in (c) and (f) are guides to the eye.

excited states of Zn_2GeO_4 to $^{IV}\text{Mn}^{2+}$. As expected, the typical green PL band is also observed when the $^{IV}\text{Mn}^{2+}$ is directly excited (Fig. 5b). The PL intensity of the $^{IV}\text{Mn}^{2+}$ -related band decreases gradually with increasing Yb^{3+} concentration (Fig. 4b and c, 5b and c). This implies energy transfer from Mn^{2+} to Yb^{3+} . Also, the peak position for green PL from $^{IV}\text{Mn}^{2+}$ red shifts slightly from 535 to 540 nm with increasing Yb^{3+} doping concentration. The latter observation reflects the fact that the higher energy configurations of $^{IV}\text{Mn}^{2+}$ preferably contribute to the energy transfer from Mn^{2+} to Yb^{3+} .

The PLE spectra of NIR PL from Yb^{3+} centers ($\lambda_{\text{em}} = 981$ nm, Fig. 4d and 5d) are full in agreement with the above results. As expected, no NIR PL is found in the studied spectral region from ZGM-0Yb. Only after co-doping with a small amount of Yb^{3+} ($x = 0.004$), a sharp peak with a maximum at ~ 981 nm (FWHM of ~ 37 nm) and three shoulders at ~ 988 , 1002 and 1050 nm (inset of Fig. 4e) arises. This emission can be excited *via* both the UV band at 330 nm (Fig. 4e) and the $^{IV}\text{Mn}^{2+}$ -related band at 424 nm (Fig. 5e). Since neither Mn^{2+} nor the Zn_2GeO_4 host exhibits known NIR PL in this spectral region, all observed NIR bands are readily attributed to radiative decay from the lowest stark level of Yb^{3+} , $^2\text{F}_{2/5}$, to four different stark levels of the ground state of Yb^{3+} , $^2\text{F}_{7/2}$ (inset of Fig. 4d). The intensity of these bands decreases with increasing Yb^{3+} concentration due to concentration quenching (Fig. 4d-f and 5d-f).^{50,51} The position of the main band red-shifts slightly from 981 to 983 nm with increasing Yb^{3+} concentration, probably due to the increasing extent of self-quenching.^{50,51} The appearance of the characteristic NIR PL from Yb^{3+} centers is taken as direct evidence for the energy transfer of $\text{Mn}^{2+} \rightarrow \text{Yb}^{3+}$. In this case, Mn^{2+} acts as a sensitizer by absorbing UV-Vis photons and transferring the absorbed energy to Yb^{3+} centers.

Normalized decay curves of green PL from $^{IV}\text{Mn}^{2+}$ (direct excitation) are depicted in Fig. 6a. The best fit of all curves is obtained by a second-order exponential function, $I(t) = A + B_1 \exp(-t/\tau_{\text{fast}}) + B_2 \exp(-t/\tau_{\text{slow}})$. This indicates an overlap of a fast and a slow decay component with lifetimes τ_{fast} and τ_{slow} . The fast decay process is caused by coupling in Mn^{2+} - Mn^{2+} pairs or clusters,⁵² whereas the slow decay process is attributed to isolated Mn^{2+} ions.⁵³⁻⁵⁵ The effective lifetime $\tau_{1/e}$ is defined as the time within which the intensity decays to $1/e$ of its initial value.^{56,57} Since the transition of $^{IV}\text{Mn}^{2+}:^4\text{T}_1(^4\text{G}) \rightarrow ^6\text{A}_1(^6\text{S})$ is parity-forbidden, a relatively long lifetime is expected. The deconvoluted values of τ_{fast} , τ_{slow} and $\tau_{1/e}$ are summarized in Fig. 6b. They all decrease with increasing Yb^{3+} concentration: energy transfer from Mn^{2+} to Yb^{3+} provides a new pathway to de-populate the excited state of $^{IV}\text{Mn}^{2+}:^4\text{T}_1(^4\text{G})$.

Fig. 7a shows the corresponding normalized decay curves of green PL from $^{IV}\text{Mn}^{2+}$ under NUV excitation. Here, the effective lifetime of the Yb^{3+} -free sample is ~ 3.7 ms, which is longer than that directly excited $^{IV}\text{Mn}^{2+}$ in ZGM-0Yb. It decreases gradually to ~ 1.6 ms with increasing Yb^{3+} concentration (Fig. 7b). Consistently, the external quantum efficiency (EQE) of the green PL drops from 45.2% to 5.7% with increasing Yb^{3+} doping concentration under UV excitation (Fig. 7b). Both observations further confirm the conclusion of the occurrence of energy transfer from Mn^{2+} to Yb^{3+} , which increases the decay rate of the $^{IV}\text{Mn}^{2+}:^4\text{T}_1(^4\text{G})$ level.

The energy gap between $^{IV}\text{Mn}^{2+}:^4\text{T}_1(^4\text{G})$ and the $\text{Yb}^{3+}:^2\text{F}_{2/5}$ level is ~ 8870 cm^{-1} . The maximum phonon energy in Zn_2GeO_4 is ~ 800 cm^{-1} .⁴¹ Thus, at least 11 phonons are needed to overcome the gap between $^{IV}\text{Mn}^{2+}:^4\text{T}_1(^4\text{G})$ and the $\text{Yb}^{3+}:^2\text{F}_{2/5}$ level through multi-phonon non-radiative relaxation. We therefore neglect the possibility of non-radiative relaxation between those levels in the following discussion and assume that energy transfer occurs as a cooperative down-conversion process where one visible photon is converted into two NIR photons. This is schematically shown in Fig. 8.

Under excitation at 280 nm, electrons from the valence band of Zn_2GeO_4 are excited to the conduction band. Subsequently,

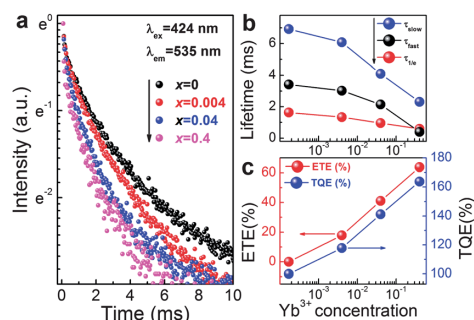


Fig. 6 (a) Normalized decay curves for green PL of $^{IV}\text{Mn}^{2+}$ in ZGM-xYb, (b) deconvoluted lifetimes for the individual decay processes τ_{fast} and τ_{slow} and effective lifetime $\tau_{1/e}$, and (c) energy transfer efficiency (ETE) and total theoretical quantum efficiency (TQE) in ZGM-xYb phosphors under excitation at 424 nm. Lines in (b) and (c) are guides to the eye.

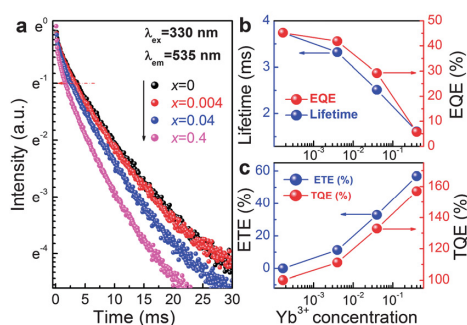


Fig. 7 (a) Normalized decay curves for PL from ${}^{\text{IV}}\text{Mn}^{2+}$ in ZGM- $x\text{Yb}$, (b) effective lifetime $\tau_{1/e}$ and external quantum efficiency EQE, and (c) ETE and TQE of ZGM- $x\text{Yb}$ under excitation at 330 nm. Lines in (b) are guides to the eye.

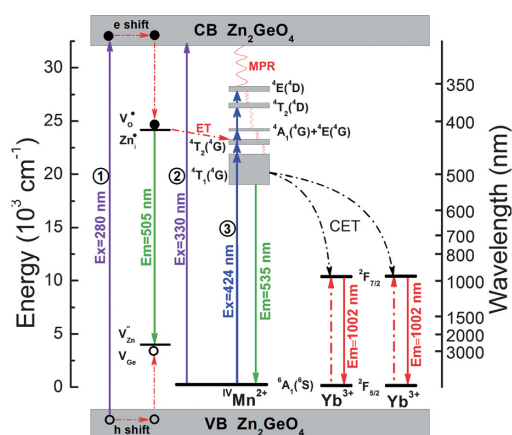


Fig. 8 Energy level diagram of the Zn_2GeO_4 host, Mn^{2+} and Yb^{3+} , and schematic of the energy transfer mechanism from the Zn_2GeO_4 host to Yb^{3+} via Mn^{2+} .

the excited free electrons are trapped by V_{O}^{\bullet} or $\text{Zn}_{\text{i}}^{\bullet}$ through non-radiative processes. Recombination of the native defects results in the intrinsic greenish white PL from Zn_2GeO_4 , but the electrons in V_{O}^{\bullet} or $\text{Zn}_{\text{i}}^{\bullet}$ can also transfer their energy to the ${}^4\text{T}_2({}^4\text{G})$ level of ${}^{\text{IV}}\text{Mn}^{2+}$. The radiative transition of ${}^{\text{IV}}\text{Mn}^{2+}:{}^4\text{T}_1({}^4\text{G}) \rightarrow {}^{\text{IV}}\text{Mn}^{2+}:{}^6\text{A}_1({}^6\text{S})$ results in green PL. In the presence of Yb^{3+} , the electrons at the ${}^{\text{IV}}\text{Mn}^{2+}:{}^6\text{A}_1({}^6\text{S})$ level can also transfer their energy to two neighboring $\text{Yb}^{3+}:{}^2\text{F}_{2/5}$ levels simultaneously by a one step second-order cooperative energy transfer (CET) process which results in two photons with a wavelength of ~ 1000 nm through relaxation of $\text{Yb}^{3+}:{}^2\text{F}_{2/5}$ to $\text{Yb}^{3+}:{}^2\text{F}_{7/2}$.

When excited at 330 nm, electrons from the ground state of ${}^{\text{IV}}\text{Mn}^{2+}:{}^6\text{A}_1({}^6\text{S})$ are lifted to the conduction band of Zn_2GeO_4 through a charge transfer reaction, $\text{Mn}^{2+} + \hbar\nu \rightarrow \text{Mn}^{3+} + \text{e}^-$. Then, multiphonon-assisted relaxation occurs from the conduction band of Zn_2GeO_4 to ${}^{\text{IV}}\text{Mn}^{2+}:{}^4\text{T}_1({}^4\text{G})$. The subsequent processes are similar to those following 280 nm excitation.

The energy transfer efficiency η_{ETE} is estimated by⁵⁸

$$\eta_{\text{ETE},x\% \text{Yb}} = 1 - \frac{\tau_{x\% \text{Yb}}}{\tau_{0\% \text{Yb}}} \quad (2)$$

In eqn (2), $\tau_{x\% \text{Yb}}$ is the lifetime of Mn^{2+} -related emission for co-doping with x mol% Yb_2O_3 . Here, the effective lifetime values were used for the calculations. The calculated η_{ETE} increases from 17.8% to 63.8% and from 11.2% to 57.0% under excitation at 424 and 330 nm, respectively, when increasing the Yb^{3+} doping concentration from $x = 0.004$ to 0.4 (Fig. 6c and 7b). The total theoretical quantum efficiency (TQE) is then calculated in dependence of the Yb^{3+} doping concentration *via*⁵⁸

$$\eta = \eta_{\text{Mn}}(1 - \eta_{\text{ETE},x\% \text{Yb}}) + 2\eta_{\text{Yb}}\eta_{\text{ETE},x\% \text{Yb}} \quad (3)$$

where η_{Mn} and η_{Yb} are the quantum efficiencies of Mn^{2+} and Yb^{3+} PL. Both of them were set to unity. A calculated value of TQE of 163.8% and 157.0% (for ZGM-04Yb) was obtained for excitation at 424 and 330 nm, respectively (Fig. 6c and 7c). These values may be taken as qualitative estimates and for referencing to alternative materials. The actual quantum efficiency is lower due to concentration quenching and other non-radiative losses which occur in real systems.

4 Conclusions

In summary, we reported spectral down-conversion in $\text{Zn}_{1.96-x}\text{GeO}_{4+1/2x}\text{Mn}_{0.04}\text{Yb}_x$ phosphors *via* the pair of Mn^{2+} - Yb^{3+} . In the Zn_2GeO_4 lattice, Mn^{2+} ions partition on Zn^{2+} sites in the form of tetrahedral MnO_4 groups. The absorption of Zn_2GeO_4 and Mn^{2+} spans the spectral range of 250–500 nm. This enables broadband sensitization of Yb^{3+} . Energy transfer occurs either from defect levels of Zn_2GeO_4 to two neighboring $\text{Yb}^{3+}:{}^2\text{F}_{2/5}$ centers *via* ${}^{\text{IV}}\text{Mn}^{2+}:{}^6\text{A}_1({}^6\text{S})$ or through direct excitation of ${}^{\text{IV}}\text{Mn}^{2+}:{}^6\text{A}_1({}^6\text{S})$. The occurrence of this energy process is evidenced by reduced green PL from ${}^{\text{IV}}\text{Mn}^{2+}$, reduced corresponding PL lifetime and reduced external quantum efficiency with increasing Yb^{3+} concentration, and identical PLE spectra for monitoring PL from ${}^{\text{IV}}\text{Mn}^{2+}$ and NIR PL from Yb^{3+} . The transfer process results in cooperative down-conversion of one visible photon into two NIR photons. The estimated maximum energy transfer efficiency (ETE) from Mn^{2+} to Yb^{3+} is $\sim 64\%$. The total theoretical quantum efficiency is $\sim 164\%$. The results suggest that $\text{Zn}_{1.96-x}\text{GeO}_{4+1/2x}\text{Mn}_{0.04}\text{Yb}_x$ phosphors could be employed for solar spectral down-conversion.

Acknowledgements

The authors gratefully acknowledge financial support by the Deutsche Forschungsgemeinschaft (DFG) through the Cluster of Excellence "Engineering of Advanced Materials – EAM".

Notes and references

- M. A. Green, K. Emery, Y. Hishikawa, W. Warta and E. D. Dunlop, Solar cell efficiency tables (version 39), *Prog. Photovoltaics*, 2012, **20**, 12.
- A. Polman and H. A. Atwater, Photonic design principles for ultrahigh-efficiency photovoltaics, *Nat. Mater.*, 2012, **11**, 174.
- B. M. van der Ende, L. Aarts and A. Meijerink, Near-Infrared Quantum Cutting for Photovoltaics, *Adv. Mater.*, 2009, **21**, 3073.

- 4 D. Yu, S. Ye, M. Peng, Q. Zhang and L. Wondraczek, Sequential three-step three-photon near-infrared quantum splitting in $\beta\text{-NaYF}_4\text{:Tm}^{3+}$, *Appl. Phys. Lett.*, 2012, **100**, 191911.
- 5 D. Yu, X. Huang, S. Ye, M. Peng, Q. Zhang and L. Wondraczek, Three-photon near-infrared quantum splitting in $\beta\text{-NaYF}_4\text{:Ho}^{3+}$, *Appl. Phys. Lett.*, 2011, **99**, 161904.
- 6 D. Yu, S. Ye, M. Peng, Q. Zhang, J. Qiu, J. Wang and L. Wondraczek, Efficient near-infrared downconversion in $\text{GdVO}_4\text{:Dy}^{3+}$ phosphors for enhancing the photo-response of solar cells, *Sol. Energy Mater. Sol. Cells*, 2011, **95**, 1590–1593.
- 7 M. Peng and L. Wondraczek, Bismuth-doped oxide glasses as potential solar spectral converters and concentrators, *J. Mater. Chem.*, 2009, **19**, 627–630.
- 8 X. Huang, S. Han, W. Huang and X. Liu, Enhancing solar cell efficiency: the search for luminescent materials as spectral converters, *Chem. Soc. Rev.*, 2013, **42**, 173.
- 9 B. S. Richards, Enhancing the performance of silicon solar cells *via* the application of passive luminescence conversion layers, *Sol. Energy Mater. Sol. Cells*, 2006, **90**, 2329.
- 10 V. D. Rodríguez, V. K. Tikhomirov, J. Méndez-Ramos, A. C. Yanes and V. V. Moshchalkov, Towards broad range and highly efficient down-conversion of solar spectrum by $\text{Er}^{3+}\text{-Yb}^{3+}$ co-doped nano-structured glass-ceramics, *Sol. Energy Mater. Sol. Cells*, 2010, **94**, 1612.
- 11 Q. Zhang and X. Huang, Recent progress in quantum cutting phosphors, *Prog. Mater. Sci.*, 2010, **55**, 353.
- 12 R. T. Wegh, H. Donker, K. D. Oskam and A. Meijerink, Visible quantum cutting in $\text{LiGdF}_4\text{:Eu}^{3+}$ through downconversion, *Science*, 1999, **283**, 663.
- 13 B. M. van der Ende, L. Aarts and A. Meijerink, Near-infrared quantum cutting for photovoltaics, *Adv. Mater.*, 2009, **21**, 3073.
- 14 P. Vergeer, T. J. H. Vlught, M. H. F. Kox, M. I. den Hertog, J. P. J. M. van der Eerden and A. Meijerink, Quantum cutting by cooperative energy transfer in $\text{Yb}_x\text{Y}_{1-x}\text{PO}_4\text{:Tb}^{3+}$, *Phys. Rev. B: Condens. Matter Mater. Phys.*, 2005, **71**, 014119.
- 15 K. Deng, T. Gong, L. Hu, X. Wei, Y. Chen and M. Yin, Efficient near-infrared quantum cutting in $\text{NaYF}_4\text{:Ho}^{3+}$, Yb^{3+} for solar photovoltaics, *Opt. Express*, 2011, **19**, 1749.
- 16 J. J. Eilers, D. Biner, J. T. van Wijngaarden, K. Krämer, H. U. Güdel and A. Meijerink, Efficient visible to infrared quantum cutting through downconversion with the $\text{Er}^{3+}\text{-Yb}^{3+}$ couple in $\text{Cs}_3\text{Y}_2\text{Br}_9$, *Appl. Phys. Lett.*, 2010, **96**, 151106.
- 17 H. Lin, D. Chen, Y. Yu, A. Yang and Y. Wang, Near-infrared quantum cutting in $\text{Ho}^{3+}/\text{Yb}^{3+}$ codoped nanostructured glass ceramic, *Opt. Lett.*, 2011, **36**, 876.
- 18 J.-M. Meijer, L. Aarts, B. M. van der Ende, T. J. H. Vlught and A. Meijerink, Downconversion for solar cells in $\text{YF}_3\text{:Nd}^{3+}$, Yb^{3+} , *Phys. Rev. B: Condens. Matter Mater. Phys.*, 2010, **81**, 035107.
- 19 Q. Zhang, G. Yang and Z. Jiang, Cooperative downconversion in $\text{GdAl}_3(\text{BO}_3)_4\text{:RE}^{3+}$, Yb^{3+} (RE = Pr, Tb, and Tm), *Appl. Phys. Lett.*, 2007, **91**, 051903.
- 20 W. Zhou, J. Yang, J. Wang, Z. Li, X. Kuang, J. Tang and H. Liang, Study on the effects of 5d energy locations of Ce^{3+} ions on NIR quantum cutting process in $\text{Y}_2\text{SiO}_5\text{:Ce}^{3+}$, Yb^{3+} , *Opt. Express*, 2012, **20**, A510.
- 21 X. Huang, X. Ji and Q. Zhang, Broadband downconversion of ultraviolet light to near-infrared emission in $\text{Bi}^{3+}\text{-Yb}^{3+}$ -codoped Y_2O_3 phosphors, *J. Am. Ceram. Soc.*, 2011, **94**, 833.
- 22 Q. Zhang, J. Wang, G. Zhang and Q. Su, UV photon harvesting and enhanced near-infrared emission in novel quantum cutting $\text{Ca}_2\text{BO}_3\text{Cl:Ce}^{3+}$, Tb^{3+} , Yb^{3+} phosphor, *J. Mater. Chem.*, 2009, **19**, 7088.
- 23 J. Zhou, Y. Zhuang, S. Ye, Y. Teng, G. Lin, B. Zhu, J. Xie and J. Qiu, Broadband downconversion based infrared quantum cutting by cooperative energy transfer from Eu^{2+} to Yb^{3+} in glasses, *Appl. Phys. Lett.*, 2009, **95**, 141101.
- 24 G. Gao, R. Meszaros, M. Peng and L. Wondraczek, Broadband UV-to-green photoconversion in V-doped lithium zinc silicate glasses and glass ceramics, *Opt. Express*, 2011, **19**, A312–A318.
- 25 C. Bertail, S. Maron, V. Buissette, T. L. Mercier, T. Gacoin and J.-P. Boilot, Structural and photoluminescent properties of $\text{Zn}_2\text{SiO}_4\text{:Mn}^{2+}$ nanoparticles prepared by a protected annealing process, *Chem. Mater.*, 2011, **23**, 2961.
- 26 G. Gao, S. Reibstein, M. Peng and L. Wondraczek, Dual-mode photoluminescence from nanocrystalline Mn^{2+} -doped Li, Zn-aluminosilicate glass ceramics, *Phys. Chem. Glasses: Eur. J. Glass Sci. Technol., Part B*, 2011, **52**, 59.
- 27 G. Lakshminarayana and L. Wondraczek, Photoluminescence and energy transfer in $\text{Tb}^{3+}/\text{Mn}^{2+}$ co-doped ZnAl_2O_4 glass ceramics, *J. Solid State Chem.*, 2011, **184**, 1931.
- 28 M. Shang, G. Li, D. Yang, X. Kang, C. Peng and J. Lin, Luminescence properties of Mn^{2+} -doped $\text{Li}_2\text{ZnGeO}_4$ as an efficient green phosphor for field-emission displays with high color purity, *Dalton Trans.*, 2012, **41**, 8861.
- 29 H. Guo, R. Wei, Y. Wei, X. Liu, J. Gao and C. Ma, $\text{Sb}^{3+}/\text{Mn}^{2+}$ co-doped tunable white emitting borosilicate glasses for LEDs, *Opt. Lett.*, 2012, **37**, 4275.
- 30 N. Guo, H. You, Y. Song, M. Yang, K. Liu, Z. Zheng, Y. Huang and H. Zhang, White-light emission from a single-emitting-component $\text{Ca}_9\text{Gd}(\text{PO}_4)_7\text{:Eu}^{2+}$, Mn^{2+} phosphor with tunable luminescent properties for near-UV light-emitting diodes, *J. Mater. Chem.*, 2010, **20**, 9061.
- 31 C. Yan and P. S. Lee, Synthesis and structure characterization of ternary Zn_2GeO_4 nanowires by chemical vapor transport, *J. Phys. Chem. C*, 2009, **113**, 14135.
- 32 C. Yan, N. Singh and P. S. Lee, Wide-bandgap Zn_2GeO_4 nanowire networks as efficient ultraviolet photodetectors with fast response and recovery time, *Appl. Phys. Lett.*, 2010, **96**, 053108.
- 33 S. Yan, L. Wan, Z. Li and Z. Zou, Facile temperature-controlled synthesis of hexagonal Zn_2GeO_4 nanorods with different aspect ratios toward improved photocatalytic activity for overall water splitting and photoreduction of CO_2 , *Chem. Commun.*, 2011, **47**, 5632.
- 34 Q. Liu, Y. Zhou, J. Kou, X. Chen, Z. Tian, J. Gao, S. Yan and Z. Zou, High-yield synthesis of ultralong and ultrathin Zn_2GeO_4 nanoribbons toward improved photocatalytic

- reduction of CO₂ into renewable hydrocarbon fuel, *J. Am. Chem. Soc.*, 2010, **132**, 14385.
- 35 Z. Liu, X. Jing and L. Wang, Luminescence of native defects in Zn₂GeO₄, *J. Electrochem. Soc.*, 2007, **154**, H500.
- 36 G. Anoop, K. M. Krishna and M. K. Jayaraj, The effect of Mg incorporation on structural and optical properties of Zn₂GeO₄:Mn phosphor, *J. Electrochem. Soc.*, 2008, **155**, J7.
- 37 H. W. Kim, H. G. Na, J. C. Yang and C. Lee, Temperature-controlled synthesis of Zn₂GeO₄ nanowires in a vapor-liquid-solid mode and their photoluminescence properties, *Chem. Eng. J.*, 2011, **171**, 1439.
- 38 M. Shang, G. Li, D. Yang, X. Kang, C. Peang, Z. Cheng and J. Lin, (Zn, Mg)₂GeO₄:Mn²⁺ submicrorods as promising green phosphors for field emission displays: hydrothermal synthesis and luminescence properties, *Dalton Trans.*, 2011, **40**, 9379.
- 39 Y. Takahashi, M. Ando, K. Iwasaki, H. Masai and T. Fujiwara, Defect activation in willemite-type Zn₂GeO₄ by nanocrystallization, *Appl. Phys. Lett.*, 2010, **97**, 071906.
- 40 Q. Zhang and J. Wang, Synthesis and characterization of Zn₂GeO₄:Mn²⁺ phosphor for field emission display, *Appl. Phys. A*, 2012, **108**, 943.
- 41 S. Takeshita, J. Honda, T. Isobe, T. Sawayama and S. Niikura, Size-tunable solvothermal synthesis of Zn₂GeO₄:Mn²⁺ nanophosphor in water/diethylene glycol system, *Cryst. Growth Des.*, 2010, **10**, 4494.
- 42 R. Martín-Rodríguez, R. Valiente and M. Bettinelli, Room-temperature green upconversion luminescence in LaMgAl₁₁O₁₉:Mn²⁺, Yb³⁺ upon infrared excitation, *Appl. Phys. Lett.*, 2009, **95**, 091913.
- 43 C. Reinhard, P. Gerner, F. Rodríguez, S. García-Revilla, R. Valiente and H. Güdel, Near-infrared to green photon upconversion in Mn²⁺ and Yb³⁺ doped lattices, *Chem. Phys. Lett.*, 2004, **386**, 132.
- 44 J. F. Suyver, A. Aebischer, D. Biner, P. Gerne, J. Grimm, S. Heer, K. W. Krämer, C. Reinhard and H. U. Güdel, Novel materials doped with trivalent lanthanides and transition metal ions showing near-infrared to visible photon upconversion, *Opt. Mater.*, 2005, **27**, 1111.
- 45 R. Valiente, O. S. Wenger and H. U. Güdel, Near-infrared-to-visible photon upconversion process induced by exchange interactions in Yb³⁺-doped RbMnCl₃, *Phys. Rev. B: Condens. Matter Mater. Phys.*, 2011, **63**, 165102.
- 46 P. Gerner, O. S. Wenger, R. Valiente and H. U. Güdel, Green and red light emission by upconversion from the near-IR in Yb³⁺ doped CsMnBr₃, *Inorg. Chem.*, 2001, **40**, 4534.
- 47 R. Shannon, Revised effective ionic radii and systematic studies of interatomic distances in halides and chalcogenides, *Acta Crystallogr., Sect. A: Cryst. Phys., Diffr., Theor. Gen. Crystallogr.*, 1976, **32**, 751.
- 48 L. N. Demyanets, S. F. Radaev, B. F. Mamin and B. A. Maksimov, Synthesis and atomic-structure of pyrochlore-type Yb₂Ge₂O₇ crystals, *J. Struct. Chem.*, 1988, **29**, 485.
- 49 K. H. Yoon and J. H. Kim, Structural analysis and luminescent study of thin film zinc germanate doped with manganese, *Thin Solid Films*, 2010, **519**, 1583.
- 50 G. Gao, S. Reibstein, E. Spiecker, M. Peng and L. Wondraczek, Broadband NIR photoluminescence from Ni²⁺-doped nanocrystalline Ba–Al titanate glass ceramics, *J. Mater. Chem.*, 2012, **22**, 2582.
- 51 G. Gao, M. Peng and L. Wondraczek, Temperature dependence and quantum efficiency of ultrabroad NIR photoluminescence from Ni²⁺ centers in nanocrystalline Ba–Al titanate glass ceramics, *Opt. Lett.*, 2012, **37**, 1166.
- 52 A. Winterstein, H. Akamatsu, D. Möncke, K. Tanaka, M. A. Schmidt and L. Wondraczek, Magnetic and magneto-optical quenching in (Mn²⁺, Sr²⁺) metaphosphate glasses, *Opt. Mater. Express*, 2013, **3**, 184.
- 53 A. Patra, G. A. Baker and S. N. Baker, Effects of dopant concentration and annealing temperature on the phosphorescence from Zn₂SiO₄:Mn²⁺ nanocrystals, *J. Lumin.*, 2005, **111**, 105.
- 54 S. Takeshita, J. Honda, T. Isobe, T. Sawayama and S. Niikura, Solvothermal synthesis of Zn₂GeO₄:Mn²⁺ nanophosphor in water/diethylene glycol system, *J. Solid State Chem.*, 2012, **189**, 112.
- 55 N. Da, M. Peng, S. Krolkowski and L. Wondraczek, Intense red photoluminescence from Mn²⁺-doped (Na⁺, Zn²⁺) sulfophosphate glasses and glass ceramics as LED converters, *Opt. Express*, 2010, **18**, 2549.
- 56 G. Gao, N. Da, S. Reibstein and L. Wondraczek, Enhanced photoluminescence from mixed-valence Eu-doped nanocrystalline silicate glass ceramics, *Opt. Express*, 2010, **18**, A575.
- 57 G. Gao, S. Reibstein, M. Peng and L. Wondraczek, Tunable dual-mode photoluminescence from nanocrystalline Eu-doped Li₂ZnSiO₄ glass ceramic phosphors, *J. Mater. Chem.*, 2011, **21**, 3156.
- 58 P. Vergeer, T. J. H. Vlugt, M. H. F. Kox, M. I. den Hertog, J. P. J. M. van der Eerden and A. Meijerink, Quantum cutting by cooperative energy transfer in Yb_xY_{1-x}PO₄:Tb³⁺, *Phys. Rev. B: Condens. Matter Mater. Phys.*, 2005, **71**, 014119.

2.9. Thermal collapse of SAPO-34 molecular sieve towards a perfect glass

Controlled collapse of a silicoaluminophosphate molecular sieve CHA-type SAPO-34 by thermal aging was investigated. Structural changes and the mechanism of order–disorder–order transitions during collapse were followed for varying annealing conditions between 1000 and 1100 °C.

L. Wondraczek, **G. Gao**, D. Moencke, T. Selvam, A. Kuhnt, W. Schwieger, D. Palles and E. I. Kamitsos, *J. Non-cryst. Solids* 2013, **360**, 36-40.-Reproduced by permission of Elsevier B.V., 2013.

<http://www.sciencedirect.com/science/article/pii/S0022309312005777>



Thermal collapse of SAPO-34 molecular sieve towards a perfect glass

Lothar Wondraczek^{a,b,*}, Guojun Gao^{a,b}, Doris Möncke^{a,b}, Thangaraj Selvam^c, Andreas Kuhnt^c, Wilhelm Schwieger^c, Dimitrios Palles^d, Efstratios I. Kamitsos^d

^a Otto-Schott-Institute, University of Jena, 07743 Jena, Germany

^b Department of Materials Science, University of Erlangen-Nuremberg, 91058 Erlangen, Germany

^c Department of Chemical and Bioengineering, University of Erlangen-Nuremberg, 91058 Erlangen, Germany

^d Theoretical and Physical Chemistry Institute, National Hellenic Research Foundation, 11635 Athens, Greece

ARTICLE INFO

Article history:

Received 22 August 2012

Received in revised form 2 October 2012

Available online 7 November 2012

Keywords:

Zeolite;

SAPO-34;

Collapse;

Recrystallization;

Thermal aging

ABSTRACT

Controlled collapse of a silicoaluminophosphate molecular sieve CHA-type SAPO-34 by thermal aging was studied in a multi-method approach. Structural changes and the mechanism of order–disorder–order transitions during collapse were followed for varying annealing conditions between 1000 and 1100 °C. Collapse of SAPO-34 occurs via the formation of an intermediate amorphous state by the loss of long-range order but preservation to a high degree of short-range order and macroscopic morphology. This intermediate amorphous state with low entropy may be classified as a “perfect glass”. Prolonged aging in the collapse regime results in the precipitation of crystalline AlPO_4 while the SiO_2 species initially remain in an amorphous phase. Further increasing the aging temperature leads to virtually complete recrystallization and, ultimately, melting.

© 2012 Elsevier B.V. All rights reserved.

1. Introduction

Glasses represent a – compared to their hypothetical crystalline reference state – high-density amorphous (HDA) configurational state of low affinity and high entropy. They are traditionally formed via a high temperature route, *i.e.*, by freezing-in of a supercooled melt [1,2]. Crystalline zeolites with molecular or nanoscopic porosity, on the other hand, can transform into a low-entropy and low-density amorphous (LDA) phase when exposed to either high pressures or high temperatures [3–5]. This zeolite–LDA transition, the so-called zeolite collapse, offers an alternative route for the preparation of a distinct amorphous state, where the collapse of the crystalline network occurs more rapidly than the formation of the HDA liquid.

The notion of a “perfect glass” was originally introduced by Kauzmann [6]. It refers to a glass with zero configurational entropy as obtained by infinitely slow cooling. As an alternative to slow cooling, first-order phase transitions have been proposed to approach this hypothetical state where the structure of the glass differs only slightly from that of a crystalline reference [7]. The zeolite–LDA transition represents an example of the latter route, where a highly ordered glass can be obtained, provided that the LDA phase can be isolated before recrystallization [8]. In principle, the corresponding HDA reference phase can then be obtained by further heating to beyond the liquidus temperature of the system, and subsequent

quenching to a conventional glass. While both glasses exhibit equivalent chemical composition, they evolve from different crystalline reference states, *i.e.*, the zeolite for the LDA and some hypothetical species for the HDA material. If the sequence of transitions from zeolite to LDA to dense crystal to HDA could be controlled, glassy matrices of specific degrees of order could be fabricated, as an example for the incorporation of optically active dopant species in a controlled ligand setting [9–11]. In practice, however, direct comparison of LDA and HDA is typically complicated by the chemical composition of the employed zeolite, which may experience significant evaporation losses at elevated temperature and/or form highly fragile melts.

The molecular sieve SAPO-34 belongs to a family of synthetic silicoaluminophosphate zeolites with an 8-ring pore opening with chabazite, $(\text{Ca},\text{K}_2,\text{Na}_2)_2[\text{Al}_2\text{Si}_4\text{O}_{12}]_2 \cdot 12\text{H}_2\text{O}$ (CHA) topology. Recently, SAPO-34 has drawn much attention as an excellent catalyst support for methanol-to-olefin (MTO) conversion due to its mild acidity and small pore openings (~3.8 Å in diameter) [12,13]. SAPO-type zeolites are also characterized by medium to strong acidity [14] and high thermal stability [15], both of which might be favorable for the incorporation of dopants in specific (low) redox states [16,17]. The thermal stability of SAPO-34 was examined by Watanabe et al. [18]. In their study, however, the authors focus entirely on the stable region below 1100 °C, in which dehydration and rehydration are reversible. They only hint at the structural changes which may occur at higher temperatures, and do not consider amorphization. A recent attempt by Leardini et al. to amorphize SAPO-34 by high pressure treatment at up to 6.4 GPa failed [19]. In the present paper, we report on the controlled collapse of the SAPO-34 framework structure by prolonged

* Corresponding author at: Otto-Schott-Institute, University of Jena, 07743 Jena, Germany. Tel.: +49-9131 852 7553.

E-mail address: lothar.wondraczek@uni-jena.de (L. Wondraczek).

treatment at elevated temperatures. We give specific attention to the isolation of the LDA phase and consider the conservation of the macroscopic geometry of SAPO-34 particles as an evidence for bypassing the liquid state.

2. Experimental

SAPO-34 was synthesized by a hydrothermal method using morpholine (99%) as template according to the procedure reported in literature [20]. Pseudoboehmite (77.9% Al_2O_3), phosphoric acid (85%) and silica sol (30.4% SiO_2) were used as sources for Al, P and Si, respectively. Morpholine (99%) was used as a template. The synthesis gel was prepared by mixing phosphoric acid with 50% of the total water amount and adding pseudoboehmite slowly under vigorous stirring. The resulting mixture was stirred for 2 h until homogeneous. Silica sol, morpholine and the rest of the water amount were mixed in a beaker and added dropwise to the first mixture and stirred for another 3 h. The resulting nominal composition of the synthesis gel was 1.0 Al_2O_3 :1.06 P_2O_5 :0.7 SiO_2 :2.5 morpholine:66.0 H_2O . After stirring, the final gel was transferred to a Teflon-lined autoclave, which was held at a constant temperature of 190 °C for 24 h. The autoclave was then removed from the oven, quenched with water and the product was filtered and washed with distilled water. After drying at 80 °C overnight, the obtained sample was calcined for 10 h at 550 °C under air flow to remove the template. To facilitate the collapse of the calcined SAPO-34, the samples were heat treated at 1000 to 1100 °C for different time periods. The elemental composition (Si, Al, P) of the calcined sample was determined using inductively coupled plasma optical emission spectroscopy (ICP-OES, Cirros CCD, Spectro). In this way, a composition of SAPO-34 of 1.0 Al_2O_3 –0.89 P_2O_5 –0.59 SiO_2 was found. The collapse process was studied *in situ* by high-temperature powder X-ray diffraction (PXRD), and also *ex situ* at room temperature by PXRD (Siemens Kristalloflex D500, Bragg-Brentano, 30 kV/30 mA, $\text{Cu K}\alpha$) on the annealed sample. Thermal properties were studied by differential scanning calorimetry (DSC, Netzsch DSC 404 F1), thermogravimetric analysis and differential thermal analysis (TGA/DTA, Netzsch Gerätebau, Selb, Germany), all employed at a heating rate of 10 K/min. The morphology of the samples was examined by scanning electron microscopy (SEM, Quanta 200, FEI, Prag, Czech Republic, operated at 20 kV). Infrared spectra were recorded on a Fourier transform infrared spectrometer (FTIR, Equinox55, Bruker Optics) equipped with a single reflection diamond attenuated total reflection (ATR) unit (DuraSample II, SENSIR). The spectra were recorded over the wavenumber range of 525–7000 cm^{-1} with a resolution of 2 cm^{-1} and averaged over 100 scans. The spectra were automatically corrected for the frequency dependence of the penetration depth of the probe beam. Raman spectra were recorded on a confocal micro-Raman instrument (Renishaw) at an excitation wavelength of 488 nm at room temperature over the spectral range of 100–2000 cm^{-1} at a resolution of 2 cm^{-1} .

3. Results and discussion

In situ high-temperature PXRD was used to study directly the structural transformation induced by heat treatment (Fig. 1a). The PXRD pattern of the as calcined sample corresponds to pure SAPO-34 with no diffraction peaks associated with impurity phases. Characteristic diffraction patterns of SAPO-34 (CHA framework) are recorded up to 1050 °C, which indicates that the microporous structure of SAPO-34 is thermally stable up to this temperature (as a result of thermal expansion, all diffraction peaks shift to higher 2θ with increasing temperature) [18,21]. At 1050 °C and above, the intensity of all diffraction peaks decreases significantly, what reflects the beginning collapse of the crystalline structure of SAPO-34. A distinct change in the diffraction pattern occurs at 1100 °C. At this temperature, no diffraction pattern associated with SAPO-34 can be detected anymore. Instead, newly-evolving diffraction peaks at $2\theta \sim 20.48$, ~ 21.62 and $\sim 35.60^\circ$

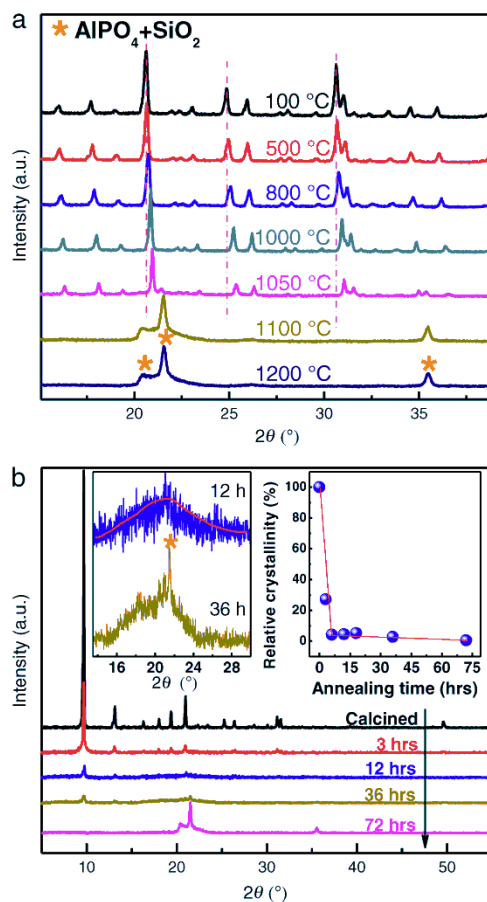


Fig. 1. (a) Temperature-dependent *in situ* and (b) time-dependent *ex situ* PXRD patterns. Aging experiments shown in (b) were conducted at 1000 °C.

can be ascribed to the precipitation of crystalline AlPO_4 and SiO_2 (JCPDS card nos. 01-072-1161 and 00-001-0424, respectively). Due to the structural similarity of both species, it is not possible to distinguish unambiguously between SiO_2 and AlPO_4 [22]. In a preliminary conclusion, these results imply that the structural collapse of SAPO-34 occurs between 1050 and 1100 °C, which is consistent with the findings of Watanabe et al. [18].

In order to more clearly assess the collapse process and to study the corresponding structural changes of SAPO-34 at higher temperatures, powdered samples were annealed at 1000, 1050 and 1075 °C for different time periods (Figs. 1 and 2). The results of *ex situ* PXRD of SAPO-34 annealed at 1000 °C for up to 72 h are shown in Fig. 1b. For annealing below 3 h, SAPO-34 retains its zeolite structure, even though peak intensities appear to weaken (which is indicative of the beginning of the collapse). Annealing for more than 12 h results in a significant decrease of crystallinity (right inset of Fig. 1b), what reflects the fundamental collapse of SAPO-34 under these conditions. In parallel, an amorphous hump at $2\theta \sim 21^\circ$ grows-in as a clear sign for the formation of an amorphous phase (left inset of Fig. 1b). Traces of recrystallization can be detected for even longer annealing, *i.e.* ~ 36 h, when a new diffraction peak was found to develop at $2\theta \sim 21.54^\circ$. As noted before, the latter peak is associated with the occurrence of crystalline AlPO_4 and SiO_2 . A similar observation can be made at higher annealing temperatures, *i.e.*, at 1050 and 1075 °C, where, however,

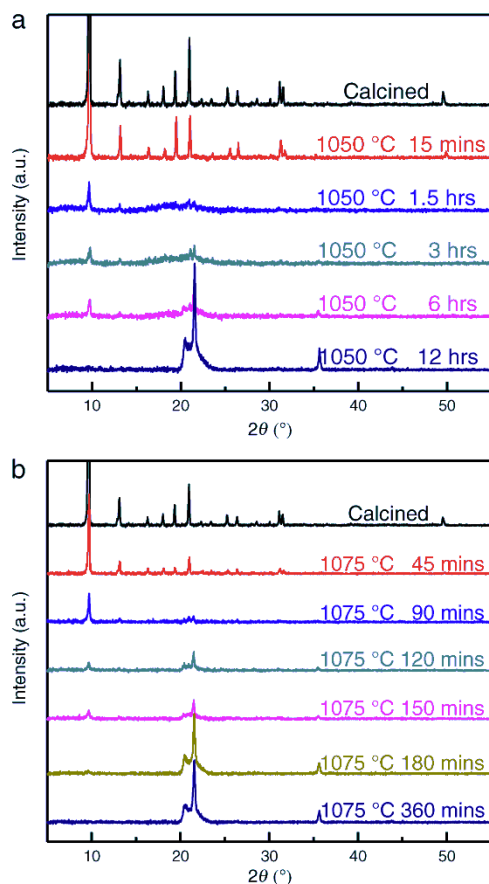


Fig. 2. *Ex situ* PXRD patterns of SAPO-34 after thermal aging at (a) 1050 °C and (b) 1075 °C as a function of aging time.

the collapse of SAPO-34 occurs at progressively shorter annealing durations (see Fig. 2a and b). The *ex situ* PXRD data lead to the second conclusion that a new intermediate amorphous phase in which the long-range order is lost results from the thermal collapse of SAPO-34. We expect that for specific annealing conditions (time and temperature), this new phase, assumedly LDA, can be isolated.

TGA/DTA were used to further examine the thermal stability of SAPO-34 (Fig. 3). A first phase of weight-loss was found in the temperature range of 20 to 250 °C, where about 20 wt.% of the sample evaporates. This observation is due to the loss of molecular water from within the pores of the SAPO-34 framework. A second weight-loss regime is located within ~900 to 1065 °C. This coincides with the temperature range where the zeolitic framework starts to collapse. The DTA curve reveals a corresponding pattern: the very strong endothermic peak at ~123 °C reflects the high water loss around this temperature, whereas the sharp exothermic peak at ~1099 °C arises from the recrystallization of AlPO_4 and SiO_2 species.

Fig. 3b depicts the DSC curves of SAPO-34 samples after thermal aging at 1075 °C for different time periods. During thermal aging at this temperature, partial collapse and, assumedly, recrystallization occur, what should reflect in a gradual decrease of the recrystallization exotherm. The first endothermic peak at ~165 °C is again assigned to the loss of molecular water. The intensity of the endothermic peak decreases with increasing annealing time as the sample becomes more dehydrated. In agreement with the DTA results is the second

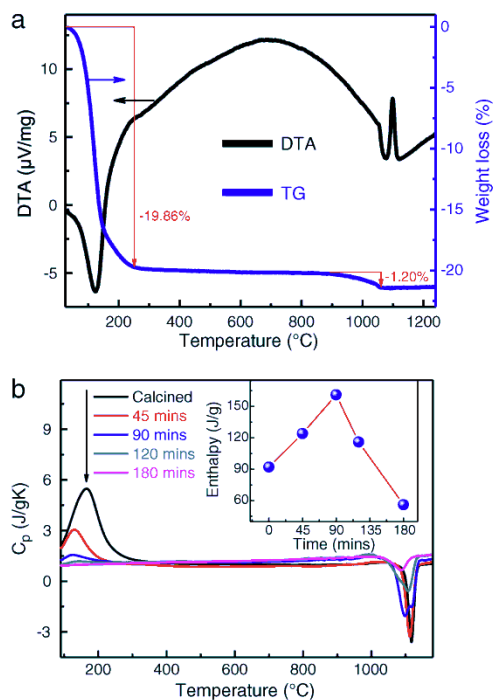


Fig. 3. (a) TG/DTA traces of calcined SAPO-34. (b) DSC curves of SAPO-34 after thermal aging at 1075 °C for different times.

exothermic peak, here found at ~1118 °C, assigned to the recrystallization of AlPO_4 and SiO_2 . For annealing times exceeding 90 min, the exothermic peak is found to split into two weaker peaks, implying separation of two individual recrystallization events. We tentatively assign these peaks to the distinct precipitation of AlPO_4 and SiO_2 . For annealing times over 180 min, the peak intensity decreased to such an extent that the two peaks cannot be distinguished anymore. This indicates that the zeolite-LDA collapse and recrystallization have occurred to a large extent already during thermal aging, and that only a small amount of the amorphous phase remains. The apparent enthalpy ΔH of the recrystallization process is taken as a measure of the progress of collapse and recrystallization during aging. It is calculated by integration of the exothermic DSC signal at ~1100 °C (inset of Fig. 3b). Here, a peak in ΔH is observed for an aging time of 90 min, for which a value of ~161 J/g is reached. For longer annealing times, ΔH decreases significantly, *i.e.* to ~56 J/g for 180 min of aging. Taking into account the PXRD data (Figs. 1 and 2), we interpret this observation as follows: up to an aging time of ~90 min at 1075 °C, the zeolite structure collapses into the LDA phase with no notable recrystallization. During the DSC scan, nucleation and recrystallization occur rapidly at relatively high temperature, what reflects in a sharp and asymmetric exotherm and lower apparent ΔH . For longer aging, partial recrystallization and nucleation, respectively, occur already during the aging process so that the crystallization peak shifts to lower temperature and the value of ΔH decreases.

SEM was carried out to visualize the effect of aging on the morphology of SAPO-34 (Fig. 4a–d). Calcined SAPO-34 exhibits the typical CHA morphology of individual cubes with an edge length of about 5–20 μm . Within the considered experimental regime, this morphology is retained completely throughout the complete aging process: neither collapse nor recrystallization reflects in any visible morphological changes of the sample. This clearly shows that the zeolite-LDA transition occurs without the formation of a liquid phase.

ATR infrared and Raman spectroscopy were used to probe structural changes of the silicate, phosphate and aluminate entities in SAPO-34 after annealing at 1050 °C for different time spans (Fig. 5). As shown in the inset of Fig. 5a, the broad infrared envelope from ~2500 to 3700 cm^{-1} decreases progressively in intensity with annealing time. Since this feature results from O–H stretching vibrations of molecular water and hydroxyl (–OH) groups [23–26], the observed trend confirms the dehydration process during heat treatment as already discussed for thermal analysis. The band at 1630 cm^{-1} observed in both ATR and Raman spectra is due to the bending mode of molecular water [25,26], and is found to exhibit the same trend with that of the ~2500 to 3700 cm^{-1} envelope. The weak doublet centered at around 2355 cm^{-1} in the inset of Fig. 5a can be ignored as it arises from the uncompensated atmospheric CO_2 .

The IR spectra are dominated by a band envelope around 900–1300 cm^{-1} . With increasing aging time, the maximum of this envelope shifts from 1020 cm^{-1} to 1100 cm^{-1} and the shape of the envelope changes. Strong and broad infrared bands at ~1100 cm^{-1} were measured for SAPO-34 materials and attributed to P–O stretching vibrations in PO_4 tetrahedral units [27]. Also, this band was reported to shift to higher frequencies upon increasing crystallinity of the sample [27]. Along these lines, the trend exhibited by the 900–1300 cm^{-1} envelope in Fig. 4a is suggesting the gradual crystallization of the structural entities involving PO_4 tetrahedral units in SAPO-34.

Besides the high frequency envelope, the infrared spectra show bands at ~625 cm^{-1} and 710 cm^{-1} which can be attributed to stretching modes of octahedral and tetrahedral aluminate polyhedral [23,24,28–31]. The ATR spectra show that increasing annealing time causes the gradual disappearance of the 625 cm^{-1} band and its replacement by the band at 710 cm^{-1} . This suggests the transformation of aluminate entities from predominantly six-fold coordination, most probably including the presence of hydroxyl-ligands, to a predominantly four-fold coordination. Such a coordination change for Al^{3+} was reported by Zhang et al. who used NMR spectroscopy to probe the sol–gel processing of Al_2O_3 -containing glasses [31].

Changes with heat treatment are more prominent in the Raman spectra where the initial envelope at 1065 cm^{-1} upshifts with heat treatment and peaks at 1125 cm^{-1} after 12 h of treatment, with its bandwidth decreasing progressively to $\Delta\nu$ ~43 cm^{-1} . Raman bands at about 1060 cm^{-1} were measured for aluminophosphate glasses and attributed to stretching vibrations of P–O–Al bonds [29]. We note at this point the very high similarity of the Raman and infrared

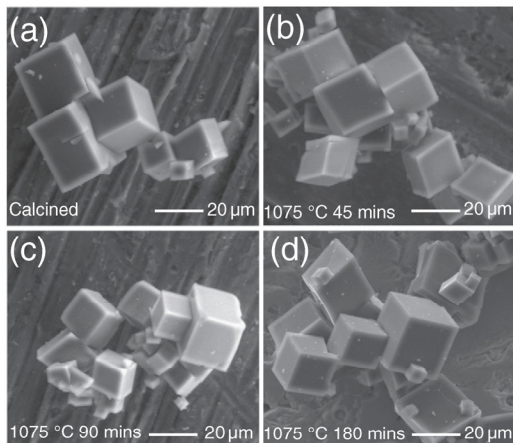


Fig. 4. SEM micrographs of SAPO-34 after aging at 1075 °C for different times.

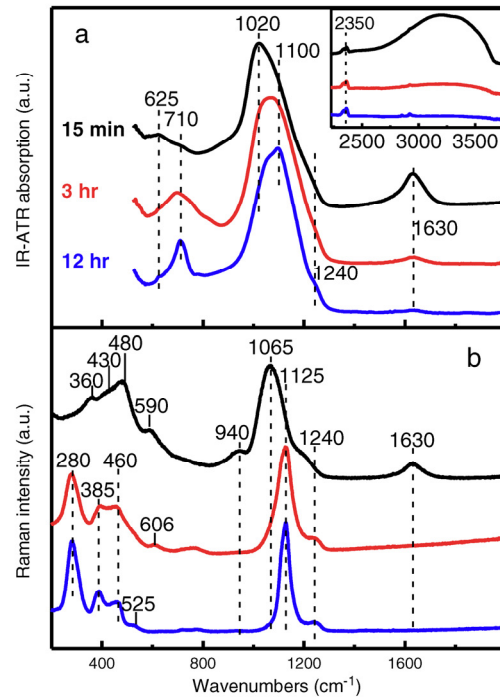


Fig. 5. Normalized (a) ATR infrared and (b) Raman spectra of SAPO-34 after aging at 1050 °C for different times.

spectra of the SAPO-34 sample heat-treated for 12 h with the corresponding spectra of the phosphotridymite polymorph of crystalline AlPO_4 reported by Rokita et al. [22]. The vibrational characteristics of phosphotridymite AlPO_4 were described in terms of internal vibrations of the PO_4^{3-} anion and pseudolattice Al^{3+} vibrations in tetrahedral sites [22]. Therefore, the evolution of both infrared and Raman spectra shows the development of the crystalline AlPO_4 phase in the 12 h heat-treated SAPO-34 sample.

The SAPO-34 composition developed in this work (1.0 Al_2O_3 :0.89 P_2O_5 :0.59 SiO_2) can be rewritten as 1.78 AlPO_4 :0.11 Al_2O_3 :0.59 SiO_2 . Therefore, besides its main AlPO_4 component there is a small excess of Al_2O_3 and a considerable amount of SiO_2 incorporated into the structure. However, the 12 h-treated SAPO-34 sample gives ATR and Raman spectra which are dominated by the response of the AlPO_4 phase (Fig. 5). The question then arises as to the presence of spectroscopic evidence for the SiO_2 phase. The stronger infrared band of silica glass is measured at ~1100 cm^{-1} [32], where the PO_4 tetrahedral units exhibit also their strongest band. Due to this band overlapping, it is difficult to extract information concerning the SiO_2 phase from the infrared range measured by ATR. Nevertheless, relevant information can be obtained from the 15 min Raman spectrum in Fig. 5b, where the bands at ~590 and 480 cm^{-1} and the shoulder at ~430 cm^{-1} are reminiscent of an amorphous silica phase [32]. In particular, the 590 cm^{-1} band (known as defect D2) has been related to the symmetric ring breathing vibration of three-member rings of SiO_4 tetrahedra [33]. Likewise, the band at 480 cm^{-1} (defect D1) can be related to the corresponding mode of four-member silicate rings, and the shoulder at ~430 cm^{-1} to five-fold or six-fold silicate rings. Along these lines, the band resolved at 360 cm^{-1} may signify the presence of even larger silicate rings in the SAPO-34 sample calcinated at 1050 °C for 15 min. The remaining Raman feature of this sample not considered so far is the band at ~940 cm^{-1} . This

can be attributed to the P–OH stretching vibration [23,25,31], while the Si–OH stretching is measured at $\sim 980\text{ cm}^{-1}$ in the Raman spectra of silica gels [32]. Increasing time of heat treatment leads to dehydration, as this is manifested also by the disappearance of the 940 cm^{-1} Raman band. This indicates the transformation of P–OH containing phosphate tetrahedral to PO_4^{3-} anions which give eventually the crystalline AlPO_4 phase. The stronger Raman activity of PO_4^{3-} anions compared to that of the amorphous silicate phase, results in a great reduction of the relative intensity of the silicate signatures in the spectra of the SAPO-34 samples heat treated for 3 and 12 h. Nevertheless, the presence of three-member rings of SiO_4 tetrahedra in the 3 h treated sample is still obvious from the band at 606 cm^{-1} . The absence of this band from the 12 h treated sample suggests the destruction of three-member silicate rings upon prolonged calcinations at $1050\text{ }^\circ\text{C}$.

It results from the above that infrared and Raman spectroscopy provide evidence for the recrystallization of SAPO-34 to a new AlPO_4 phase upon aging, while the silicate phase initially remains in the amorphous state.

4. Conclusions

In conclusion, we first reported on the controlled collapse of the molecular sieve SAPO-34 by thermal aging. The zeolite structure of SAPO-34 is thermally stable up to $1000\text{ }^\circ\text{C}$. Zeolite–LDA collapse occurs in the temperature range of 1000 to $1100\text{ }^\circ\text{C}$ followed by recrystallization at higher temperature or prolonged aging. Thereby, the latter results in the initial precipitation of crystalline AlPO_4 while SiO_2 species retain their amorphous configuration. The macroscopic morphology is retained throughout the whole process of amorphization and recrystallization, indicating that no liquid phases are involved in the transformation process. For specific aging conditions, the LDA phase can be isolated. ATR infrared and Raman results show that the coordination change of Al–polyhedra is from predominantly six-fold with hydroxyl-ligands to predominantly four-fold condensed tetrahedral. SiO_4 tetrahedra are excluded from the AlPO_4 lattice with increase of annealing time, and appear to form an amorphous silica phase with silicate rings of various sizes. Future work will focus on short- and intermediate-range order structure of this new intermediate amorphous state.

Acknowledgments

The authors gratefully acknowledge the financial support by the German Science Foundation (DFG) through the Cluster of Excellence “Engineering of Advanced Materials” – EAM, and also the research program FORETA within the “Klimaprogramm Bayern 2020” of the Bavarian State Government.

References

- [1] G.N. Greaves, S. Sen, *Adv. Phys.* 56 (2007) 1–166.
- [2] J.-L. Garden, H. Guillou, J. Richard, L. Wondraczek, *J. Phys. Chem.* 137 (2012) 024505.
- [3] G.N. Greaves, F. Meneau, F. Kargl, D. Ward, P. Holliman, F. Albergamo, *J. Phys. Condens. Matter* 19 (2007) 415102.
- [4] G.N. Greaves, F. Meneau, A. Sapelkin, L.M. Colyer, I. ap Gwynn, S. Wade, G. Sankar, *Nat. Mater.* 2 (2003) 622–629.
- [5] I. Peral, J. Iñiguez, *Phys. Rev. Lett.* 97 (2006) 225502.
- [6] W. Kauzmann, *Chem. Rev.* 43 (1948) 219–256.
- [7] C.A. Angell, C.T. Moynihan, M. Hemmati, *J. Non-Cryst. Solids* 274 (2000) 319–331.
- [8] J. Haines, C. Levelut, A. Isambert, P. Hébert, S. Kohara, D. Keen, T. Hammouda, D. Andraut, *J. Am. Chem. Soc.* 131 (2009) 12333–12338.
- [9] G. Gao, S. Reibstein, M. Peng, L. Wondraczek, *J. Mater. Chem.* 21 (2011) 3156–3161.
- [10] G. Gao, S. Reibstein, E. Spiecker, M. Peng, L. Wondraczek, *J. Mater. Chem.* 22 (2012) 2582–2588.
- [11] R. Cao, M. Peng, L. Wondraczek, *J. Qiu, Opt. Express* 20 (2012) 2562–2571.
- [12] B.M. Lok, C.A. Messina, R.L. Patton, R.T. Gajek, T.R. Cannan, E.M. Flanigen, *J. Am. Chem. Soc.* 106 (1984) 6092–6093.
- [13] J.Q. Chen, A. Bozzano, B. Glover, T. Fuglerud, S. Kvisle, *Catal. Today* 106 (2005) 103–107.
- [14] S. Ashtekar, S.V.V. Chilukuri, D.K. Chakrabarty, *J. Phys. Chem.* 98 (1994) 4878–4883.
- [15] J. Yu, R. Xu, *Chem. Soc. Rev.* 35 (2006) 593–604.
- [16] A. Winterstein, S. Manning, H. Ebdorff-Heidepriem, L. Wondraczek, *Opt. Mater. Express* 2 (2012) 1320–1328.
- [17] K.H. Nielsen, M.M. Smedskjaer, M. Peng, Y.Z. Yue, L. Wondraczek, *J. Non-Cryst. Solids* 358 (2012) 3193–3199.
- [18] Y. Watanabe, A. Koiwai, H. Takeuchi, S.A. Hyodo, S. Noda, *J. Catal.* 143 (1993) 430–436.
- [19] L. Leardini, S. Quartieri, G. Vezzalini, *Microporous Mesoporous Mater.* 127 (2010) 219–227.
- [20] L. Marchese, A. Frache, E. Gianotti, G. Martra, M. Causà, S. Coluccia, *Microporous Mesoporous Mater.* 30 (1999) 145–153.
- [21] F. Akhtar, L. Bergström, *J. Am. Ceram. Soc.* 94 (2010) 92–98.
- [22] M. Rokita, M. Handke, W. Mozgawa, *J. Mol. Struct.* 555 (2000) 351–356.
- [23] A.C. Chapman, L.E. Thirlwell, *Spectrochim. Acta* 20 (1964) 937–947.
- [24] I. Konidakis, C.P.E. Varsamis, E.I. Kamitsos, *J. Non-Cryst. Solids* 357 (2011) 2684–2689.
- [25] D. Moncke, M. Dussauze, E.I. Kamitsos, C.P.E. Varsamis, D. Ehr, *Phys. Chem. Glasses Eur. J. Glass Sci. Technol. B* 50 (2009) 229–235.
- [26] M. Roulia, K. Chassapis, J.A. Kapoutsis, E.I. Kamitsos, T. Savvidis, *J. Mater. Sci.* 41 (2006) 5870–5881.
- [27] H. van Heyden, S. Mintova, T. Bein, *Chem. Mater.* 20 (2008) 2956–2963.
- [28] A. Belkèbir, J. Rocha, A.P. Esculcas, P. Berthet, B. Gilbert, Z. Gabelica, G. Llabres, F. Wijzen, A. Rulmont, *Spectrochim. Acta A Mol. Biomol. Spectrosc.* 55 (1999) 1323–1336.
- [29] R.K. Brow, D.R. Tallant, Z.A. Osborne, Y. Yang, D.E. Day, *Phys. Chem. Glasses* 32 (1991) 188–195.
- [30] D. Moncke, D. Ehr, L.L. Velli, C.P.E. Varsamis, E.I. Kamitsos, S. Elbers, H. Eckert, *Phys. Chem. Glasses Eur. J. Glass Sci. Technol. B* 48 (2007) 399–402.
- [31] L. Zhang, H. Eckert, *Solid State Nucl. Magn. Reson.* 26 (2004) 132–146.
- [32] E.I. Kamitsos, A.P. Patsis, G. Kordas, *Phys. Rev. B* 48 (1993) 12499–12505.
- [33] F.L. Galeener, *J. Non-Cryst. Solids* 49 (1982) 53–62.

3. Summary

A glass ceramic route of reducing Eu^{3+} to Eu^{2+} has been demonstrated in two glass ceramic systems. During the controlled nucleation and crystallization processes under air, Eu^{3+} ions are partially incorporated into the newly deposited crystalline phases, i.e., $\text{BaAl}_2\text{Si}_2\text{O}_8/\text{LaBO}_3$ and $\text{Li}_2\text{ZnSiO}_4$, and are gradually reduced to Eu^{2+} . The reduction process may be understood by a charge compensation model. The PL properties of Eu^{3+} and Eu^{2+} are studied in detail. For the SABBL glass system, heat treatments at temperatures ≥ 850 °C result in the appearance of hexacelsian $\text{BaAl}_2\text{Si}_2\text{O}_8$ and monoclinic LaBO_3 . Meanwhile, Eu^{3+} species are incorporated on La^{3+} sites in LaBO_3 , leading to the strongly increased PL intensity and the prolonged lifetime of the excited state of $\text{Eu}^{3+}:^5\text{D}_0$. No Eu^{2+} species are observed in the as-melted glass. However, Eu^{3+} ions are partially incorporated on two Ba^{2+} sites of different coordination in the hexacelsian phase and they are reduced to Eu^{2+} after crystallization. For the SLZAKP glass system, the precipitation of crystalline $\text{Li}_2\text{ZnSiO}_4$ phase is controlled simply by thermal annealing of the as-melted precursor glass. During this process, a significant amount of Eu^{3+} ions is incorporated into the crystalline phase and subsequently reduced to Eu^{2+} . Dual-mode PL from both Eu-species is demonstrated upon excitation at 361 nm. Depending on the employed annealing temperature and, hence, the degree of crystallization, the resulting color of the PL can be finely tuned from orange via red and violet to blue. Energy transfer from Eu^{2+} to Eu^{3+} is observed.

Tunable dual-mode [$^{\text{IV}}\text{Mn}^{2+}$]/[$^{\text{VI}}\text{Mn}^{2+}$] PL properties of Mn^{2+} doped SLZAKP glasses and $\text{Li}_{4-2(x+y)}\text{Zn}_x\text{Mn}_y\text{SiO}_4$ glass ceramics are investigated. Mn^{2+} is octahedrally coordinated in the SLZAKP glassy matrix, giving rise to the orange to red emission of $^{\text{VI}}\text{Mn}^{2+}$. During the controlled crystallization process, Mn^{2+} ions are partially incorporated into the $\text{Li}_{4-2(x+y)}\text{Zn}_x\text{Mn}_y\text{SiO}_4$ crystal phase on tetrahedral Zn^{2+} sites, which provides the green emission of $^{\text{IV}}\text{Mn}^{2+}$. The ratio of $^{\text{IV}}\text{Mn}^{2+}/^{\text{VI}}\text{Mn}^{2+}$ and thus the corresponding green/red PL bands respectively can be adjusted simply by controlling the annealing temperature and the degree of crystallization in the glass ceramics. The PL band of $^{\text{IV}}\text{Mn}^{2+}/^{\text{VI}}\text{Mn}^{2+}$ covers a very broad range from 480 to 800 nm with a FWHM of more than 110 nm. The overall emission intensity of $^{\text{IV}}\text{Mn}^{2+}/^{\text{VI}}\text{Mn}^{2+}$ increases with the degree of crystallization mainly due to the multiple scattering.

Broadband whitish green PL of V^{5+} doped SLZAKP glasses and corresponding nanocrystalline $\text{Li}_2\text{ZnSiO}_4$ glass ceramics with possible use as broadband UV-to-Vis photoconverters is studied. The V^{5+} ion presents a broad whitish green PL band from 400

to 700 nm centered at 550–590 nm with a FWHM of ~250 nm and with a lifetime of ~34 μ s due to the relaxation of $\equiv V-O^-$ to $\equiv V=O$. While the position of the PL band remains unaffected by dopant concentration (within the considered range), a notable blue-shift occurs after crystallization. The optimal dopant concentration is found to be at ~0.5 mol% V_2O_5 . The broad PLE band covers the complete UV-B to UV-A spectral region. After crystallization, the emission intensity of V^{5+} shows a strong increase by a factor of ~10, which is attributed to the incorporation of V^{5+} species into the crystal phase.

Broadband NIR PL of $VI Ni^{2+}$ doped nanocrystalline Ba-Al titanate glass ceramics from supercooled TBSA melts is demonstrated. Volume crystallization occurs sequentially in $BaTiO_3$ and Ba-Al hollandite-type crystallites. The crystallite size is ~30 nm. The CN of Ni^{2+} is well controlled by the crystallization process. Ni^{2+} ions are tetrahedrally coordinated in the precursor glass and do not show any NIR PL band, whereas after crystallization the Ni^{2+} -species are incorporated into the crystalline environment in octahedral coordination giving rise to a NIR band. The NIR PL of $VI Ni^{2+}$ covers a broad spectral range of 1.0–1.6 μ m with a FWHM greater than 350 nm and a lifetime of ~60 μ s due to the spin-allowed relaxation of $VI Ni^{2+}:^3T_{2g}(^3F) \rightarrow ^3A_{2g}(^3F)$. The optimal PL efficiency of $VI Ni^{2+}$ is found for an absolute NiO concentration of 0.05–0.1 mol% and crystallization at 800–850 $^{\circ}C$ for 1–2 hrs. Interestingly, the NIR emission can be excited with conventional NUV light sources. Under excitation at 352 nm, an η_{IQE} of 65% is obtained for the optimized sample. The stimulated emission cross-section σ_{em} and figure of merit for an optical gain medium $\sigma_{em} * \tau$ at room temperature are calculated to be $8.2 \times 10^{-20} \text{ cm}^2$ and $3.1 \times 10^{-24} \text{ cm}^2\text{s}$, respectively. Decay kinetics as well as position and shape of the emission band can be adjusted via dopant concentration and synthesis conditions.

NIR down-conversion based on Pr^{3+}/Yb^{3+} and Mn^{2+}/Yb^{3+} pairs is investigated. For Pr^{3+}/Yb^{3+} pair, down-conversion of one blue photon to two NIR photons (~10,000 cm^{-1}) is obtained from Pr^{3+}/Yb^{3+} co-doped SLABS glasses and corresponding $LaBO_3$ glass ceramics. Pr^{3+} ions act as sensitizers by absorbing 415–505 nm photons and transferring the absorbed energy to Yb^{3+} ions in a cooperative down-conversion process, resulting in NIR emission of Yb^{3+} at ~1000 nm. The energy transfer occurs through both $Pr^{3+}:^3P_0$ and $Pr^{3+}:^1D_2$ levels to Yb^{3+} , which is evidenced by the decrease of Pr^{3+} PL in intensity and the lifetime of both $Pr^{3+}:^3P_0$ and $Pr^{3+}:^1D_2$ levels with increasing Yb^{3+} doping concentration, along with the observation of typical Pr^{3+} PLE bands by monitoring PL of Yb^{3+} at 976 nm. The energy transfer from $Pr^{3+}:^3P_0$ level to Yb^{3+} is a down-conversion process of one visible photon into two NIR photons, whereas that from $Pr^{3+}:^1D_2$ level to Yb^{3+} is a down-shifting process. The efficiency of the former is higher than that of the latter. The highest total

theoretical quantum efficiency is ~183%, if only the down-conversion energy transfer process from $\text{Pr}^{3+}:^3\text{P}_0$ to Yb^{3+} is considered. The optimum doping concentration of Yb_2O_3 for down-conversion is ~0.5 mol%. Crystallization of the as-melt SLABS glass sample leads to the formation of a main crystal phase LaBO_3 and a minor crystal phase $\text{SrAl}_2\text{B}_2\text{O}_7$. Both Pr^{3+} and Yb^{3+} ions occupy the La^{3+} ion sites in the LaBO_3 crystal phase after crystallization, resulting in improved PL properties.

NIR down-conversion of $\text{Mn}^{2+}/\text{Yb}^{3+}$ pair in crystalline $\text{Zn}_{1.96-x}\text{GeO}_{4+1/2x}:\text{Mn}_{0.04}\text{Yb}_x$ is demonstrated. In the Zn_2GeO_4 lattice, Mn^{2+} ions partition on Zn^{2+} sites in the form of tetrahedral MnO_4 groups, give rise to the typical green PL band of $^{\text{IV}}\text{Mn}^{2+}$. The absorption of Zn_2GeO_4 and Mn^{2+} covers a very broad spectral range of 250–500 nm, which is responsible for the broadband sensitization of Yb^{3+} . Energy transfer occurs either from defect levels of Zn_2GeO_4 to two neighboring $\text{Yb}^{3+}:^2\text{F}_{5/2}$ centers via $^{\text{IV}}\text{Mn}^{2+}:^6\text{A}_1(^6\text{S})$ or through intrinsic excitation of $^{\text{IV}}\text{Mn}^{2+}:^6\text{A}_1(^6\text{S})$. The occurrence of this energy transfer process is evidenced by reduced green PL intensity from $^{\text{IV}}\text{Mn}^{2+}$, corresponding reduced PL lifetime and reduced η_{EQE} with increasing Yb^{3+} concentration, and identical PLE spectra when monitoring PL from $^{\text{IV}}\text{Mn}^{2+}$ and NIR PL from Yb^{3+} . The transfer process results in the cooperative down-conversion of one visible photon into two NIR photons. The estimated maximum η_{IQE} and total theoretical quantum efficiency are ~64 and 164%, respectively.

4. Zusammenfassung

Für zwei Glaskeramiksysteeme wird eine Prozessroute zur Reduzierung von Eu^{3+} zu Eu^{2+} aufgezeigt. Unter kontrollierten Keimbildungs- und Kristallisationsschritten an Luft werden Eu^{3+} -Ionen teilweise in die abgeschiedene kristalline Phase, $\text{BaAl}_2\text{Si}_2\text{O}_8/\text{LaBO}_3$ und $\text{Li}_2\text{ZnSiO}_4$, eingebaut und nach und nach auf Grund der Ladungskompensation zu Eu^{2+} reduziert. Die Reduktion kann nach einem Ladungsausgleichsmodell verstanden werden. Die Photolumineszenzeigenschaften von Eu^{3+} und Eu^{2+} werden im Detail untersucht. Wärmebehandlung eines SABBL-Glassystems bei über $850\text{ }^\circ\text{C}$ führt zur Bildung von $\text{BaAl}_2\text{Si}_2\text{O}_8$ und monoklinen LaBO_3 . Gleichzeitig werden Eu^{3+} -Ionen an La^{3+} -Plätzen in LaBO_3 eingebaut. Dies führt zu einer stark erhöhten Photolumineszenzintensität und verlängerter Lebensdauer der angeregten $^5\text{D}_0$ -Zustände von Eu^{3+} -Ionen. Im Ursprungsglas konnten keine Eu^{2+} -Ionen gefunden werden. Eu^{3+} -Ionen werden dagegen teilweise an zwei Ba^{2+} -Plätzen unterschiedlicher Koordinierung in der Hexacelsianphase eingebaut und zu Eu^{2+} reduziert. Bei einem SLZKAP-Glassystem wird die Ausscheidung von $\text{Li}_2\text{ZnSiO}_4$ über thermisches Anlassen des erschmolzenen Ausgangsglases an Luft kontrolliert. Bei diesem Vorgang wird eine beträchtliche Menge an Eu^{3+} -Ionen in die kristalline Phase eingebaut und anschließend zu Eu^{2+} reduziert. Dual-mode Photolumineszenz, angeregt bei 361 nm , wird für beide Redoxzustände nachgewiesen. Die Farbe der Lumineszenz kann abhängig von der Anlasstemperatur durch den Grad der Kristallisation in kleinen Schritten von orange bis blau über rot und violett eingestellt werden. Energieübergangsprozesse von Eu^{2+} zu Eu^{3+} werden beobachtet.

Ferner werden einstellbare dual-mode $[\text{IVMn}^{2+}]/[\text{VIMn}^{2+}]$ Photolumineszenzeigenschaften von Mn^{2+} dotierten SLZAKP-Gläsern und $\text{Li}_{4-2(x+y)}\text{Zn}_x\text{Mn}_y\text{SiO}_4$ -Glaskeramiken vorgestellt. Im SLZAKP-Glas sind die Mn^{2+} -Ionen oktaedrisch angeordnet, was zu einer orangenen bis roten Emission von VIMn^{2+} führt. Mn^{2+} wird während der kontrollierten Kristallisation teilweise in die $\text{Li}_{4-2(x+y)}\text{Zn}_x\text{Mn}_y\text{SiO}_4$ -Kristallphase an Zn^{2+} -Tetraederplätzen eingebaut, die eine grüne Emission von IVMn^{2+} aufweisen. Das Verhältnis von IVMn^{2+} zu VIMn^{2+} und damit die entsprechenden grünen und roten Photolumineszenzbänder können über die Anlasstemperatur und dem Grad der Kristallisation der Glaskeramiken eingestellt werden. Das Photolumineszenzband von $\text{IVMn}^{2+}/\text{VIMn}^{2+}$ deckt den weiten Bereich von 480 nm bis 800 nm ab und besitzt eine Halbwertsbreite von mehr als 110 nm . Die Emissionsintensität von $\text{IVMn}^{2+}/\text{VIMn}^{2+}$ erhöht sich mit dem Grad der Kristallisation hauptsächlich wegen mehrfacher Streuprozesse.

Breitbandige, weißlich grüne Photolumineszenz von V^{5+} -dotierten Zink-Silikat-Gläsern und den zugehörigen nanokristallinen Li_2ZnSiO_4 -Glaskeramiken wird untersucht. Eine mögliche Anwendung sind Breitband UV-zu-Vis-Photokonverter. Das V^{5+} -Ion besitzt eine breite, weißlich grüne Photolumineszenz von 400 nm bis 700 nm, mit einem Maximum zwischen 550 nm und 590 nm bei einer Halbwertsbreite von rund 250 nm und einer Lebensdauer von 34 μs , die durch die Relaxation von $\equiv V-O^-$ zu $\equiv V=O$ bedingt ist. Innerhalb des betrachteten Konzentrationsbereichs ist die Position des Photolumineszenzbandes unabhängig von der Dotandenkonzentration, eine merkliche Blauverschiebung findet jedoch nach der Kristallisation statt. Die optimale Dotandenkonzentration wird bei rund 0,5 mol% V_2O_5 ermittelt. Der breite Photolumineszenzanregung deckt den ganzen UV-B bis UV-A Bereich des Spektrums ab. Nach der Kristallisation erhöht sich die Emissionsintensität der V^{5+} -Ionen um den Faktor zehn, was auf den Einbau von V^{5+} -Ionen in die Kristallphase zurückzuführen ist.

Für $^{VI}Ni^{2+}$ dotierte nanokristalline Ba-Al-Titanat-Glaskeramiken, hergestellt aus unterkühlten TBSA-Schmelzen, wird eine Breitband NIR-Photolumineszenz gezeigt. In $BaTiO_3$ und Ba-Al-hollanditartigen Kristalliten tritt eine Volumen kristallisation auf. Die Kristallitgröße beträgt rund 30 nm. Die Koordinationszahl von Ni^{2+} wird durch den Kristallisationsprozess gut kontrolliert. Im Ausgangsglas sind Ni^{2+} -Ionen tetraedrisch koordiniert und zeigen kein NIR-Photolumineszenzband. Dagegen sind Ni^{2+} -Ionen (nach der Kristallisation) in kristalliner Umgebung oktaedrisch angeordnet, folglich besitzen diese ein NIR-Band. Die NIR-Photolumineszenz von $^{VI}Ni^{2+}$ deckt einen breiten spektralen Bereich von 1,0 μm bis 1,6 μm ab. Die Halbwertsbreite ist größer als 350 nm. Die Lumineszenzlebensdauer beträgt wegen der spin-erlaubten Relaxation von $^{VI}Ni^{2+}:^3T_{2g}(^3F)$ zu $^3A_{2g}(^3F)$ rund 60 μs . Die optimale Effizienz der Lumineszenz von $^{VI}Ni^{2+}$ liegt bei einer absoluten NiO-Konzentration von 0,05–0,1 mol% und einer Kristallisation bei 800–850 $^{\circ}C$ für ein bis zwei Stunden. Erstaunlicherweise kann die NIR-Emission mit einer konventionellen NUV-Lichtquelle angeregt werden. Bei einer Anregung von 352 nm wird eine interne Quanteneffizienz von 65% für die optimierte Probe erreicht. Der angeregte Emissionsquerschnitt σ_{em} und die Gütezahl eines optischen Verstärkermediums $\sigma_{em} \cdot \tau$ bei Raumtemperatur werden zu $8,2 \times 10^{-20} \text{ cm}^2$ und $3,1 \times 10^{-24} \text{ cm}^2 \text{ s}$ berechnet. Sowohl die Abklingkinetik als auch die Position und Form des Emissionsbandes können über die Dotandenkonzentration und Synthesebedingungen eingestellt werden.

Es wird des Weiteren über einen NIR-down-conversion Prozess berichtet, die auf Pr^{3+}/Yb^{3+} - und Mn^{2+}/Yb^{3+} -Paaren beruht. Für Pr^{3+}/Yb^{3+} -Paare in Pr^{3+}/Yb^{3+} -dotierten SLABS-Gläsern und entsprechenden $LaBO_3$ -Glaskeramiken erhält man eine down-

conversion von einem blauen Photon zu zwei NIR-Photonen (rund 10.000 cm^{-1}). Pr^{3+} -Ionen agieren als „Sensibilisatoren“, da sie Photonen im Bereich 415–505 nm absorbieren und die absorbierte Energie Yb^{3+} -Ionen in einem mitwirkenden down-conversion Prozess übergeben, der in einer NIR-Emission des Yb^{3+} bei rund 1000 nm resultiert. Der Energieübergang findet zwischen $\text{Pr}^{3+}:^3\text{P}_0$ und $\text{Pr}^{3+}:^1\text{D}_2$ -Niveaus zu Yb^{3+} statt, was durch die Abnahme aller Pr^{3+} -Photolumineszenzbänder gezeigt wird. Die Lebensdauer beider $\text{Pr}^{3+}:^3\text{P}_0$ und $\text{Pr}^{3+}:^1\text{D}_2$ -Niveaus nimmt mit zunehmender Yb^{3+} -Dotandenkonzentration ab, was die typischen Pr^{3+} -Bänder zeigen, die durch Photolumineszenz von Yb^{3+} bei 976 nm beobachtet werden. Der Energieübergang von dem $\text{Pr}^{3+}:^3\text{P}_0$ -Niveau zu Yb^{3+} ist ein down-conversion Prozess eines sichtbaren Photons in zwei NIR-Photonen. Dagegen ist der Energieübergang vom $\text{Pr}^{3+}:^1\text{D}_2$ Niveau zum Yb^{3+} ein down-shifting-Prozess. Der Energieübergang des ersten Vorgangs ist effizienter als der letztgenannte. Die höchste theoretische Quanteneffizienz wird zu rund 183% berechnet, wenn nur der down-conversion-Energietransfer von $\text{Pr}^{3+}:^3\text{P}_0$ zu Yb^{3+} berücksichtigt wird. Die optimale Dotandenkonzentration von Yb_2O_3 für einen down-conversion Prozess liegt bei ca. 0,5 mol%. Eine Kristallisation der erschmolzenen SLABS-Glasproben führt vorwiegend zur Bildung von LaBO_3 -Kristallphasen. Daneben bilden sich noch $\text{SrAl}_2\text{B}_2\text{O}_7$ -Kristallphasen. Sowohl Pr^{3+} -Ionen als auch Yb^{3+} -Ionen nehmen Plätze der La^{3+} -Ionen in den LaBO_3 -Kristallphasen ein, was zu einer Verbesserung der Photolumineszenzeigenschaften führt.

Zum ersten Mal wird eine NIR-down-conversion von $\text{Mn}^{2+}/\text{Yb}^{3+}$ -Paaren in kristallinem $\text{Zn}_{1,96-x}\text{GeO}_{4+1/2x}:\text{Mn}_{0,04}\text{Yb}_x$ gezeigt. Im Zn_2GeO_4 -Gitter nehmen Mn^{2+} -Ionen Zn^{2+} -Plätze in Form von tetraedrischen MnO_4 -Gruppen ein. Dies führt zu einem typischen grünen Photolumineszenzband von $^{\text{IV}}\text{Mn}^{2+}$. Die Absorption von Zn_2GeO_4 und Mn^{2+} deckt einen breiten Spektralbereich zwischen 250 und 500 nm ab, was für die Sensibilität von Yb^{3+} verantwortlich ist. Ein Energieübergang kann entweder durch Defektniveaus von Zn_2GeO_4 zu zwei benachbarten $\text{Yb}^{3+}:^2\text{F}_{5/2}$ -Zentren über $^{\text{IV}}\text{Mn}^{2+}:^6\text{A}_1(^6\text{S})$ oder durch die intrinsische Anregung von $^{\text{IV}}\text{Mn}^{2+}:^6\text{A}_1(^6\text{S})$ vonstattengehen. Das Auftreten dieses Energieübergangs wird nachgewiesen durch:

- Verkürzte Lebensdauer der grünen Photolumineszenz von $^{\text{IV}}\text{Mn}^{2+}$
- reduzierter externer Quanteneffizienz bei zunehmender Yb^{3+} Konzentration
- identisches Photolumineszenz-Anregungsspektrum bei der Photolumineszenz von $^{\text{IV}}\text{Mn}^{2+}$ und NIR-Photolumineszenz von Yb^{3+} .

Der Übergang führt zu dem kooperativen down-conversion Prozess eines sichtbaren Photons in zwei NIR-Photonen. Die abgeschätzte maximale Effizienz des

Energieübergangs beträgt rund 64%, die gesamte theoretische Quanteneffizienz etwa 164%.

5. References

1. G. Blasse, and B. C. Grabmaier, *Luminescent materials*, Springer-Verlag, 1994.
2. C. Ronda, *Luminescence: From Theory to Applications*, 2007.
3. S. Shionoya, W. M. Yen, and H. Yamamoto, *Phosphor Handbook*, CRC Press, 2010.
4. E. Desurvire, J. R. Simpson, and P. C. Becker, *Opt. Lett.*, 1987, **12**, 888–890.
5. M. J. Weber, *J. Non-Cryst. Solids*, 1990, **123**, 208–222.
6. D. Ehrt, *IOP Conf. Ser.: Mater. Sci. Eng.*, 2009, **2**, 012001.
7. E. W. J. L. Oomen, and A. M. A. van Dongen, *J. Non-Cryst. Solids*, 1989, **111**, 205–213.
8. M. Wachtler, A. Speghini, K. Gatterer, H. P. Fritzer, D. Ajò, and M. Bettinelli, *J. Am. Ceram. Soc.*, 1998, **81**, 2045–2052.
9. X. Huang, S. Han, W. Huang, and X. Liu, *Chem. Soc. Rev.*, 2012, **42**, 173–201.
10. Q. Zhang, and X. Huang, *Prog. Mater. Sci.*, 2010, **55**, 353–427.
11. M. Yamane, and Y. Asahara, *Glasses for Photonics*, Cambridge University Press, 2000.
12. F. Gan, *Laser Materials*, World Scientific, 1995.
13. W. Holand, and G. H. Beall, *Glass Ceramic Technology*, John Wiley & Sons, 2012.
14. E. L. Bourhis, *Glass*, John Wiley & Sons, 2008.
15. W. Vogel, *Glass chemistry*, Springer-Verlag, 1994.
16. C. Zhang, J. Yang, C. Lin, C. Li, and J. Lin, *J. Solid State Chem.*, 2009, **182**, 1673–1678.
17. R. D. Shannon, *Acta Crystallogr. A*, 1976, **32**, 751–767.
18. S.-B. Sohn, S.-Y. Choi, G.-H. Kim, H.-S. Song, and G.-D. Kim, *J. Am. Ceram. Soc.*, 2004, **87**, 254–260.
19. Y. Zhuang, Y. Teng, J. Luo, B. Zhu, Y. Chi, E. Wu, H. Zeng, and J. Qiu, *Appl. Phys. Lett.*, 2009, **95**, 111913.
20. C. Bertail, S. Maron, V. Buissette, T. Le Mercier, T. Gacoin, and J.-P. Boilot, *Chem. Mater.*, 2011, **23**, 2961–2967.
21. M. Shang, G. Li, D. Yang, X. Kang, C. Peng, and J. Lin, *Dalton Trans.*, 2012, **41**, 8861–8868.
22. N. Guo, H. You, Y. Song, M. Yang, K. Liu, Y. Zheng, Y. Huang, and H. Zhang, *J. Mater. Chem.*, 2010, **20**, 9061–9067.
23. Y. Fujimoto, H. Tanno, K. Izumi, S. Yoshida, S. Miyazaki, M. Shirai, K. Tanaka, Y. Kawabe, and E. Hanamura, *J. Lumin.*, 2008, **128**, 282–286.
24. M. Anpo, I. Tanahashi, and Y. Kubokawa, *J. Phys. Chem.*, 1980, **84**, 3440–3443.
25. L. F. Johnson, R. E. Dietz, and H. J. Guggenheim, *Phys. Rev. Lett.*, 1963, **11**, 318–320.
26. S. Zhou, N. Jiang, B. Zhu, H. Yang, S. Ye, G. Lakshminarayana, J. Hao, and J. Qiu, *Adv. Funct. Mater.*, 2008, **18**, 1407–1413.
27. T. Suzuki, G. Senthil Murugan, and Y. Ohishi, *J. Lumin.*, 2005, **113**, 265–270.
28. P. T. Diallo, P. Boutinaud, R. Mahiou, and J. C. Cousseins, *phys. status sol. (a)*, 1997, **160**, 255–263.
29. K. L. Ley, M. Krumpelt, R. Kumar, J. H. Meiser, and I. Bloom, *J. Mater. Res.*, 1996, **11**, 1489–1493.
30. G. Anoop, K. M. Krishna, and M. K. Jayaraj, *J. Electrochem. Soc.*, 2008, **155**, J7–J10.
31. E. Snitzer, *Phys. Rev. Lett.*, 1961, **7**, 444–446.
32. A. Žukauskas, R. Vaicekauskas, F. Ivanauskas, H. Vaitkevičius, and M. S. Shur, *Appl. Phys. Lett.*, 2008, **93**, 051115.
33. S. Neeraj, N. Kijima, and A. Cheetham, *Chem. Phys. Lett.*, 2004, **387**, 2–6.

34. R. Schmechel, M. Kennedy, H. von Seggern, H. Winkler, M. Kolbe, R. A. Fischer, L. Xiaomao, A. Benker, M. Winterer, and H. Hahn, *J. Appl. Phys.*, 2001, **89**, 1679–1686.
35. D. Tu, Y. Liu, H. Zhu, R. Li, L. Liu, and X. Chen, *Angew. Chem. Int. Edit.*, 2013, **52**, 1128–1133.
36. M. Banski, A. Podhorodecki, J. Misiewicz, M. Afzaal, A. L. Abdelhady, and P. O'Brien, *J. Mater. Chem. C*, 2013, **1**, 801–807.
37. A. Katelnikovas, J. Plewa, S. Sakirzanovas, D. Dutczak, D. Enseling, F. Baur, H. Winkler, A. Kareiva, and T. Jüstel, *J. Mater. Chem.*, 2012, **22**, 22126–22134.
38. F. Du, Y. Nakai, T. Tsuboi, Y. Huang, and H. J. Seo, *J. Mater. Chem.*, 2011, **21**, 4669–4678.
39. P. F. Smet, A. B. Parmentier, and D. Poelman, *J. Electrochem. Soc.*, 2011, **158**, R37–R54.
40. C. H. Kam, and S. Buddhudu, *J. Quant. Spectrosc. Ra.*, 2004, **87**, 325–337.
41. Y. Li, A. C. A. Delsing, G. de With, and H. T. Hintzen, *Chem. Mater.*, 2005, **17**, 3242–3248.
42. X. Zhang, and X. Liu, *J. Electrochem. Soc.*, 1992, **139**, 622–625.
43. S. Thomas, J. Oró-Solé, B. Glorieux, V. Jubera, V. Buissette, T. L. Mercier, A. Garcia, and A. Fuertes, *J. Mater. Chem.*, 2012, **22**, 23913–23920.
44. M. Zeuner, S. Pagano, and W. Schnick, *Angew. Chem. Int. Edit.*, 2011, **50**, 7754–7775.
45. T. Nakanishi, and S. Tanabe, *phys. status sol. (a)*, 2009, **206**, 919–922.
46. Z. Shan, D. Chen, Y. Yu, P. Huang, H. Lin, and Y. Wang, *J. Mater. Sci.*, 2010, **45**, 2775–2779.
47. S. Fujita, S. Yoshihara, A. Sakamoto, S. Yamamoto, and S. Tanabe, *2005 SPIE Fifth International Conference on Solid State Lighting*, 2005, 594111.
48. S. Zhou, G. Feng, B. Wu, N. Jiang, S. Xu, and J. Qiu, *J. Phys. Chem. C*, 2007, **111**, 7335–7338.
49. J. de Wild, A. Meijerink, J. K. Rath, W. G. J. H. M. van Sark, and R. E. I. Schropp, *Energy Environ. Sci.*, 2011, **4**, 4835–4848.
50. D. Chen, Y. Wang, and M. Hong, *Nano Energy*, 2012, **1**, 73–90.
51. P. Dorenbos, *J. Mater. Chem.*, 2012, **22**, 22344–22349.
52. B. M. van der Ende, L. Aarts, and A. Meijerink, *Phys. Chem. Chem. Phys.*, 2009, **11**, 11081–11095.
53. J. C. Poggendorff, E. Wiedemann, and G. H. Wiedemann, *Annalen der Physik*, J.A. Barth, 1888.
54. B. Valeur, and M. N. Berberan-Santos, *J. Chem. Educ.*, 2011, **88**, 731–738.
55. C. Feldmann, T. Jüstel, C. r. Ronda, and P. j. Schmidt, *Adv. Funct. Mater.*, 2003, **13**, 511–516.
56. H. A. Höppe, *Angew. Chem. Int. Edit.*, 2009, **48**, 3572–3582.
57. N. A. Atari, *Phys. Lett. A*, 1982, **90**, 93–96.
58. T. Jüstel, H. Nikol, and C. Ronda, *Angew. Chem. Int. Edit.*, 1998, **37**, 3084–3103.
59. C. Zhang, and J. Lin, *Chem. Soc. Rev.*, 2012, **41**, 7938–7961.
60. A. Sharma, and S. G. Schulman, *Introduction to Fluorescence Spectroscopy*, Wiley-Interscience, 1st edn., 1999.
61. G. Gauglitz, and T. Vo-Dinh, *Handbook of Spectroscopy*, Wiley-VCH Verlag GmbH & Co. KGaA, 2005.
62. K. A. Franz, W. G. Kehr, A. Siggel, J. Wiczoreck, and W. Adam, *Ullmann's Encyclopedia of Industrial Chemistry*, Wiley-VCH Verlag GmbH & Co. KGaA, 2000.
63. A. Kitai, *Luminescent Materials and Applications*, John Wiley & Sons, 2008.
64. E. Matioli, C. Neufeld, M. Iza, S. C. Cruz, A. A. Al-Heji, X. Chen, R. M. Farrell, S. Keller, S. DenBaars, U. Mishra, S. Nakamura, J. Speck, and C. Weisbuch, *Appl. Phys. Lett.*, 2011, **98**, 021102.

65. J. M. F. van Dijk, and M. F. H. Schuurmans, *J. Chem. Phys.*, 1983, **78**, 5317–5323.
66. B. S. Richards, *Sol. Energ. Mat. Sol. C*, 2006, **90**, 1189–1207.
67. R. T. Wegh, H. Donker, K. D. Oskam, and A. Meijerink, *Science*, 1999, **283**, 663–666.
68. B. M. van der Ende, L. Aarts, and A. Meijerink, *Adv. Mater.*, 2009, **21**, 3073–3077.
69. S. H. Park, K. H. Lee, S. Unithrattil, H. S. Yoon, H. G. Jang, and W. B. Im, *J. Phys. Chem. C*, 2012, **116**, 26850–26856.
70. G. Gao, G. Wang, C. Yu, J. Zhang, and L. Hu, *J. Lumin.*, 2009, **129**, 1042–1047.
71. Y. Guo, G. Gao, M. Li, L. Hu, and J. Zhang, *Mater. Lett.*, 2012, **80**, 56–58.
72. J.-C. G. Bünzli, and S. V. Eliseeva, *Chem. Sci.*, 2013.
73. M. Humphries, *Rare Earth Elements: The Global Supply Chain*, DIANE Publishing, 2010.
74. S. V. Eliseeva, and J.-C. G. Bünzli, *Chem. Soc. Rev.*, 2009, **39**, 189–227.
75. P. H. Hänninen, and H. Härmä, *Lanthanide Luminescence: Photophysical, Analytical and Biological Aspects*, Springer, 2011.
76. J. Rubio O., *J. Phys. Chem. Solids*, 1991, **52**, 101–174.
77. P. Dorenbos, *J. Lumin.*, 2000, **91**, 155–176.
78. G. H. Dieke, *Spectra and Energy Levels of Rare Earth Ions in Crystals*, Interscience Publ., 1968.
79. S. Pimputkar, J. S. Speck, S. P. DenBaars, and S. Nakamura, *Nat. Photon.*, 2009, **3**, 180–182.
80. S. Kück, *Appl. Phys. B-Lasers O.*, 2001, **72**, 515–562.
81. S. Ye, F. Xiao, Y. Pan, Y. Ma, and Q. Zhang, *Mater. Sci. Eng. R Rep.*, 2010, **71**, 1–34.
82. F. Auzel, *Chem. Rev.*, 2004, **104**, 139–174.
83. M. T. Jose, and A. R. Lakshmanan, *Opt. Mater.*, 2004, **24**, 651–659.
84. Y. Jin, J. Zhang, S. Lu, H. Zhao, X. Zhang, and X. Wang, *J. Phys. Chem. C*, 2008, **112**, 5860–5864.
85. Z. Xia, and R.-S. Liu, *J. Phys. Chem. C*, 2012, **116**, 15604–15609.
86. Y. Zhang, D. Geng, M. Shang, X. Zhang, X. Li, Z. Cheng, H. Lian, and J. Lin, *Dalton Trans.*, 2012.
87. B. Han, J. Zhang, and Y. Lü, *J. Am. Ceram. Soc.*, 2013, **96**, 179–183.
88. B. Han, H. Liang, Y. Huang, Y. Tao, and Q. Su, *J. Phys. Chem. C*, 2010, **114**, 6770–6777.
89. M. Xie, Y. Tao, Y. Huang, H. Liang, and Q. Su, *Inorg. Chem.*, 2010, **49**, 11317–11324.
90. Q. Su, Z. Pei, L. Chi, H. Zhang, Z. Zhang, and F. Zou, *J. Alloys Compd.*, 1993, **192**, 25–27.
91. Y.-C. Li, Y.-H. Chang, Y.-F. Lin, Y.-S. Chang, and Y.-J. Lin, *J. Alloys Compd.*, 2007, **439**, 367–375.
92. G. Li, C. Li, C. Zhang, Z. Cheng, Z. Quan, C. Peng, and J. Lin, *J. Mater. Chem.*, 2009, **19**, 8936–8943.
93. S. Tanabe, *C. R. Chimie*, 2002, **5**, 815–824.
94. J. E. Geusic, H. M. Marcos, and L. G. Van Uitert, *Appl. Phys. Lett.*, 1964, **4**, 182–184.
95. J. W. Stouwdam, and F. C. J. M. van Veggel, *Nano Lett.*, 2002, **2**, 733–737.
96. D. . Machewirth, K. Wei, V. Krasteva, R. Datta, E. Snitzer, and G. . Sigel Jr., *J. Non-Cryst. Solids*, 1997, **213–214**, 295–303.
97. K. Wei, D. P. Machewirth, J. Wenzel, E. Snitzer, and J. Sigel, *Opt. Lett.*, 1994, **19**, 904–906.
98. A. P. Vink, P. Dorenbos, J. T. M. de Haas, H. Donker, P. A. Rodnyi, A. G. Avanesov, and C. W. E. van Eijk, *J. Phys.: Condens. Matter*, 2002, **14**, 8889.
99. L. Shaw, B. Harbison, B. Cole, J. Sanghera, and I. Aggarwal, *Opt. Express*, 1997, **1**, 87–96.
100. M. C. Brierley, and P. W. France, *Electron. Lett.*, 30, **23**, 815–817.
101. Z. Yang, G. Tang, L. Luo, and W. Chen, *Appl. Phys. Lett.*, 2006, **89**, 131117–131117–3.
102. R. J. Mears, L. Reekie, I. M. Jauncey, and D. N. Payne, *Electron. Lett.*, 10, **23**, 1026–1028.

103. J. F. Philipps, T. Töpfer, H. Ebendorff-Heidepriem, D. Ehrhart, and R. Sauerbrey, *Appl. Phys. B*, 2001, **72**, 399–405.
104. H. M. Pask, R. J. Carman, D. C. Hanna, A. C. Tropper, C. J. Mackechnie, P. R. Barber, and J. M. Dawes, *IEEE J. Sel. Top. Quant.*, 1995, **1**, 2–13.
105. D. D. Hudson, S. D. Jackson, and B. J. Eggleton, *2012 IEEE 3rd International Conference on Photonics (ICP)*, 2012, 381–385.
106. J. S. Sanghera, L. Brandon Shaw, and I. D. Aggarwal, *IEEE J. Sel. Top. Quant.*, 2009, **15**, 114–119.
107. S. D. Jackson, *Nat. Photon.*, 2012, **6**, 423–431.
108. D. J. Richardson, J. Nilsson, and W. A. Clarkson, *J. Opt. Soc. Am. B*, 2010, **27**, B63–B92.
109. N. G. Boetti, E. Mura, J. Lousteau, D. Milanese, D. Negro, G. C. Scarpignato, and G. Perrone, *International conference on Spce Optics (ICSO)*, 2012, 1–5.
110. J. Heo, Y. B. Shin, and J. N. Jang, *Appl. Opt.*, 1995, **34**, 4284–4289.
111. H. Lin, X. Wang, L. Lin, C. Li, D. Yang, and S. Tanabe, *J. Phys. D: Appl. Phys.*, 2007, **40**, 3567.
112. J. Heo, *J. Mater. Sci. Lett.*, 1995, **14**, 1014–1016.
113. Z. Pan, C. Duan, and P. A. Tanner, *Phys. Rev. B*, 2008, **77**, 085114.
114. C. Wickleder, *J. Alloys Compd.*, 2000, **300–301**, 193–198.
115. M. Peng, Z. Pei, G. Hong, and Q. Su, *J. Mater. Chem.*, 2003, **13**, 1202–1205.
116. Z. Lian, J. Wang, Y. Lv, S. Wang, and Q. Su, *J. Alloys Compd.*, **430**, 257–261.
117. Y. Li, G. de With, and H. T. Hintzen, *J. Lumin.*, 2006, **116**, 107–116.
118. C.-H. Huang, T.-W. Kuo, and T.-M. Chen, *ACS Appl. Mater. Interfaces*, 2010, **2**, 1395–1399.
119. J. M. Phillips, M. E. Coltrin, M. H. Crawford, A. J. Fischer, M. R. Krames, R. Mueller-Mach, G. O. Mueller, Y. Ohno, L. E. S. Rohwer, J. A. Simmons, and J. Y. Tsao, *Laser Photonics Rev.*, 2007, **1**, 307–333.
120. W.-R. Liu, C.-H. Huang, C.-P. Wu, Y.-C. Chiu, Y.-T. Yeh, and T.-M. Chen, *J. Mater. Chem.*, 2011, **21**, 6869–6874.
121. J. Zhou, Z. Xia, M. Yang, and K. Shen, *J. Mater. Chem.*, 2012, **22**, 21935–21941.
122. W. B. Im, N. George, J. Kurzman, S. Brinkley, A. Mikhailovsky, J. Hu, B. F. Chmelka, S. P. DenBaars, and R. Seshadri, *Adv. Mater.*, 2011, **23**, 2300–2305.
123. V. Bachmann, C. Ronda, and A. Meijerink, *Chem. Mater.*, 2009, **21**, 2077–2084.
124. S. P. Feofilov, A. B. Kulinkin, R. I. Zakharchenya, J. Hölsä, and M. Malkamäki, *phys. status sol. (b)*, 2013, **250**, 249–253.
125. C. Liu, H. Liang, X. Kuang, J. Zhong, S. Sun, and Y. Tao, *Inorg. Chem.*, 2012, **51**, 8802–8809.
126. M. Anson, M. W. McGeoch, and R. C. Smith, *J. Chem. Phys.*, 1973, **59**, 2143–2144.
127. K.-B. Kim, Y.-I. Kim, H.-G. Chun, T.-Y. Cho, J.-S. Jung, and J.-G. Kang, *Chem. Mater.*, 2002, **14**, 5045–5052.
128. Y.-C. Chiu, W.-R. Liu, C.-K. Chang, C.-C. Liao, Y.-T. Yeh, S.-M. Jang, and T.-M. Chen, *J. Mater. Chem.*, 2010, **20**, 1755–1758.
129. D.-Y. Wang, C.-H. Huang, Y.-C. Wu, and T.-M. Chen, *J. Mater. Chem.*, 2011, **21**, 10818–10822.
130. C.-H. Huang, Y.-C. Chen, T.-W. Kuo, and T.-M. Chen, *J. Lumin.*, 2011, **131**, 1346–1349.
131. R. Yu, H. Li, H. Ma, C. Wang, H. Wang, B. K. Moon, and J. H. Jeong, *J. Lumin.*, 2012, **132**, 2783–2787.
132. C.-H. Huang, Y.-C. Chiu, Y.-T. Yeh, T.-S. Chan, and T.-M. Chen, *ACS Appl. Mater. Interfaces*, 2012, **4**, 6661–6668.

133. X. Piao, K. Machida, T. Horikawa, H. Hanzawa, Y. Shimomura, and N. Kijima, *Chem. Mater.*, 2007, **19**, 4592–4599.
134. C.-W. Yeh, W.-T. Chen, R.-S. Liu, S.-F. Hu, H.-S. Sheu, J.-M. Chen, and H. T. Hintzen, *J. Am. Chem. Soc.*, 2012, **134**, 14108–14117.
135. E. Beurer, J. Grimm, P. Gerner, and H. U. Güdel, *J. Am. Chem. Soc.*, 2006, **128**, 3110–3111.
136. O. S. Wenger, C. Wickleder, K. W. Krämer, and H. U. Güdel, *J. Lumin.*, 2001, **94–95**, 101–105.
137. W. J. Schipper, A. Meijerink, and G. Blasse, *J. Lumin.*, 1994, **62**, 55–59.
138. S. Lizzo, A. Meijerink, G. J. Dirksen, and G. Blasse, *J. Lumin.*, 1995, **63**, 223–234.
139. F. A. Cotton, *Progress in Inorganic Chemistry*, John Wiley & Sons, 2009.
140. J. Solé, *An Introduction to the Optical Spectroscopy of Inorganic Solids*, John Wiley and Sons, 2005.
141. Y. Tanabe, and S. Sugano, *J. Phys. Soc. Jpn.*, 1954, **9**, 753–766.
142. Y. Tanabe, and S. Sugano, *J. Phys. Soc. Jpn.*, 1954, **9**, 766–779.
143. S. Kück, and P. Jander, *Opt. Mater.*, 1999, **13**, 299–310.
144. S. A. Payne, L. L. Chase, L. K. Smith, W. L. Kway, and H. W. Newkirk, *J. Appl. Phys.*, 1989, **66**, 1051–1056.
145. R. F. Curl, and F. K. Tittel, *Annu. Rep. Prog. Chem., Sect. C: Phys. Chem.*, 2002, **98**, 219–272.
146. J.-P. Meyn, T. Danger, K. Petermann, and G. Huber, *J. Lumin.*, 1993, **55**, 55–62.
147. L. F. Johnson, and H. J. Guggenheim, *J. Appl. Phys.*, 1967, **38**, 4837–4839.
148. W. Knierim, A. Honold, U. Brauch, and U. Durr, *J. Opt. Soc. Am. B*, 1986, **3**, 119–124.
149. S. Kück, L. Fornasiero, E. Mix, and G. Huber, *J. Lumin.*, 2000, **87–89**, 1122–1125.
150. T. H. Maiman, *Nature*, 1960, **187**, 493–494.
151. N. B. Manson, G. A. Shah, B. Howes, and C. D. Flint, *Mol. Phys.*, 1977, **34**, 1157–1174.
152. R. Kasa, and S. Adachi, *J. Electrochem. Soc.*, 2012, **159**, J89–J95.
153. D. Galanciak, M. Grinberg, W. Gryk, S. Kobayakov, A. Suchocki, G. Boulon, and A. Brenier, *J. Phys.: Condens. Matter*, 2005, **17**, 7185–7197.
154. S. Kück, S. Hartung, S. Hurling, K. Petermann, and G. Huber, *Phys. Rev. B*, 1998, **57**, 2203–2216.
155. H. Manaa, Y. Guyot, and R. Moncorge, *Phys. Rev. B*, 1993, **48**, 3633–3645.
156. M. Duarte, E. Martins, S. L. Baldochi, S. P. Morato, N. D. Vieira, and M. M. F. Vieira, *Opt. Commun.*, 1998, **151**, 366–373.
157. I. Zakosky-Neuberger, I. Shafir, L. Nagli, and A. Katzir, *Appl. Phys. Lett.*, 2011, **99**, 201111.
158. C. Albrecht, S. Cohen, I. Mayer, and D. Reinen, *J. Solid State Chem.*, 1993, **107**, 218–228.
159. D. Ehrentraut, M. Pollnau, and S. Kück, *Appl. Phys. B*, 2002, **75**, 59–62.
160. T. C. Brunold, H. U. Güdel, S. Kück, and G. Huber, *J. Opt. Soc. Am. B*, 1997, **14**, 2373–2377.
161. H.-J. Schulz, and M. Thiede, *J. Phys. C: Solid State Phys.*, 1988, **21**, L1033.
162. S. Kück, K. Petermann, U. Pohlmann, and G. Huber, *Phys. Rev. B*, 1995, **51**, 17323–17331.
163. D. Welford and M. A. Jaspan, *J. Opt. Soc. Am. B*, 2004, **21**, 2137–2141.
164. A. Sennaroglu, *Prog. Quant. Electron.*, 2002, **26**, 287–352.
165. H. R. Verdun, L. M. Thomas, D. M. Andrauskas, T. McCollum, and A. Pinto, *Appl. Phys. Lett.*, 1988, **53**, 2593–2595.
166. U. Oetliker, M. Herren, H. U. Güdel, U. Kesper, C. Albrecht, and D. Reinen, *J. Chem. Phys.*, 1994, **100**, 8656–8665.
167. M. Herren, and H. U. Guedel, *Inorg. Chem.*, 1992, **31**, 3683–3684.

168. R. H. Page, K. I. Schaffers, L. D. DeLoach, G. D. Wilke, F. D. Patel, J. Tassano, J.B., S. A. Payne, W. F. Krupke, K.-T. Chen, and A. Burger, *IEEE J. Quant. Electron.*, 1997, **33**, 609–619.
169. C. I. Rablau, J.-O. Ndap, X. Ma, A. Burger, and N. C. Giles, *J. Elec. Mater.*, 1999, **28**, 678–682.
170. S. Mirov, V. Fedorov, I. Moskalev, D. Martyshkin, and C. Kim, *Laser Photonics Rev.*, 2010, **4**, 21–41.
171. L. D. DeLoach, R. H. Page, G. D. Wilke, S. A. Payne, and W. F. Krupke, *IEEE J. Quant. Electron.*, 1996, **32**, 885–895.
172. E. F. Schubert, and J. K. Kim, *Science*, 2005, **308**, 1274–1278.
173. S. Pimputkar, J. S. Speck, S. P. DenBaars, and S. Nakamura, *Nat. Photon.*, 2009, **3**, 180–182.
174. H. Daicho, T. Iwasaki, K. Enomoto, Y. Sasaki, Y. Maeno, Y. Shinomiya, S. Aoyagi, E. Nishibori, M. Sakata, H. Sawa, S. Matsuishi, and H. Hosono, *Nat. Commun.*, 2012, **3**, 1132.
175. E. F. Schubert, J. K. Kim, H. Luo, and J.-Q. Xi, *Rep. Prog. Phys.*, 2006, **69**, 3069.
176. E. F. Schubert, T. Gessmann, and J. K. Kim, *Kirk-Othmer Encyclopedia of Chemical Technology*, John Wiley & Sons, Inc., 2000.
177. X. Fang, M. Roushan, R. Zhang, J. Peng, H. Zeng, and J. Li, *Chem. Mater.*, 2012, **24**, 1710–1717.
178. X. Zhang, A. Marathe, S. Sohal, M. Holtz, M. Davis, L. J. Hope-Weeks, and J. Chaudhuri, *J. Mater. Chem.*, 2012, **22**, 6485–6490.
179. K.-W. Huang, W.-T. Chen, C.-I. Chu, S.-F. Hu, H.-S. Sheu, B.-M. Cheng, J.-M. Chen, and R.-S. Liu, *Chem. Mater.*, 2012, **24**, 2220–2227.
180. J. Y. Han, W. B. Im, G. Lee, and D. Y. Jeon, *J. Mater. Chem.*, 2012, **22**, 8793–8798.
181. W.-R. Liu, C.-H. Huang, C.-W. Yeh, J.-C. Tsai, Y.-C. Chiu, Y.-T. Yeh, and R.-S. Liu, *Inorg. Chem.*, 2012, **51**, 9636–9641.
182. Z. Xia, J. Zhuang, and L. Liao, *Inorg. Chem.*, 2012, **51**, 7202–7209.
183. V. Sivakumar, and U. V. Varadaraju, *J. Solid State Chem.*, 2008, **181**, 3344–3351.
184. B. S. Richards, *Sol. Energy Mater. Sol. C.*, 2006, **90**, 2329–2337.
185. T. Trupke, A. Shalav, B. S. Richards, P. Würfel, and M. A. Green, *Sol. Energy Mater. Sol. C.*, 2006, **90**, 3327–3338.
186. T. Trupke, M. A. Green, and P. Würfel, *J. Appl. Phys.*, 2002, **92**, 1668–1674.
187. D. Chen, Y. Wang, Y. Yu, P. Huang, and F. Weng, *Opt. Lett.*, 2008, **33**, 1884.
188. X. Wei, S. Huang, Y. Chen, C. Guo, M. Yin, and W. Xu, *J. Appl. Phys.*, 2010, **107**, 103107.
189. X. Huang, X. Ji, and Q. Zhang, *J. Am. Ceram. Soc.*, 2011, **94**, 833–837.
190. A. K. Varshneya, *Fundamentals of Inorganic Glasses*, Gulf Professional Publishing, 1994.
191. P. Hartmann, R. Jedamzik, S. Reichel, and B. Schreder, *Appl. Opt.*, 2010, **49**, D157–D176.
192. G. Partridge, *Adv. Mater.*, 1992, **4**, 668–673.
193. W. Pannhorst, *J. Non-Cryst. Solids*, 1997, **219**, 198–204.
194. K. Binnemans, *Chem. Rev.*, 2009, **109**, 4283–4374.
195. R. Casasola, J. M. Rincón, and M. Romero, *J. Mater. Sci.*, 2012, **47**, 553–582.
196. G. H. Beall, *Annu. Rev. Mater. Sci.*, 1992, **22**, 91–119.
197. G. H. Beall, and L. R. Pinckney, *J. Am. Ceram. Soc.*, 1999, **82**, 5–16.
198. Y. Wang, and J. Ohwaki, *Appl. Phys. Lett.*, 1993, **63**, 3268–3270.
199. A. de Pablos-Martín, N. Hémono, G. C. Mather, S. Bhattacharyya, T. Höche, H. Bornhöft, J. Deubener, F. Muñoz, A. Durán, and M. J. Pascual, *J. Am. Ceram. Soc.*, 2011, **94**, 2420–2428.
200. C. Rüssel, *Chem. Mater.*, 2005, **17**, 5843–5847.
201. R. D. Rawlings, J. P. Wu, and A. R. Boccaccini, *J. Mater. Sci.*, 2006, **41**, 733–761.
202. A. Sakamoto, and S. Yamamoto, *Int. J. Appl. Glass Sci.*, 2010, **1**, 237–247.

Acknowledgements

The work for the dissertation was carried out primarily at Chair of Glass and Ceramics (WW3), Department of Materials Science, University of Erlangen-Nuremberg from October 1st 2009 to January 31th 2013, and partly at the Otto-Schott-Institut, University of Jena from February 1st 2013 to July 1st 2013. The dissertation could not have been finished without the kind help of so many people.

Firstly, I owe my deepest gratitude to my supervisor Prof. Dr. Lothar Wondraczek for offering me the opportunity to pursue a Ph. D degree in Germany. I thank him very much for his support, encouragement, helpful discussions and careful guidance during my Ph.D. study of the past four years.

I would like to express my sincere gratitude to Prof. Dr. Mingying Peng (South China University of Technology) who provided many helpful suggestions and valuable discussions during the first year of my Ph. D. study as well as the low temperature photoluminescence measurements. Thanks also to Dr. Doris Möncke for the FTIR and Raman measurements, corresponding data analysis, and valuable suggestions on my thesis. I would like to give many thanks to Dipl.-Min. Sindy Reibstein for XRD and TEM measurements and data analysis, and thesis proof reading. A very special thanks to M.Sc. Karsten Hansgaard Nielsen for help and guidance with UV-Vis absorption measurements, and valuable discussions. I would like to express my gratitude to Dipl.-Ing. Alfons Stiegelschmitt for his professional help on XRD measurements, to Ms. Eva Springer for the SEM measurements, and to Ms. Sabine Brungs for the TGA-DTA, DSC and EPR measurements. I would like to give a special thanks to Dr. rer. nat. Wolfgang Wisniewski for thesis preparation and proof reading. Special thanks also go to Dr. Xinjiao Wang and Dr. Qing Ye for their kind help on my thesis.

I would like to thank other glass group members in Otto-Schott-Institut in Jena: M.Sc. Bruno Poletto Rodrigues, M.Sc. Dominik Orzol, Dipl.-Ing. Anja Winterstein-Beckmann, M.Sc. Rene Limbach, Dipl.-Chem. Theresia Palenta, Dr. Alvise Parma, Dipl.-Chem. Kristin Griebenow and Dr. rer. nat. Andreas Herrmann for all kind help on my thesis and the nice time we spent together.

I am also grateful to all other glass group members in Erlangen: Dipl.-Ing. Sebastian Krolikowski, M.Sc. Ning Da, Dipl.-Ing. (FH) Robert Meszaros, M.Sc. Lukaš Simurka and Dr. Sergey Sirotkin, and to other members of WW3 in Erlangen: Dipl.-Ing. (FH) Helmut Hädrich, Ms. Evelyn Gruber, Ms. Hana Strelec, Mr. Andreas Thomsen, Dr. Tobias Fey,

Ms. Karin Bichler, Ms. Candice Iwai, Ms. Evelyne Penert-Müller, Ms. Ursula Klarmann and Mr. Timotheus Barreto-Nunes for all kind help and the nice time we spent together.

Last but not least, I would like to express my gratitude to my parents and all of my friends for their help and support. I own my warmest thanks to my wife Yanle Wang for company, encouragement and care in Germany. I could not finish my thesis without her support and help. I dedicate the dissertation to my wife and my daughter, Menglei Gao, who is two years old.

Bestätigung der Autorenschaft

Hiermit wird bestätigt, dass Guojun Gao der Autor der folgenden Publikationen ist:

1. **G. Gao** and L. Wondraczek, “Near-infrared downconversion in Pr³⁺/Yb³⁺ co-doped boro-aluminosilicate glasses and LaBO₃ glass ceramics,” *Opt. Mater. Express* 2013, **3**, 633–644.
2. **G. Gao** and L. Wondraczek, “Near-Infrared down-conversion in Mn²⁺–Yb³⁺ co-doped Zn₂GeO₄,” *J. Mater. Chem. C* 2013, **1**, 1952–1958.
3. L. Wondraczek, **G. Gao**, D. Moencke, T. Selvam, A. Kuhnt, W. Schwieger, D. Palles and E. I. Kamitsos, “Thermal collapse of SAPO-34 molecular sieve towards a perfect glass,” *J. Non-cryst. Solids* 2013, **360**, 36-40.
4. **G. Gao**, M. Peng and L. Wondraczek, “Temperature dependence and quantum efficiency of ultrabroad NIR photoluminescence from Ni²⁺ centers in nanocrystalline Ba–Al titanate glass ceramics” *Opt. Lett.* 2012, **37**, 1166–1168.
5. **G. Gao**, S. Reibstein, E. Spiecker, M. Peng and L. Wondraczek, “Broadband NIR photoluminescence from Ni²⁺-doped nanocrystalline Ba–Al titanate glass ceramics” *J. Mater. Chem.* 2012, **22**, 2582–2588.
6. **G. Gao**, R. Meszaros, S. Reibstein and L. Wondraczek, “Broadband UV-to-green photoconversion in V-doped lithium zinc silicate glasses and glass ceramics,” *Opt. Express* 2011, **19**, A312–A318.
7. **G. Gao**, S. Reibstein, M. Peng and L. Wondraczek, “Enhanced broadband green and red photoluminescence from transparent Mn²⁺-doped nanocrystallized silicate glass ceramics,” *Phys. Chem. Glass - Euro. J. Glass Sci. Tech. Part B* 2011, **52**, 59–63.
8. **G. Gao**, S. Reibstein, M. Peng and L. Wondraczek, “Tunable dual-mode photoluminescence from nanocrystalline Eu-doped Li₂ZnSiO₄ glass ceramic phosphors,” *J. Mater. Chem.* 2011, **21**, 3156–3161.
9. **G. Gao**, N. Da, S. Reibstein and L. Wondraczek, “Enhanced photoluminescence from mixed-valence Eu-doped nanocrystalline silicate glass ceramics,” *Opt. Express* 2010, **18**, A576–A583.

Jena, den 1. August 2013

.....
Prof. Dr. Lothar. Wondraczek

List of publications

1. **G. Gao** and L. Wondraczek, “Near-infrared downconversion in $\text{Pr}^{3+}/\text{Yb}^{3+}$ co-doped boro-aluminosilicate glasses and LaBO_3 glass ceramics,” *Opt. Mater. Express* 2013, **3**, 633–644.
2. **G. Gao** and L. Wondraczek, “Near-Infrared down-conversion in $\text{Mn}^{2+}-\text{Yb}^{3+}$ co-doped Zn_2GeO_4 ,” *J. Mater. Chem. C* 2013, **1**, 1952–1958.
3. L. Wondraczek, **G. Gao**, D. Moencke, T. Selvam, A. Kuhnt, W. Schwieger, D. Palles and E. I. Kamitsos, “Thermal collapse of SAPO-34 molecular sieve towards a perfect glass,” *J. Non-cryst. Solids* 2013, **360**, 36-40.
4. **G. Gao**, M. Peng and L. Wondraczek, “Temperature dependence and quantum efficiency of ultrabroad NIR photoluminescence from Ni^{2+} centers in nanocrystalline Ba–Al titanate glass ceramics” *Opt. Lett.* 2012, **37**, 1166–1168.
5. **G. Gao**, S. Reibstein, E. Spiecker, M. Peng and L. Wondraczek, “Broadband NIR photoluminescence from Ni^{2+} -doped nanocrystalline Ba–Al titanate glass ceramics” *J. Mater. Chem.* 2012, **22**, 2582–2588.
6. **G. Gao**, R. Meszaros, S. Reibstein and L. Wondraczek, “Broadband UV-to-green photoconversion in V-doped lithium zinc silicate glasses and glass ceramics,” *Opt. Express* 2011, **19**, A312–A318.
7. **G. Gao**, S. Reibstein, M. Peng and L. Wondraczek, “Enhanced broadband green and red photoluminescence from transparent Mn^{2+} -doped nanocrystallized silicate glass ceramics,” *Phys. Chem. Glass - Euro. J. Glass Sci. Tech. Part B* 2011, **52**, 59–63.
8. **G. Gao**, S. Reibstein, M. Peng and L. Wondraczek, “Tunable dual-mode photoluminescence from nanocrystalline Eu-doped $\text{Li}_2\text{ZnSiO}_4$ glass ceramic phosphors,” *J. Mater. Chem.* 2011, **21**, 3156–3161.
9. **G. Gao**, N. Da, S. Reibstein and L. Wondraczek, “Enhanced photoluminescence from mixed-valence Eu-doped nanocrystalline silicate glass ceramics,” *Opt. Express* 2010, **18**, A576–A583.

Oral presentations

1. “Near-infrared down-conversion in $\text{Pr}^{3+}/\text{Yb}^{3+}$ co-doped boro-aluminosilicate glasses and LaBO_3 glass ceramics”
The 23rd International Congress on Glass, Prague, Czech Republic, (2013)
2. “Efficient red-emitting phosphors from high level Eu^{3+} -doped boro-aluminosilicate glasses”
Oberseminar, Otto-Schott-Institut, University of Jena (2013)
3. “Near-infrared down-conversion in $\text{Mn}^{2+}-\text{Yb}^{3+}$ co-doped Zn_2GeO_4 ”
Oberseminar, Otto-Schott-Institut, University of Jena (2013)
4. “Tunable photoluminescence from mixed-valence Eu-doped silicate glass ceramics”
The 4th international workshop on photoluminescence in rare-earth (PRE’12), Kyoto, Japan (2012)
5. “Broadband NIR photoluminescence from Ni^{2+} -doped nanocrystalline Ba–Al titanate glass ceramics”
The 11th ESG conference and ICG annual meeting, Maastricht, Netherlands (2012)
6. “Tunable ultra-broadband luminescence from Ni^{2+} -doped Ba–Al titanate glass ceramics”
The 10th International Symposium on Crystallization in Glasses and Liquids, Goslar, Germany (2012)
7. “Novel rare-earth and transition metal ions activated silicate glasses and glass ceramics for photoluminescence applications”
Chair of Glass and Ceramics (WW3), University of Erlangen-Nuremberg, Erlangen (2011)
8. “Luminescence from transition metal and rare-earth ions doped silicate glasses and glass ceramics”
Chair of Glass and Ceramics (WW3), University of Erlangen-Nuremberg, Erlangen (2010)

Posters

1. “Tunable dual-mode photoluminescence from Eu-doped $\text{Li}_2\text{ZnSiO}_4$ silicate glass ceramic phosphors”
G. Gao, S. Reibstein and L. Wondraczek, the 11th ESG conference and ICG annual meeting, Maastricht, Netherlands (2012)
2. “Tunable ultra-broadband luminescence from Ni^{2+} -doped Ba–Al titanate glass ceramics”
G. Gao, N. Da, S. Reibstein, S. Krolkowski and L. Wondraczek, EAM Young Researchers' Day, Erlangen, (2012)
3. “NIR luminescence from Ni^{2+} -doped nanocrystalline Ba–Al titanate glass ceramics”
G. Gao, S. Reibstein, E. Spiecker and L. Wondraczek, the third annual symposium of EAM, Oberhof (2011)
4. “Multi-mode luminescence from Eu- and Mn-doped glasses and glass ceramics”
G. Gao, N. Da, S. Reibstein and L. Wondraczek, the second annual symposium of EAM, Kloster Banz, Bad Staffelstein (2010)
5. “Viscosity, softening, crystallization and optical properties of sodium zinc sulfophosphate glasses”
G. Gao, N. Da, S. Reibstein, S. Krolkowski and L. Wondraczek, the 17th international symposium on non-oxide and new optical glasses, Ningbo, China (2010)
6. “Nucleation and crystallization behavior of sulfophosphate glasses”
G. Gao, S. Reibstein, N. Da, S. Krolkowski, L. Wondraczek, B. Champagnon, the 10th ESG conference and 84th DGG annual meeting, Magdeburg, Germany (2010)

Lebenslauf

Persönliche Daten

Name: **Guojun Gao**
Geburtsdatum und -ort: 14.01.1983 in Shanxi, China
Familienstand: Verheiratet
Staatsangehörigkeit: Chinesisch
E-Mail: guojun.gao@uni-jena.de

Ausbildung

09.1990 – 07.1995 Dongmao Grundschule, Shanxi
09.1995 – 07.1998 Linxian Dritten Mittelschule, Shanxi
09.1998 – 07.2002 Linxian erste Gymnasium, Shanxi
09.2002 – 07.2006 Studium der Werkstoffwissenschaften an der Technischen Universität Wuhan in Wuhan mit dem Abschluss B.Sc.
09.2006 – 07.2009 Studium der Werkstoffwissenschaften an der Chinesischen Akademie der Wissenschaften in Shanghai mit dem Abschluss M.Sc.

Berufliche Tätigkeit

10.2009 – 01.2013 Wissenschaftlicher Mitarbeiter am Lehrstuhl für Werkstoffwissenschaften (Lehrstuhl für Glas und Keramik) der Universität Erlangen-Nürnberg, Erlangen
seit 02.2013 Wissenschaftlicher Mitarbeiter am Otto-Schott-Institut der Friedrich-Schiller-Universität, Jena

Jena, den 1. August 2013

.....
Guojun Gao

Declaration of authorship/Selbständigkeitserklärung

I state that all works for this thesis are based on my own research, except as acknowledged.
It has not been previously submitted for a Ph. D. degree at this or at any other university.

Jena, the 1st of Aug 2013

.....

Guojun Gao

Ich erkläre, dass ich die vorliegende Arbeit selbständig und nur unter Verwendung der angegebenen Hilfsmittel, persönlichen Mitteilungen und Quellen angefertigt habe.

Jena, den 1. August 2013

.....

Guojun Gao